Dissertation

submitted to the
Combined Faculty of Mathematics, Engineering and Natural Sciences
of Heidelberg University, Germany
for the degree of
Doctor of Natural Sciences

Put forward by
Inga Kristina Kerber, M. Sc.
born in Weinheim
Oral examination: 08.11.2023

Precision, timing and frequency distribution of Th/U dated secondary carbonates

Referees:
Prof. Dr. Norbert Frank
Prof. Dr. Werner Aeschbach

Precision, timing and frequency distribution of Th/U dated secondary carbonates:

Many carbonate-based climate archives are dated using the ^{230}Th/U technique. Thus, further progress in measurement protocols for fast, accurate and precise age determination is required. With regard to growing age datasets, the closer examination of methods to extract information from age frequency curves through time becomes relevant. This thesis focusses on both aspects.
A simultaneous measurement protocol using a multi collector inductively coupled plasma mass spectrometer was optimized. New correction strategies for scattering signals with large impact (percent range) on age accuracy were described. A reference material was introduced for this, and a graphical user interface to ensure reproducible age analysis is presented.
A statistical data descriptor (adaptive Kernel Density Estimation) was systematically tested with an artificial dataset. This proved its ability to reconstruct complex variable signals, as are expected for the factors driving cold-water coral occurrence. Potential biases on datasets were discussed. Patterns of temporal coral occurrence were analyzed for several regions in the North Eastern Atlantic and Mediterranean Sea, and show signatures of multimodal growth in the last glacial in the Gulf of Cadiz, and different peak occurrences of two species during the Holocene in the Alboran Sea.

Präzision, Zeitintervalle und Frequenzverteilungen von Th/U datierten sekundären Karbonaten:

Viele karbonatbasierte Klimaarchive werden mit der ^{230}Th/U Methode datiert. Daher ist weiterer Fortschritt bei Messprotokollen für schnelle, akkurate und präzise Altersbestimmung vonnöten. Aufgrund wachsender Altersdatensätze wird die genauere Untersuchung von Methoden zur Extraktion von Informationen aus Altersverteilungskurven über die Zeit relevant. Diese Dissertation beschäftigt sich mit beiden Aspekten.
Ein simultanes Messprotokoll für ein Multikollektor induktiv gekoppeltes Plasma Massenspektrometer wurde optimiert. Neue Korrekturstrategien für Streusignale mit großem Einfluss (im Prozentbereich) auf die Altersexaktheit wurden beschrieben. Ein Referenzmaterial wurde eingeführt, und eine graphische Benutzeroberfläche für reproduzierbare Altersanalyse wird präsentiert.
Ein statistisches Datenbeschreibungs-Werkzeug (adaptive Kernel Density Estimation) wurde systematisch mit einem künstlichen Datensatz getestet. So wurde gezeigt, dass es in der Lage ist, komplexe variierende Signale zu rekonstruieren, wie man sie für die Faktoren erwartet, die die Muster des Auftretens von Kaltwasserkorallen beeinflussen. Möglicher bias in Datensätzen wurde diskutiert. Muster von zeitlichem Kaltwasserkorallen-Auftreten wurden für verschiedene Regionen im östlichen Nordatlantik und im Mittelmeer analysiert. Diese zeigen Signaturen von multimodalem Wachstum im letzten Glazial im Golf von Cadiz, und verschiedene Spitzenhäufigkeiten für zwei Spezies in der Alboransee.

Contents

1 Motivation

Without the development of radiometric dating methods, a great amount of our present scientific knowledge on the Earth's and other planets' geological history, the past and present of climate and environmental systems, and even the evolution and cultural progress of our own species would not have been accessible (e. g., Farley (2002), Siebel and Van den Haute (2009), Hellstrom and Pickering (2015), Gopalan (2017), Hajdas (2008)). In times of ongoing anthropogenic climate change, these insights become even more important.
One of the key chronometric techniques for the last 800 000 years is ^{230}Th/U dating, which produces precise ages for terrestrial and oceanic carbonate archives (Bourdon et al., 2003). The accessible carbonate archives, such as stalagmites and coral skeletons, are very well suited to reconstruct reactions of the atmosphere and the ocean to changing climatic forcings in the past. To do so, proxies such as trace elements or isotopic ratios are measured on the dated archives and allow for reconstruction of e. g. precipitation patterns, water mass evolution or seawater temperature (e. g., Fairchild and Treble (2009), McDermott (2004), Thompson (2022), Montagna et al. (2014), Henderson (2002)). Past climates are an important test case for climate models, i. e. on the (in geological terms) recent timescales accessible by ^{230}Th/U dating (Tierney et al. (2020), Braconnot et al. (2012)). Moreover, ^{230}Th/U dating can contribute to better understanding of specific ecological and geological processes. An example is the coral bleaching and mortality event history for individual reefs over the last centuries, as well as their recovery (Clark et al., 2014). Jackson et al. (2023) used water-table reconstructions based on ^{230}Th/U dated speleothems to better understand groundwater recharge in a dry region (Nevada, USA) under changing climatic conditions. Ages of surface travertines allowed Miocic et al. (2019) to calculate leakage rates of a naturally occuring CO_2 reservoir and conclude geological CO_2 storage (as in CCS - Carbon Capture and Storage techniques) to be secure.
The archaeological contributions of ^{230}Th/U dating are manifold: from dating cave art (e. g., Pike et al. (2017)) to understanding the influence of climatic changes on the rise and fall of the Maya civilization (e. g., Kennett et al. (2012)) and reconstructing the peopling of the Americas (e. g., Stinnesbeck et al. (2020)).
Given our current warming world pathway, it is of uttermost importance and urgency to collect more information about terrestrial and oceanic palaeoclimates as well as the changes ecological systems such as coral reefs undergo. Only equipped with this knowledge about local scenarios, adequate adaption strategies and measures to prevent damage can be taken. Thus, further progress in fast, but also precise and accurate, ^{230}Th/U dating measurement protocols is necessary to make this chronometer an even more accessible tool.

Large datasets of ^{230}Th/U ages, however, carry their own challenges. As age data pro-

duction has already accelerated over the last two decades, i. e. due to a change in the mainly employed mass spectrometer type, by now a large amount of coral and speleothem ages has been obtained (e. g., Cheng et al. (2013), Andersen et al. (2004), Scholz and Hoffmann (2008)). This number is going to increase further. Strategies for data organisation in databases have been established, e. g. SISAL for speleothem records (Comas-Bru et al. (2020), Atsawawaranunt et al. (2019)). The first studies that try to establish probability density of ages in an archive over time as a palaeoproxy itself have been conducted for speleothems (e. g., Baker et al. (1993)). Fewer of them have dealt with methodical developments (Hercman (2000), Weij et al. (2020)). The approach of using distributions of ages instead of, or additional to, full records offers some benefits: for example, in some settings, caves might be of high cultural and/or environmental value (Scroxton et al., 2016), so the extraction of full stalagmites is no option. Random sampled "rubble" from the floor, from which an age distribution as palaeoclimate proxy is determined, can be helpful (Weij et al., 2020). The same holds for the ocean floor, where drilling and coring might not be feasible everywhere. In addition, very local events that concern only one stalagmite or gravity core are averaged out. So there is also an advantage in looking at carbonate growth probabilities for settings in which also full records are available.

Statistical methods for large age datasets have not yet been explored in the field of cold-water corals, one of the most important archives accessible by ^{230}Th/U dating. Learning about the factors that enable the occurrence of cold-water corals on temporal and spatial scales is crucial to better understand their reaction to environmental changes. Cold-water coral structures are also an important carbon storage and contribute to oceanic carbon uptake (Titschack et al., 2009).

Research questions:

This thesis aims at increasing the knowledge we can gain from accurate and precise ages. This is tackled in the following chapters by adressing both complementary aspects: data generation and evaluation. The need for fast and reliable ^{230}Th/U data production will be the focus of Part 1. In Part 2, a method for age distribution construction including uncertainties is developed and applied to cold-water coral occurrences in the Mediterranean and Atlantic Ocean.
First of all, general fundamentals will be explained (Chapter 2). As the methods for both parts have no overlap, they will be explained directly within the chapters of Part 1 and 2. The following research questions will guide through the chapters of the two parts:

1. **Part 1: Improvements in ^{230}Th/U dating**
    a) How does an optimized simultaneous Th and U measurement routine look like? What is the influence of different raw data corrections on the final age accuracy for typical samples? **(Chapter 3)**
    b) Can the influence of scattering signals on specific masses be properly reduced

and accounted for?**(Chapter 4)**

c) How can a reproducible and user-friendly data analysis and age calculation routine be ensured? **(Chapter 5)**

2. **Part 2: Age frequency distributions**

a) Can complex input signals that influence the formation of carbonate archives (i. e. cold-water corals) be reconstructed by building age probability density curves? **(Chapter 6)**

b) What are the perspectives for this method? **(Chapter 7)**

Three publications and publication drafts are part of this thesis (Chapters 3, 5 and 6). Herein, Chapter 3 is already published in *Nuclear Instruments and Methods in Physics Research Section B: Beam Interactions with Materials and Atoms* (NIMB) (Kerber et al., 2023). Chapter 5 is going to be submitted to *Geochronology*, and Chapter 6 will be submitted to *Geochemistry, Geophysics, Geosystems*. All further information on the manuscripts is shown at the beginning of the respective chapters.

2 Fundamentals

This thesis addresses the improvement of the ^{230}Th/U dating method (Part 1: Chapters 3-5) and the development of tools for using age frequency distributions as a proxy for past environmental conditions (Part 2: Chapters 6 and 7). In this chapter, the basic principles relevant to both parts will be presented.
This applies to the ^{230}Th/U dating technique, the mass-spectrometric setup used for obtaining ages and (i. e. cold-water) corals. All introduction specific to only one part, such as the evolution of the statistical methods in Part II, will be described in the corresponding chapters.

2.1 ^{230}Th/U dating

Many carbonate-based archives of the past, such as corals or speleothems, can be dated accurately using the ^{230}Th/U dating technique (Bourdon et al., 2003). It is a radiometric method making use of the decay chain of ^{238}U and works for the time range up to 600 ka, in some cases even up to 800 ka (Cheng et al., 2013). In the literature, it is referred to as U-series, Th/U or ^{230}Th/U dating. In this thesis, the term ^{230}Th/U dating is used to be consistent with other works of this group. However, for the accepted publication in Chapter 3, the more general expression U-series dating was chosen.
Ages are measured by quantifying the return of the system to the secular equilibrium state, in which all activity ratios of isotopes along the decay chain are 1. Figure 2.1 shows the relevant isotopes of the decay chain of ^{238}U, which has ^{206}Pb as its stable end product. For age determination, the very short-lived isotopes ^{234}Th and ^{234}Pa are neglected, and only ^{234}U and ^{230}Th are used. Ivanovich and Harmon (1992) derive the following equations to calculate ages:

$$\left(\frac{^{234}\mathrm{U}}{^{238}\mathrm{U}}\right)(\mathrm{t}) = \left(\left(\frac{^{234}\mathrm{U}}{^{238}\mathrm{U}}\right)_{\mathrm{init}} - 1\right) \mathrm{e}^{-\lambda_{234}\cdot \mathrm{t}} + 1 \tag{2.1}$$

$$\left(\frac{^{230}\mathrm{Th}}{^{238}\mathrm{U}}\right)(\mathrm{t}) = 1 - \mathrm{e}^{-\lambda_{230}\cdot \mathrm{t}} + \frac{\delta^{234}\mathrm{U}}{1000} \cdot \left(\frac{\lambda_{230}}{\lambda_{230} - \lambda_{234}}\right) \cdot \left(1 - \mathrm{e}^{-(\lambda_{230}-\lambda_{234})\cdot \mathrm{t}}\right) \tag{2.2}$$

with

$$\delta^{234}\mathrm{U} = \left(\left(\frac{^{234}\mathrm{U}}{^{238}\mathrm{U}}\right)_{\mathrm{meas}} - 1\right) \cdot 1000\,(\,‰)\,. \tag{2.3}$$

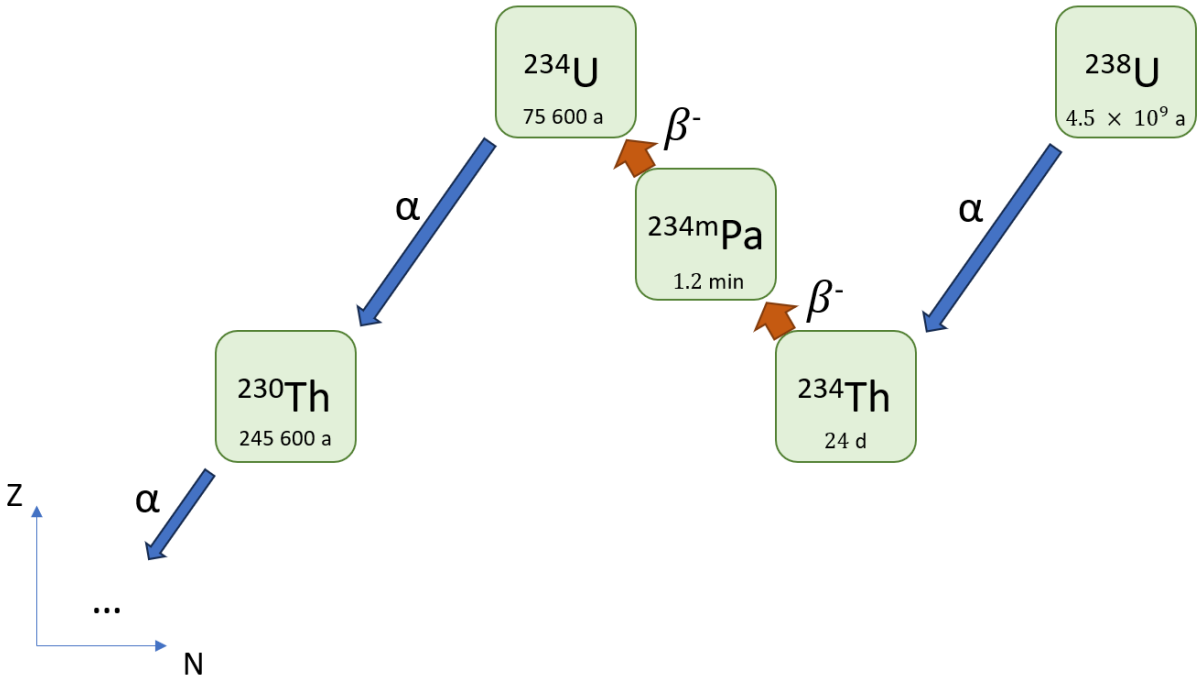

Figure 2.1: The first isotopes of the decay chain of ^{238}U, which is the part used in ^{230}Th/U dating, are presented with their half-lives denoted in the isotope boxes. The coordinate system denotes the change in the number of neutrons (N) and protons (Z) along the axis. Half-lives are rounded and taken from Jaffey et al. (1971) for ^{238}U, Bourdon et al. (2003) for ^{234}Th, Duchemin et al. (1994) for ^{234m}Pa and Cheng et al. (2013) for ^{234}U and ^{230}Th. In some sources, ^{234}Pa with a half-life of $\approx$ 7 hours is shown in the decay chain. However, ^{234}Th decays at 100 % to the excited ^{234m}Pa. Branching only occurs in the decay of ^{234m}Pa, in which $<$0.5 % decay not directly to ^{234}U, but via internal transition to ^{234}Pa first.
Due to their short half-lives, which implies no relevant build-up of those isotopic populations, ^{234m}Pa and ^{234}Th are neglected in ^{230}Th/U dating.

Here, t denotes the sample's age, λ_i the isotopes' decay constants and values in parentheses the activity ratios of the two isotopes. The equations are solved numerically and errors are calculated via Monte Carlo simulation.
During formation of a carbonate archive, the incorporated uranium is being purified from the thorium due to their different behaviour in the environment (Scholz and Hoffmann, 2008). Uranium is soluble in water because it mainly occurs as U^{6+} which forms uranyl ions $(UO_2)^{2+}$ when in solution (Bourdon et al., 2003). At the surface of the earth, the insoluble U^{4+} oxidation state is only more common than U^{6+} in reducing environments. The most common state for thorium is Th^{4+} with low solubility (Langmuir and Herman, 1980). Instead, it is particle reactive, and can e. g. stick to clay particles. As a consequence, natural waters do contain dissolved uranium but no thorium. All classical archives for ^{230}Th/U dating form $CaCO_3$ structures from water, and dissolved U can replace Ca at some positions in the lattice (Frank and Hemsing, 2021). This causes the elemental fractionation at formation, which is one of the conditions for the method to work and needed to "reset" the radiometric clock. The actual formation process depends on the type of archive: In the case of corals, their skeletons form via biomineralization processes and incorporate U dissolved in seawater. Speleothem formation is abiogenic and here U stems from the drip waters running through the karst above a cave, from which the carbonate precipitates (Fairchild and Baker, 2012).
Furthermore, archives need to fulfill the "closed system hypothesis". This means that no loss or additional deposition of the isotopes occurs after formation of the system (Scholz and Hoffmann, 2008).

2.1.1 Detritus correction

The above mentioned condition of no initial Th in the sample is not fulfilled by most real-world archives. Thus the age needs to be corrected for the initial ^{230}Th. Although ^{232}Th is the far most abundant Th isotope with approx. 100 % of Th atoms being of mass 232, the initially incorporated ^{230}Th is not zero. ^{232}Th has a half-life of 1.4×10^{10} a (Bourdon et al., 2003), so it can be considered stable on the time scales of ^{230}Th/U dating. In addition, it is no part of the ^{238}U decay chain. This means that the initial ^{230}Th can be corrected for by determining the ^{232}Th content of the sample and having an assumption on the initial $\left(\frac{^{230}\mathrm{Th}}{^{232}\mathrm{Th}}\right)$. The actual ratio between ^{230}Th and ^{232}Th can be very different for different archives and locations. If no additional information on their ratio in the detritus can be gained, the detrital material is assumed to be in secular equilibrium. Thus, the activity of ^{230}Th is the same as the one of ^{238}U (as well as the rest of the decay chain). Wedepohl (1995) determined the Th/U weight ratio of the continental crust as (4.10 ± 2.05), which is approx. the ratio of ^{232}Th and ^{238}U because both of them are the most abundant isotopes of their element (≈ 99.3 % for ^{238}U). Then the $\left(\frac{^{230}\mathrm{Th}}{^{232}\mathrm{Th}}\right)_{\mathrm{detr,init}}$ can be calculated from

$$\left(\frac{^{230}\mathrm{Th}}{^{232}\mathrm{Th}}\right)_{\mathrm{detr,init}} = \left(\frac{^{238}\mathrm{U}}{^{232}\mathrm{Th}}\right)_{\mathrm{m}} \cdot \frac{\lambda_{238}}{\lambda_{232}}. \tag{2.4}$$

The value is around (0.750 ± 0.375). To obtain corrected ages, the $\left(\frac{^{230}\mathrm{Th}}{^{238}\mathrm{U}}\right)_{\mathrm{corr}}$ ratio is used in the age equation 2.2 with

$$\left(\frac{^{230}\mathrm{Th}}{^{238}\mathrm{U}}\right)_{\mathrm{corr}} = \left(\frac{^{230}\mathrm{Th}}{^{238}\mathrm{U}}\right)_{\mathrm{meas}} - \left(\frac{^{232}\mathrm{Th}}{^{238}\mathrm{U}}\right)_{\mathrm{meas}} \left(\frac{^{230}\mathrm{Th}}{^{232}\mathrm{U}}\right)_{\mathrm{detr,init}} \exp^{-\lambda_{230}\mathrm{t}}. \tag{2.5}$$

The above mentioned value of (0.750 ± 0.375) is applied to standard materials, as e. g. described in section 3.2, and to speleothems with no additional information on the initial detrital thorium ratio. For cold-water corals, normally a $\left(\frac{^{230}\mathrm{Th}}{^{232}\mathrm{Th}}\right)$ in the water column of (8 ± 4) is assumed (Frank et al. (2009), Schröder-Ritzrau et al. (2003)). Hellstrom (2006) presents different methods for detritus correction in speleothems. This topic will be presented in more detail in Chapter 5. The uncertainties on the initial thorium ratios are often rather large. This error propagates to the final age uncertainty through the Monte Carlo simulations. Thus, any avoidable Th on the samples should be removed, so e. g. for corals there are thorough cleaning protocols (Schröder-Ritzrau et al., 2003).

2.2 Multi-Collector inductively-coupled-plasma mass spectrometry (MCICPMS)

The isotopic abundance ratios needed for age calculation are determined with a mass spectrometer, by separating ions based on their mass-to-charge ratio. Multi-collector inductively coupled plasma mass spectromters (MCICPMS) are the state of the art technology today in most ^{230}Th/U labs in the world, as well as for isotopic analysis in general (Hellstrom (2003), Shen et al. (2012), Cheng et al. (2013), Andersen et al. (2004), Chiang et al. (2019), Shao et al. (2019)). The structure and configuration of this instrument play an important role for understanding the corrections of the raw data, which are the fundament of Part 1 of this thesis and are explained in detail in Chapter 3.
The MCICPMS instrument hosted at the Institute for Environmental Physics, Heidelberg University, is a ThermoFisher Scientific *Neptune Plus* (Fig. 2.2). Taking the *Neptune Plus* as an example, the different modules and detectors of an MCICPMS will be explained in this section. The presentation in the following is based on Thermo Fisher Scientific (2009) and Arps (2017). For a historical overview and evolution of instruments used in ^{230}Th/U dating, as well as the advantages of MCICPMS over the other methods, the reader is referred to Arps (2017). This introduction focusses on an overview of the relevant concepts; quantification and further detail is part of Chapter 3.

Modules of the *Neptune Plus* mass spectrometer

Figure 2.2 presents the different functional units of the *Neptune Plus* MCICPMS. The sample enters the mass spectrometer through an **inlet system** (nebulizer), which is no part of the MS (and not presented in Fig. 2.2). For Th and U measurements at the

Institute for Environmental Physics, a CETAC Aridus II is used as a nebulizer. The main task of the inlet system is to produce an aerosol spray from the liquid, acid-based sample. This spray is then transferred to the plasma while being mixed with argon.
The first module of the MS itself is the **inductively coupled plasma (ICP)** module, which is responsible for the ionization of the atoms. This happens in the argon plasma (temperature > 8000K), which is contained by the so-called plasma torch consisting of two quartz tubes. The plasma is generated by an RF field, which is coupled into it by a load coil around the torch.
Around 2-3 % of the atoms pass the ionization and transmission stages and enter the **electrostatic analyzer (ESA)** in the case of the *Neptune Plus* hosted at IUP (Arps, 2017). The boundary between ICP and ESA is called plasma interface. It is the transition from normal pressure to high vacuum, which is completed in two steps via the sample and skimmer cone. Ions then get pulled into the ESA by the extraction lens. The ion optics focus the beam onto the entrance of the mass analyzer and accelerate it to finally 10 keV. The separation of isotopes according to their mass-to-charge ratio takes place in the 60° sector field of the **multicollector (MC)** module. The detector block, located at the end of the spectrometer, is equipped with a fixed centre Faraday cup (FC) and eight movable FCs. Ions that are focussed on the centre can also be counted on a secondary electron multiplier (SEM) instead of the central FC. In front of the SEM, a retarding potential quadrupole (RPQ) is installed. It filters out ions that have undergone e. g. a scattering event and have thus obtained a different energy and trajectory as the ions intended to hit the SEM. The RPQ will be further introduced in Chapter 3, as it is a relevant part in applying accurate tailing correction. The availability of multiple detectors that can measure ions of different masses at the same time is one of the main advantages of MCICPMS.
FCs measure signals in V and consist of the cup (a conductive material), which is part of a circuit with a high ohmic resistor. The available resistors (or amplifiers) are $10^{10}\Omega$, $10^{11}\Omega$, $10^{12}\Omega$ and $10^{13}\Omega$. They are referred to as amplifiers because the signal is the voltage measured over the high ohmic resistor. This implies that the $10^{13}\Omega$ amplifier is the most sensitive.
For the smallest signals, however, SEMs are used. When ions hit their surface, an electron cascade is produced between a stack of dynodes with potential differences. These electrical pulses are counted, so the signal is expressed as counts per second (cps). Calibration of SEMs against FCs (the so-called yield) is unstable over time (Arps, 2017). Thus, for isotopic ratios the same detector type should be used for both measurements.

Raw data corrections

Different processes influence the raw data (= signals) measured on the mass-spectrometer and need to be corrected for (e. g., Hoffmann et al. (2007), Shao et al. (2019)). The corrections will be described in detail in Chapter 3, here only a short overview shall be given.

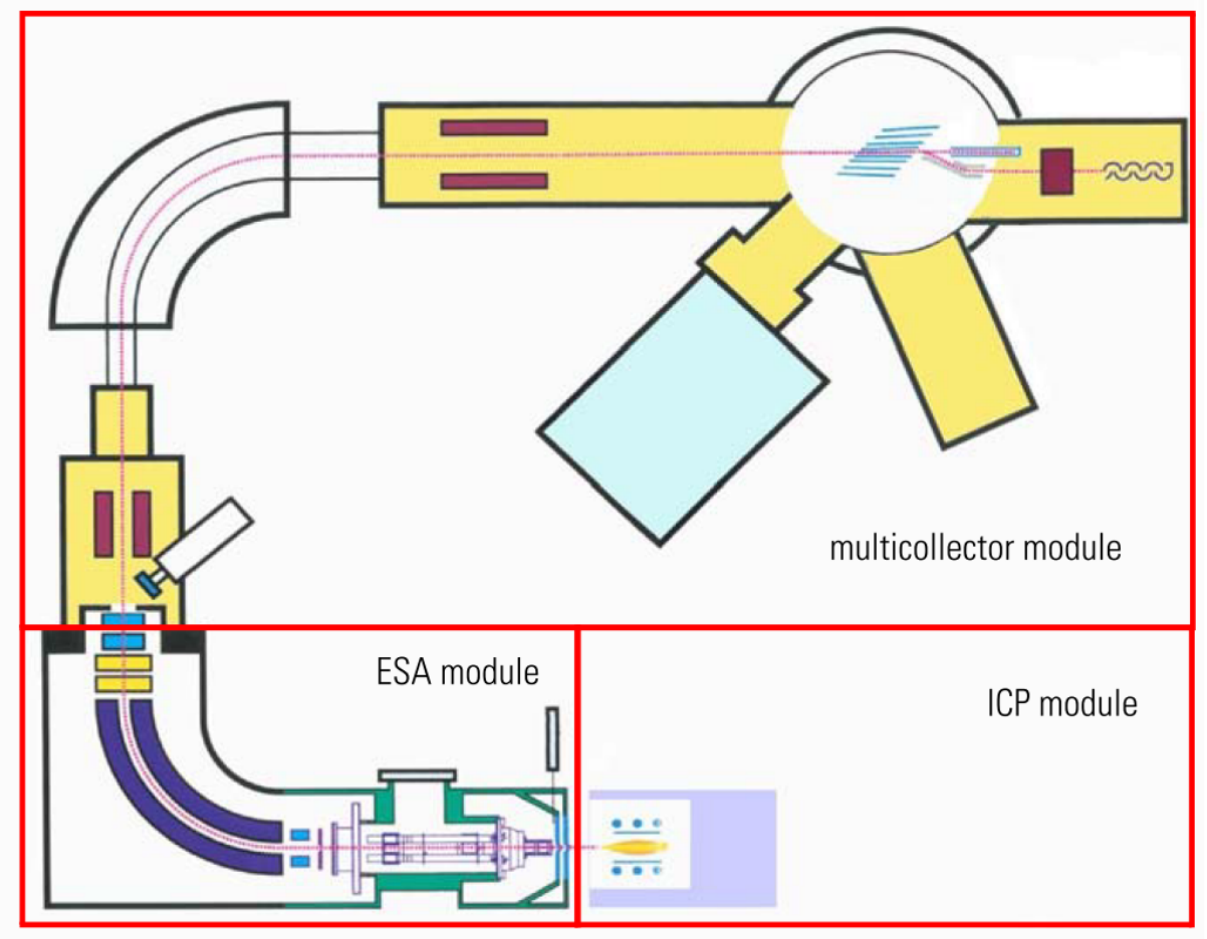

Figure 2.2: Setup of the *NeptunePlus* with its three funcional modules. The detector block is located at the right end of the multicollector module. The sample inlet system is no part of the spectrometer and not shown here. Image reprinted from Thermo Fisher Scientific (2009) with permission from ThermoFisher.

These effects have a variety of causes: firstly, there is scattering of ions. Highly abundant isotopes such as ^{238}U cause a relevant amount of additional counts on rare masses. The two corrections based on this principle are tailing and ghost signal correction. Furthermore, formation of multiple-atom-substances can cause interferences. This is relevant in the case of UH^+ and ThH^+ (hydride correction). Lastly, washouts of the inlet system between sample measurements are crucial. Otherwise, residual atoms of the previous sample are introduced in the spectrometer. The elevation of this background is determined before every measurement and then subtracted (process blank correction).

2.3 Corals

Before looking at the habitat and specifics of cold-water corals, let us zoom out and define corals. According to Cairns (2007) (page 312), corals are *"Animals in the cnidarian classes Anthozoa and Hydrozoa that produce either calcium carbonate (aragonitic or calcitic) secretions resulting in a continuous skeleton or as numerous, usually microscopic, individual sclerites, or that have a black, horn-like, proteinaceous axis."* This defintion applies to seven taxa within the two classes: order Scleractinia (= Madreporaria), order Zoanthidea (in part), order Antipatharia, subclass Octocorallia (= Alcyonaria), family Stylasteridae, family Hydractiniidae (in part), family Milleporidae (Cairns (2007)). This encompasses a broad collection of organisms.
All species within this thesis are from the order Scleractinia, which are also referred to as stony or hard corals as common names. Many of them allow for obtaining accurate ^{230}Th/U ages due to their robust aragonite skeletons. Among the Scleractinian corals are some of the species probably everyone thinks of first, which for example build the Great Barrier Reef. These make up about half of the Scleractinian species and live in symbiosis with zooaxanthellae which are photosynthetic algae (Roberts et al. (2009), Falkowski et al. (1984)). The so-called "zooxanthellate" corals can exist down to depths of 150 m (the limit, to which photosynthesis is possible) (Roberts et al., 2009). Some Scleractinian zooxanthellate species such as *Porites* have become important application fields for ^{230}Th/U dating to e. g. reconstruct past coral mortality events (Clark et al. (2014), Yu et al. (2006), Yu et al. (2010)). The two tropical corals used in the systematic dating part of this thesis are *Orbicella* species, belonging to the Scleractinian zooxanthellate as well.

Cold-water corals

There is, however, also a vast majority of coral species that are far less known than tropical reef corals. They live in colder waters and have no zooaxanthellae (thus they are "azooxanthellate") because most of them exist in water depths below the euphotic zone (the upper layer of the ocean, where photosynthesis is feasible) (Roberts et al., 2009). These species cover ocean depths as deep as 6328 m (Keller, 1976). These corals are synonymously referred to as cold-water and deep-water corals. Within this thesis, the term cold-water corals (CWC) is used. CWC are found within five of the seven coral taxa, except for Hydractiniidae and Milleporidae. Most of the Scleractinian CWC are non-constructional, meaning that they do not form reefs (Cairns (2007), Roberts et al. (2009)). There are 711 azooxanthellate Scleractinian species in total (Roberts et al., 2009). Around 25 % of them are colonial, while the rest lives solitarily (Cairns, 2007). Only 18 species are framework-forming, and as few as 6 build reefs (Roberts et al., 2009).

CWC have sparked interest as palaeoclimate archives over the last decades, because many trace elements they incorporate from the surrounding seawater during skeleton biomineral-

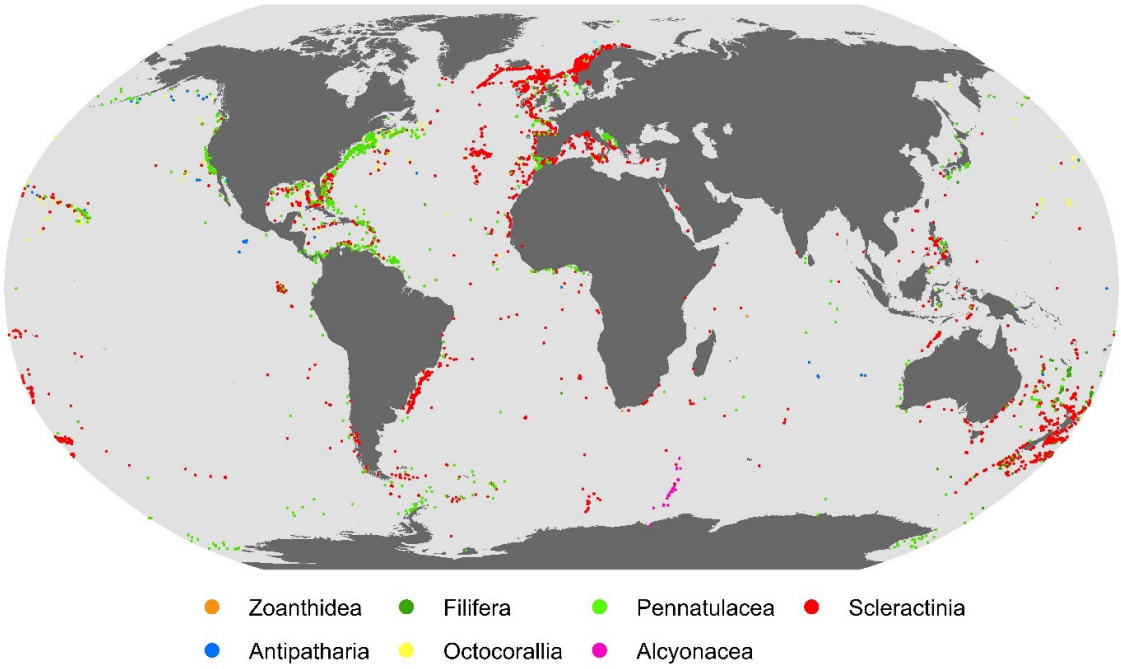

Figure 2.3: Global distribution of cold-water corals. The clustering of data points in the North Atlantic is probably due to sampling bias. Image extracted from Freiwald et al. (2021).

isation can be used as tracers for paleoceanographic parameters. For example for seawater temperature reconstruction the empirical Li/Mg calibration curve can be employed (Montagna et al. (2014), Cuny-Guirriec et al. (2019)). Other applications are summarized in Raddatz and Rüggeberg (2021) and Robinson et al. (2014). Another advantage is their cosmopolitan occurrence: CWC cover all ocean basins from Antarctic to Arctic (Freiwald et al., 2021), as can be seen in Fig. 2.3. Among all CWC, the framework-forming scleractinian species have been best researched so far (Freiwald, 2005). As habitat builders they offer ecosystems for many other marine species and are thus of exceptional interest among the CWC species (Henry and Roberts, 2017). They are also important hotspots for biodiversity in the deep sea (Henry and Roberts, 2017).

The most common framework-forming Scleractinian CWCs are *Lophelia pertusa* and *Madrepora oculata*, depicted in Fig. 2.4 and 2.5. Both species were among the first CWC to be described, already in 1758 by Carl von Linné (Linnaeus) (Roberts et al., 2009).
Lophelia pertusa is the most abundant of the framework-forming CWC species (Tong et al., 2022). Recently, Addamo et al. (2016) found a close genetic relationship between *Desmophyllum dianthus* (a solitary CWC) and *L. pertusa* and suggested to reassign the

species to the genus *Desmophyllum*. Here, the term *L. pertusa* is used to avoid confusion with earlier publications and following the suggestion of S. Cairns in WoRMS (World Register of Marine Species) (Cairns, 2019). As can be seen in Fig. 2.4, the skeleton of the coral is relatively robust, i. e. compared to *M. oculata* in Fig. 2.5. It can grow in bush-like colonies from several thousand coral polyps that extend to several metres (Roberts et al., 2009). Within these colonies, branches can fuse and further strengthen the structure (Roberts et al., 2009). The geographical distribution of *L. pertusa* is worldwide with the highest concentration in the Atlantic (Tong et al., 2022).
Madrepora oculata has a thinner and more fragile skeleton, as Fig. 2.5 shows. Hence, for this species it is more difficult to maintain as robust reef structures as for other species and they often co-occur with e. g. *L. pertusa* (Roberts et al., 2009). This species has a similar geographical extent as *L. pertusa* (Roberts et al., 2009). The two species have slightly different environmental preferences, as will be described later, so some areas are dominated by *M. oculata*. One example are today's Mediterranean Sea coral communities (Corbera et al., 2021).

Environmental controls

For inital settlement of coral larvae, an ocean ground of hard substrate, such as cliff structures, but also dropstones or shell fragments, is the limiting factor (Wienberg and Titschack (2017), Roberts et al. (2009), Wheeler et al. (2007)). This changes after the first growth phases, when fossil corals build the substrate their successors can grow on and rocky ocean floor is no neccessary condition anymore (Wilson, 1979). Oceanographic and environmental conditions that decide on the possibility of coral growth are firstly oxygen and food availability, but also include temperature, salinity, and chemical and biological parameters such as aragonite saturation, pH and primary and export production (Davies et al. (2008), Davies and Guinotte (2011), Flögel et al. (2014), Movilla et al. (2013), Naumann et al. (2014), Wienberg and Titschack (2017), Hebbeln et al. (2020)). Different species have slightly different preferences regarding their environmental parameter tolerance limits (Wienberg and Titschack, 2017). Once the other tolerance limits are met, the most important among the control factors for occurrence is food availability (Buhl-Mortensen et al., 2017). Wienberg and Titschack (2017) evaluated the environmental parameters for *L. pertusa* and *M. oculata* in the North Atlantic, including the Mediterranean Sea and the Gulf of Mexiko. They find both species appearing in waters between 1 and 14 °C. *L. pertusa* prefers slightly colder waters (6.5-8 °C), and *M. oculata* warmer environments of 8.5-10 °C (Wienberg and Titschack, 2017). Ocean floor environments with internal waves are particularyly favourable for coral growth, as this increases food transport to the sessile corals (Frederiksen et al. (1992), Duineveld et al. (2007), Mienis et al. (2007), Mohn et al. (2014)).
The conditions in different locations can change over time and thus change the presence or absence of CWC (Frank et al., 2011). This is demonstrated for different regions and time intervals in Fig. 2.6 (Wienberg and Titschack, 2017), where the distribution of North

Atlantic CWC ages on the Holocene (0-11.7 ka BP), the Younger Dryas (11.7-12.9 ka BP), the Bølling-Allerød (12.9-14.6 ka BP) and the last glacial (14.6-71 ka BP) is shown. The last glacial consists of the marine isotope stages (MIS) 2 to 4.

Sampling of cold-water corals

There are different methods to extract fossil and living corals from the seafloor. The earliest devices, which were employed for most of the twentieth century as well, were dredges (DR) (Roberts et al., 2009). They consist of metal grates and a chain bag connected to them. Today, they are not in use anymore due to their harmful impact to the seafloor's ecosystems and the non-selective sampling method (Roberts et al., 2009). Some ^{230}Th/U ages of CWC sampled by dredging are included in the dataset in Chapter 6. Other methods to sample corals near the surface are box corers (BC), grab sampler (GS) and remotely operating vehicles (ROV). BC and GS can sample from the seafloor, and the latter are videoguided in some cases (Hebbeln et al. (2017), Roberts et al. (2009)). ROVs are well-suited for selective sampling, e. g. of individual corals (Roberts et al., 2009).
Gravity corers (GC) consist of a metal pipe and an internal plastic pipe with a standard length of 5.85 m, wherein several of those can be connected (Hebbeln et al., 2017). On top of the pipe is a weight to push it into the sediment. They can penetrate several meters into the seafloor, which enables the extraction of coral-bearing sediments from cold-water coral mounds. Other types of corers are piston corers (PC) and drill corers (DC) (Roberts et al., 2009). Seafloor drill rigs, e. g. the MARUM-MeBo70 and MeBo200, are neccessary when the setting is to lithified for extraction with the other tools Roberts et al. (2009). MeBo can drill cores of 70 m resp. 200 m (Freudenthal and Wefer, 2013).

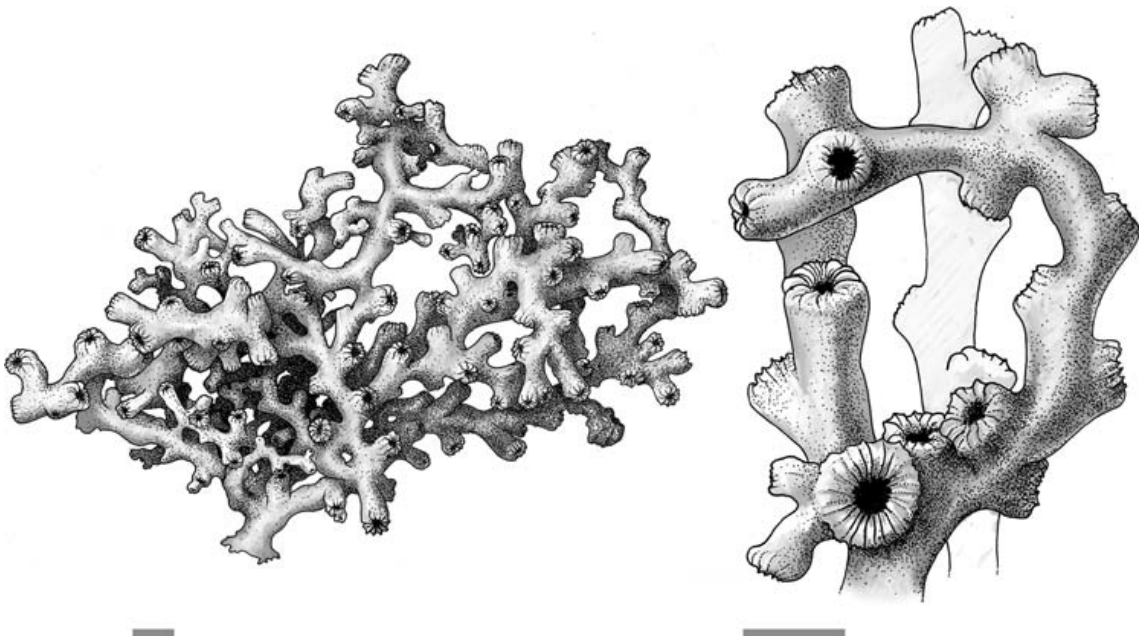

Figure 2.4: Drawing of *L. pertusa*. The scale bars represent 10 mm. On the left, a framework is shown, while the right depicts corallites with ther calices (the skeletal cups housing the coral polyps) in which the polyps live. Image reprinted from Roberts et al. (2009) with permission from Cambridge University Press.

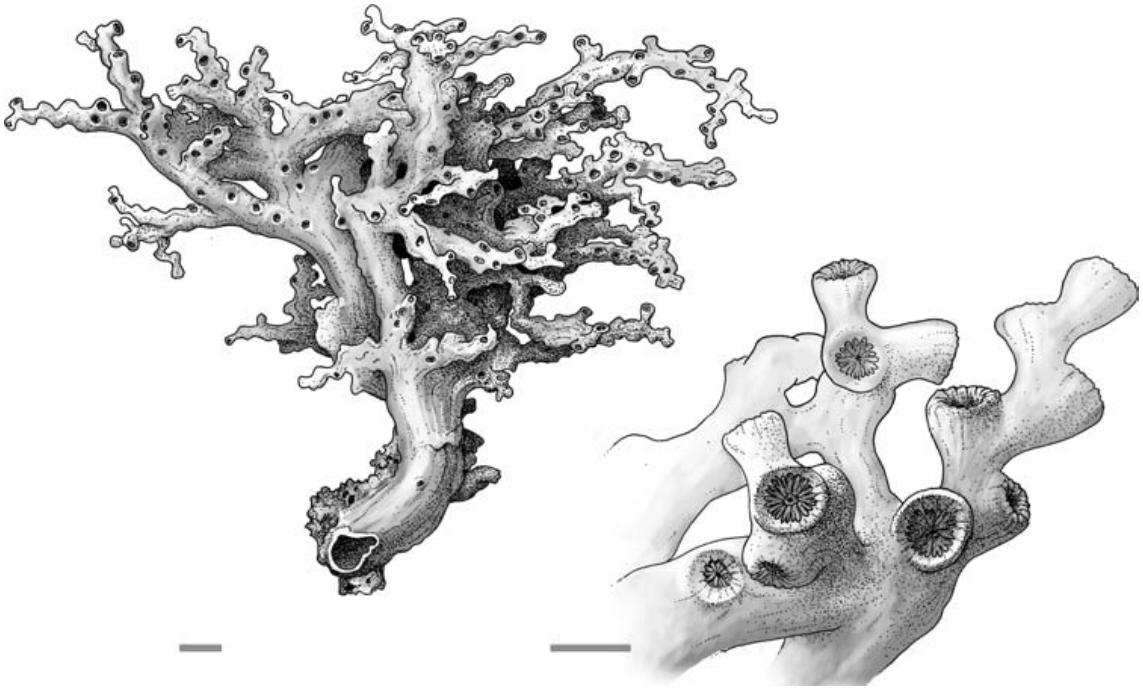

Figure 2.5: Drawing of *M. oculata*. The left scale bar is 10 mm, and the right one represents 4 mm. Again, on the left, a framework is shown, and on the right corallites with ther calices in which the polyps live. Image reprinted from Roberts et al. (2009) with permission from Cambridge University Press.

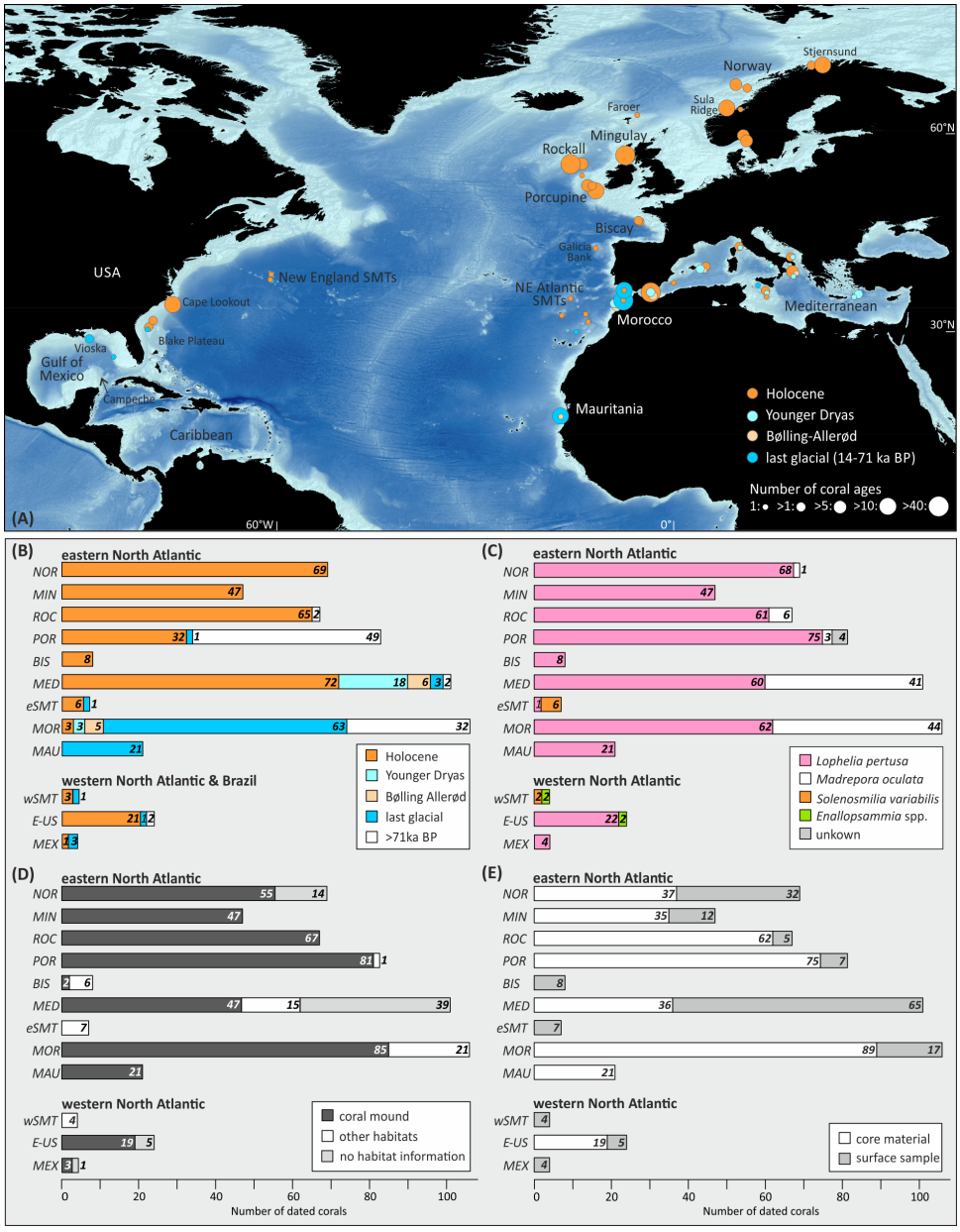

Figure 2.6: Geographical and temporal distribution and classification of cold-water corals in the North Atlantic. Image reprinted from Wienberg and Titschack (2017) with permission from Springer. Panel a) shows the spatial origin of 580 ^{230}Th/U and ^{14}C CWC ages. The climatic time intervals the dataset is grouped into are shown in the lower right of Panel a). Panel b) presents the temporal subdivision per region as a bar chart. The regional abbreviations are: NOR- Norway/ Faroer, MIN- Mingulay Reef, ROC- Rockall Bank, POR- Porcupine Seabight, BIS- Bay of Biscay, MED- Mediterranean Sea, eSMT- North East Atlantic seamounts, MOR- Moroccan margin, MAU- Mauritanian margin, wSMT- New England seamounts in the NW Atlantic, E-US- eastern US margin, MEX- Gulf of Mexico. In Panel c), the coral species are plotted and in panel d), their distribution on different habitats is shown (other settings are e. g. fjords or seamounts). Panel e) shows the sampling origin of the dated corals.

Part I

Improvements in ^{230}Th/U dating

3 Simultaneous U and Th isotope measurements for ^{230}Th/U dating using MCICPMS

In this chapter, the ^{230}Th/U dating measurement protocol at IUP Heidelberg will be described, with a particular focus on the effects of different raw data corrections on age accuracy. The chapter is published in *Nuclear Instruments and Methods in Physics Research Section B: Beam Interactions with Materials and Atoms* (NIMB) (Kerber et al., 2023). The figures here are black and white as in the original publication. Some results, i. e. in tables, are presented in the supplementary material of Kerber et al. (2023) for better readibility. In this chapter, these parts have been moved to the main text. Some of the remaining additional information of the supplement is presented in the Appendix of this thesis. Unlike in the rest of the thesis, in this chapter the term U-series dating (instead of ^{230}Th/U dating) is used.

The evaluation of the performance and stability of the measurement protocol, as well as the analysis of influences of the correction factors were carried out by myself during my PhD project. The progress achieved here built up on the PhD project of Jennifer Arps (Arps, 2017), who had introduced MCICPMS ^{230}Th/U dating for this research group in Heidelberg, and carried out tests on precision, correction factors and (in a bachelor project she supervised; bachelor thesis by Christoph Dornick) decay times of the amplifiers. Since then, new strategies and effects were discovered and analysed (e. g. the RPQ factors or the ghost signals). Some first descriptions were included in my master thesis (RPQ factors), and in the master thesis of Athulya Babu on young corals, which I co-supervised (ghost signals). The implementation of the optimized measurement protocol and data evaluation was accomplished during my PhD.

3.1 Introduction

U-series dating (also referred to as ^{230}Th/U dating) is a vital chronographic tool for determining the timing of carbonate palaeoclimate archives (Bourdon et al., 2003). Recent examples for new insights gained by its broad applications are ^{14}C calibration using speleothems, travertine and speleothem growth reconstructions, cave art dating, reconstruction of the evolution of human civilization, precise timing of past sea level changes and dating tectonic movements and climate change as well as the evolution of marine coral ecosystems (Gao et al. (2013), Yu et al. (2006), Hernández-Mendiola et al. (2011),

Shao et al. (2017), Spötl and Cheng (2014), Cheng et al. (2016), Lascu et al. (2016), Moseley et al. (2016), Al-Mikhlafi et al. (2018), Fensterer et al. (2010), Reimer et al. (2013), Asmerom et al. (2010), Beck et al. (2001), Biller-Celander et al. (2021), Wefing et al. (2017), Warken et al. (2021), Steidle et al. (2021), Therre et al. (2020), Frank and Hemsing (2021)). In addition, sub-‰ precision of ^{234}U-excess measurements of marine carbonates opened up new routes for the study of global weathering patterns and ocean dynamics (Robinson et al. (2004a), Robinson et al. (2004b), Chen et al. (2016), Chutcharavan et al. (2018), Esat and Yokoyama (2006), Esat and Yokoyama (2010), Chiang et al. (2019)), while precision measurements of the natural $\left(\frac{^{238}\mathrm{U}}{^{235}\mathrm{U}}\right)$ atomic ratio allow its use as a palaeo-redox tracer (Bopp et al. (2010), Romaniello et al. (2013), Brennecka et al. (2010)).

Obtaining precise and accurate radiometric U-series ages requires accounting for the large differences in abundance between ^{238}U, ^{235}U and ^{234}U (e.g., $\left(\frac{^{238}\mathrm{U}}{^{235}\mathrm{U}}\right) \sim 140$ and $\left(\frac{^{238}\mathrm{U}}{^{235}\mathrm{U}}\right) \sim 10^4$) and between ^{230}Th, ^{232}Th and the U isotopes (up to $\left(\frac{^{238}\mathrm{U}}{^{230}\mathrm{Th}}\right) \sim 10^8$ in simultaneous Th and U isotope measurements). Other important factors are the concentrations of the abundant ^{238}U and ^{232}Th isotopes, which can vary by over four orders of magnitude in natural materials, and the high ionization energies. Double focussing multi-collector inductively coupled plasma source mass spectrometry (MCICPMS) has become the leading technique in U-series disequilibrium dating and for precise U-isotope measurements, as it offers solutions to these issues, such as high ionization and transmission efficiencies (on the order of a few percent) and a high abundance sensitivity allowing for the simultaneous measurement of rare and prevalent isotopes (Frank and Hemsing (2021), Hoffmann et al. (2007)). The technical developments in combination with adapted measurement protocols and detector setups made ϵ-precision (i.e., $1\,\epsilon$-unit $= 10^{-4}$) feasible (Andersen et al. (2004), Cheng et al. (2013), Hellstrom (2003)). As the use of MCICPMS has allowed for acceleration of data production and has yielded an ever-growing wealth of new applications, systematic studies are emerging that focus on particular aspects such as the high precision dating of annually layered speleothems and corals (Chiang et al. (2019), Shen et al. (2008)). As a consequence of the constantly increasing amount of data, guidelines for the publication of U-series data have been proposed (Dutton et al., 2017). Measurement protocols, either in peak-jumping mode or using a combination of simultaneous Faraday cup (FC) and secondary electron multiplier (SEM) measurements, have been improved with regard to smaller sample input masses and/or by offering increased precision and accuracy (Chiang et al. (2019), Hoffmann et al. (2007), Cheng et al. (2013), Shen et al. (2012), Cheng et al. (2000b)). In general, measurements are composed of a sequence of calibration routines followed by an arrangement of blank – standard – blank – sample measurements using a bracketing method to account for all isobaric interferences and drifts as well as instrumental mass discrimination. The reference material Harwell-Uraninite 1 (HU-1), thought to be in secular equilibrium, is often used as a bracketing standard in such sequences (Wefing et al., 2017).

All measurement protocols require numerous raw data corrections. Here, we revisit the importance of factors determining the accuracy and precision of measurements through a

systematic study of simultaneous Th and U isotope measurements. First, the nonlinear tailing is evaluated, which is created by the significant scattering of ^{238}U and ^{232}Th beams on the lighter isotopes due to their high abundance. The extent of the tailing is normally determined by measuring half-mass counts of a specific standard solution at the start of a measurement sequence and extrapolating to full masses by applying a fitting function (Hoffmann et al., 2007). Different sets of half-masses and types of fitting functions, such as combined exponential and linear functions, have been described in the literature (Hoffmann et al. (2007), Shao et al. (2019), Shen et al. (2002)). Shao et al. (2019), for example, use a combination of exponential and linear functions. Shen et al. (2002) and Hoffmann et al. (2007) describe the tail by an exponential function. Here, we propose the use of a Hermite interpolating polynomial, which best fits the observations. Second, hydride correction is necessary due to the formation of UH^+ and ThH^+ ions (1 amu heavier than the respective U or Th ion) in the plasma source of the mass spectrometer. These isobaric interferences are normally determined before a measurement sequence by measuring 239 amu and 233 amu together with the tailing half-masses. Furthermore, there is the process blank, referring to the monitored residual signal on all relevant isotopic masses after the acid rinse between the sample and a standard ('instrumental background'). Despite the similar term, it needs to be differentiated from the total procedural blank during the chemical preparation step (blank sample). The acid rinses after each sample or standard measurement shall minimize the memory effect caused by isotopes contaminating the next sample, e.g., by clinging to the inlet system's tubing. Last, a so-called "ghost signal" on mass 230, possibly due to a scattering peak, has been reported (Chiang et al., 2019). This study describes only one such peak and did not observe similar signals on other masses, e.g., at 229 and 232 amu. If these signals occur, subtracting them is another essential aspect of raw data correction.

In this study, we present experimental procedures for highly precise measurements of Th and U isotopes and ages compared to the method previously published (Wefing et al., 2017). We further determine the influences of detector fade-out times using ultrahigh ohmic resistors and describe updated procedures for tailing determination and the correction for "ghost signals". We systematically reanalysed the effect of the described raw data corrections on the ages. The achieved precision is demonstrated on three samples of different ages and isotopic compositions. We demonstrate the success of the full data treatment by improving the ^{230}Th/U age accuracy of modern corals dated via the layer counting method. Moreover, a previously dated speleothem from Spannagel cave in the Austrian Alps is measured close to our $5\,\epsilon$ theoretical limit of statistical precision with a total age uncertainty of $7.5\,\epsilon$ ($2\,\sigma$).

3.2 Materials and methods

3.2.1 Standard materials and spikes

For calibration purposes and standard–sample bracketing, we use the Harwell Uraninite HU-1, for which the activity ratios $\left(\frac{^{230}\mathrm{Th}}{^{238}\mathrm{U}}\right)$ and $\left(\frac{^{234}\mathrm{U}}{^{238}\mathrm{U}}\right)$ are assumed to be 1, since our HU-1 was originally produced from the initially distributed powder without insoluble residue. For the determination of the peak tailing of the abundant ^{238}U mass, we employ the standard material CRM-112A with a ^{238}U concentration of $(4.3021 \pm 0.0015)\,\mu$g/g ($2\,\sigma$ uncertainty), which is diluted such that we reach $\sim$100 V on ^{238}U (Bingham, 1987). The peak tailing of ^{232}Th is measured using an in-house Th standard that has a ^{232}Th concentration of (505.8 ± 1.02) ng/g ($2\,\sigma$ uncertainty). For concentration measurements, our in-house triple spike (TriSpike) solution is used, which is a mixture of an U double spike (UDop) and the ^{229}Th spike solution ThSpike that were previously calibrated as described by Hoffmann et al. (2007). We recalibrated the TriSpike as described in the Appendix. ^{238}U has a concentration of (3.86778 ± 0.00009) ng/g in the spike, and ^{229}Th's concentration is (0.018055 ± 0.000008) ng/g. All spike concentration uncertainties are given as 2 standard errors of the mean. ^{233}U is only present in the spike for historical reasons and is not used here in measurement evaluation.

3.2.2 Sample materials

To estimate our measurement precision and uncertainty, we chose three samples that differ in U and Th concentrations and ages (Table 3.1) in addition to the frequently measured secular equilibrium standard HU-1. This is because the signal intensities of the isotopes measured by the detectors of the mass spectrometer directly depend on the isotope concentration in the raw material. A high signal intensity implies excellent measurement statistics and thus allows for higher precision than a smaller signal, presuming a statistical nature of the signal. Since not all samples measured in everyday operation are ideal samples, we investigated typical precision levels for different combinations of isotope concentrations. Our selection spans a range from the young stalagmite E8-21 ($\sim$400 years), which has low concentrations in U and Th, to SPA52A, a flowstone of particularly high U concentration and low Th concentration that is thus very close to the "ideal" sample described before. SPA52A was collected from Spannagel Cave located in the Zillertal Alps (Austria) and has been employed previously to date the onset of speleothem growth at the end of the last glaciation $\sim$135 ka ago (Spötl et al., 2002b). The sample used for systematic analysis here was taken at 6 cm dft from the Unit 3 growth phase as defined by Spötl et al. (2002b). The two speleothem samples are complemented by a fossil cold-water coral from the Azores region that has an age of $\sim$50 ka.
To constrain the existence of potential interferences on the mass 230 amu, we have additionally analysed two modern tropical corals with known ages derived from band counting. BOC2-45mm is a sample from a coral core drilled from an *Orbicella faveolata* in Mexico

that corresponds to the 2009 calendar year, while CPR-55mm (*Orbicella annularis*) is a section of a core collected in the Eastern Caribbean (La Parguera, Puerto Rico) and dates to the year 1982. Finally, to demonstrate the overall precision of routine measurements, we employ averaged uncertainties of measured activity ratios and ages from two cold-water coral-bearing gravity cores off of Angola, which cover an age range between 0.1 and 25 ka BP (in preparation: Lausecker et al.).

Lab Code	Sample ID	Material	Origin	[^{238}U]	[^{230}Th]	Age BP [a]	Study
IUP-11341	E8-21	Stalagmite	Áaktun Kóopo', Estrella, Mexico	∼1.1 ppm	∼0.07 ppt	335.8 ± 8.0	this study
IUP-10392	GeoB23183-1 L.p.2 (ref. to as GeoB coral)	Cold-water coral	Azores, Portugal	∼3.5 ppm	∼23 ppt	47 308 ± 144	this study
IUP-7184	SPA52A (referred to as SPA52)	Flowstone	Spannagel cave, Austria	∼84 ppm	∼1 ppb	134 975 ± 101	(Spötl et al., 2002b) (Arps, 2017)

Table 3.1: Properties of the carbonate samples used within this study.

3.2.3 Sample preparation

Depending on the U concentration and age, input sample masses are ∼50 mg for corals. Coral U concentrations are typically in a narrow range of 2-3 μg/g for tropical corals and 3-5 μg/g for cold-water corals, which allows us to sample mostly the same amount of material (here ∼50 mg). For speleothems and other continental carbonates, there is no reference sample mass value due to the enormous range of possible U concentrations spanning from a few ng/g to hundreds of μg/g. For the analyses presented here, the sample sizes used for chemistry and mass spectrometry were ∼80 mg for E8-21, ∼50 mg for the coral and ∼100 mg for SPA52. Unlike for the other two samples, Th and U fractions were separated for SPA52, and only a small part of the U fraction (<10 %) was admixed to the Th fraction for measurement according to the protocol presented by Matos et al. (2015). Sample masses of the modern tropical corals were ∼240 mg for both CPR-55mm and BOC2-45mm.

U and Th need to be purified from their calcium matrices to avoid interferences in the mass spectrum and to provide optimal ionization efficiency. Our chemical preparation method follows previously published procedures (Wefing et al. (2017), Matos et al. (2015), Douville et al. (2010)). It involves sample dissolution and spiking followed by wet column extraction chromatography using Eichrom UTEVA resin. Chemical yields are on average 90 % for U and Th (Wefing et al., 2017). Total chemistry blanks were frequently included in the extraction series and were determined to be < 0.4 fg for ^{234}U and < 40 ag for ^{230}Th. U and Th fractions were admixed in 1 % HNO3 and 0.05 % HF solution to minimize Th and U memory effects in the tubing and torch of the interface during mass spectrometric measurements.

3.2.4 Instrumental setup and measurement procedure

Activity ratios are measured with an MCICPMS (ThermoFisher NeptunePlus) coupled with an Aridus II desolvating system. This setup reaches 2-3% ionization and transmission efficiency (Arps, 2017), which is similar to the number reported by Chiang et al. (2019) and twice as much as described in Shen et al. (2012).
The MCICP mass spectrometer is equipped with an SEM placed behind a static retarding potential quadrupole (RPQ) in the centre and the FCs are connectable to high ohmic amplifiers of different resistances from $10^{10}\,\Omega$ to $10^{13}\,\Omega$. The chosen connections of the amplifiers at our instrument are presented in the Appendix (Table B.2). Most importantly, the $10^{13}\,\Omega$ amplifier is connected to the centre cup. The ion optical element RPQ exerts its filtering effect by decelerating the ions to almost zero potential, resulting in the rejection of all ions not focused on the central beam or having the wrong velocity due to scattering events. This improves abundance sensitivity by an order of magnitude to <500 ppb and is thus a crucial device for ^{230}Th and ^{234}U isotope measurements.
The principle measurement procedure is outlined as follows: The reference material, HU-1, is measured before and after each sample with the same settings. Standard-Sample-Standard bracketing is used to ultimately normalize isotope ratios for machine drift and deviation from secular radioactive equilibrium values, which comprises all unknown influences that cannot be removed by the corrections presented in the following sections. The process blank (1% HNO3 and 0.05% HF) was measured for approximately 70 seconds before each sample or standard. It indicates whether the instrument has returned to a clean state. Typical blank levels indicating a clean state of the instrument are 2 counts per second (cps) for ^{229}Th, 0.5 cps for ^{230}Th, $9 \cdot 10^{-3}$ mV for ^{232}Th, $4 \cdot 10^{-3}$ mV for ^{233}U, 6 cps for ^{234}U, 0.015 mV for ^{235}U, $4 \cdot 10^{-3}$ mV for ^{236}U and 2.4 mV for ^{238}U. Cps is the unit for isotopes measured on SEM and mV for isotopes measured on FC; generally, 1 mV corresponds to 62500 cps. Process blanks are subtracted from the subsequent measurement. Over the course of a measurement day or when working with particularly high-intensity samples and standards, the process blank may increase over time. Samples are therefore always arranged in order of increasing intensity.
Figure 3.1 shows the nonlinear behaviour of the ^{238}U tailing. This is presented analogously for ^{232}Th (Fig. 3.2). To correct for this, at the start of each sequence, an unspiked CRM-112A solution is measured to quantify the tailing and hydride formation. For the ^{238}U tailing, we measured the half-masses 228.5, 233.5, 236.5, 236.7, 237.05 and 237.5. Due to an instrument-specific scattering peak (see Fig. 3.1), we choose the first half-mass included in the fit between 227.5 and 228.5 depending on the location of that peak. This does not change the extrapolation function since it only needs to be ensured that the half-mass is not affected by a scattering peak. The ^{232}Th tailing is determined by measuring 227.5, 228.5, 229.5, 230.5 and 231.5 of the in-house ^{232}Th standard equally at the start of each sequence. We then correct the isotopes ^{233}U, ^{234}U, ^{235}U, ^{236}U, ^{229}Th, ^{230}Th and ^{232}Th for the ^{238}U tailing and subsequently ^{229}Th as well as ^{230}Th for ^{232}Th tailing. In Fig. 3.1, we compare an exponential fit of the ^{238}U tail with a piecewise cubic

Hermite interpolating polynomial (PCHIP) approximation. The latter method employs a combination of monotonic cubic splines for extrapolation. We find a better match of the PCHIP fit compared to the exponential fit, especially for mass 236. In the case of ^{232}Th, the same fitting method is chosen (see Fig. 3.2).
To ensure enough counts ($\sim$ 5-10 cps) on the least abundant masses, the solutions for tailing determination should be measured at signals of approximately 100 V for ^{238}U and 2 V for ^{232}Th. As stated, hydride correction is measured together with the tailing, which means that masses of 239 amu and 233 amu are observed in the solutions. As these masses do not occur in the standard solutions, they must be produced by the hydride formation of ^{238}U and ^{232}Th, respectively. During raw data analysis, UH^+ correction is applied to ^{234}U, ^{235}U and ^{236}U, and ThH^+ correction is applied to ^{230}Th.

3.2.5 Data treatment and age calculation

Baseline and dark noise subtraction as well as gain and yield correction are carried out online, i.e., using the mass spectrometer's software. For offline raw data treatment, corrections and age calculation, we use an integrated Python-based algorithm that can be accessed at `https://github.com/EnvArchivesHD/UTh_Analysis`. The offline corrections comprise signal outlier removal, mass fractionation correction, and tailing and hydride and process blank correction. Age calculation is based on the equations from Ivanovich and Harmon (1992), which are solved numerically. The age uncertainty is determined using a Monte Carlo simulation.

3.3 Results

3.3.1 Detector characteristics and data acquisition

The measurement protocol was created with respect to instrumental detector availability. When measuring signals on FCs, their fade-out times need to be considered in the measurement protocols when jumping to the next magnetic field setting. Fade-out time refers to the time it takes for a signal on the cup to decay and depends on the design of the respective circuit. Starting the next measurement too early results in a remnant signal from the isotope measured before, while an idle time that is too long leads to changing measurement conditions, e.g., induced by plasma fluctuations, and should thus be avoided as well. We measured fade-out times at different signal intensities by establishing a ^{238}U signal on the cup using CRM-112A solution. The respective amplifier was set to an integration time of 0.131 seconds and an idle time of 0 seconds for data collection. Signal intensities were chosen in the range typically met when measuring samples. When the signal reached sufficient stability, the analyser gate was closed, and the time span was determined until the signal was indistinguishable from baseline noise. The fade-out time of the amplifying system depends on the resistor. Each measurement was repeated twice

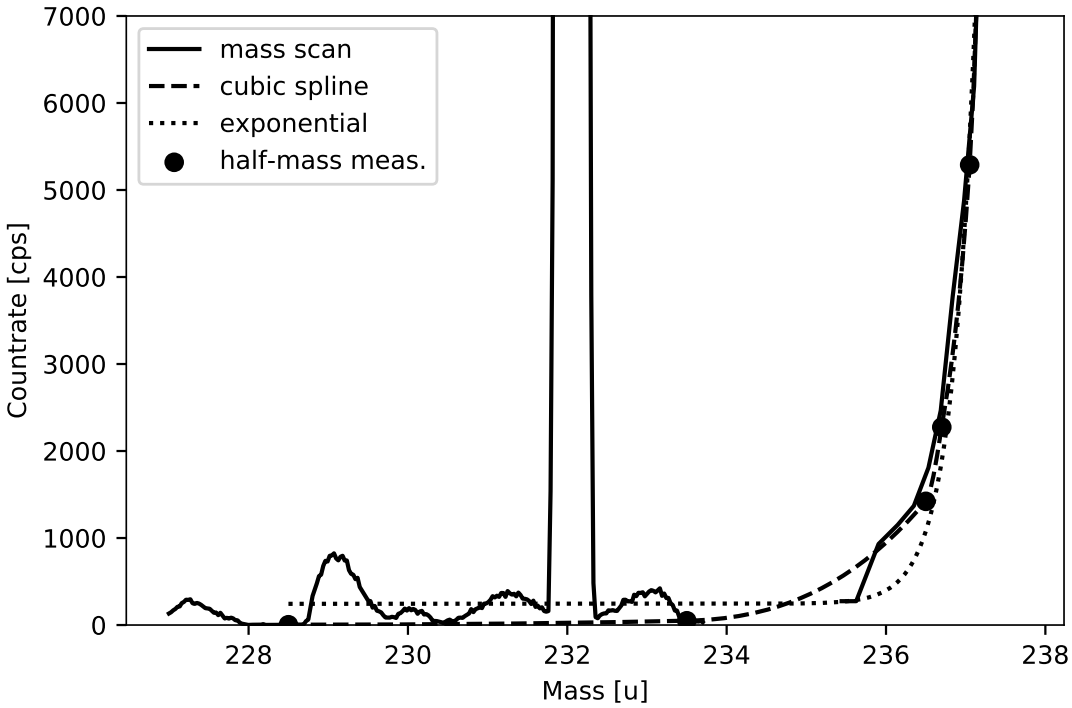

Figure 3.1: ^{238}U tail measured using CRM-112A with ^{238}U tuned at 110 V with an integration time of 0.5 s and 250 steps (black line). Masses 234 and 235 were skipped because they are present in CRM-112A solution and not a feature of the tailing baseline. Hence, the mass scan is divided into a section from 227-233.7 amu and from 235.4-237.7 amu. The data points are half-mass measurements as carried out at the start of each measurement sequence. The data point for 237.5 is out of the range of the y-axis. The dashed line presents the piecewise cubic Hermite interpolating polynomial extrapolation of the half-mass measurements, while the dotted line shows the exponential interpolation. The measurements displayed were taken in cps by SEM.

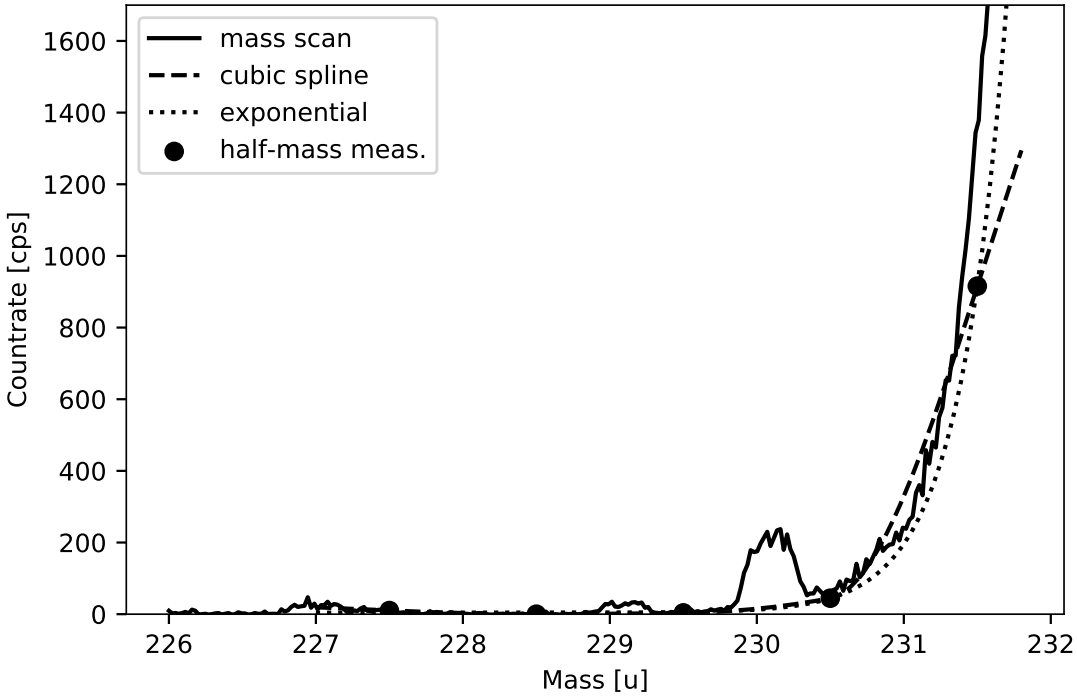

Figure 3.2: ^{232}Th tailing measured using the inhouse ^{232}Th standard with ^{232}Th tuned at 3.3 V and an integration time of 0.5 s and 250 steps (black line). The mass range covers 226-231.7 amu. Data points are half-mass measurements, and the dashed line is the piecewise cubic Hermite interpolating polynomial extrapolated function, while the dotted one shows the exponential fit. The discrepancy between extrapolation and actual tail between 230.5 and 231.5 amu is not relevant because no correction is derived for mass 231. This would be, however, relevant in case of simultaneous ^{231}Pa measurements.

to check the reproducibility. With up to 4 seconds, the $10^{13}\,\Omega$ amplifier has an approximately four times larger fade-out time than the $10^{10}\,\Omega$ resistor system with a value of 1 seconds. This means that the idle time limiting detector is the one connected to the $10^{13}\,\Omega$ resistor, which is the central cup in our setup. For a table of all fade-out time measurements, we refer to the Appendix (Table B.3).
With these boundary conditions, we chose the cycle protocol and cup configuration presented in Table 3.2 for optimal measurement performance. The selected idle times for lines II and III are shorter because there are no isotopes measured on the same cup as in the line before. This is the case because ^{230}Th and ^{229}Th in the centre were almost always measured on SEM and the ion counter accepts shorter idle times. In this study, ^{230}Th and ^{229}Th for SPA-52 were measured on the $10^{13}\,\Omega$ amplified central cup. ^{234}U is measured either on the centre FC or by SEM, depending on the sample's intensity: If a signal above 2 mV can be reached, the $10^{13}\,\Omega$ FC is chosen (Arps, 2017). This is the case for the vast majority of samples (∼95%). Lines I – III, measured one line after the other, represent one cycle, which is subsequently repeated to build a measurement (see below).

Detector	L1	CC/ SEM	H1	H2	H3	Int. time [s]	Idle time [s]
Line I	^{233}U	^{234}U	^{235}U	^{236}U	^{238}U	2	4
Line II	^{229}Th	^{229}Th		^{232}Th		2	0.2
Line III		^{229}Th	^{230}Th			2	0.2

Table 3.2: Isotope cup configuration for all three magnetic field configurations (Line I – III). For each configuration, an integration time is defined as well as the idle time before starting the measurement of the next line. L1, H1, H2 and H3 are the names of the FC detectors.

During operation, the calibration of the FCs against each other as well as the yield of the SEM need to be controlled. While there is an internal electronic calibration function for the calibration of $10^{10}\,\Omega$ and $10^{11}\,\Omega$ amplifiers, the $10^{13}\,\Omega$ amplifier in our setup needs to be calibrated manually. Thus, its gain factor is determined regularly by measuring ^{235}U alternately on the $10^{13}\,\Omega$ and $10^{11}\,\Omega$ amplified cup. The calibration of the $10^{11}\,\Omega$ amplifiers has been shown to be very stable with a change of only 0.24 ppm/day (Arps, 2017). In an analogous manner, the SEM yield is routinely determined by measuring ^{235}U alternating on the SEM and on a $10^{11}\,\Omega$ FC at a signal intensity of ∼5 mV. Since HU-1 standards are measured with the same detector configuration in standard bracketing mode, the observation of the (^{234}U/^{238}U) values of HU-1 measurements allows monitoring and manual optimization of gain and yield values for each measurement sequence in the data analysis scheme.
Beyond the detector hardware requirements, instrumental stability determines how specifics of the measurement sequence need to be set up, i.e., the number of cycles and peak integration time. In routine operation, samples are typically measured over 55 cycles, standards over 40. The three samples examined in this study were measured using the configuration from Table 3.2. For the stalagmite E8-21 and the GeoB coral, ^{234}U was measured on the

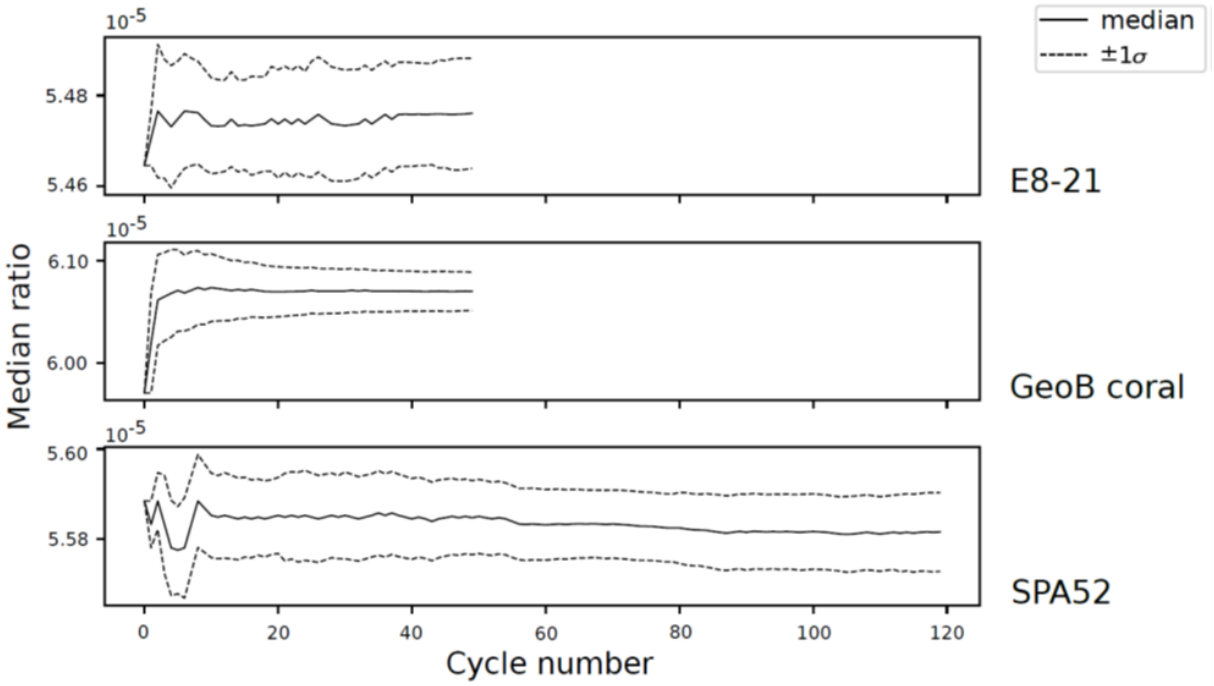

Figure 3.3: Median and standard deviation of the raw signal ratio (before applying any offline raw data corrections) of $^{234}U/^{238}U$ calculated on all values less or equal than the respective measurement number. E8-21 with 50 cycles is presented in the top over the GeoB coral (50 cycles) and SPA52 (120 cycles).

$10^{13}\,\Omega$ amplified centre cup, while ^{230}Th and ^{229}Th were measured on SEM. The E8-21 ^{238}U signal intensity was at 85 V and the GeoB coral ^{238}U signal intensity accounted for 115 V. For flowstone SPA52, all of the three least abundant isotopes were measured on the centre cup and ^{238}U was around 300 V. Measurements reach a stable state after 50 cycles, without significant changes to the median and standard deviation through additional cycles, as is shown in Fig. 3.3.

3.3.2 Tailing

All tailing half-mass measurements are conducted on the centred SEM and thus make use of the RPQ. This needs to be considered when transferring tailing measurements to isotopes measured on FCs since the FCs do not hold RPQs. Therefore, for applying tailing correction to values that were measured on FCs, a second tailing correction fit is needed. Arps (2017) describes a procedure where half-masses are measured on the centred SEM using the RPQ and then a second time on the IC2 ion counter that has no RPQ; however, this procedure showed up to 50 % variability over two months of monitoring. This may be due to the position of IC2 at the lower mass end deflection unit L5, which could lead to a worse focus. Here, we opt for a modified protocol: For FC measurements,

the extrapolated tailing correction for each isotope is multiplied with a constant factor (referred to as 'RPQ factors'). These factors were obtained by measuring tailing half-masses on the centred SEM with activated RPQs and afterwards repeating the same measurement with a manually deactivated RPQ using the same standard solution. From both sets of half-mass values, the tailing on the isotope masses is extrapolated with the abovementioned PCHIP fit. The RPQ factors are then defined as:

$$F_{RPQ} = \frac{T_{RPQ,off}}{T_{RPQ,on}} \tag{3.1}$$

with T being the extrapolated relative tailing count rates, depending on the isotope. Repeating this method multiple times successively allows for the determination of the RPQ factors, which are presented in Table 3.3. This implies that in routine measurements, tailing half-masses are always determined on the centred SEM with RPQ. The RPQ determination procedure and application are illustrated in an infographic in the Appendix (Figure B.3). To monitor the obtained values, the measurements are repeated every couple

Tail	**Isotope**	F_{RPQ} **(mean)**	**Δ (SD)**	**Δ (%)**
^{238}U	(^{229}Th)	(167)	(53)	(31)
	(^{230}Th)	(91)	(23)	(25)
	^{232}Th	45	6	13
	^{233}U	37	4	12
	^{234}U	18	3	16
	^{235}U	7	1	16
	^{236}U	5	1	17
^{232}Th	(^{229}Th)	(50)	(22)	(43)
	(^{230}Th)	(9)	(2)	(24)

Table 3.3: RPQ factors for the correction of the tailing resulting from ^{238}U and ^{232}Th beams. The correction factors and their error (standard deviation) are calculated based on 15 measurements (daily to monthly scale) in 2017 and 2019, filtered for outliers. Values for ^{229}Th and ^{230}Th are in brackets because they are almost never used, as these two isotopes are almost always measured by SEM. One exception is the SPA52 sample. The relative errors on ^{229}Th and ^{230}Th F_{RPQ} are high because of the small count rates.

of months. On all timescales, the obtained F_{RPQ} were found to be very stable. This shows that the method works more reliably than the previous procedure.

3.3.3 "Ghost signals"

For masses of 229 and 230 amu, we can observe signals that appear not to be created by real ^{229}Th and ^{230}Th isotopes or known interfering masses in the measured solutions. On

both masses, we observe a linear increase of the count rate depending solely on the intensity of the ^{238}U ion beam. This creates a higher count rate on these masses than actually expected from the ^{229}Th and ^{230}Th content, and is thus most relevant for simultaneous Th and U isotope measurements. We could exclude potential isobaric lead interferences by a series of test measurements. Therefore, these so-called "ghost signals" must be caused by scattering ions of the uranium beam, which has also been suggested by Chiang et al. (2019). Another hint is the irregular peak shape that is visible in Fig. 3.4. It is to note, however, that we observe multiple of these "ghost peaks", which differs from the one peak described previously (Chiang et al., 2019). Hence, we part with the assumption that the signals must reflect systematically scattered ^{238}U ions, which contrasts the tailing effect. To account for the scatter signals, we introduce the additional correction factors k_{230} and k_{230}, which are given by the slopes of the linear dependency of the scatter signals on the ^{238}U intensity, measured in cps/V (see Fig. 3.5 for ^{229}Th). In the isotopic ratio calculation, $k_x \cdot ^{238}$ U[V] is subtracted from the ^{229}Th and ^{230}Th signals, respectively, during offline data correction. Apart from 229 amu and 230 amu, we also observe a peak around 227 amu and 228 amu, as has been mentioned before when describing tailing correction. It is visible in the tailing baseline presented in Fig. 3.1.

We determined the final value from the slope of the ^{229}Th signal over uranium on CRM-112A, which is plotted in Fig. 3.5. As CRM-112A does not contain any ^{229}Th, the counts on this mass stem completely from the scattering signal. The use of CRM-112A avoids adding errors from different ionization efficiencies or from samples with a carbonate matrix. The value determined is $k_{229} = 4.970 \pm 0.094$ cps/V. This corresponds to an atomic ratio $^{238}U_{scatter}/^{238}U$ of approximately $(7.95 \pm 0.15) \cdot 10^{-8}$.

We determined k_{230} using two different methods: first, by matching band-counting ages of recent tropical coral samples with the U-series ages measured, and second, by accurately dating the CRM-112A solution. The U-series age of coral sample BOC2-45mm was determined to be 12.6 ± 0.6 years, and CPR-55mm was found to be 39.7 ± 1.1 years old (both ages refer to the time of analysis, December 2021). For calculation of these ages, the correction factor $k_{230} = 0.37$ cps/V was estimated, which is lower than the one observed for ^{229}Th by a factor of 10. In addition, the spiked CRM-112A standard solution can be Th/U-dated, and the result can be compared to its production date. The employed batch of uranium was purified in 1957 (± 2 years) at the Mallinckrodt Chemical Company and delivered to NBS (nbl, Westbrook and Bloom (2007), Bingham (1987)). The measurements confirm that the coral value of $k_{230} = 0.37$ cps/V. We will use CRM-112A to track the temporal evolution of k_{229} and k_{230}.

These measurements and analysis have only been finalized after the submission and revision of the publication. The details on the temporal evolution of the ghost signals, and further development of the correction, will be given in Chapter 4.

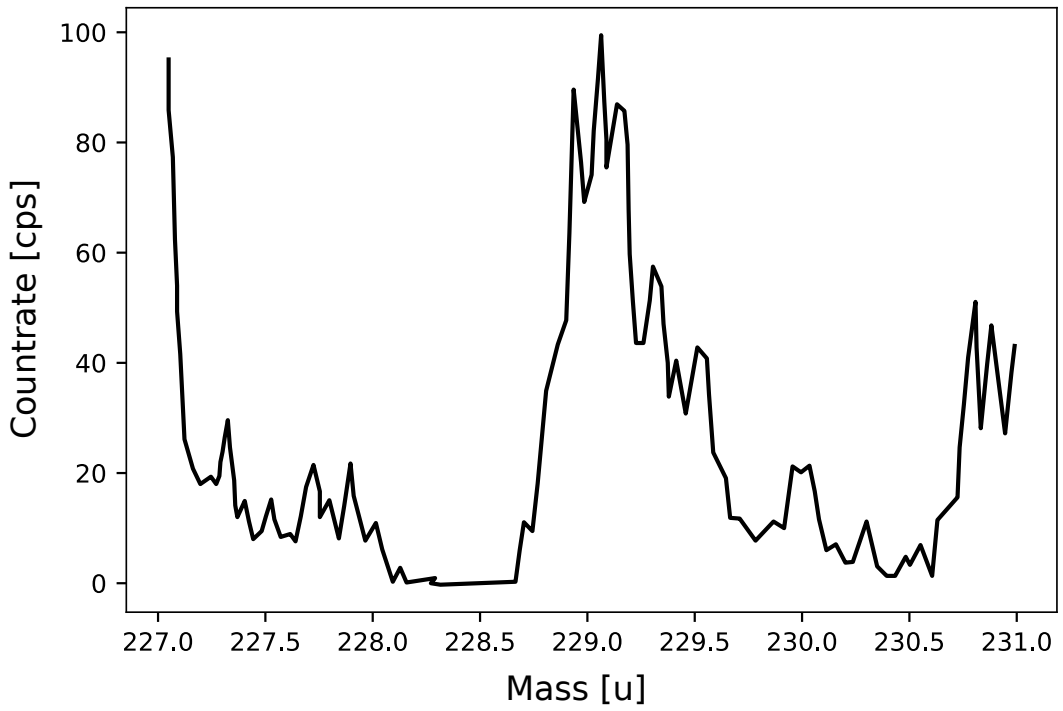

Figure 3.4: Mass scan from 227 amu to 231 amu of a lead element standard mixed with CRM-112A. ^{208}Pb is tuned at ∼2 V, ^{238}U at ∼8 V and the integration time is set to ∼1 s. The 229 amu peak shows an asymmetrical shape that does not conform to a typical, tuned mass peak with a plateau and steep slopes.

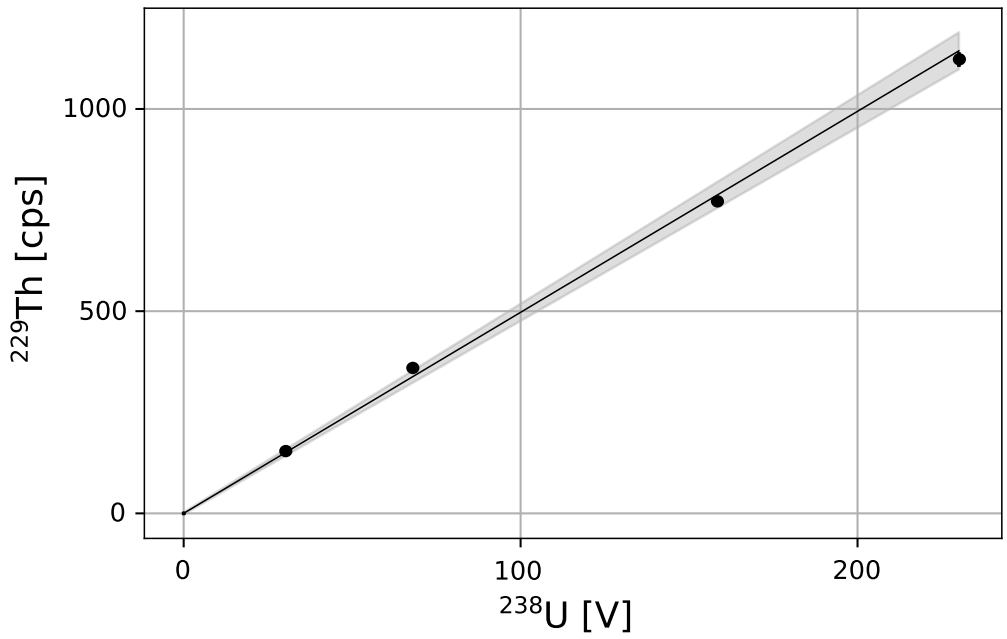

Figure 3.5: Linear fit (black line) through four measurements of ^{229}Th over ^{238}U on CRM-112A solution. The fit parameters were determined to be a = 4.970 ± 0.094 cps/V and b = 0.134 ± 1.211 cps (1 σ uncertainty). The grey band shows the 2 σ area of slope a. Error bars are mostly smaller than the symbol size.

3.3.4 HU-1 measurements

To demonstrate the accuracy and reproducibility of our protocol, we compiled (^{234}U/^{238}U) and (^{230}Th/^{238}U) measurements of the HU-1 standard. HU-1 has been measured in many different laboratories with different protocols and is supposed to be in secular equilibrium, which implies activity ratios of 1 (Wefing et al. (2017), Shao et al. (2019)).
The HU-1 data presented here are 52 standard bracketing measurements of HU-1 alongside cold-water coral samples from 6 measurement days in October 2022. ^{234}U was measured on the centre cup, and ^{230}Th was measured by the SEM. The average of (^{234}U/^{238}U) is 1.00001 ± 0.00091 with the uncertainty being two standard deviations. The mean individual error (average of the individual 2σ measurement uncertainties) is 1 ‰. The average value agrees with the values determined in Shao et al. (2019) and Shen et al. (2012). The mean value for (^{230}Th/^{238}U) is 0.9994 ± 0.0019. The mean individual error is 2.2 ‰. This matches the supposed activity ratio of 1. Again, individual measurement errors and reproducibility agree well. The activity ratios are plotted in the Appendix (Fig. B.1 and B.2).

3.3.5 Influences of correction factors on accuracy

In Table 3.4, the dating results obtained with our optimized routine correction protocol for the three demonstration samples are presented. In the following, we analyse how data corrections that are slightly "off" from their ideal reference value may affect the accuracy of the activity ratios (^{234}U/^{238}U) and (^{230}Th/^{238}U) and consequently the age. The origin of fluctuations in correction factors is suspected in both changes of the ionization and ion extraction in the plasma source and cones as well as the ion beam path and overall energy and mass filtering stability. When a correction (such as tailing) has changed its values between the time of correction determination and sample measurement, such short-term changes are not accounted for during the data retreatment routine. For this analysis, we calculate the relative difference between the (^{234}U/^{238}U), (^{230}Th/^{238}U) and corrected age results for the correction factor, respectively, multiplied with α=1 and multiplied with α=x according to Equation 3.2. x denotes a reasonable relative deviation, e.g., 20 %, which leads to x=1.2. The degree of assumed variability results from long-term (multiannual) observations of the studied parameters, i.e., many thousand individual sample and standard measurements.

$$Var_{result} = \frac{Result_{\alpha=x}}{Result_{\alpha=1}} - 1 \tag{3.2}$$

The resulting variation then denotes the offset in accuracy, not the increase in uncertainty (the latter corresponding to a loss in precision).

For tailing correction, we assume a maximum possible daily variation of ±20 % for both U and Th from the extrapolated count rates of the full masses. For every mass, we calculated the relative error on the extrapolated count rates of four measurements over the course of three months in 2019. The extrapolated count rates on the two thorium

Sample	E8-21	GeoB coral	SPA52
^{238}U (μg/g)	1.082617 ± 0.000042	3.52908 ± 0.00015	83.9197 ± 0.0015
^{232}Th (ng/g)	0.029200 ± 0.000079	0.34444 ± 0.00061	132.816 ± 0.022
^{230}Th (pg/g)	0.0673 ± 0.0013	22.961 ± 0.055	998.60 ± 0.24
(^{234}U/^{238}U)	1.01046 ± 0.00056	1.12115 ± 0.00060	1.02131 ± 0.00025
(^{230}Th/^{238}U)	0.003802 ± 0.000072	0.39804 ± 0.00094	0.72800 ± 0.00018
(^{230}Th/^{232}Th)	430.8 ± 8.3	12464.1 ± 37.1	1405.8 ± 0.4
Age uncorr. BP (a)	339.1 ± 7.8	47 336 ± 143	135 016 ± 99
Age corr. BP (a)	335.8 ± 8.0	47 308 ± 144	134 975 ± 101

Table 3.4: Concentrations, activity ratios and detritus corrected as well as uncorrected age measured for the three demonstration samples. All reported uncertainties are 2 σ uncertainties. Correction for detrital contamination assumes a bulk Earth ^{232}Th/^{238}U weight ratio of 4.1 ± 2.05 and ^{230}Th, ^{234}U and ^{238}U in secular equilibrium [51]. As the initial ^{230}Th/^{232}Th ratio, 3.50 ± 1.75 was assumed for E8-21. For SPA52, detrital values of 0.75 ± 0.375 were assumed; nevertheless, they are negligible here, as the correction is smaller than the age uncertainty. For the GeoB coral, the ratio was assumed to be 8 ± 4 (Wefing et al., 2017). The ages are calculated using the half-lives determined by Cheng et al. (2013). The final age errors do not contain half-life uncertainties.

masses varied by 49% and 15%, respectively, over those four measurements. Count rates of the uranium tailing fitted masses varied by 15% for 229 amu, 13% for 230 amu, 24% for 232 amu, 25% for 233 amu, 18% for 234 amu, 14% for 235 amu and 17% for 236 amu. The high variation at 229 amu for the Th tailing is not surprising, as the count rate at 228.5 is smaller than 10 cps. The variation is thus in the range of counting statistics. We measure tailings at the start and the end of each measurement sequence, in which a sequence runs for several hours. On this timescale, the variation is smaller than that described above. For continuous U and Th tailing measurements of one hour each, no significant trends in abundance sensitivity could be found. Two tailing measurements over several hours thus normally keep the variation in the low percent range.

Applying the maximum value of 20 % larger tailing correction than that actually measured decreases the (^{234}U/^{238}U) and (^{230}Th/^{238}U) for all samples. This means that an unnoticed increase in tailing correction leads to higher ratios than is actually correct, while an unnoticed decrease in tailing yields lower ratios than the ideal values would be. The details are presented in Table 3.5. While the GeoB coral is only affected on the ϵ-level for both activity ratios as well as the resulting age, both E8-21 and SPA52 have significant accuracy effects on the permille scale. The elevated tailing makes E8-21 0.3 % younger; however, the coral and old speleothem become older by 0.03 % and 0.5 %, respectively. This is caused by the different tailing effects on the ^{230}Th/^{232}Th ratio, which is then used

for initial ^{230}Th age correction. It should be noted here that the large tailing impact on SPA52 is due to the measurement protocol adapted for this sample with all isotopes on the cup. This means that for the ^{229}Th and ^{230}Th, tailings without RPQ need to be applied, and hence, the effect is 90 to 170 times larger (see Table 3.3). Thus, monitoring the tailing correction is most important for young materials as well as for measurements with all isotopes detected on FC. For hydride correction, we analysed the variation in

Sample	**(^{234}U/^{238}U) deviation**	**(^{230}Th/^{238}U) deviation**	**Age deviation**
E8-21	-0.16%	-0.44%	-0.29%
GeoB coral	-0.05%	-0.03%	0.03%
SPA52	-0.12%	-0.09%	0.47%

Table 3.5: Deviation of the activity ratios (^{234}U/^{238}U) and (^{230}Th/^{238}U) and the (detritus corrected) age from the value with Th and U tailing correction at 1, when applying a Th tailing correction of 1.2 and a uranium tailing correction of 1.2. The minus sign denotes deviations towards a smaller ratio resp. a younger age. For a tailing correction smaller than assumed, the sign of results would be inverted. Please note that for SPA52 229Th and ^{230}Th were measured on cup which requires the multiplication with RPQ factors. Thus the influence of tailing is larger than for the GeoB coral.

239 amu and 233 amu over three months in 2019 by calculating the standard deviation over the mean, which constituted 7 % for thorium and 12 % for uranium. The effect of this deviation from the optimal hydride correction was calculated for activity ratios and age for all samples. The impact of the hydride correction is below the uncertainty threshold in all cases (Table 3.6). The deviation employed here (12 % for uranium, 7 % for thorium) even overestimates daily variation, making clear that hydride correction is an absolutely minor factor in accuracy. The impact of process blanks differs between the

Sample	**(^{234}U/^{238}U) deviation**	**(^{230}Th/^{238}U) deviation**	**Age deviation**
E8-21	-0.00002 %	-0.00700 %	-0.02500 %
GeoB coral	-0.00001 %	-0.00006 %	-0.00006 %
SPA52	0.00001 %	-0.00070 %	-0.00100 %

Table 3.6: Deviation of the activity ratios (^{234}U/^{238}U) and (^{230}Th/^{238}U) and the (detritus corrected) age from the value with Th and U hydride correction at 1, when applying a Th hydride correction of 1.07 and a uranium hydride correction of 1.12. The minus sign denotes deviations towards a smaller ratio resp. a younger age.

three samples due to the different intensities in their respective measurement sequences. E8-21 and GeoB coral yield process blanks of about the values presented in section 3.2. SPA52, however, has a significantly elevated process blank in the Th isotopes (both over 100 cps). This is because it was measured in a series with other high-intensity samples, and Th is less soluble from the inlet system than U. We chose to work with a maximum

variation of 50 % in the process blank of the respective sample. As the blanks are measured directly before the samples, this variation can only occur due to samples producing their own increased process blank over time. Here, 50 % is to be seen as an upper limit. The impact of process blank deviations on the accuracy decreases with age and isotopic concentrations (Table 3.7). For the GeoB coral and SPA52, the impact is negligible. For E8-21, however, (^{230}Th/^{238}U) and corrected age can deviate up to the permille level. The direction of the effect on activity ratios and corrected ages is not uniform and depends on the specific process blank of the individual samples. Finally, the ghost signal has a

Sample	**(^{234}U/^{238}U) deviation**	**(^{230}Th/^{238}U) deviation**	**Age deviation**
E8-21	0.0030 %	-0.4500 %	-0.4700 %
GeoB coral	0.0003 %	0.0020 %	0.0030 %
SPA52	-0.0001 %	-0.0003 %	-0.0002 %

Table 3.7: Deviation of the activity ratios (^{234}U/^{238}U) and (^{230}Th/^{238}U) and the (detritus corrected) age from the value of a process blank correction at 1, when applying a process blank correction of 1.5. The minus sign denotes deviations towards a smaller ratio resp. a younger age.

major effect on accuracy (Table 3.8). Here, we tested the accuracy effect of setting one or both correction factors to 0, which corresponds to "missing" the ghost signal corrections. The effect of "missing" both corrections is drastic for young samples: E8-21 (335.8 years) shows deviations in both (^{230}Th/^{238}U) and the resulting age of more than 10 % (41 years), which is more than 5 times larger than the uncertainty in the age (8 years). The dominant correction for young ages is k_{230}. In general, the two factors do not only concern young ages. For the GeoB coral (47 308 ± 144 ka), the age deviation is still three times larger than the age uncertainty, while SPA52 (with an age of more than 100 ka) is only affected on the ϵ-level. However, it should be noted that the age uncertainty for SPA52 is also only at 7.5 ϵ. The k_{230} correction alone makes samples younger, as it removes the ^{230}Th that was erroneously assigned to the sample. k_{230} without k_{230} in turn increases the age. Depending on the ratio between spike and sample mass, different results with regard to the age deviation of both corrections combined are thus plausible.

3.4 Discussion

3.4.1 Measurement protocol

Our method for transferring SEM abundance sensitivity measurements to FCs has been tested and reviewed for several years. The RPQ factors performed stably within the error margins over years. This shows the general applicability of this method to correct for the difference in abundance sensitivity with and without RPQ. It further highlights that only punctuated (annual) measures are needed to inform on this value. Our measurement

Correction factors	Sample	(^{230}Th/^{238}U) deviation	Age deviation
k_{229}=0 and k_{230}=0	E8-21	12.20 %	12.30 %
	Coral	-0.70 %	-0.90 %
	SPA52	-0.07 %	-0.13 %
k_{229} = 0 and k_{230}= 0.37	E8-21	-0.54 %	-0.54 %
	Coral	-0.90 %	-1.10 %
	SPA52	-0.07 %	-0.14 %
k_{229} = 4.97 and k_{230}= 0	E8-21	12.80 %	12.90 %
	Coral	0.18 %	0.22 %
	SPA52	0.01 %	0.01 %

Table 3.8: Deviation from the ideal value (which is calculated with k_{229} = 4.97 and k_{230}= 0.37) of (^{230}Th/^{238}U) and the corrected age for one and both corrections set to 0. As the interference correction factors do not concern the calculation of (^{234}U/^{238}U), the effect on this activity ratio is always 0 and is not presented here. The minus sign denotes deviations towards a smaller ratio resp. a younger age.

protocol combines FC and SEM detectors to measure Th and U isotopes simultaneously in one solution. The correction factors and ghost signal correction allow us to use the full precision level of MCICPMS on all relevant isotopes simultaneously, with ϵ-precision for individual isotope ratios that span the full age range from the modern era to >500 ka. A routine sample measurement with 55 cycles using this setup takes ∼11 minutes, while standards (40 cycles) are measured in ∼9 minutes. Initial tailing measurements including washes take ∼15 minutes once at the start and once in the middle of each measurement sequence. Washes and process blank measurements between a sample and standard account for approximately 9 minutes. All of these time intervals include the uptake time of the measurement solution and the time the autosampler needs for changing solutions. This implies that 37 sample-standard combinations, and thereby 37 radiometric ages, can be measured in 24 hours. That value is approximately 75 % of the 50 ICP–MS ages/day reported in Douville et al. (2010). With our protocol, we could determine the age of postmodern samples to ∼2.4 %, the GeoB coral (∼ 50 ka) at an age precision of ∼3 ‰, and SPA52 (∼135 ka) at 7.5 ϵ. This highlights the feasibility, of efficiency and utmost precision. In theory, a dedicated MCICPMS instrument would be able to produce more than 10 000 ages per year, which implies fast chemical separation using the methods described previously (Wefing et al., 2017).

3.4.2 Correction impacts

The (^{234}U/^{238}U) precision levels obtained for the demonstration samples in this study are 6 ϵ for E8-21, 5 ϵ for the GeoB coral and 2 ϵ for SPA52. Precision of (^{230}Th/^{238}U) in turn is 1.8 % for E8-21, 0.2 % for the GeoB coral and 2 ϵ for SPA52. Comparing the deviations calculated in our raw data correction analysis to these uncertainty levels underlines the

importance of regular determinations of the correction factors. Unnoticed deviations in tailing corrections can cause offsets on the permille level on the activity ratios as well as the corrected ages for "young" samples and for those with all isotopes on cup. Younger samples have comparatively low count rates on the least abundant isotopes and thus experience a strong effect of small deviations in the tailing matrix. The absolute change in age would be at ∼1 a for E8-21. For the old sample we employed, SPA52, the strong effect (∼ 675 a, which is almost a factor of seven higher than the measurement precision) is due to the high intensity of the beams (^{238}U at ∼300 V) and, more importantly, the larger tailing effect on the cups. This is not representative for samples of similar age and/or concentration that are measured with the least abundant thorium isotopes by SEM. For those, the effect would be smaller than for the GeoB coral, which is only affected on the ϵ-level (corresponding to ∼14 a, which is at 10 % of the measurement uncertainty). This means that for E8-21, such a deviation in the tailing corrections would place (^{234}U/^{238}U) out of the 2σ uncertainties, while for SPA52, the impact on accuracy is larger than the measurement precision for all three values. The corrected age for SPA52 exceeds the uncertainty by a factor greater than 6. As our measurement sequences are normally restricted to a few hours and abundance sensitivity is measured at the start of each sequence, the variation can be kept below the tested 20 %. If a measurement scenario similar to that described in section 3.4.1 ran for 24 hours, abundance sensitivity measurements should be repeated at least 3 times. A variable hydride correction, on the other hand, is negligible for all samples. Even assuming a variation on a monthly timescale, this only yields an age deviation on the ϵ-level for E8-21 as the largest of all impacts. Additionally, this is much smaller than the age uncertainty for this sample. Nevertheless, hydride formation can be easily monitored to determine the absolute value of the correction. Process blank impacts are also smaller than the measurement uncertainties for all samples and values. However, (^{230}Th/^{238}U) and corrected age are concerned with the permille level for E8-21, corresponding to an absolute age effect of ∼2 a. This can be monitored very well by the measurement protocol, as the blanks are measured directly before every individual sample. This method emphasises the relevance of sufficient rinses before the blank and then sample measurements, so no jumps or systematic changes in blank levels can occur anymore during the sample measurement. This also implies the sorting of samples in order of increasing isotopic concentrations in the measurement solutions. The most impactful of all correction factors is the "ghost signal" interference. Not applying those produces ages and (^{230}Th/^{238}U) ratios far outside of the 2σ uncertainties. In the case of E8-21, those deviations are >10 % (∼50 a). However, for SPA52, the age deviation is still a factor of 2 larger than the measurement uncertainty (∼200 a). For very young, e.g., recent, samples, the accuracy offset can become even larger than 10 %. This shows that thorough baseline scans for atypical peaks are highly important to produce accurate U-series ages. These peaks might also concern tailing determination and make it necessary to adapt the selected half-masses around them. It does not seem to be a unique feature of our spectrometer, as something similar has been reported previously (but only for mass 230) (Chiang et al., 2019). We strongly recommend running thorough baseline checks

on similar measurement setups to assess if such "ghost signal" corrections are necessary. Alternatively, measurements can be conducted by separating U and Th isotopes to avoid the scattering peaks, which is the method chosen by numerous laboratories (e.g., Cheng et al. (2013), Hellstrom (2003)). However, the value of k_{230} can vary between different machines; therefore, Chiang et al. (2019) report a ghost signal 80 times larger than the one we observe. This implies a still significant effect for measuring separated solutions. Here, we have opted for the combined approach to minimize the analytical measurement time and because the observed influences and correction factors can be constrained well.

3.4.3 Routine precision in Th/U measurements

Applying the measurement protocol, we have presented here and accounting for all of the correction factors, we recalculated the average relative errors of the activity ratios and ages of corals from two gravity cores that contained corals, for a total of 102 ages. They span a range from ∼0.1 to 25 ka. The median relative errors are 0.04 ± 0.01 % for (^{234}U/^{238}U), 0.27 ± 0.36 % for (^{230}Th/^{238}U) and 0.29 ± 0.52% for the uncorrected ages. Uncertainties are one standard deviation. These values, including the ages, have relative errors in the low permille regime or below and prove the reliability and reproducibility of the system. (^{234}U/^{238}U) is routinely measured even at ϵ-precision. Generally, the relative errors, and thus the obtained precision, are best for (^{234}U/^{238}U). For (^{230}Th/^{238}U), the isotopes are not measured in the same magnetic field line and with lower intensity than (^{234}U/^{238}U), which results in a lower precision. This state is a further development from the measurement methods described in Wefing et al. (2017), i.e., with regard to accuracy considerations due to the interference corrections and tailing SEM-FC transfer methods. In terms of precision, we achieved similar levels as Chiang et al. (2019), who applied a multisequence SEM approach. As they used an SEM peak-jumping protocol, the obtained precision levels for (^{234}U/^{238}U) and (^{230}Th/^{238}U) do not differ as much as ours, in which (^{234}U/^{238}U) can be measured significantly better than (^{230}Th/^{238}U). An advantage of our method is that U and Th are measured together in one solution, which helps to significantly increase efficiency and saves effort in chemical preparation. This in general is an advantage of combined FC-SEM protocols compared to peak-jumping routines. The benefit offered by the latter is that no ratios of signals measured on SEM and signals measured on FC need to be taken. Those ratios would need to be treated with caution, as the SEM-FC yield can fluctuate randomly (Chiang et al. (2019), Andersen et al. (2004)). In our combined protocol, we avoid this for the vastly predominant majority of samples by measuring ^{234}U in the same configuration as ^{238}U on the 10^{13} Ω amplified FC and ^{230}Th and ^{229}Th both on SEM. Only the rare samples with very low U concentrations and thus a ^{234}U signal below 2 mV are measured in a combination of SEM and FC. For these samples, the impact of yield variation on (^{234}U/^{238}U) is controlled by standard bracketing. This allows for our measurement routine to operate twice as quickly as published peak-jumping protocols (Chiang et al., 2019). Our high precision sample, SPA52, is accurate within the precision levels reported in Cheng et al. (2013) with an uncertainty of 100 a at an age of

130 ka, i.e., $\sim 7.5\,\epsilon$.

3.4.4 Implication of the SPA52 speleothem growth onset

Spötl et al. (2002b) dated the start of calcite deposition in Spannagel Cave from SPA52 to 135.0 ± 1.2 ka. Here, we improved the precision of this value by a factor of ten (134.975 ± 0.101 ka) for one age from the respective growth phase. Spötl et al. (2002b) argued that warming after Termination II (the end of Marine Isotope Stage 6) must have started before the maximum summer insolation at 65° N at 127 ka, since SPA52 started growing before this date. Our more precise value is still clearly older than 127 ka, but shows through the improved precision that the onset of growth clearly coincides with the initial rise of the insolation curve.

3.5 Conclusions

We present an updated protocol for U-series dating using an FC and SEM detector combination that is able to reach average isotopic precisions and accuracy on the ϵ-level without separating U and Th during column chemistry. Furthermore, we present a reliable and stable method to transfer tailing measurements from SEM with an RPQ to FC without an RPQ, which is crucial for combined FC-SEM protocols. Our fade-out times for the FC have been determined at typical signal intensities for U-series dating and are respected in the measurement protocol. Finally, we tested variations in correction parameters and analysed their effect on activity ratios and age accuracies. We find that "ghost signals" on masses of 230 and 229 amu, which are linearly related to the ^{238}U signal, have a strong impact on the isotope ratios at high precisions and accuracies or at very low ^{230}Th abundance. Our measurement protocol allowed us to better constrain the age from a speleothem growth phase in the Alps, which appears linked to the start of Northern Hemisphere solar insulation intensification. Tests of a larger ensemble of dated corals permitted us to clarify the routine high precisions and accuracies of the ages.

4 Tracking ghost signals

This chapter describes the detailed examination of the correction for ghost signals (scattering effects) on masses 229 and 230 amu, i. e. with regard to temporal variation and suitable reference materials. That correction is highly relevant for obtaining accurate ^{230}Th/U ages, as outlined in Chapter 3. Here, a further development of the state in section 3.3.3 is presented. This is the case as the measurements and analysis within this chapter were not completed yet at the time of submission and revision of the manuscript in Chapter 3.

4.1 Introduction

During long-term ^{230}Th/U dating operation, the ghost signals on masses 229 and 230 amu show to be variable over time. This behaviour can be detected when comparing the age of individual measurements of spiked CRM-112A solution for k_{230}, respectively, the counts on 229 amu per V ^{238}U in unspiked CRM-112A for k_{229}. Thus, we must part with the assumption of static signals from section 3.3.3 and find methods to limit the effect of this variation on i. e. young ages.
In addition, there is an offset between the estimated age for CRM-112A (production date investigated as 1957 $\pm$ 2 years from literature, see section 3.3.3) and realistic ages for young corals, as some very young corals get negative ages with the ghost signals optimized for the assumed CRM-112A production year.
This section deals with the tracking of their temporal variance and the subsequent updates in the measurement protocol. Furthermore, to enable corrections backed by a uranium material with validated age, the new reference material VRM 06/23 (internally also referred to as JRC) is introduced and characterized.

4.2 Time variance

Figure 4.1 shows the temporal variation of the age of CRM-112A solution over multiple measurement days. The age calculated with a fixed k_{230} is directly correlated to the actual value of k_{230}: A higher age than expected corresponds to a higher value for k_{230} to reach the reference age. Variation can be detected both on intra- and inter day scale. The deviation is in the order of $<$0.03 cps/V over the course of a day (corresponding to approx. 10 years of difference in the ages determined for CRM-112A). The measurements from section a) and b)-e) in Fig. 4.1 were taken four years apart. It is visible that the deviation of the ages determined in a) from the other measurements is significantly larger

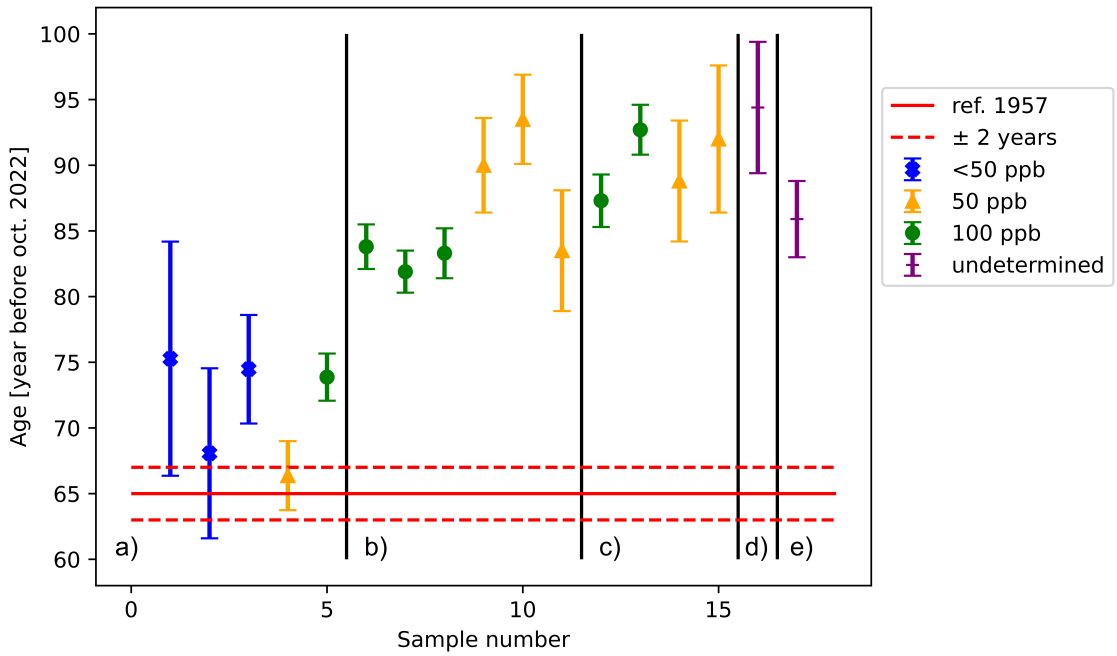

Figure 4.1: The age of CRM-112A solution (in years, standardised to October 2022) is shown for multiple measurement days. All ages were evaluated with $k_{230} = 0.37$ cps/V and $k_{229} = 4.97$ cps/V. The colours and symbols represent the different concentrations of the measured solutions. "Undetermined" refers to solutions which were admixed from the rests of the previous CRM-112A vials of different concentrations, so not exact input concentration is known. The red lines represent the literature value age of CRM-112A and its uncertainties (equally standardised to October 2022). The measurement days were: a) 17.08.2018, b) 27.10.2022, c) 28.10.2022, d) 02.11.2022, e) 03.11.2022.

than the differences between b)-e), which were taken within one week. So there seems to be a long-term variability. As shown in section 3.3.5, for very young materials k_{230} has the far larger effect than k_{229} because of the small amount of physical counts on mass 230. Also for k_{229}, variation could be detected. This became evident when comparing measurements of unspiked CRM-112A from 2017 and 2022. The dataset is different from Fig. 4.1 because for the data in Fig. 4.1 no corresponding unspiked CRM112A measurements were taken.

To examine if there is a correlation between the variation in both ghost signal constants, we compared them for two measurement days in Fig. 4.2. No correlation between the variation of the two signals can be detected.

In fact, the two constants should be denoted as $k_{230}(t)$ and $k_{229}(t)$ due to their time variance. For reasons of simplicity, the (t) will be omitted in the following sections.

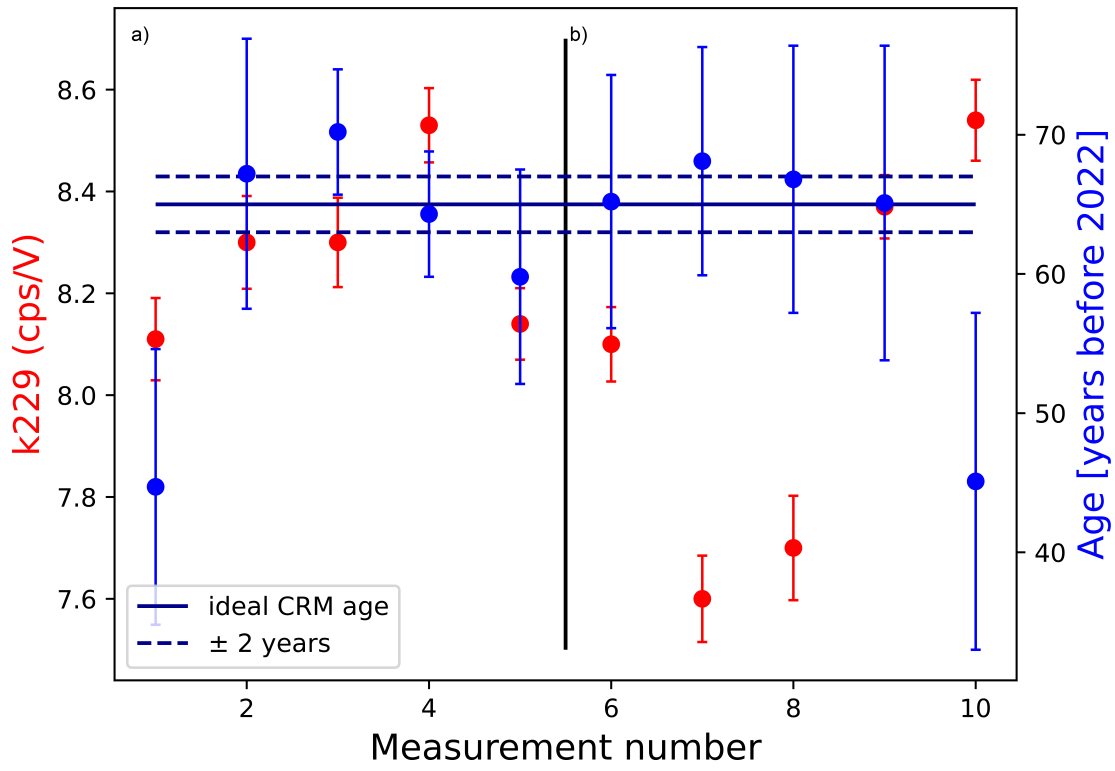

Figure 4.2: Results from ten measurements of both unspiked and spiked CRM-112A during two measurement days. Each measurement number corresponds to two subsequent measurements of the spiked respectively unspiked solution. k_{229} is presented in cps/V on the left y-axis, while the age of CRM-112A is presented on the right y-axis. For the age determination, the respective measurement day's mean k_{229} was used, which was $k_{229} = 8.200\,\text{cps/V}$ for the first day and $k_{229} = 8.062\,\text{cps/V}$ for the second. k_{230} was assigned a fixed value for each of the days, such that the majority of ages come as close as possible to the assumed value of 65 years. This was $k_{230} = 0.767\,\text{cps/V}$ for the first day, and $k_{230} = 0.830\,\text{cps/V}$ for the second. Errors for k_{229} were determined from the 229Th and 238U intensity errors via error propagation, while the age errors stem from age calculation. The reference value for the age of CRM-112A and its uncertainty is plotted in dark blue. Measurement days were: a) 07.12.2022 and b) 08.12.2022.

4.3 Introducing a reference material with a confirmed age

The evaluation of some recent cold-water corals during routine operation resulted in negative ages when optimizing CRM-112A to 1957 ± 2 years (pers. communication, R. Eichstädter).
This implies that the k_{230} value obtained via age optimization of CRM-112A is unphysically high. Two hypothesis are possible to explain this observation: Firstly, CRM-112A could be "older" than determined from literature research on its production age. This would be due to initial thorium contamination bringing in a small amount of ^{230}Th. We consider this a potential explanation, i. e. given the purification of the uranium already in 1957 which might have left traces of thorium. As a second hypothesis, corals and standards could behave different due to matrix effects, such as residual Ca in the ionization process.
To test the age offset hypothesis, CRM-112A was measured against a standard solution with precisely known production date (2011).

4.3.1 Materials

VRM 06/23 was obtained from Zsolt Varga from the Joint Research Centre for Nuclear Safety and Security of the European Commission at Karlsruhe. It is a nuclear forensics uranium reference material validated for its date of production and was characterised in Varga et al. (2015), a predecessing interlab-comparison study for the certified reference materials IRMM-1000a and IRMM-1000b (Varga et al. (2016), Venchiarutti et al. (2016)). The certified reference materials are both low-enriched with approx. 3.6 % of ^{235}U (Varga et al., 2016). Thus we opted for the natural uranium material with 0.71 % of ^{235}U to roughly match the ^{235}U/^{238}U ratio in our samples. The last purification from thorium step of VRM 06/23 was carried out on 19.07.2011 (Varga et al., 2015). Their study also states that the ^{230}Th/^{234}U ratio was at $10^{-11} - 10^{-13}$ during preparation and residual ^{230}Th is neglible, so 19.07.2011 can be considered the date of production.
VRM 06/23 was obtained as 50 mg of uranylnitrate powder containing 30 mg of pure uranium. The dissolution procedure followed the instructions of the Joint Research Centre Karlsruhe, also described in Varga et al. (2015). The powder was dissolved in concentrated HNO_3 in its original teflon beaker, then transferred to a pre-cleaned (with acid and milliQ water) teflon bottle and filled up to 300 ml. In the next dilution step, 1 ml of this concentrated solution was filled up to 250 ml in a new bottle. The final solution has roughly 0.4 ppm of uranium.

Both reference material solutions (VRM 06/23 as well as CRM-112A) contain no residual Ca matrix. Thus, testing against "real" carbonate samples was neccessary as well. Therefore, the same two tropical corals as in section 3.2.2 were used as test cases. Here, different depths were chosen for sampling: CPR was sampled at a depth of 40 mm with

the band counting year 1992. BOC was sampled at 35 mm of depth, with 2010 as the corresponding year obtained by band counting.

4.3.2 Results

VRM 06/23 was measured against CRM-112A, in a protocol following the sequence HU1 - CRM-112A (spiked) - VRM - HU1 - CRM-112A - VRM - HU1 - ... . By selecting this measurement order, the effect of the ^{230}Th process blank of HU1 on VRM could be minimized. The results are presented in Table 4.1. With a mean age of (12.2 ± 1.3) years, VRM agrees very well with the expected value of 11.9 years at the time of the measurements. The mean age of CRM-112A is (88.3 ± 2.5) years, which implies an offset of approx. 22.5 years to its year of production. For measurements 1, VRM is slightly younger than expected, while CRM-112A is slightly older. This effect also occurs for measurement 4, however vice versa. It might be due to asynchronous small changes in k_{230} and k_{229}. Table 4.2 presents the measured ages of the two tropical corals compared to the band-counting ages. Respecting the offset in CRM-112A age, the values agree. This shows that the dominant source of deviation was initial thorium contamination of CRM-112A and no matrix effect.

Measurement day	**No.**	**Age (a) VRM**	**Age (a) 112A**
30.05.2023	1	11.1 ± 1.5	92.3 ± 2.9
30.05.2023	2	12.7 ± 1.7	89.6 ± 2.2
30.05.2023	3	12.1 ± 1.8	87.3 ± 2.6
01.06.2023	4	14.8 ± 2.1	84.2 ± 2.6
01.06.2023	5	11.7 ± 1.8	87.6 ± 2.2
01.06.2023	6	10.9 ± 1.4	88.9 ± 1.7
mean		**12.2 ± 1.3**	**88.3 ± 2.5**

Table 4.1: Ages and their measurement uncertainties for VRM 06/23 and CRM-112A. Ages are corrected ages. $k_{230} = 0.37$ and $k_{229} = 6.7$ for the first measurement day, and $k_{230} = 0.39$ and $k_{229} = 6.6$ for the second. The errors on the mean values are the standard deviations of the measurements.

Coral sample	**Age (a)**	**Age (a) band-counting**
CPR	36.7 ± 4.3	31
BOC	12.3 ± 1.2	11

Table 4.2: Measured and band-counted ages for BOC and CPR samples. $k_{230} = 0.4$ cps/V and $k_{229} = 4.4$ cps/V to shift CRM-112A to (88.3 ± 2.5) years. As a detrital thorium correction factor, (2 ± 1) was selected. The ages refer to the time of measurement (March 2023).

4.4 Adapting the measurement protocol

4.4.1 Measurement sequence update

To be able to track the daily changes of k_{230} and k_{229}, we introduce the uranium reference materials with a known age as another standard being measured at least twice per measurement session. A measurement session sequence looks like this:
HU1 - RM (unspiked) - RM (spiked) - HU1 - sample - HU1 - sample - ... - HU1 - RM (unspiked) - RM (spiked) - HU1
RM here refers to "reference material". In the case of young samples, VRM is used because of its precisely known age. For older samples (with typically higher intensities), CRM-112A is employed with its offset corrected age value as target. As VRM is a very young material of only 12 years and thus very little counts on ^{230}Th, it would be stronger affected than CRM-112A by the increase of the process blank over the course of a measurement session of older samples. At the same time, i. e. k_{230} is less dominant for those samples.
For both measurements at the beginning and end of the session, k_{230} resp. k_{229} are determined and the mean values are used for evaluation. In case of longer sessions, i. e. of more than 8 hours, one block of reference material measurements is put into the middle of the series.

4.4.2 Measurements with separate U and Th solutions

As shown above, variation during one day can still be around 0.03 cps/V for k_{230}, the more influential correction (in almost all cases). To reduce the impact of the ghost signals, the signal intensity of ^{238}U needs to be reduced. This can be achieved via separate measurements of Th and U solutions. However, this is not necessary for all samples. For older samples that are lesser affected by the ghost signal corrections, the increase in effort during chemical preparation and the additional measurement time do not weigh up against the gain in accuracy, when it is much smaller than the measurement uncertainty. Figures 4.3 to 4.5 explore the threshold for the necessity to split up the fractions. For this dataset of CWC and few speleothem ages, the deviation caused by daily variation of k_{230} is clearly smaller than the uncertainty of the corrected ages. This however depends on the thorium content of the samples and would be different for samples with less detrital thorium, so the relevant quantity for comparison is the uncorrected age (Fig. 4.4 and 4.5). As can be derived from Fig. 4.5, 1.5 ka is the minimum age for measuring U and Th in one solution. Often, expected ages for a new series of samples (such as a so-far unsampled coral cores or speleothems) cannot easily be estimated. In these cases, test measurements on some samples should be carried out.
The column chemistry separation works well at the moment, with very little U in the Th fraction (down to none at all for standards). About 5 % of the U fraction are admixed to the Th fraction for measurements. A close monitoring of the separation efficiency over

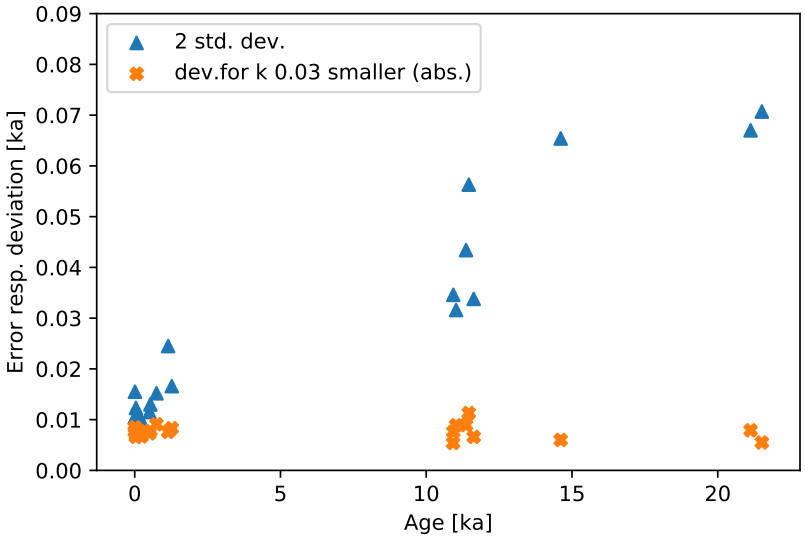

Figure 4.3: For the age range 0-20 ka, the measurement uncertainties (being 2 standard deviations) of corrected CWC ages are plotted. The orange crosses represent the deviation from the "ideal" age value caused by a change in k_{230} of 0.03 cps/V. The deviation is symmetrical for addition and subtraction. The samples measured were routine measurements.

time is neccessary.

4.5 Conclusions

This chapter underlines the relevance of fully understanding the "ghost signal" corrections for fast and precise measurement protocols. The temporal variation of the signals has been tackled by adapting the measurement protocols (extra bracketing with a reference material at the beginning and end of each sequence - both spiked and unspiked) and measuring young samples up to 1.5 ka in separated solutions. This however is only an intermediate solution: a future instrument with enough detector slots (one more) which would allow to measure the isotopes in 2 lines would not require the separated solutions any more, because then ^{238}U could be collected in a cup and the effect is reduced (Chiang et al., 2019). More thoughts on this topic can be found in the Conclusion of the thesis.
Furthermore, a reference material with a validated age is needed to allow for adaequate k_{230} corrections. By introducing VRM06/23, we do not only have a reliable reference for adjusting the k_{230} values, but could also track the age offset of CRM-112A. With its "true" radiometric age of (88.3 ± 2.5) years, it can be employed as a reference for ghost signal correction, too.

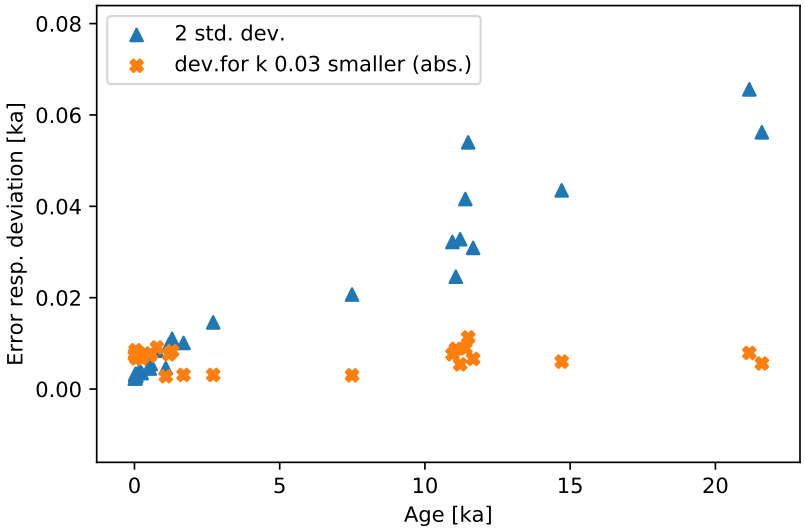

Figure 4.4: The same dataset as in Fig. 4.3, complemented by a few speleothem ages to fill age gaps, is presented with the blue triangles now representing the uncorrected ages.

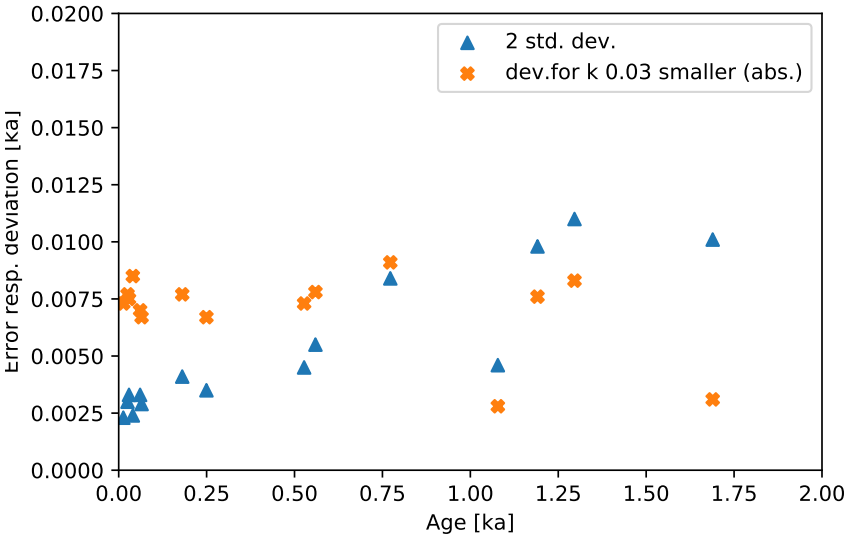

Figure 4.5: Zoom-in on Fig. 4.4.

5 Technical note: „U-Th Analysis" – an open-source software dedicated to MCICPMS U-series-data treatment and evaluation

In this chapter, an open-source graphical user interface (GUI) developed for ^{230}Th/U age evaluation in the Physics of Environmental Archives group at IUP Heidelberg is presented. It is intended to make the evaluation of ages reproducible and user-friendly.
In the scope of this PhD project, a bachelor project was conceptualized, designed and supervised, in which the GUI development was mainly carried out (bachelor student Fabian Kontor, (Kontor, 2021)).
Within this chapter, excerpts from a paper manuscript (Kerber et al.) with the title "Technical note: „U-Th Analysis" – an open-source software dedicated to MCICPMS U-series-data treatment and evaluation" are presented. It shall be submitted to the journal *Geochronology*. In the original manuscript, also an application study around stalagmite B1 from Cueva Larga, Puerto Rico, is presented, which was mainly contributed by Sophie Warken and Norbert Frank. The example study is not part of this chapter. The data visible as examples in Fig. 5.1 to 5.3 are measurements of B1 (provided by S. Warken). The methods section and small parts of the introduction have been shortened to avoid overlap with Chapter 3.

5.1 Introduction

U-series disequilibrium methods, ^{230}Th/U dating, is a precise chronometer covering the last circa 650 ka, and has proven indispensable for the age determination of marine and continental carbonate archives and their applications (Bourdon et al. (2003), Cheng et al. (2013)). The applications relying on this dating method are manifold in geochemistry, archaeology and climate science (Burley et al. (2012), Cheng et al. (2016), Frank et al. (2004), García-Diez et al. (2013), Hellstrom and Pickering (2015), Lascu et al. (2016), Moseley et al. (2015), Robinson et al. (2014), Schwarcz et al. (1979), Thompson (2022), Warken et al. (2022), Wilcox et al. (2020)). Further development of this dating method includes both improvements in instrumentation and measurement protocols, as well as reproducible data analysis and age calculation schemes (Andersen et al. (2004), Breton et al. (2015), Cheng et al. (2013), Chiang et al. (2019), Hellstrom (2003), Hoffmann et al. (2007), Kerber et al. (2023), Pourmand et al. (2014), Shao et al. (2019), Shen et al.

(2002), Shen et al. (2012)). A recent development for multi collector inductively coupled plasma source mass spectrometry (MCICPMS), which is presently the most sensitive technology for U and Th isotope measurements, is the implementation of high ohmic amplifiers allowing detection of small signals on Faraday cups (FC) instead of secondary electron multipliers (SEM) (Breton et al., 2015). Measurement protocol updates aim at increasing measurement precision and/or decreasing input sample masses by combining new detector layouts, improving the understanding of correction factors, and ensuring a stable measurement environment (Andersen et al. (2004), Cheng et al. (2013), Chiang et al. (2019), Hellstrom (2003), Hoffmann et al. (2007), Kerber et al. (2023), Shao et al. (2019), Shen et al. (2002), Shen et al. (2012)).
We here focus on the third route for the enhancement of ^{230}Th/U dating which is clear and reproducible data analysis and age calculation schemes (Pourmand et al. (2014), Shao et al. (2019)). Up to now, only two ^{230}Th/U dating data analysis routines have been published (Pourmand et al. (2014), Shao et al. (2019)). However, regarding the rising amount of data being produced in MCICPMS labs, data management is becoming more and more important. For example, scatter peaks as described in Chapter 4 may depend on the specific instrument or vary through time, so these corrections need to be adaptable constants in the data evaluation routine, with the possibility to also apply them retroactively. Easy re-analysis of data is also important for applying different correction models for initial detrital thorium (e. g., Hellstrom (2006)). Another aspect is updating half-lives (such as e. g. from Cheng et al. (2000b) to Cheng et al. (2013)), which makes re-evaluation of previously measured data necessary. These tasks are error-prone, in particular when they require copy-and-pasting data in e. g. Excel sheets. Also, a clear and unified documentation of the applied constants and the way of saving data is desirable. Additionally, the statistical methods, for example for outlier correction, should undergo clear documentation. Altogether, this helps to report ^{230}Th/U ages in a standardized way (Dutton et al., 2017).
In this study, we present our easy-to-use user-friendly GUI and the underlying algorithm for data treatment and age calculation. Methods to treat outliers in measurement data are particularly highlighted.

5.2 Methods

Spike and standard materials, chemical preparation and measurement setup are exactly the same as described in section 3.2. In the GUI screenshots, data for speleothem B1 are presented (B1 data provided by S. Warken).

5.3 Data treatment and analysis procedures

Our GUI makes use of the open source PyQt5 Python library (`https://pypi.org/project/PyQt5/`). Via `https://github.com/EnvArchivesHD/UThAnalysis`, the stan-

dalone GUI application (.exe) and the code can be downloaded. Both data read-in as well as the output are in .csv or .xlsx files. The GUI consists of three consecutive tabs, for which the functionalities and the underlying calculations and processes will be described in the following.

5.3.1 Input tab

In 'Input', as presented in Figure 5.1, the user can navigate to the folder containing the raw mass spectrometer data and start the calculation of corrected isotopic ratios (marked as (1) in Figure 5.1). Prior to the calculations, a configuration file containing all necessary constants used in the calculations needs to be loaded (2). This file contains all the constants used for evaluation of the activity ratios and ages, such as mass fractionation coefficients, decay constants, the exact masses of the isotopes and the values applied for initial Th correction. All constants can be edited manually either in the configuration file directly, or within the GUI using the button "edit".
This approach allows to include the possibility to apply a correction of the ^{230}Th concentration due to the presence of initial Th derived from non-carbonate contamination such as detrital residues, or the direct incorporation of ^{230}Th from the aquatic environment, such as seawater. Per data series, only one correction constant, the (^{230}Th/^{232}Th) activity ratio of the contamination, can be added to the calculation. Hence, in case several factors need to be explored the data series requires repeated treatment. Exemplary templates for corals and speleothems with conventionally used correction models are provided (compare the *dist* folder on `https://github.com/EnvArchivesHD/UThAnalysis`). For speleothems, a typical activity ratio of (^{230}Th/^{232}Th) of the detritus is estimated to (0.750 ± 0.375), which is derived from a bulk earth Th/U weight ratio of (4.10 ± 2.05) and the assumption of ^{230}Th, ^{234}U, and ^{238}U being in secular equilibrium (Wedepohl, 1995). Nevertheless, this ratio may require adjustment according to local conditions (e. g., Hellstrom (2006), Warken et al. (2020)). The coral template assumes as default value an activity ratio of 8 ± 4, which is estimated for corals dwelling in waters of the northeast Atlantic upper thermocline (Schröder-Ritzrau et al. (2003), Wefing et al. (2017)). Depending on water depth and coral sites this value must be adjusted, as will be discussed later.
Figure 5.1 shows the layout of the GUI 'Input' tab. Once the constants are implemented and the input data are selected, it is optional to choose an output path to store the analysis output (3). If no path is specified, the results will be stored in the raw data folder. When clicking the settings button next to the output path (4), a menu opens in which the following parameters about the sample can be noted: denomination, type of archive, lab numbers, geographic origin, and a general description. The first and last laboratory number are automatically read out from the raw data. The final output results files will then be saved in a newly created folder under the name [labnumber$_1$ – labnumber$_n$] denomination in the directory chosen before. The metadata information transferred through the GUI dialogue window is stored in a .json file in the respective folder. In the 'custom

constants' box (5), some settings can be selected, for example, if the blank has already been subtracted in the mass spectrometric software or not. Next to this box, an overview over the files read in from the folder is shown (6). After running the evaluation script with the loaded data and adjusted settings (Button "run", (7)), the results of tailing (8) and hydride correction (9) as well as the calculated ratios (10) are displayed in the tab. In addition, four excel .xlsx output files are created by the software at this stage and stored in the directory path folder: Ratios.xlsx, Tailing.xlsx, PrBlank.xlsx and Intensities.xlsx. Ratios.xlsx contains all calculated ratios and their errors as also presented in the GUI (10). Tailing.xlsx summarizes the U and Th tailing values (in cps/V ^{238}U) for each mass. In PrBlank.xlsx, the average values for each mass of the procedural blank measurements before each standard and sample are presented. Intensities.xlsx contains the full data tables, with the signals in cps or V for each mass over all cycles. Every standard or sample has its own sheet.

The algorithm of the 'Input' tab starts by reading in the '.exp' measurement files for sample and standard measurements, process blank (=instrumental background) and uranium and thorium abundance sensitivity measurements. The lines for all cycles for all isotopes are imported into a pandas data frame. Firstly, matrices for tailing, hydride and process blank correction are produced that are later subtracted from the isotopic masses used for ratio building. The individual steps are carried out as follows:

- **Tailing:** Uranium tailing is determined by measuring the off-masses 228.5, 233.5, 236.5, 236.7, 237.05 and 237.5 before a measurement sequence starts. The first half-mass can be changed between 228.5 and 227.5 as we observe a scattering peak around this mass that switches its exact position every few months. Tailing off-masses are 227.5, 228.5, 229.5, 230.5 and 231.5. For interpolation to full masses, we use piecewise cubic Hermite interpolating polynomial fits. The masses that undergo ^{238}U tailing correction are ^{233}U, ^{234}U, ^{235}U, ^{236}U, ^{229}Th, ^{230}Th and ^{232}Th, while ^{232}Th correction is applied to ^{229}Th and ^{230}Th.

- **Hydride isobaric interference:** Hydride correction is determined by measuring 239 amu for UH^+ and 233 amu for ThH^+ during the abundance sensitivity measurements. The instrumental background (or memory) is here referred to as process blank. It is measured between all sample and standard measurements for 70 s. Typical blank levels afterwards are 0.5 cps for ^{230}Th and 6 cps for ^{234}U. The matrices from these three corrections are then used for data reduction of each isotope.

- **Detector setting:** Three main different detector layouts are possible and are detected automatically by the software: 1) all isotopes on cup, 2) ^{234}U, ^{230}Th and ^{229}Th on SEM and 3) ^{234}U on FC, ^{230}Th and ^{229}Th on SEM. In normal operation, option 2) and 3) are used, depending on the ^{234}U concentration of the respective samples. ^{234}U signals above 2 mV are measured on the centre FC which is the case for the absolute majority of samples.

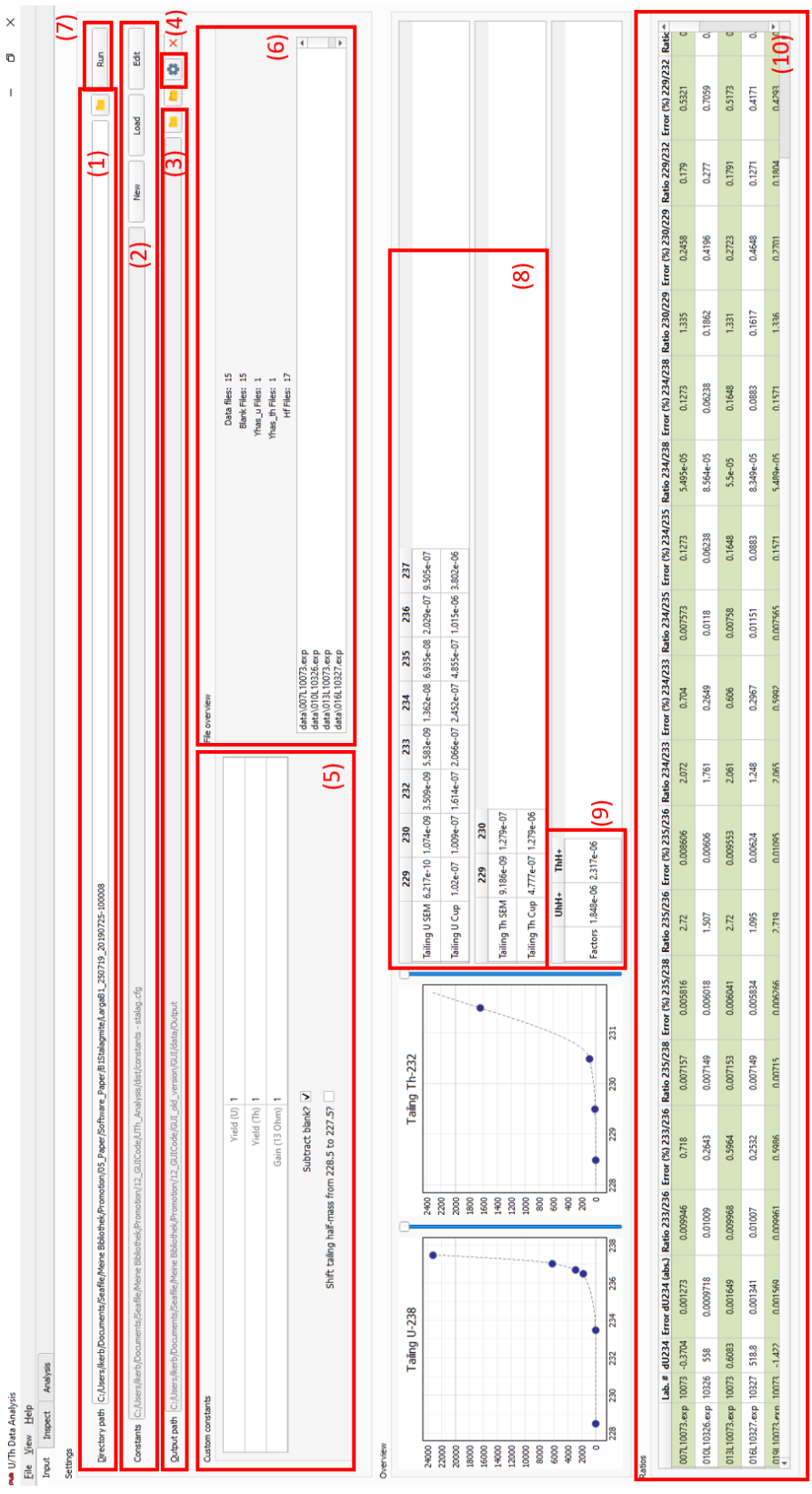

Figure 5.1: Input tab. (1) Selection of data folder, (2) load constants file, (3) optional: setting of an output path, (4) "settings" button to enter metadata for saving, (5) custom constants box, (6) file overview for the selected folder, (7) "run" button to start the ratio calculation, (8) numerical values of U and Th tailing (plots left to this box show the interpolated tailing functions), (9) numerical values of hydride correction, (10) calculated ratio panel.

The treated data are now used for the calculation of all relevant isotopic ratios followed by subsequent outlier tests.

5.3.2 Inspect tab

Following the initial raw data treatment in the Input Tab, the 'Inspect' tab (presented in Figure 5.2) allows to visualize and retreat the data prior to final age calculation. In particular, the settings for the outlier test can be adapted.
The Inspect tab allows the user to plot the signal datapoints over the measurement cycle number for all isotopes in the individual measurement files of the sequence. In the top of the tab (1), the ratio results table from the 'Input' tab is presented. On the left (2), the list of measurement files (.exp) is shown. By clicking on a specific file, the metadata and the signal plotted over the measurement cycle number are presented (3). On the bottom left (4), four dropdown menus are available: The first one, "Isotope", allows to select one isotope from all of the isotope species measured. "Mean" offers to switch between mean and median of the signal. The "Deviation" menu provides three options for the assessment of data dispersion: standard deviation, median absolute deviation and interquartile range. By setting "Scaling" to absolute or relative, the y-axis of the plot on the right can be changed between signal intensities in V or cps and relative values. Any selection in the dropdown menus leads to an automatic update of the plot on the right. Mean resp. median, as well as the dispersion ranges are presented as blue dashed lines. Data points outside of the dispersion range are marked in red as outliers. The "Calculate ratios" button (5) provides the option to recalculate the ratios using the updated mean and deviation selection for all isotopes. The default settings are median and standard deviation. However, these updated options are then used to exclude outliers from the ratio arrays, not the signal intensity arrays themselves. This means that not necessarily exactly the same data points marked as outliers in the signal intensity plots will be excluded, but the ones where signal ratios of two isotopes are outside of the accepted deviation range. The option selected in "Mean" will then also be used to calculate the average of the isotope ratios. The method of calculating the uncertainty of outlier-corrected isotopic ratios, however, is fixed:

$$err_{ratio} = 2\frac{s}{\sqrt{n}} \tag{5.1}$$

with s being the standard deviation and n the number of data points (after outlier correction).

The arithmetic mean ($\bar{x} = (x_1 + ... + x_n)/n$) and the median $\bar{M}$ (central value of all values) are different ways of determining the average of a distribution. The three different options for dispersion are defined as follows:
Standard deviation s is defined as

$$s = \sqrt{\frac{1}{n-1}\sum_{i=1}^{n}(x_i - \bar{x})^2} \tag{5.2}$$

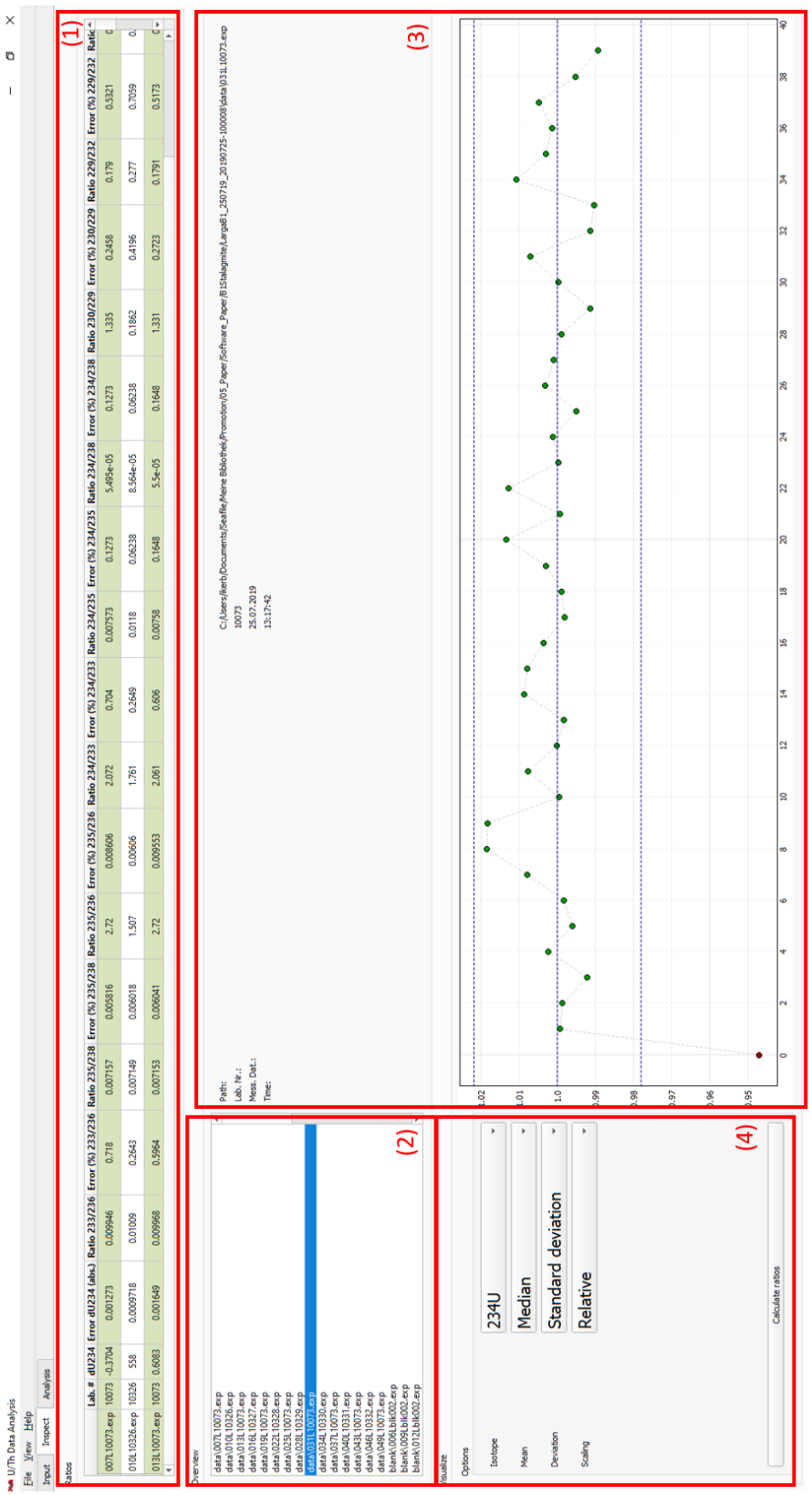

Figure 5.2: Inspect tab. (1) Ratio results table (from Input tab), (2) measurement file list, (3) metadata of a selected file and signal over measurement cycle number for one isotope (which can be selected in (4)), (4) option selection panel for the signal plotting.

with $\bar{x}$ being the mean.
Interquartile range in turn is defined as the range containing the "middle" 50 % of data points (Tukey et al., 1977). The median absolute deviation MAD is the median of absolute deviations from the median (Huber (2004), Leys et al. (2013), Rousseeuw and Croux (1993)). For the calculation of the uncertainty MAD we assume normal distributed data, thus k =1.4286.

5.3.3 Analysis tab

In a last step, age calculation is carried out in the 'Analysis' tab presented in Figure 4. Here, additional input data is necessary from the sample weight tables (1). There are several ways to import these tables: Either by clicking "Load" and navigating to the respective folder, or by manually creating the table directly in the GUI ("Create"). In the panel "Metadata history", the previously loaded sample weight tables in the directory path folder are shown, and can be directly imported (2). "Start Analysis" calculates the ages (3). Outputs are both presented in the GUI (4) and stored in an Results.xlsx file. In case an output path was specified, Results.xlsx is created both in the output and in the directory path folder. If the output path is missing, the file is only saved in the directory path folder. If an output directory has been created for specific lab numbers, all following analysis of these same files will be written to the same output directory, but not overwrite earlier Results.xlsx. The Results.xlsx has five sheets: Inputs, Calc, Results, Constants and Options. Inputs presents sample weight and metadata as well as the calculated ratios. In Calc, all steps of the age calculation such as concentrations and activity ratios are shown. Results is a summary of the most important calculation steps and final age values and the same table as is presented in the GUI as (4). Constants contains the whole list of values from the (potentially edited) '.cfg' file. In Options the average and dispersion measure option are stored. Age determination follows the equations presented in section 2.1.

5.4 Discussion

5.4.1 Outlier correction

Outlier correction is carried out automatically by the software adapting the dispersion measure of the raw data and in the following we argue that generally means should be replaced by medians. Shao et al. (2019) had addressed this problem by implementing manual outlier removal by comparison to boxplots based on interquartile ranges. We opted for the automatic version as this is more time efficient for large datasets. The different dispersion measure options described before are relevant because measurements are not always ideal cases with normally distributed data and thus outliers. During measurements, short-term system instabilities occur for a variety of reasons, such as varying gas flow in the inlet system, plasma instabilities, and varying size of sample aerosols causing outliers in the signal intensities. Even though only the ratios between the different isotopes are of

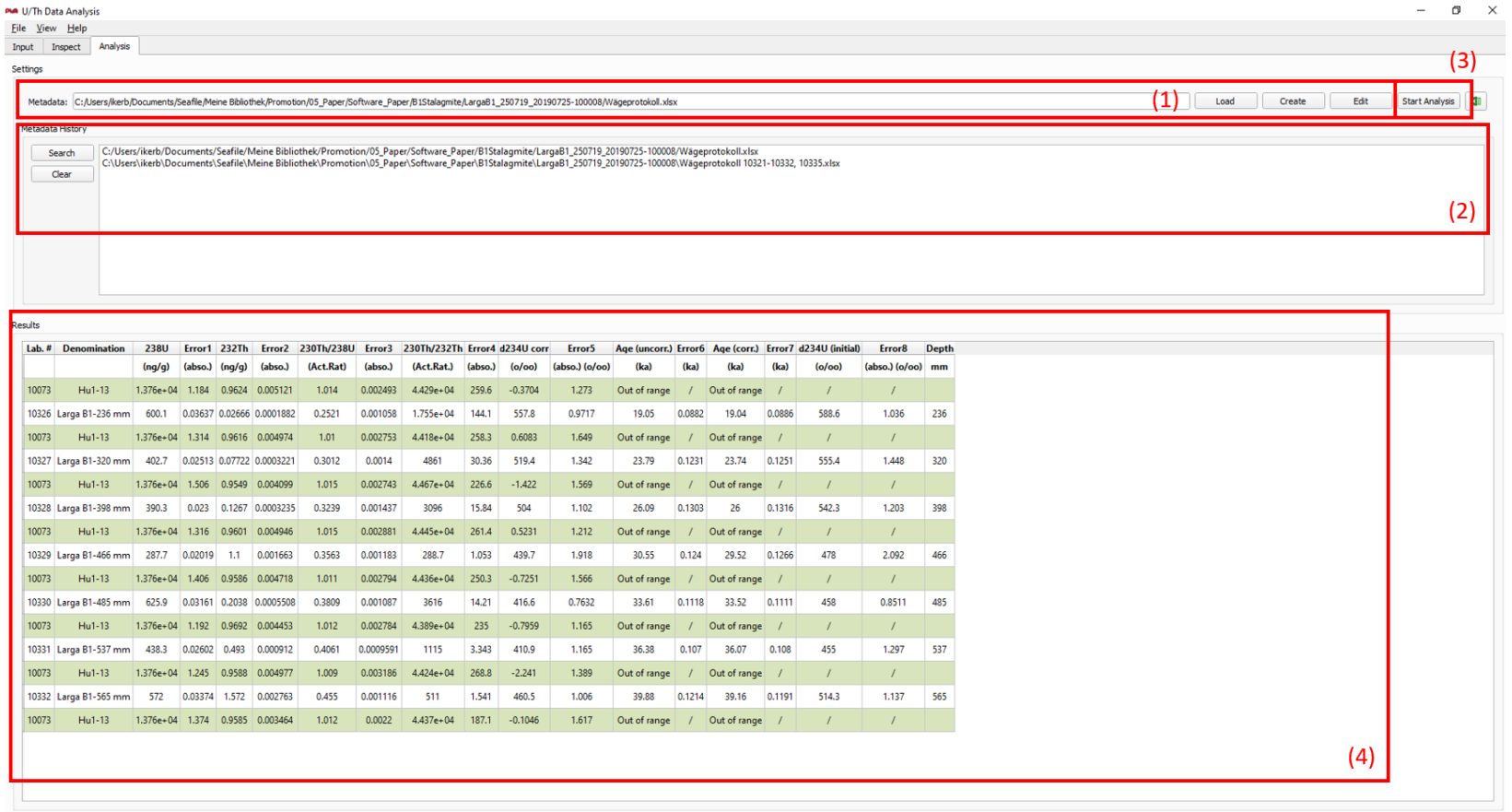

Lab. #	Denomination	238U	Error1	232Th	Error2	230Th/238U	Error3	230Th/232Th	Error4	d234U corr	Error5	Age (uncorr.)	Error6	Age (corr.)	Error7	d234U (initial)	Error8	Depth
		(ng/g)	(abso.)	(ng/g)	(abso.)	(Act.Rat)	(abso.)	(Act.Rat.)	(abso.)	(o/oo)	(abso.) (o/oo)	(ka)	(ka)	(ka)	(ka)	(o/oo)	(abso.) (o/oo)	mm
10073	Hu1-13	1.376e+04	1.184	0.9624	0.005121	1.014	0.002493	4.429e+04	259.6	-0.3704	1.273	Out of range	/	Out of range	/	/	/	
10326	Larga B1-236 mm	600.1	0.03637	0.02666	0.0001882	0.2521	0.001058	1.755e+04	144.1	557.8	0.9717	19.05	0.0882	19.04	0.0886	588.6	1.036	236
10073	Hu1-13	1.376e+04	1.314	0.9616	0.004974	1.01	0.002753	4.418e+04	258.3	0.6083	1.649	Out of range	/	Out of range	/	/	/	
10327	Larga B1-320 mm	402.7	0.02513	0.07722	0.0003221	0.3012	0.0014	4861	30.36	519.4	1.342	23.79	0.1231	23.74	0.1251	555.4	1.448	320
10073	Hu1-13	1.376e+04	1.506	0.9549	0.004099	1.015	0.002743	4.467e+04	226.6	-1.422	1.569	Out of range	/	Out of range	/	/	/	
10328	Larga B1-398 mm	390.3	0.023	0.1267	0.0003235	0.3239	0.001437	3096	15.84	504	1.102	26.09	0.1303	26	0.1316	542.3	1.203	398
10073	Hu1-13	1.376e+04	1.316	0.9601	0.004946	1.015	0.002881	4.445e+04	261.4	0.5231	1.212	Out of range	/	Out of range	/	/	/	
10329	Larga B1-466 mm	287.7	0.02019	1.1	0.001663	0.3563	0.001183	288.7	1.053	439.7	1.918	30.55	0.124	29.52	0.1266	478	2.092	466
10073	Hu1-13	1.376e+04	1.406	0.9586	0.004718	1.011	0.002794	4.436e+04	250.3	-0.7251	1.566	Out of range	/	Out of range	/	/	/	
10330	Larga B1-485 mm	625.9	0.03161	0.2038	0.0005508	0.3809	0.001087	3616	14.21	416.6	0.7632	33.61	0.1118	33.52	0.1111	458	0.8511	485
10073	Hu1-13	1.376e+04	1.192	0.9692	0.004453	1.012	0.002784	4.389e+04	235	-0.7959	1.165	Out of range	/	Out of range	/	/	/	
10331	Larga B1-537 mm	438.3	0.02602	0.493	0.000912	0.4061	0.0009591	1115	3.343	410.9	1.165	36.38	0.107	36.07	0.108	455	1.297	537
10073	Hu1-13	1.376e+04	1.245	0.9588	0.004977	1.009	0.003186	4.424e+04	268.8	-2.241	1.389	Out of range	/	Out of range	/	/	/	
10332	Larga B1-565 mm	572	0.03374	1.572	0.002763	0.455	0.001116	511	1.541	460.5	1.006	39.88	0.1214	39.16	0.1191	514.3	1.137	565
10073	Hu1-13	1.376e+04	1.374	0.9585	0.003464	1.012	0.0022	4.437e+04	187.1	-0.1046	1.617	Out of range	/	Out of range	/	/	/	

Figure 5.3: Analysis tab. (1) Load sample weight tables (metadata files), (2) history of previously loaded tables, (3) "start Analysis" button to calculate ages, (4) age results.

interest, strong changes in signal intensity may lead to varying isotope ratios, as a result of changing variance. Such difference may be amplified by the use of different detectors or with respect to different magnetic field settings, which are not necessarily responding at exactly the same amplitude . Moreover, signal decreases cause the statistical variance to increase locally. Figure 5.4 shows an example: The upper panel displays periodic dips in the ^{238}U signal intensity during a measurement. In the lower panel of Fig. 5.4, the uncorrected ^{230}Th/^{238}U ratio for the same measurement is plotted. For both curves, the different measures to calculate dispersion are shown. The default method (2 standard deviations) does not remove all the systematic outliers. Also, it is clearly visible that the median agrees much better with the majority of signal intensity values than the mean, which is much stronger influenced by the periodic dips due to the asymmetry in the statistical distribution. Such an obvious difference is not visible in the isotope ratio, but within the resulting uncertainty. Consequently, we propose to generally use the median instead of mean by default. This is more accurate in the case of asymmetric small-scale oscillations inside the non-outlier interval and has no disadvantages. Applying standard deviation as a dispersion measure in Figure 5.4 does not cover most of these outliers due to their large number and relatively small deviation. Thus, applying another dispersion measure for outlier removal is necessary here, and in addition more robust and easier to accomplish than manual deletion of all of the outliers. It is important, however, to stress that the outlier correction using the selected dispersion option is run on the calculated ratios after correction, not on the signal intensities themselves. This implies that when all isotopes are affected in the same way, they pass the outlier test. This is, however, unlikely at least for ratios of isotopes measured in different magnetic field settings. The dispersion measure of the outlier corrected ratio array is the same in every case, as described by Equation 5.1.

5.4.2 Detrital thorium correction

Thorium correction is often crucial for studying speleothems where the correction is significant, but the initial Th value is unknown and/or potentially variable or when studying "dirty" carbonates such as tufa and travertine (Mallick and Frank (2002), Hellstrom (2006)). Besides the terrestrial regime, this aspect of ^{230}Th/U dating is also relevant for marine archives, such as corals. Cheng et al. (2000a) set the range as 80 ± 80 for deep-sea solitary corals, Shen et al. (2008) determined 0.4 – 3.1 for tropical corals and Lomitschka and Mangini (1999) 17 – 30 for cold water corals. Frank et al. (2004) calculated 10 ± 4 from seawater in the Eastern North Atlantic deep sea and Schröder-Ritzrau et al. (2003) found values between 5 and 20 from isochrones of coral coating. This demonstrates the importance of an easily adaptable correction factor in the software.

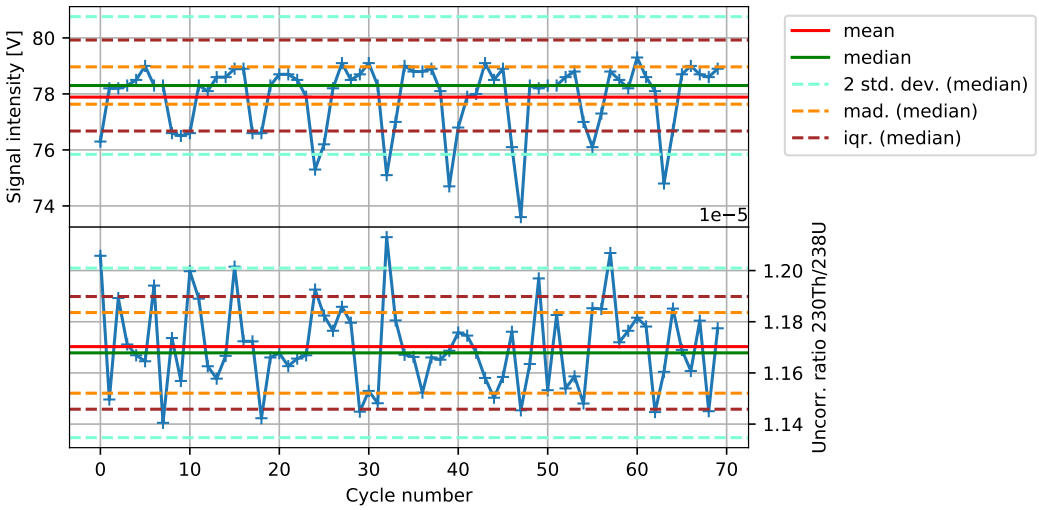

Figure 5.4: Upper panel: ^{238}U signal intensities in Volt over measurement cycles for a carbonate sample during routine lab measurements. Lower panel: Corresponding uncorrected ^{230}Th/^{238}U ratio. Mean and median as well as the three different dispersion measures are plotted.

5.5 Conclusion

We here provide an algorithm combined with a user-friendly GUI application for ^{230}Th/U MCICPMS data treatment and age calculation. The two so far published programs explicitly aimed at ^{230}Th/U dating data reduction and age calculation are both written for ThermoFisher Neptune instruments as well. Pourmand et al. (2014) described a Mathematica routine, distributed as a Computable Document Format (.cdf) file, while Shao et al. (2019) had published a Matlab algorithm with GUI. We here have chosen to use Python for our algorithm and GUI to keep it open-source. The advanced user might want to change settings, which makes an open-source language and libraries a major advantage. Our program supports multiple types of detector configurations: the FC-FC based approach as well as FC-SEM combining protocols. It is however adapted for combined Th and U measurements in three magnetic field lines (compare Kerber et al. (2023)), but other methods (such as separate solutions for Th and U) can be implemented with small changes in the code. Our application is especially designed to take reproducible and clear data management into account by a collection of methods: This includes that automatic creation of folders containing the results files and information on the sample metadata is possible and that .xlsx output files automatically contain all constants used for calculation, as well as the settings for outlier correction. Manually changing input constants, e. g. detritus correction, does not require to go to the code directly. So, the whole analysis scheme does not require any copy-and-pasting from one excel table to the other, and the constants used for calculation are easy to update.

Part II

Age frequency distributions

6 Statistical analysis of temporal cold-water coral occurrence throughout the Atlantic Ocean and the Mediterranean Sea

This chapter focusses on the application of a statistical method for distribution analysis (Kernel Density Estimation, KDE) to cold-water corals in order to better understand their temporal and spatial occurrence patterns. Typically, for such studies histograms are employed (e. g. de Carvalho Ferreira et al. (2022)), or in rare cases Probability Density Plots (Bonneau et al. (2018)). With rising amounts of data being published, more sophisticated data description and visualization tools such as KDE offer new insights and ensure appropriate representation and interpretation of data (e. g. Vermeesch (2012), Weij et al. (2020)). Thus, the potential of this method for cold-water corals is explored here.
The chapter is written in the style of a manuscript and will be submitted to *Geochemistry, Geophysics, Geosystems* soon, with co-authors Norbert Frank, Andrea Schröder-Ritzrau, Jürgen Titschack and Claudia Wienberg.
I had the intial idea to apply density estimation methods to cold-water corals and all steps of method exploration and data analysis within this study were carried out by myself. Method development and possibilities were mainly discussed with Jürgen Titschack and Norbert Frank. Claudia Wienberg provided a multi-region data compilation of CWC ages. Andrea Schröder-Ritzrau helped with extension of the data compilation. All co-authors contributed to the discussion about the interpretation of the age distributions with respect to environmental, climatic and ecological factors.

6.1 Introduction

Within the Earth's oceans, cold-water corals (CWCs) inhabit a large latitudinal range from the equator to both polar regions and water depths between the deep-sea (down to 6,000 m) and a few meters (Roberts et al., 2009). Some framework-forming species of the order Scleractinia (stony corals) are of utmost importance as they form large reefs, which can develop to coral mounds (three dimensional geomorphological structures) over time, which are important biodiversity hotspots in the deep-sea (Henry and Roberts, 2017). Among them, the best-studied species are *Lophelia pertusa* (recently assigned to the genus *Desmophyllum* by Addamo et al. (2016)) and *Madrepora oculata* (Wienberg and Titschack, 2017). Their highest concentration has so far been found in the Atlantic, including the Gulf of Mexico and the Mediterranean Sea. They occur mainly along the

continental margins, on the shelf and upper to mid-slope (Roberts et al. (2009), Douarin et al. (2013), Fosså et al. (2002), Raddatz et al. (2016), Tamborrino et al. (2019)), on seamounts (Mortensen et al. (2008), Clark (2006)), and within canyons (Gori et al. (2013), Wienberg et al. (2018)).
Scleractinian CWCs have evolved as relevant climatic and paleoceanographic archives (Robinson et al. (2014), Raddatz and Rüggeberg (2021)). This is because their aragonitic skeleton is accessible to precise dating via the ^{230}Th/U radiometric method (Frank and Hemsing, 2021) and different elemental or isotopic proxies incorporated into the aragonite allow to reconstruct past oceanic conditions, for example seawater temperature via the Li/Mg ratio (Cuny-Guirriec et al., 2019).
By now, a large amount of radiometric ages has been obtained from CWCs. In particular over the last two decades, a massive acceleration in data production took place, which is mainly due to a change in instruments for ^{230}Th/U dating from thermal ionisation mass spectrometry (TIMS) to multi-collector inductively coupled plasma mass spectrometry (MCICPMS) (Hellstrom (2003), Hoffmann et al. (2007), Shen et al. (2002)). Thus, studies that aim at understanding the temporal and spatial patterns of the occurrence of CWCs by using extensive datasets are becoming more numerous (de Carvalho Ferreira et al. (2022), Frank et al. (2011), Thiagarajan et al. (2013), Wienberg et al. (2022), Wienberg and Titschack (2017), Wienberg et al. (2020)).
Coral occurrence is influenced by a multitude of environmental parameters such as productivity, temperature, oxygen and currents (Davies and Guinotte (2011), Davies et al. (2008), Dodds et al. (2007), Dullo et al. (2008)). Occurrence patterns have been observed and described, leading to different hypotheses about the interplay of driving factors for coral growth and decline at specific regions and times. One example is the hypothesis of a Gibraltar glacial-interglacial seesaw pattern, which describes the occurrence of CWCs in the southern Gulf of Cadiz (off Morocco) being restricted to glacial periods and predominant occurrence of CWCs in the Alboran Sea (westernmost Mediterranean Sea) during the last deglacial and interglacial periods (Fink et al. (2013), Frank et al. (2011), Krengel (2020), Wienberg et al. (2010), Wienberg et al. (2009), Wienberg et al. (2022)). So far, such hypotheses are based on qualitative observations only and a statistical quantitative evaluation might substantiate these proposed patterns. Another aspect to consider is the question if these patterns are caused by environmental conditions or caused by a sampling bias.

To understand this better, and using meaningful statistical data description methods, we look at method development in detail in this study. The use of statistical distribution descriptors for ^{230}Th/U ages was mainly examined for speleothems so far (Weij et al. (2020), Hercman (2000), Baker et al. (1993), Gascoyne et al. (1983)). To our knowledge, the only application of age frequency analysis to corals was provided by Smart and Richards (1992) for tropical reef corals to analyse sea-level highstands during the Quaternary. However, also speleothem studies applying age frequency analysis additional to classical proxies are still sparse, because of a scarcity of large datasets. The first age dis-

tribution studies relied on histograms (Gascoyne et al., 1983), but method development lead to the adaption of probability density plots (PDPs) (Baker et al. (1993), Hercman (2000)). However, both of these techniques have disadvantages. For example, peaks in histograms are not necessarily stable under different bin definitions, and it is also impossible to include measurement age uncertainties into histograms (Zambom and Ronaldo (2013), Weij et al. (2020)). PDPs are constructed by adding up Gaussian functions for each data point (here =age). The mean of these functions is the value of the respective data point and the width σ its uncertainty. However, as the area under the curves is conserved, the amplitude of the individual functions changes. This produces very sharp peaks in areas of high measurement precision that do not correspond to high probability densities (Weij et al., 2020). To avoid such artificial peaks, Weij et al. (2020) proposed Kernel Density Estimation (KDEs) for ^{230}Th/U ages up to 500 ka BP, which has already been adapted in multiple fields. In contrast to PDP, KDE smoothes out different measurement uncertainties by using a fixed bandwidth as σ for every data point. In the geosciences and palaeoclimatic research, examples for KDE use are ^{14}C ages (Ramsey, 2017), but also zircon grain dating (Vermeesch (2012), Vermeesch and Garzanti (2015)). KDEs have also been applied in other scientific fields, e. g. Zambom and Ronaldo (2013) for econometrics, Desforges et al. (1998) in engineering and Qin et al. (2011) for renewable energy systems.

In this study, we demonstrate the potential of appropriate statistical data visualization for the analysis of CWC age datasets. We want to show how hypotheses on the temporal occurrence of CWCs can be better supported by solid statistical descriptors including uncertainty treatment. We present how to handle potential biases and apply the method to resolve multiple phases of coral occurrence during the last glacial in the Gulf of Cadiz and different peak occurrences for *L. pertusa* and *M. oculata* in the Alboran Sea. Furthermore, the growth dynamics of CWC in the North Eastern Atlantic is resolved. We focus on the time with the best coral coverage for each region. At maximum, these are the last 71 ka BP (for the Gulf of Cadiz), an interval of time that comprises the last glacial period (MIS2-4), the last deglaciation (after the Last Glacial Maximum; the latter lasting from 26.5 to 19-20 ka BP, (Clark et al., 2009)) associated with a major global warming, sea-level rise and large-scale reorganization of the oceanic-atmospheric system, and the present interglacial, the Holocene ($<$ 11.7 ka BP).

6.2 Materials and Methods

6.2.1 Cold-water coral age dataset

A total of 978 CWC ages is available for the regions used in this study, which originate from various sites in the NE Atlantic (Gulf of Cadiz, Porcupine Seabight, Rockall Trough, Norwegian shelf) and the western Mediterranean Sea (Alboran Sea; Fig. 6.1). By focussing on different time intervals for the regions, the total number is reduced to

770 (see Table 6.1 and Tables in the Appendix for metadata and references). The dated CWC fragments have been collected during various expeditions using a variety of sampling gears. We refer to samples from dredges, grab samplers, box corers and remotely operated vehicles as "surface samples". Samples from gravity cores, drill cores and piston cores are counted as "core samples". The overwhelming majority of ages in the dataset stems from coral mounds.

Most CWC ages (80 %) were obtained via ^{230}Th/U dating, a technique very well suited for secondary carbonate materials up to ages of roughly 600 ka BP (Cheng et al., 2013). Different protocols for isotope dilution MCICPMS have been published over the last years and allow for higher precision and smaller sample amounts (Cheng et al. (2013), Hellstrom (2003), Kerber et al. (2023), Shao et al. (2019), Shen et al. (2012)). Some ^{230}Th/U ages within the dataset have also been produced by coupling Laser Ablation (LA) systems to mass spectrometers instead of using the isotope dilution method, which is more time efficient albeit precision of final ages is lower (Corbera et al. (2021), Spooner et al. (2016)). Also some (20 %) CWC ages obtained by ^{14}C dating were included. This method relies on the steady state between uptake and decay of radiocarbon in living organisms, which changes to only decay after death (Libby et al., 1949). Using this relation, roughly the last 55 kyrs can be dated, normally based on measurements using accelerator mass spectrometers (AMS) (Hajdas, 2008). The radiocarbon ages for CWC are converted to calendar ages using the marine calibration curve, which then gives the timing of the deposition of the carbonate (Reimer et al., 2013).

All ages are given in years BP. Demands on accuracy and precision of individual data points are not as strict in this approach as in age models for individual cores, e.g. to establish core stratigraphy (Wienberg et al., 2022). Highest demands on precision are only needed when combining dating methods to obtain ventilation ages (Mangini et al. (1998), Adkins et al. (1998), Frank et al. (2004), Raddatz et al. (2022), Beisel et al. (2023)). Thus, also LA ages are accepted, and the quality control limits on ^{232}Th content were very soft, which lead to the acceptance of all ages in the relevant time frames. Data points without quoted error were excluded, because the calculation of uncertainty bands requires uncertainties on all values. This concerned less than 10 ages for the whole set of 978 ages.

KDE was performed on different time intervals for the five regions, depending on the time with best coral coverage.

For the Gulf of Cadiz, in total 208 ages are available. Our KDE focusses on the last 71 ka BP. For this time interval, 162 ages are available, which comprise 147 ^{230}Th/U ages and 15 ^{14}C ages, and 138 core samples and 24 surface samples, respectively (Table 6.1).

451 ages are available in total for the Alboran Sea. The KDE applied considers the time interval of the last 30 ka BP and encompasses a total of 275 CWC ages. 209 ages were obtained by ^{230}Th/U (inlcuding 63 ages obtained by the LA method) and 66 samples were dated with the ^{14}C technique. The vast majority of samples (n= 240) is from cores, 31 are surface samples (for 4 samples no information of the sampling gear exists; Table 6.1). The statistical analysis of the temporal species distribution has been applied focussing on

the Holocene, because small, yet acceptable sample sizes exist for this period (101 ages for *L. pertusa* and 41 ages for *M. oculata*). For the rest of the dated samples, no species has been assigned.
For the three regions in the northern NE Atlantic (north of 50°N), the KDEs are compared for the last 20 ka BP, as for the Norwegian Shelf and the Rockall Trough almost exclusively Holocene ages (<11.7 ka BP) are available.
For the Porcupine Seabight, there are 142 ages published (Table 6.1). 81 CWC ages are younger than 20 ka BP. 41 are dated via ^{230}Th/U and 40 using ^{14}C, and 53 ages derive from cores and 28 are surface samples.
141 ages are available in total for the Rockall Trough region. Except for 3 ages, all ages are from the last 12 ka. 129 are dated via ^{230}Th/U and 9 via ^{14}C, and 132 ages derive from core samples and only 6 from surface samples (Table 6.1).
For Norway, 80 ^{230}Th/U and 31 ^{14}C ages are published. All of them are from the last 11 ka. 73 are from cores and 32 surface samples (for 6 samples, no sampling gear information exists; Table 6.1).

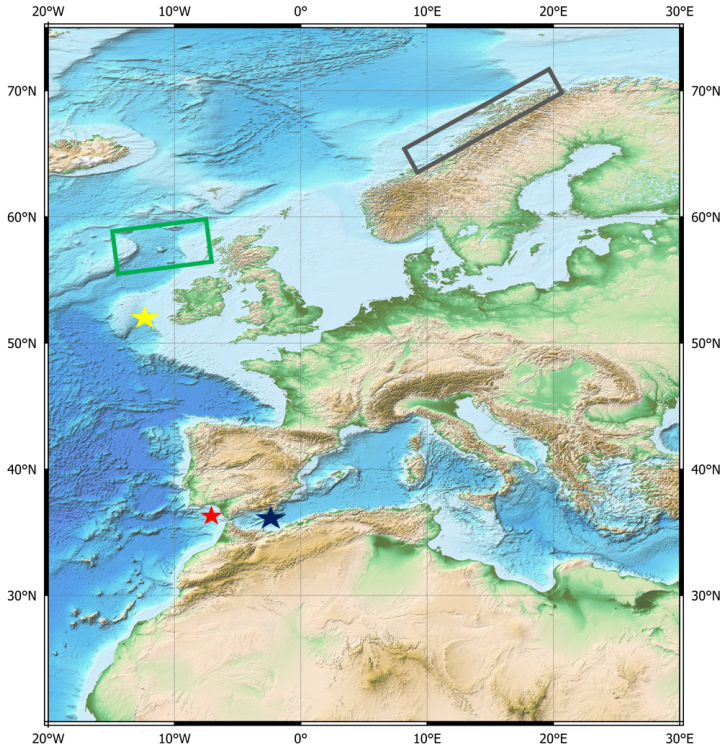

Figure 6.1: Map (ETOPO1 Global Relief Model) displaying the relevant sites of the study. The markers only roughly represent the areas within which samples were collected. The red star represents the Gulf of Cadiz, and the blue one the Alboran Sea. The yellow star locates the Porcupine Seabight. The green frame represents the area from which the Rockall Trough samples originate. The grey frame represents the Norwegian shelf. The latter dataset also contains one age from the Faroer islands.

Region	N	N for KDE	UTh	14C	Core	Surface	References
Gulf of Cadiz	208	162 (0-71 ka BP)	147	15	138	24	Taviani et al. (1991) Wienberg et al. (2009) Wienberg et al. (2010) Frank et al. (2011) Hemsing (2017) this study
Alboran Sea	451	275 (0-30 ka BP)	209*	66	240	31(**4)	McCulloch et al. (2010) Frank et al. (2011) Fink et al. (2013) Fink et al. (2015) Stalder et al. (2015) Dubois-Dauphin (2016) Wang et al. (2019) Krengel (2020) Fentimen et al. (2020) Corbera et al. (2021) Fentimen et al. (2022) Wienberg et al. (2022) this study
Porcupine Seabight	142	81 (0 - 20 ka BP)	41	40	53	28	Schröder-Ritzrau et al. (2005) Dorschel et al. (2007) Eisele et al. (2008) Frank et al. (2009) Frank et al. (2011) Van der Land et al. (2014) Wienberg et al. (2020)
Rockall Trough	141	138 (0-20 ka BP)	129	9	132	6	Frank et al. (2004) Schröder-Ritzrau et al. (2005) Mienis et al. (2009) Frank et al. (2009) Van der Land et al. (2010) Frank et al. (2011) Victorero et al. (2016) Bonneau et al. (2018)

Table 6.1: Characteristics of the CWC age dataset used for KDE analysis. N denotes the total number of available ages per region; and N for KDE is the number of ages used for KDE analysis (the considered time interval for each region is shown in brackets). Ages have been obtained via ^{230}Th/U (*Alboran Sea: 63 out of 209 ages have been dated using LA) or with the ^{14}C method, and the dated corals were collected from cores or surface samples (**number of ages for which no information on sampling exists are denoted in brackets). Table continues on the next page.

Region	N	N for KDE	UTh	14C	Core	Surface	References
Norwegian shelf	111	111 (0 – 20 ka BP)	80	31	73	32(**6)	Mikkelsen et al. (1982) Hovland et al. (1998) Hovland and Mortensen (1999) Lindberg and Mienert (2005) Schröder-Ritzrau et al. (2005) Frank et al. (2011) Correa et al. (2012) Titschack et al. (2015) Raddatz et al. (2016) Raddatz et al. (2022)
Sum	978	770	609	161	629	131	

6.2.2 Statistical methods

Kernel Density Estimation

KDE is a well established tool for probability density estimation (Heidenreich et al. (2013), Silverman (1986), Vermeesch (2012), Weij et al. (2020)). Every data point is represented by a so-called kernel, a predefined function that can take different shapes. A very common choice is the "Gaussian" kernel. Other kernel shapes, such as triangular or boxshaped, exist too, and the width of every kernel is the bandwidth which is identical for all data points (Silverman, 1986). This implies that all kernels have the same amplitude. An example illustration is provided in Fig. 6.2. We suggest that for ^{230}Th/U data, a Gaussian function around the mean value is a good approximation, agreeing with Weij et al. (2020) and Hercman (2000).

Generation of an artificial dataset for KDE sensitivity testing

We created an artificial dataset to determine how well an input signal can be reconstructed. Data points are drawn as random samples following this input signal probability function. Translated to our CWC application, the following flowchart explains the underlying mechanisms:

$$\text{climatic drivers} \xrightarrow[\text{influence}]{} \text{environmental and ecological parameters} \xrightarrow[\text{control}]{} \text{coral population health} \xrightarrow[\text{determines}]{} \text{basic population of corals per region and time} \xrightarrow[\text{provides subsample}]{} \text{available coral samples} \xrightarrow[\text{selection for dating}]{} \text{ages}$$

As an input signal, we created a function of several normal distributions with different means, widths and amplitudes added together. The complex interaction of climate drivers

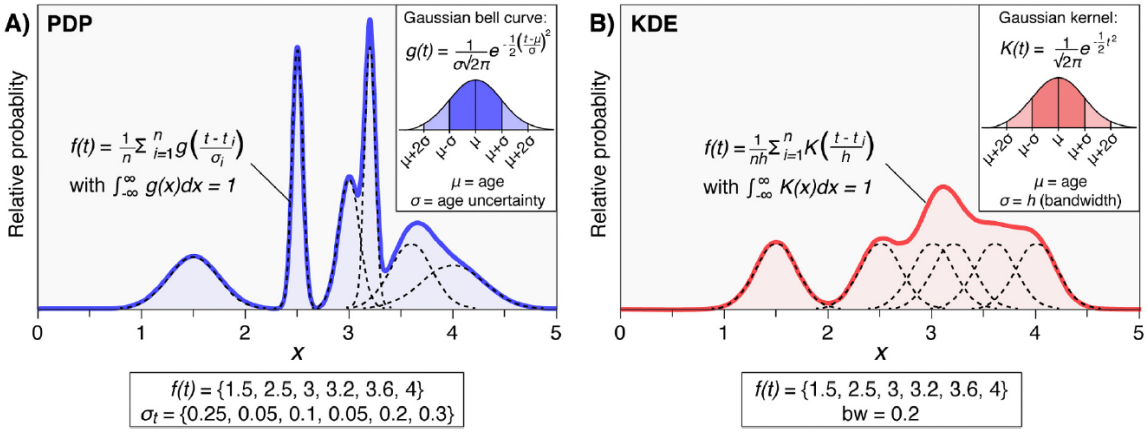

Figure 6.2: Probability density functions are created from an example dataset of 6 data points, as a PDP (A) and KDE (B). The artificial sharp peaks created by PDP are clearly visible. The equation for a Gaussian kernel is shown in the upper right of panel B. Image reprinted from Weij et al. (2020) with permission from Elsevier.

might result in environmental and ecological parameters that do not follow normal distributions, however, we used this test case to keep it simple. On this distribution, we added some noise (average white gaussian noise) with a small offset so values do not become negative. This means that there always is the possibility to find ages in non-peak intervals which is a realistic case in reality. Figure 6.3 shows the input signal and the cumulative density function (cdf) calculated from it. The cdf are the summed up probability up to its x-value and is 1 for the final value of the input signal. From the interval [0,1], values are sampled assuming a uniform distribution. They are converted to random samples of the pdf-x-values via the cdf. A histogram of random samples (sample size = 120) is plotted into Fig. 6.3 as well.

Bandwidth selection

The most crucial parameter in KDE is the bandwidth (Silverman, 1986). It highly influences the shape of the fitted curve and can lead to oversmoothing (loss of information) as well as undersmoothing (artificial peaks) of the probability density. This behaviour is a bias that does not simply average out at larger sample sizes (Van Kerm, 2003) - meaning that i. e. the undersmoothed "extra peaks" stay in the same position for multiple runs with the same data and cannot be distinguished from true peaks if the input distribution is not known. Finding the appropriate bandwidth for a given dataset is thus the most relevant step. The “optimal” bandwidth for a dataset depends on the information that should be extracted and the expected input distribution (Weij et al., 2020).
Heidenreich et al. (2013) and Zambom and Ronaldo (2013) provided detailed reviews about bandwidth selection procedures. We here compare our artificial dataset with two

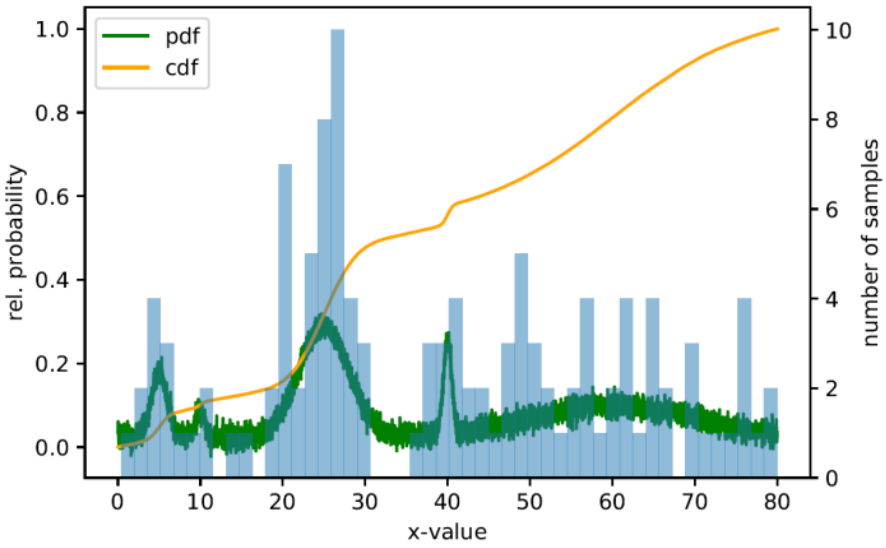

Figure 6.3: The input signal pdf and the resulting cdf curve. A histogram of an example of 120 random samples drawn from the cdf is plotted beneath.

widely-used bandwidth selection algorithms. Those are "Silverman" and the "improved Sheather-Jones (ISJ)" algorithm (Silverman (1986), Sheather and Jones (1991)). Instead of using the same bandwidth for the entire dataset, there are also algorithms for adaptative bandwidth selection (Abramson (1982), Zambom and Ronaldo (2013)). Here, we use the Python-based algorithm of Shimazaki and Shinomoto (2010), developed for the estimation of abrupt changes in neuronal spike rates.

Uncertainty treatment and sample size

By using KDE (instead of i. e. PDP), the measurement uncertainty information is discarded from the probability density function creation. It should be included, because uncertainties on the final probability density distribution are an important information for understanding the likelihood limits of phases of coral occurrence.
We calculate two different kinds of uncertainty: Firstly, as also carried out by Weij et al. (2020), Monte Carlo uncertainties (with here 5000 iterations) are calculated. For every age, a Gaussian distribution around the age (mean value) is assumed. The width σ is given by the individual value's measurement uncertainty. In every run, one value for each age is random sampled from the distribution. The KDE is run on that and all constructed KDEs are averaged over in the end.
Secondly, the 5% and 95% confidence intervals from the adaptive KDE algorithm by Shimazaki and Shinomoto (2010) are calculated by bootstrapping from the full dataset. The latter method ignores the measurement uncertainties.
In agreement with the findings of Hercman (2000), Weij et al. (2020) recommend using

N>120 as a sample size from their test series to be able to reconstruct their input climate signal. In general, this size of the dataset already counts as "moderate" for KDE (Heidenreich et al., 2013) and lower sample sizes are possible under certain circumstances, namely a simple input distribution. This could for example be a simple single pulsed normal distribution. However, due to temporal, regional and species specific differences multiple pulses must be expected in our CWC age dataset and also different distribution widths are possible. Hence, we test our artificial dataset for N=120 samples. However, most, but not all subgroups in our applications examples reach 120 samples.

Implementation in Python

All of our artificial dataset tests and regional analysis were implemented in Python. We used three different packages: The KDE fits with a fixed bandwidth made use of the statsmodels function statsmodels.nonparametric.KDEUnivariate. For the application of different bandwidth selection algorithms, we employ the KDEpy Python package (Odland, 2018), i. e. FFTKDE. The KDE fits with adaptive bandwidth selection were calculated using ssvkernel from AdaptiveKDE described in Shimazaki and Shinomoto (2010).

6.2.3 Prerequisites for a reliable dataset

Potential sampling bias on the natural CWC datasets needs to be examined and understood. For the CWC age dataset used for this study, such biases could for example (i) be related to the collection of several coral-bearing sediment cores of a certain limited core length (e. g. 10 m) and being located spatially close to each other resulting in similar age to depth functions. This would potentially produce overdominance of ages up to a cut-off age. Another example for sampling bias is (ii) the preferential sample collection of a specific coral species due to its size, skeletal thickness or microstructure and its usability for geochemical analyses. Moreover, (iii) the ratio between surface samples and corals from sediment cores has an influence on the final distribution, i. e. for active coral regions where the surface is dominated by recent corals.
To visualize the contribution of the ages from different cores to the whole record for a region, we constructed cumulative density plots for the individual cores - being the cdfs (as explained for the artificial dataset in 6.2.2) of the data points. For each subset (here one core), the cumulative density becomes one at the oldest age. Deviations of individual cores from the whole dataset for the respective region are easily visualized this way. Moreover, it is directly visible up to which age all cores cover the time interval and when coverage gets weaker.

6.3 Results

6.3.1 KDE sensitivity testing with artificial datasets

A KDE's ability to reconstruct the amount and position of peaks in an input signal massively depends on the bandwidth. Figure 6.4 presents the input signal of the artificial dataset and the reconstruction via two common algorithms for bandwidth selection, Silverman and ISJ. Silverman clearly oversmoothes the signal and can only reconstruct 3 of the 5 peaks. Also, peak widths do not match between the input and output signal. The peak reconstruction works better for the ISJ bandwidth, however here undersmoothing becomes a problem: Instead of 5, more than 15 peaks are identified (some of them overlapping). The difference to the input signal is particularly striking for the broadest peak, where many of the much smaller features are identified as individual peaks. Figure 6.4 only displays two KDE fits with bandwidths obtained by using popular bandwidth selection algorithms. The effect that no satisfying peak reconstrution is possible for this complex signal remains the same for other bandwidths.
By empirical means, we found no reliable method to distinguish "real" peaks from the ones that result from undersmoothing. This agrees with literature (Van Kerm, 2003).
Adaptive KDE works with a variable bandwidth. It estimates the bandwidth from data density, based on a L2 loss function optimization (Shimazaki and Shinomoto, 2010). Figures 6.5 and 6.6 show the application of adaptive KDE to subsamples artificial input functions. In Fig. 6.5, an input function simply consisting of a normal distribution is shown. By drawing sets of 120 samples and running a KDE, the input signal can be reproduced, as the average over 500 runs for different sample sets shows. Individual KDEs for single sample sets vary, but the vast majority produces the single pulsed peak. For the more complex artificial input signal described above, a larger sample size is needed for the reproducible reproduction, as Fig. 6.6 shows. 500 samples are employed here, and allow for signal reconstruction, except for the smallest peak. It has also been tested that repeating the adaptive KDE on the same sample set multiple times yields reproducible results.

6.3.2 Case-studies corals

Gulf of Cadiz

For the Gulf of Cadiz dataset, up to approximately 35 ka BP, almost all ages are available from all cores (except for two ages; compare the cdf plot in Fig. 6.7). There is no strong correlation between bottom core ages and their length. The thick blue function including all cores is clearly dominated by core GeoB 18141-1 for which the most ages are available. The resulting KDE with the two uncertainty bands is shown in Fig. 6.8. In this plot, as well as in the following KDEs, two types of uncertainty bands are displayed. The red shaded area around the average KDE (red line) is obtained by Monte Carlo simulation as explained in section 6.2.2. The blue and orange line are the 5% and 95% confidence

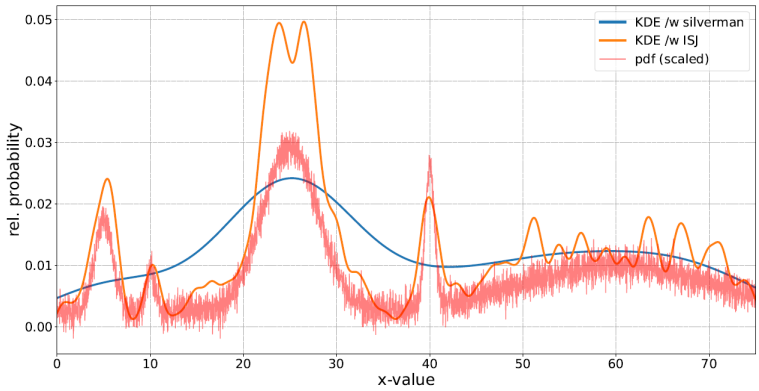

Figure 6.4: Input pdf and KDE fits with two different bandwidths are shown. The sample size of data points random sampled from the input function is 500 (not directly shown here). The relative probability on the y-axis does not apply to the pdf, which was scaled with an arbitrary value.

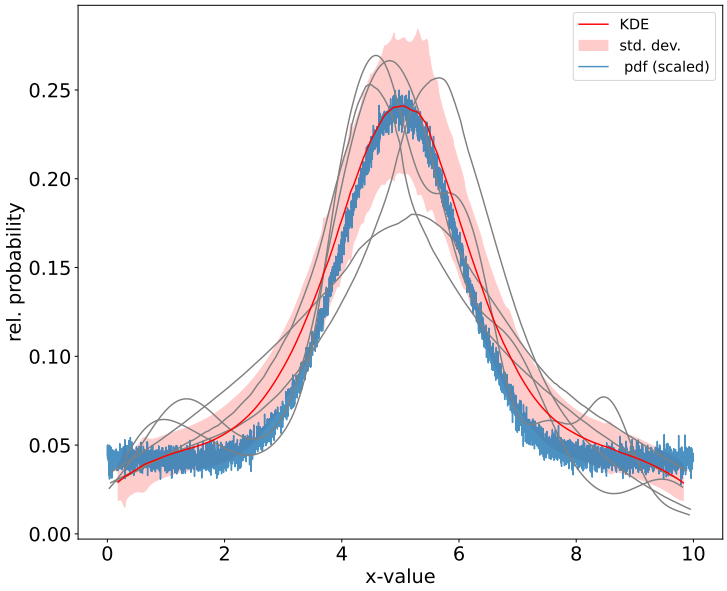

Figure 6.5: The red curve results from averaging over 500 adaptive KDE runs, each on a different subsample of 120 samples drawn from the underlying pdf input function (here plotted scaled with an arbitrary factor). 5 random individual runs for 5 different subsample sets are shown in grey for illustration. The input function is a simple normal distribution.

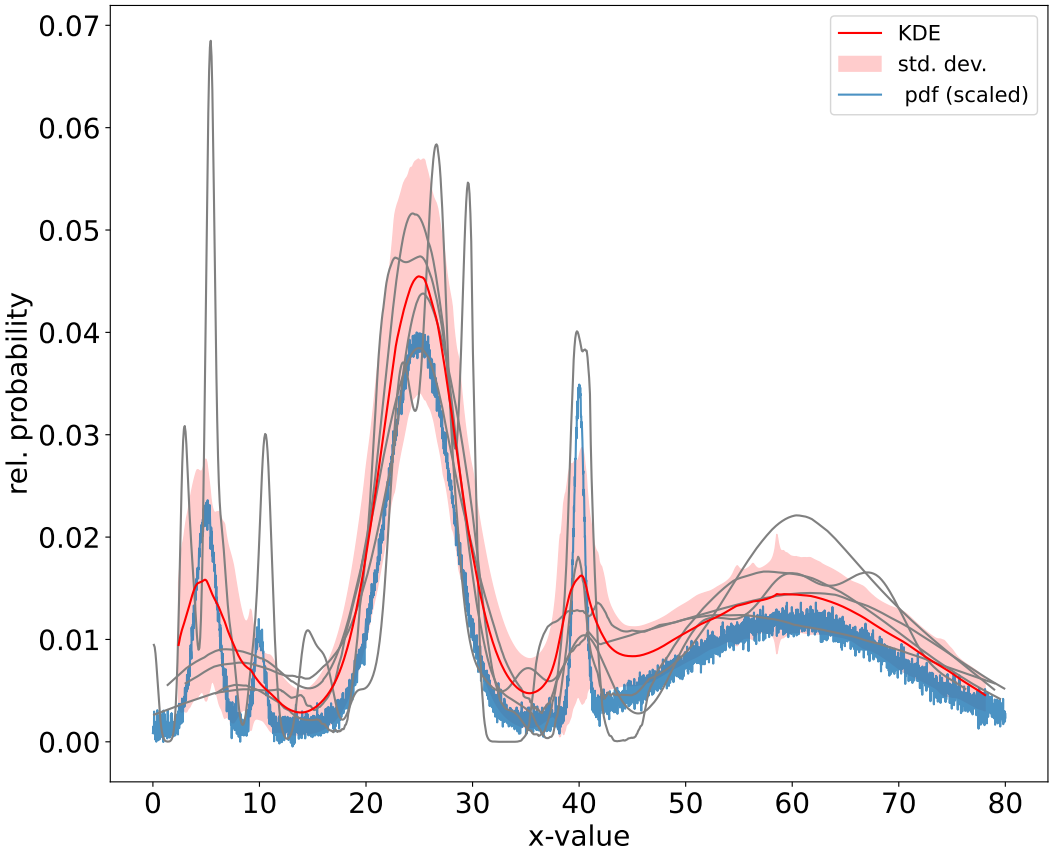

Figure 6.6: As in Fig. 6.5, the red curve is averaged over 500 adaptive KDE runs, each on a different subsample of here 500 samples drawn from the underlying pdf input function (here plotted scaled with an arbitrary factor). 5 random individual runs for 5 different subsample sets are shown in grey for illustration. The input function is the artificial dataset described before.

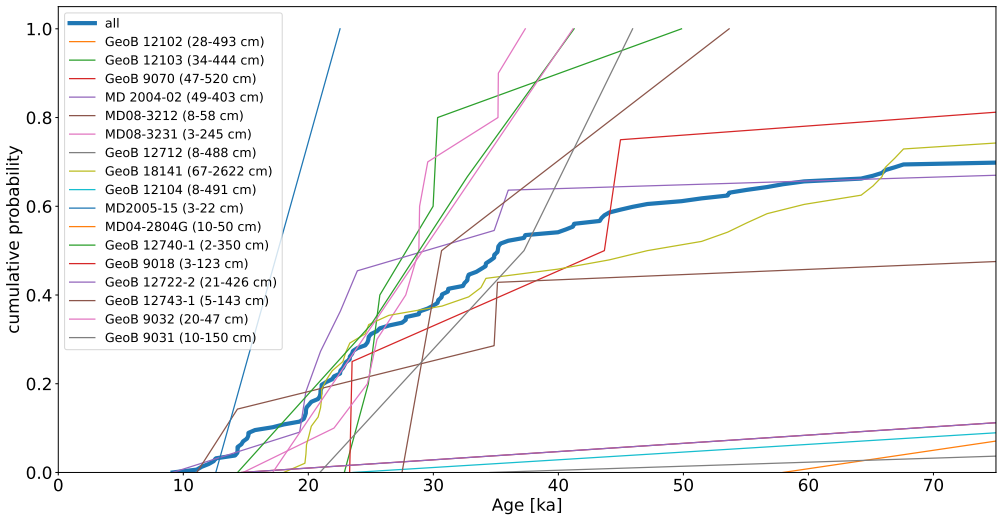

Figure 6.7: Cdf plot for individual cores for the Gulf of Cadiz. All cores contributing more than one age are shown; surface samples are not presented here. In the legend, core identifiers as well as the minimum and maximum sediment depth of dated samples within the core are shown. The thick blue line represents the cdf for all (including surface) samples. This line as well as some cores do not reach a probability of 1 within the time interval of the last 75 ka BP, this means that the remaining ages of this core/ dataset are larger than 75 ka BP.

intervals from the adaptive KDE algorithm by Shimazaki and Shinomoto (2010). The mean KDE is averaged over all Monte Carlo iterations with measurement uncertainties, and thus not the same as the KDE fit ignoring the uncertainties. In the case of the Gulf of Cadiz samples, the Monte Carlo band is slightly thinner.
The occurrence of CWCs during the last glacial consists of three individual pulses (compare Fig. 6.8): Some ages are found for the time period from 71-45 ka BP. The first pulse starts at around 45 ka BP with a plateau around 30 ka BP. Shortly after, a new growth pulse starts with peak occurrence at about 21 ka BP, which fits very well with the LGM. Abundance of corals then decreases with the onset of the Holocene, by a last plateau at around 15 ka BP. The LGM growth pulse has a full width at half maximum (FWHM) of roughly 5 kyr. The other two underlying pulses at 15 and 30 kyr are broader, with approximately 10 kyr FWHM.

Species distribution in the Alboran Sea

Although there are few cores with only two very recent ages, the vast majority of cores covers ages up to roughly 13 ka BP. Figure 6.9 shows the cdf plot for all Alboran Sea ages.

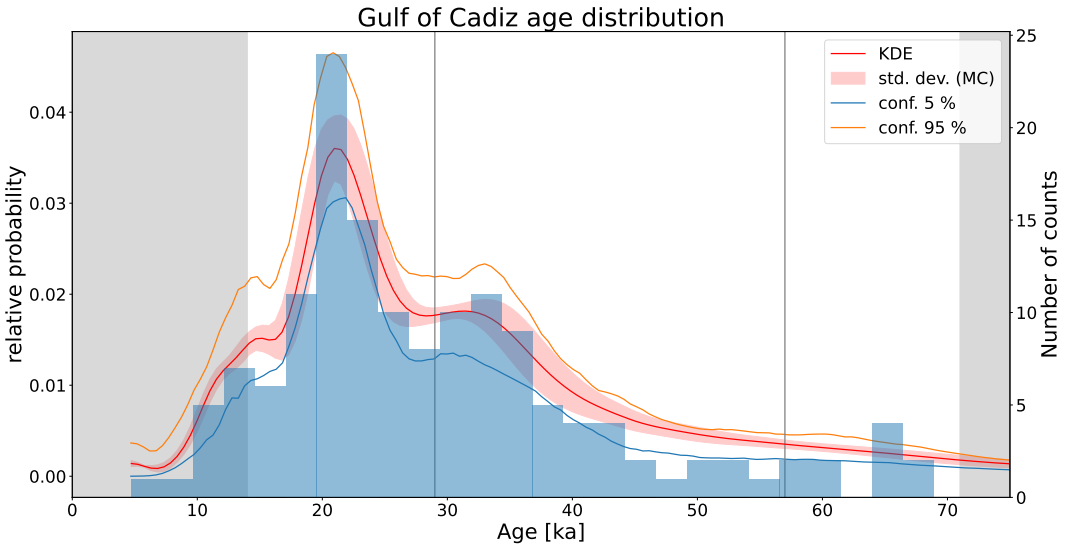

Figure 6.8: KDE for the Gulf of Cadiz. The thick red line is the adaptive KDE averaged over 5000 runs, in which for every run all ages were random sampled from a normal distribution with the measurement uncertainty as width. The red uncertainty band represents the standard deviation around the mean of this 5000 iterations. The blue and orange lines are the confidence intervals obtained by bootstrapping (Shimazaki and Shinomoto, 2010) for the KDE on the age data points without measurement uncertainties (important to note: the red line is the Monte Carlo average, not the KDE without uncertainties). For additional visualization, a histogram is plotted underneath. The grey and white areas in the background depict the interglacial (grey) and glacial (white) MIS. The vertical grey lines are the boundaries between MIS 2 and 3 as well as 3 and 4.

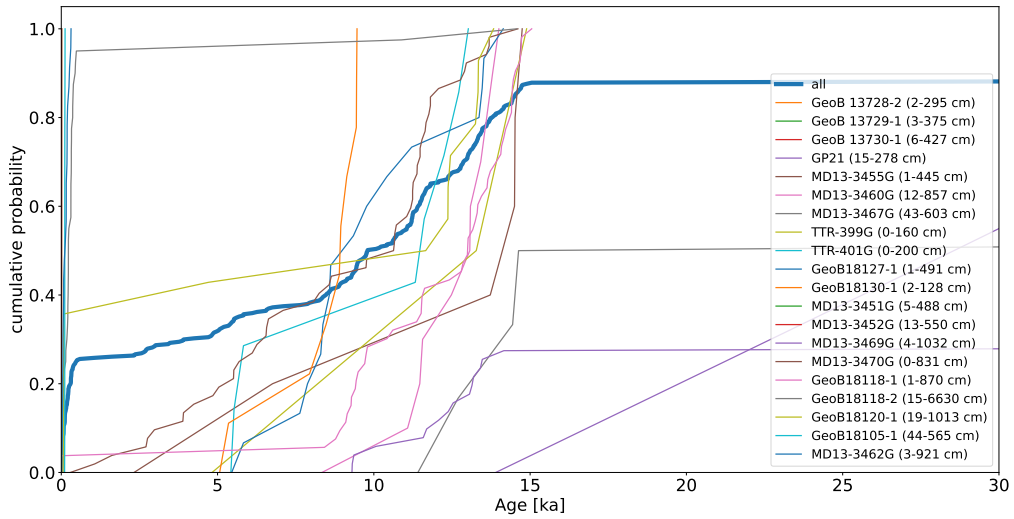

Figure 6.9: Cdf plot for individual cores for the Alboran Sea dataset. All cores contributing more than one age are shown; surface samples are not presented here. In the legend, core identifiers as well as the minimum and maximum sediment depth of dated samples within the core are shown. The thick blue line represents the cdf for all (including surface) samples. This line as well as some cores do not reach a probability of 1 within the time interval of the last 30 ka BP, this means that the remaining ages of this core/ dataset are larger than 30 ka BP.

The age distribution for all ages is presented in Fig. 6.11, and sorted by species in Fig. 6.10. The error bands by Monte Carlo are broader than the bootstrap errors from optimization. Different peak occurrence of the two framework-forming species is visible, with *L. pertusa* peaking at around 11 ka BP and *M. oculata* at 5 ka BP. The *L. pertusa* peak is asymmetrical and its FWHM is larger with approximately 3 kyr than the one of *M. oculata* (roughly 2 kyr).

Eastern Northern Atlantic (north of 50°N)

For the Porcupine Seabight, there are several cores for which the majority of ages is larger than 20 ka BP (see Fig. 6.12). They contribute only one or a few ages to the data analysed here. The KDE in Fig. 6.13 has two peaks: one at the growth onset and one in the late Holocene. Around 5 ka BP, a dip in the distribution is identified. Figure 6.14 presents the Porcupine Seabight dataset, too, but without surface samples. This almost completely removes the peak in the late Holocene. Monte Carlo bands are smaller than the confidence intervals.
The Rockall Trough cdf plot in Fig. 6.15 demonstrates that all, except one, cores cover the whole period to the growth onset. The Monte Carlo uncertainty band is slightly thinner

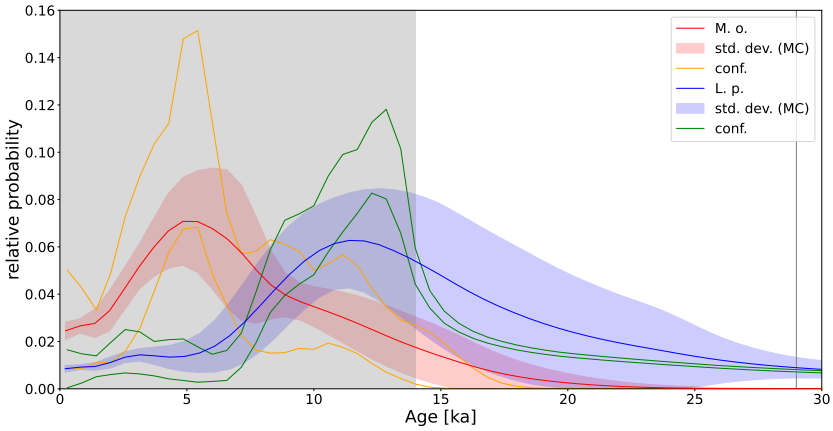

Figure 6.10: KDE for *M. oculata* (red) and *L. pertusa* (blue) in the Alboran Sea. The thick red and blue lines are the adaptive KDE averaged over 5000 runs, in which for every run all ages were random sampled from a normal distribution with the measurement uncertainty as width. The shaded uncertainty bands represent the standard deviation around the mean of this 5000 iterations. The yellow and green lines are the confidence intervals for both species, obtained by bootstrapping (Shimazaki and Shinomoto, 2010) for the KDE on the age data points without measurement uncertainties (important to note: the thick lines are the Monte Carlo averages, not the KDEs without uncertainties).

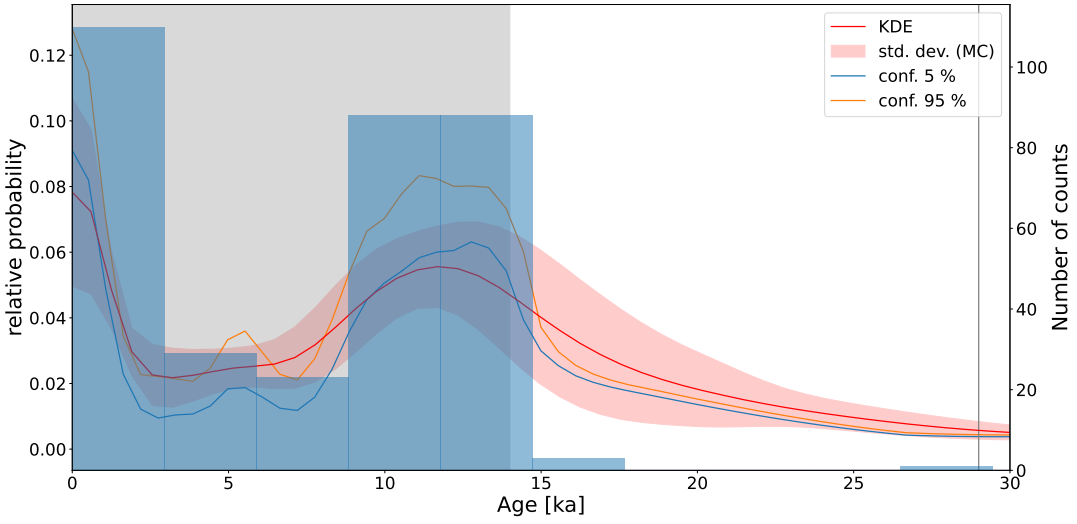

Figure 6.11: KDE for the all Alboran Sea ages up to 30 ka BP. For a detailed description of the plot, see Fig. 6.8.

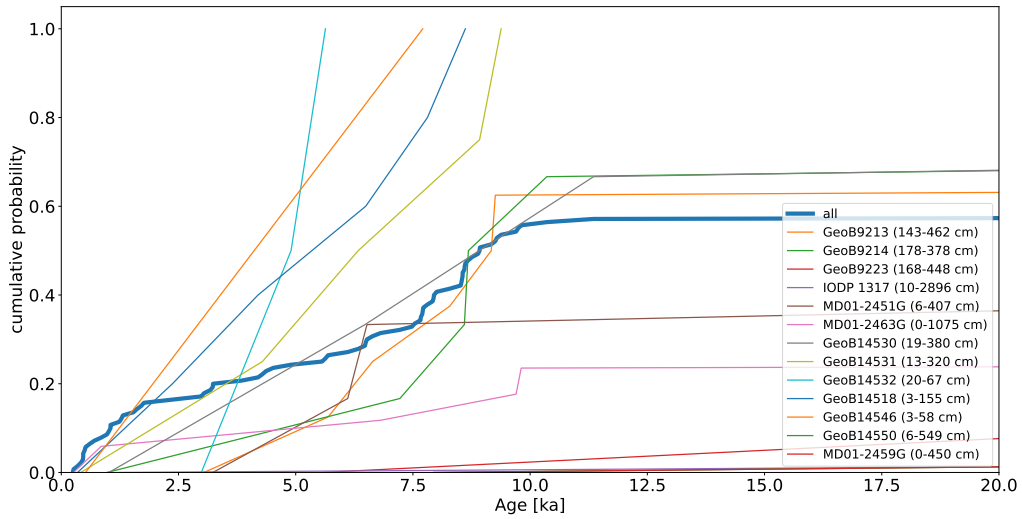

Figure 6.12: Cdf plot for individual cores for the Porcupine Seabight dataset. All cores contributing more than one age are shown; surface samples are not presented here. In the legend, core identifiers as well as the minimum and maximum sediment depth of dated samples within the core are shown. The thick blue line represents the cdf for all (including surface) samples. This line as well as some cores do not reach a probability of 1 within the time interval of the last 30 ka BP, this means that the remaining ages of this core/ dataset are larger than 30 ka BP.

than the fitting error band. Three peaks are identified for the Rockall Trough KDE in Fig. 6.16, with a temporal distance of roughly 5 kyr to each other. They are located around 10, 6 and 1 ka BP.
Some of the cores contributing fewer ages to the dataset for the Norwegian Shelf have a bottom age of around 2.5 ka BP (compare Fig. 6.17). Figure 6.18 displays peaks around 9.5 ka BP and 2.5 ka BP and a dip at 5.5 ka BP for this dataset. The Monte Carlo uncertainty band is very thin here.

6.4 Discussion

6.4.1 Peak and density function reconstruction

Artificial dataset

Weij et al. (2020) worked with an artificial dataset in their KDE study on ^{230}Th/U dated speleothems, too. They chose to derive it from a climatically driven signal (the temperature anomaly EPICA Dome C record, (Jouzel et al., 2007)). We here opted for a fully artificial input signal consisting of normal distributions of different widths and heights. As

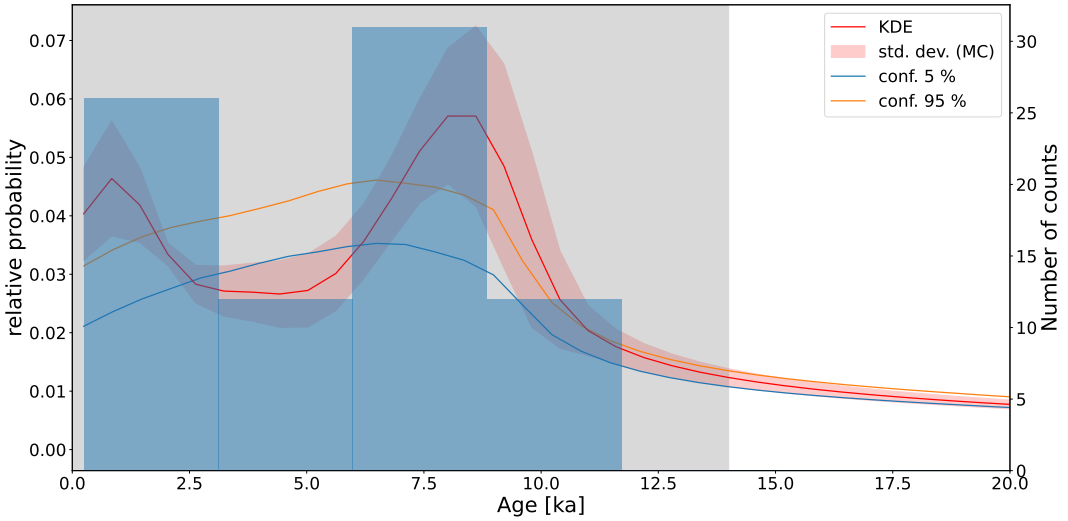

Figure 6.13: KDE for the Porcupine Seabight. For a detailed description of the plot, see Fig. 6.8.

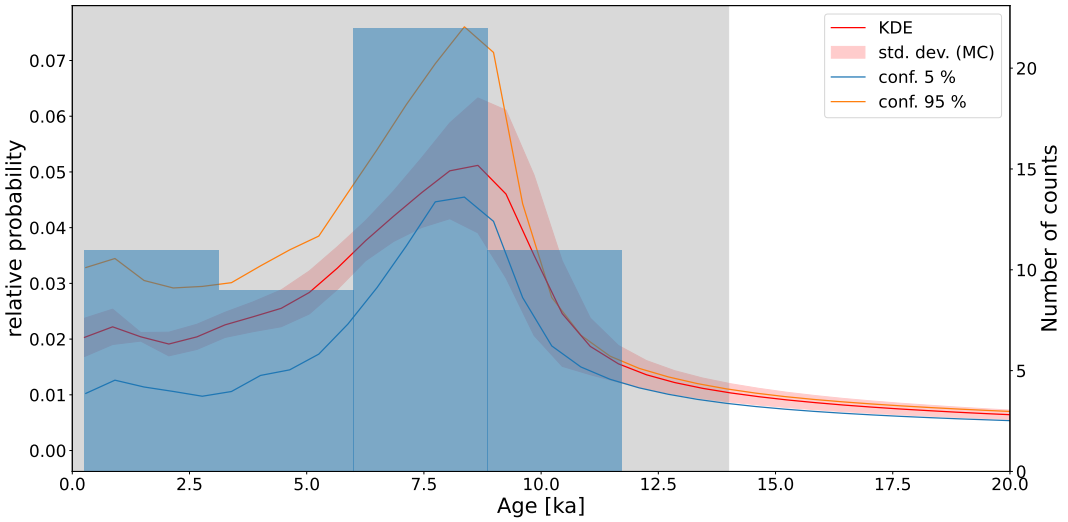

Figure 6.14: KDE for the Porcupine Seabight, without surface samples. For a detailed description of the plot, see Fig. 6.8.

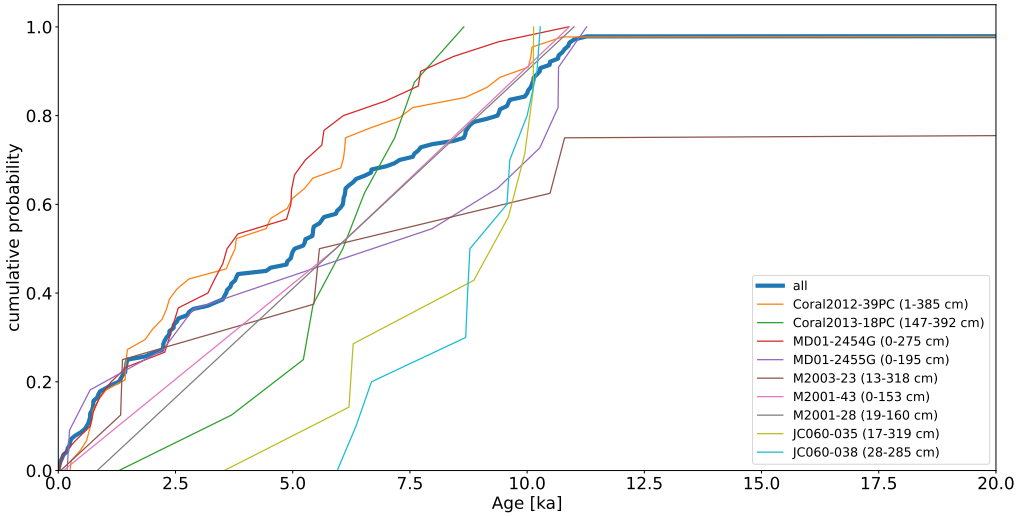

Figure 6.15: Cdf plot for individual cores for the Rockall Trough dataset. All cores contributing more than one age are shown; surface samples are not presented here. In the legend, core identifiers as well as the minimum and maximum sediment depth of dated samples within the core are shown. The thick blue line represents the cdf for all (including surface) samples. There is only one age larger than 20 ka BP, thus one core and the full dataset do not reach a probability of 1 here.

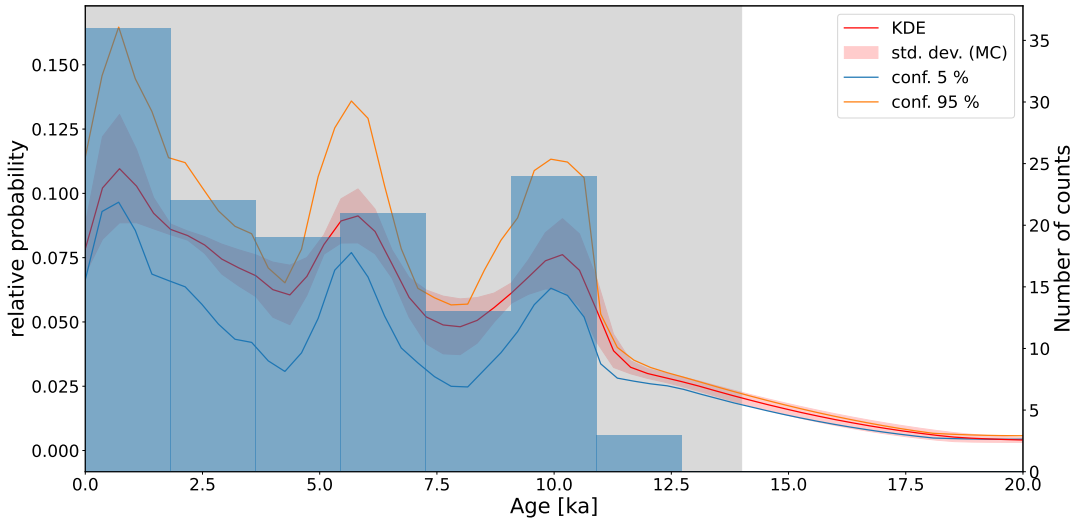

Figure 6.16: KDE for the Rockall Trough. For a detailed description of the plot, see Fig. 6.8.

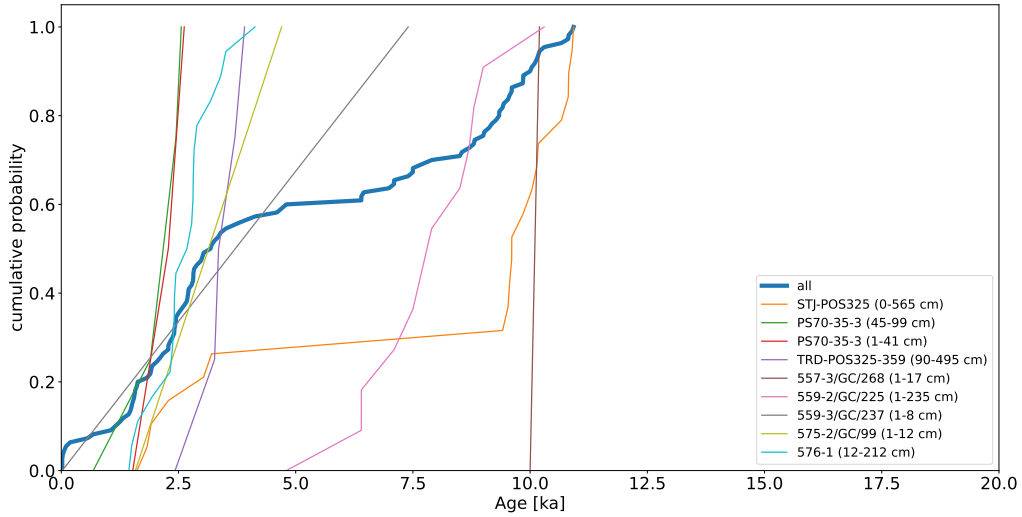

Figure 6.17: Cdf plot for individual cores for the Norwegian shelf. All cores contributing more than one age are shown; surface samples are not presented here. In the legend, core identifiers as well as the minimum and maximum sediment depth of dated samples within the core are shown. The thick blue line represents the cdf for all (including surface) samples.

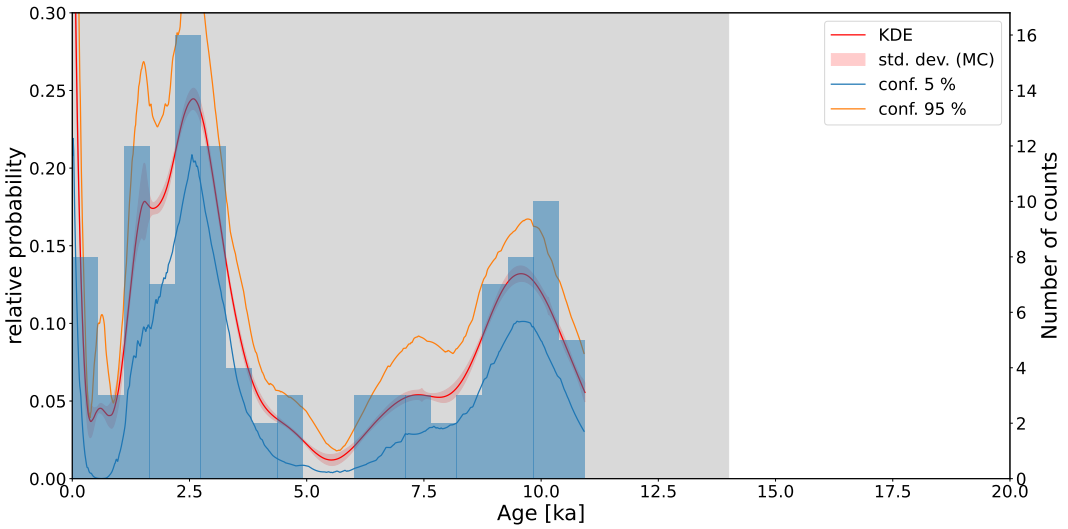

Figure 6.18: KDE for the Norwegian shelf. For a detailed description of the plot, see Fig. 6.8.

we cannot expect the ecosystem changes to happen on identical timescales and intensities, we considered a complex signal with structures of different widths. Moreover, our intention in choosing something non-climate related was to avoid optimising the method for an underlying climate signal. In especially with a fixed bandwidth approach, the bandwidth from the tests would then be exactly optimized for the typical frequencies of the climate input signal. This easily leads to identification of these features, but not of input drivers of other widths and shapes in the natural data.

Uncertainties

Unlike for example a histogram, KDE is able to present uncertainties. Because the uncertainty information is not added in via the width of the Gaussian kernels, it is introduced using Monte Carlo simulations as Weij et al. (2020) suggested. These Monte Carlo uncertainty bands are highly sensitive to already few ages with a particularly high measurement uncertainty. This is visible for Fig. 6.11, where the large proportion of LA ages with high measurement uncertainties broadens the uncertainty bands. The effect occurs for the species distribution in Fig. 6.10, too, although this dataset is not dominated by the LA ages (compare the Tables in the Appendix). The distribution for the corals off Norway in comparison has much thinner uncertainty bands.
The confidence bands adapted from the algorithm by Shimazaki and Shinomoto (2010) assume no measurement uncertainties, because there are none for their spike signals. Here, they were plotted as a comparison to the Monte Carlo bands. Some subgroups would benefit from more precision in the age determination (the Alboran Sea as discussed above), but in most cases the measurement errors are the smaller source of uncertainty.
Hercman (2000) pointed out that in fact the input isotopic ratios from dating are normally distributed and this does not neccessarily apply to the age uncertainties, too. Hercman (2000) worked with ^{230}Th/U ages, in which case the isotopic ratios for age determination are $\left(\frac{^{234}\mathrm{U}}{^{238}\mathrm{U}}\right)$, $\left(\frac{^{230}\mathrm{Th}}{^{238}\mathrm{U}}\right)$, $\left(\frac{^{232}\mathrm{Th}}{^{238}\mathrm{U}}\right)$ and $\left(\frac{^{230}\mathrm{Th}}{^{232}\mathrm{Th}}\right)_{\mathrm{initial}}$, and re-calculated every age from these isotopic ratios for every Monte Carlo run of her PDPs. However, not for all published datasets used here all necessary information for recalculation is available. Secondly, skewed distributions of the age uncertainties are only expected for ages over 250 ka BP, not for the last 71 ka BP, where the increase in the ^{230}Th/U ratio determines the increase in age (Ludwig (2003), Weij et al. (2020)). Thus, we consider the effect of assuming normally distributed age uncertainties as neglectable, i. e. in comparison to sampling biases.

Bandwidth

A fixed bandwidth does not work well for a signal with peaks of different widths, as Fig. 6.4 shows. The relevant difference to adaptive KDE is that at a fixed bandwidth, also for a rise in sample sizes some features of the input signal cannot be reconstructed, when they are too broad or narrow. We do expect such an underlying input signal for the natural coral distributions, potentially with abrupt changes, because of the interplay of a

lot of environmental parameters that can differently respond to by changes in climatic and ecological forcing. In some cases, e. g. where only one CWC occurrence pulse is expected, a fixed bandwidth approach might work, but this is not always the case. Thus the use of adaptive KDE for CWC age datasets is suggested. Selecting multiple bandwidths manually for different time intervals can lead the researcher to inadvertently pick values at which the resulting KDE best matches expectations for an underlying driver, e. g. an isotopic record. Thus the approach of adaptive bandwidth selection by an algorithm is used.
DensityPlotter by Vermeesch (2012) was tested for ^{230}Th/U data by Weij et al. (2020) and uses the adaptive algorithm of Botev et al. (2010). However, this adaptive algorithm is only implemented for sample sizes much larger than typical ^{230}Th/U datasets and thus no option. The adaptive algorithm of Shimazaki and Shinomoto (2010) also works for smaller sample sizes, as is also demonstrated with our artificial dataset tests.
Our tests in Fig. 6.5 and 6.6 demonstrate that by using this adaptive algorithm, not bandwidth, but sample size becomes the limiting factor for information extraction. The required sample size depends on the shape of the input signal.

Sample size

Our results show that for the chosen artificial input signal, 500 samples yield quite reproducible KDE reconstructions independent of the set of random samples. In Fig. 6.6, the smallest peak still is hard to reconstruct at 500 samples and peak positions of the individual runs do not always perfectly match the input signal. However, the number and approximate peak positions are about right for all individual runs. This reconstruction highly depends on the input signal itself, and also on the distribution of structures ("peaks" or "pulses") in the signal: Random samples have only a small likelihood to be drawn from the in comparison smallest structures (covering a small area) of a probability density function. This implies that they are only well reconstructed at higher sample sizes.
Figure 6.5 demonstrates that for simple input signals, e. g. one normal distribution, smaller sample sizes allow for accurate reconstruction (also see Heidenreich et al. (2013)).

Biases

Surface samples being a potential bias has been hypothesized in Frank et al. (2011). Here, the removal of surface samples from the distribution can make a large difference for some sites, as Fig. 6.13 and 6.14 demonstrate - for the Porcupine Seabight ages, the late Holocene peak almost completely vanishes. The effect is weaker for regions with none or little recent coral growth, such as the Gulf of Cadiz. The surface samples in this area cover the whole range of ages obtained from cores.

6.4.2 Faunistic subsample sets in space and time

In the last years, hundreds of new CWC ages have been obtained for different sites in the North Eastern Atlantic and the Mediterranean Sea (e. g., Douarin et al. (2013), Titschack et al. (2015), Hemsing (2017), Bonneau et al. (2018), Wienberg et al. (2018), Wienberg et al. (2020), Krengel (2020), Wienberg et al. (2022), de Carvalho Ferreira et al. (2022), Beisel et al. (2023)). Multi-site CWC studies have shown the complexity of temporal occurrence patterns of CWC in this region and that they must thus be driven by different factors (Schröder-Ritzrau et al. (2005), Frank et al. (2011), Wienberg and Titschack (2017), de Carvalho Ferreira et al. (2022)). Frank et al. (2011) identify productivity, mid-depth temperature, ecological and sedimentary processes as drivers for the whole North Eastern Atlantic, with parameter changes induced by oceanic and climatic changes. Bottom water oxygenation was added as a factor driving the occurrence patterns (Wienberg et al. (2018), de Carvalho Ferreira et al. (2022)), and Portilho-Ramos et al. (2022) showed that productivity acts as a main driver.
Here, our goal is to demonstrate the benefits of using the adaptive KDE method for obtaining statistically reasonable distributions of coral occurrence. Hence, we zoom in on some specific regions and applications and discuss the most dominant possible climate and thus environmental parameters potentially controlling the abundance patterns.

Growth dynamics in the Gulf of Cadiz

All sediment cores cover ages up to 35 ka BP for this region (Fig. 6.7). We conclude that there is no systematic bias in the age-depth distribution. This implies that only the last growth pulse is affected by a bias due to undersampling. The large fraction of ages from core GeoB18141-1 needs to be kept in mind, because local effects influencing exactly this sampling site could have an overproportional impact on the distribution.
It has been well documented that CWC growth in the Gulf of Cadiz has almost only occurred during Glacial periods (Wienberg et al. (2009), Wienberg et al. (2010), Hemsing (2017)). This is not only a local feature, but fits into the general pattern observed in the Eastern Atlantic: CWC growth occurs in glacial periods in temperate regions south of 50°, for example the Moroccan and Iberian margin (Frank et al. (2011), Wienberg et al. (2018), Wienberg et al. (2010), Hebbeln et al. (2019)).
For the Gulf of Cadiz, Wienberg et al. (2010) showed that palaeo-productivity and thus food supply to the CWC was increased during the last glacial. Multiple effects play a major role here: firstly, the input of aeolian dust was increased in comparison to later periods, partly due to higher wind strengths (Stuut et al. (2005), Wienberg et al. (2010)). Secondly, at a lower sea level, i. e. during the LGM, tidal effects were stronger (Wienberg et al., 2009). These are important for food transport to the corals (Frederiksen et al. (1992), White et al. (2007), White et al. (2005)). All of these effects in consequence concern the food availability for the corals.
Frank et al. (2011) showed a primary productivity curve for the temperate Eastern Atlantic. It showcases two peaks within the last 40 ka BP that roughly match the LGM

peak and the 30 ka BP growth pulse. The strong LGM peak coincides with the highest wind strength in the Gulf of Cadiz, as discussed in Wienberg et al. (2010), too.
At this point, it becomes clear that the small-time-scale growth dynamics within the last glacial are an interplay of multiple factors. Using data description with KDE, such features become visible, and have a much more solid justification to really display an input signal (potentially modified by biases) than other tools for data visualization.

Temporal CWC species pattern in the Alboran Sea

The global distribution patterns of *L. pertusa* and *M. oculata* are not compared here to avoid biases that result not from different species requirements and adaptations, but from climatic, ecological and environmental differences, affecting CWC in general. As *L. pertusa* is the dominant species in many regions (compare Fig. 2.6) and thus more abundant in the records than *M. oculata*, a comparison of all *M. oculata* samples with all *L. pertusa* would rather highlight differences of the Mediterranean Sea (where *M. oculata* dominates from the mid-Holocene on) to the Atlantic Ocean instead of different species requirements.
There is, however, a possible (human) sampling bias which impacts the findings for *M. oculata*. When *M. oculata* and *L. pertusa* occur together, the thickness of their skeletons often causes the selection of *L. pertusa* individuals for research (see also Fig. 2.5 and 2.4). That is the case as a more robust skeleton is easier to mechanically clean from detritus for dating and the application of tracers depends on the available sample mass. However, this bias underlines the finding of a recession of *L. pertusa* in the mid-Holocene and a flourishing of *M. oculata* even more.
The sampling bias from the distribution of ages in the individual cores is not dominant here (Fig. 6.9).
The Monte Carlo uncertainty bands in Fig. 6.10 are much larger than the bands from the optimisation procedure, unlike for the other regions. This is due to the large proportion of Laser Ablation data in the Alboran Sea subset (Corbera et al., 2021). This also leads to the smoothing out of the curve and explains why the avaraged peak for *L. pertusa* is smaller than the confidence intervals.
The sample size for both species is quite low here in comparison to the other study sites - roughly 100 for *L. pertusa* and only about 40 for *M. oculata*, thus the observation is only a hint so far. However, as the distribution appears to consist of only one pulse, a doubling in samples for *M. oculata* should be indicative already.
The lack of ages in recent times has qualitatively been described in former studies on subsets of the compilation examined here (Wienberg et al. (2022), Wienberg (2019), Fink et al. (2015), Fink et al. (2013)). Also, mound core records showed that *M. oculata* became more abundant in the Alboran Sea since the Early Holocene, eventually culminating in a *M. oculata*-dominated coral community today (Corbera et al. (2021), Stalder et al. (2015), Fentimen et al. (2020)).
Krengel (2020) showed an increase in Near Bottom Water Temperatures for the Alboran

Sea from (8 ± 2) °C to (12 ± 2) °C at the onset of the Holocene. As already mentioned in section 2.3, *M. oculata* has an environmental preference for slightly warmer waters than *L. pertusa* (Wienberg and Titschack, 2017). This agrees with aquaria experiments pointing to an acclimatisation capacity of *M. oculata* toward the presumed CWC upper thermal tolerance limit of 14-15 °C (Naumann et al., 2014). These two observations are a likely reason for the pattern we observe here.

Holocene patterns in the North Eastern Atlantic (north of 50° N)

In the case of the Porcupine Seabight and Rockall Trough, there is little influence of clustering of bottom ages at a certain age on the distributions because most cores cover the full time interval of 20 kyr, or even exeed it, i. e. for the Porcupine Seabight (Fig. 6.12 and 6.15). This is different for the Norwegian shelf dataset: a core bottom age clustering around the 2.5 ka BP peak is detectable in the cdf plot.
A potential bias that needs to be respected is the distribution of samples into surface and core samples, as discussed before. For the Porcupine Seabight, this effect is particularly strong and the late Holocene peak almost completely disappears, as is demonstrated in Fig. 6.14.
All three datasets (Porcupine Seabight, Rockall Trough and Norwegian shelf) show the growth onset of CWC with the start of the Holocene (Fig. 6.13, 6.16 and 6.18).
The start of CWC growth at the northern coral sites of the NE Atlantic has been extensively described in the literature so far (e. g., Schröder-Ritzrau et al. (2005), Dorschel et al. (2007), Rüggeberg et al. (2007), Frank et al. (2011), Correa et al. (2012), Douarin et al. (2013), Titschack et al. (2015)).
On top of this, our statistical analysis now shows differences between the three locations in their intra-Holocene CWC growth patterns, presenting different peaks and cyclicities. It shows that regional effects play a role during the Holocene. They all start at a quite similar timing, but the individual growth patterns are unique.
Bonneau et al. (2018) describe an increase in CWC abundance in the mid-Holocene and a millennial-scale variability for the late Holocene for two cores in the southwest Rockall Trough. While our KDE confirms an increase around 6 ka BP for the whole Rockall Trough dataset, we cannot find the millennial-scale variability later as a common feature. This underlines (also acknowledged in Bonneau et al. (2018)) that it is a local phenomenon. Furthermore, Bonneau et al. (2018) based their variability hypothesis on PDP of CWC ages. This might produce misleading probability density functions.
Frank et al. (2009) derived reduced CWC formation for the time periods 1.8-2.0 ka BP, 4.2-4.8 ka BP and 6-8.2 ka BP for the Rockall Bank and the Porcupine Seabight. The two latter match the dips in our Rockall distribution. Regarding the Porcupine distribution, only the 4.2-4.8 ka BP matches the dip in the KDE including the surface samples.
The distribution off Norway clearly displays two individual main pulses, with some smaller feature for both peaks. This agrees with the lack of ages described for the mid-Holocene (Titschack et al. (2015), Raddatz et al. (2016), Correa et al. (2012)), but it is not clear

yet, if this is a common or local feature.

6.5 Conclusion

We here examine a statistical data descriptor (an adaptive Kernel Density Estimation method (Shimazaki and Shinomoto, 2010)) for the identification of peaks and underlying functions of cold-water coral age distributions. Tests on random sample sets drawn from an artificially constructed input function demonstrate the method's ability to reconstruct complex signals. It offers two large advantages over other methods to visualize and investigate such age distributions: (i) Uncertainties are calculated and displayed continously over time. (ii) It is able to resolve growth dynamics, averaged for whole regions, within a time interval. Using this adaptive method, the quality of the input signal reconstruction depends mainly on sample size. This is a difference to fixed bandwidth KDE, where an increase in sample size does not allow for the better reconstruction of features of different widhts.
Care should be taken with regard to potential biases in input datasets, such as the ratio between surface and core samples that can lead to overestimation of younger ages (i. e. for actively growing coral sites) and the contribution of individual cores to the whole dataset. However, this is the case for any analysis of age distributions, and becomes easier to assess and visualize using KDE.
We applied the technique to three example CWC growth applications: For the Gulf of Cadiz, the coral occurrence in the last glacial could be resolved to consist of three superposed individual growth pulses. The KDE for *L. pertusa* and *M. oculata* underlines their different peak occurrences in the Alboran Sea, with *M. oculata* dominating the coral communities from the mid-Holocene on. Lastly, the age distributions for CWC on the Porcupine Seabight, the Rockall Trough and the Norwegian shelf were analysed. For all of these regions, it is well known that CWC growth starts with the onset of the Holocene (e. g. Frank et al. (2011)). Our KDE show several occurrence pulses with individual timing for the three regions during the Holocene. This underlines that local effects, not only large-scale climatic and oceanic changes, affect the respective coral occurrences. As the age datasets are dominated by ages from coral mounds, the three peaks of the Rockall Trough set are interpreted as short pulses of mound flourishing.

7 Further potential of KDE applications

Adaptive KDE has a large potential for many different age frequency applications. To emphasize this, a small preliminary example focussing on the age distribution of speleothem ^{230}Th/U ages from Northwestern Europe is presented in the following.

7.1 Introduction to speleothem applications

Speleothems are excellent archives for the reconstruction of terrestrial climates and archaeological applications (Fairchild and Baker, 2012). As already mentioned in Chapter 6, multiple studies have tried to establish age frequency distributions as a palaeoclimate proxy (e. g., Gascoyne et al. (1983), Baker et al. (1993), Hercman (2000), Scroxton et al. (2016), Weij et al. (2020)). There are some advantages in analysing speleothem age distributions for climatic drivers compared to individual records, e. g. local effects such as sealed drip sites average out, and thus large scale climate dynamics can be detected (Weij et al., 2020). In addition, sampling has a lower impact on cave environments because no extraction of complete stalagmites is required (Scroxton et al., 2016). However, age distributions are highly dependent on the statistical methods used for their construction (Hercman (2000), Weij et al. (2020)). As an adaptive KDE method has not been applied successfully to speleothem age distributions yet, the method presented and developed in Chapter 6 is demonstrated on a dataset of European speleothems, to revisit the climate driven secondary carbonate formation hypothesis initially proposed by Baker et al. (1993). They emphasize the potential of temporal speleothem age occurrence as a tracer of changes in temperature and aridity (Baker et al., 1993).

7.2 Materials and Methods

All ages used in this study have been measured in the Heidelberg laboratory, either on TIMS at the Heidelberg Academy of Science group on Radiometric dating or on MC-ICPMS at the IUP. The dataset is clearly dominated by alpine ages and in total contains 346 measurements. They stem from 8 caves (Spannagel, Obir, Atta, B7, Apostel, Erdmann, Betten, Schratten) and are published in Spötl et al. (2002b), Christl et al. (2004), Mangini et al. (2005), Spötl et al. (2006), Spötl and Mangini (2002), Holzkämper et al. (2005), Spötl et al. (2008), Spötl et al. (2006), Fohlmeister et al. (2012), Vollweiler et al. (2006), Spötl et al. (2002a), Fohlmeister et al. (2013), Niggemann et al. (2003b), Niggemann et al. (2003a), Fohlmeister et al. (2023), Becker et al. (2020) and Arps (2017). The

distribution on the different caves and individual stalagmites is however very unbalanced. The statistical methods are the same as in Chapter 6.

7.3 Results

Figures 7.1 and 7.2 present the age distribution for the mostly alpine European speleothem dataset, plotted against the Vostok deuterium excess record (Fig. 7.1) and the NGRIP δ^{18}O record (Fig. 7.2).

7.4 Discussion

Firstly, it needs to be stated here that the employed dataset is far from ideal for this type of study and for interpretation some biases need to be respected: (i) the sample size is quite large at more than 300 ages, but the majority of them is not independent of each other. The geographical distribution of caves has a strong bias towards Alpine locations, and the number of dated samples from the individual caves can differ by an order of magnitude. Moreover, some speleothems are extensively dated, while from others only one or two ages were obtained. (ii) As Hercman (2000) pointed out as well, there is a bimodality bias, because for some stalagmites only a top and a bottom age are determined. (iii) Another bias is the selection procedure during sampling: often, speleothems with active drip sites are sampled, or specific research questions focussing on a particular time interval shall be studied. This also leads to more extensive dating of the speleothems from these time intervals.
Nevertheless, Fig. 7.1 and 7.2 contain some interesting features. For example, this dataset displays growth peaks and then a decline to the baseline of zero. This differs from the distribution constructed by Baker et al. (1993), which displayed continous speleothem growth (probability greater than zero) and variations within. The dataset used by Baker et al. (1993) covered a different region (British Isles and Northern Germany) and employed PDP instead of KDE, which both influences the difference in the distributions. So more comparison using the same method is needed here to work out climate induced differences between both regions.
Furthermore, the time lag between the isotopic ice core records and the growth peak after the LGM is striking. This also holds for the observation of the peak in the mid-Holocene.

7.5 Conclusion and outlook

The preliminary data evaluation on the dataset here demonstrates that there are interesting hypotheses to test with KDE on European speleothem datasets. The most important step is to either generate a bias-free sample set from a large database (which would be

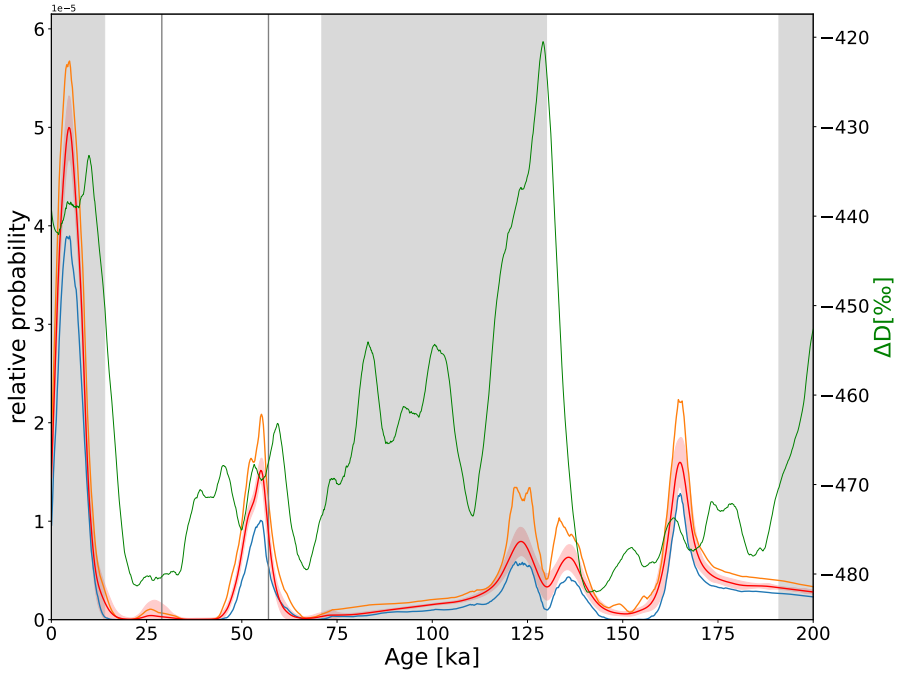

Figure 7.1: KDE for the European stalagmite dataset. The display of the KDE and uncertainty bands is analogous to Chapter 6 (except for less Monte Carlo runs, as this is only an application example): The thick red line is the adaptive KDE averaged over 1000 runs, in which for every run all ages were random sampled from a normal distribution with the measurement uncertainty as width. The red uncertainty band represents the standard deviation around the mean of this 1000 iterations. The blue and orange lines are the confidence intervals obtained by bootstrapping (Shimazaki and Shinomoto, 2010) for the KDE on the age data points without measurement uncertainties (important to note: the red line is the Monte Carlo average, not the KDE without uncertainties). For additional visualization, a histogram is plotted underneath. The grey and white areas in the background depict the interglacial (grey) and glacial (white) MIS. The vertical grey lines are the boundaries between MIS 2 and 3 as well as 3 and 4. The green curve is the deuterium excess record of the Vostok ice core (Bazin et al., 2013).

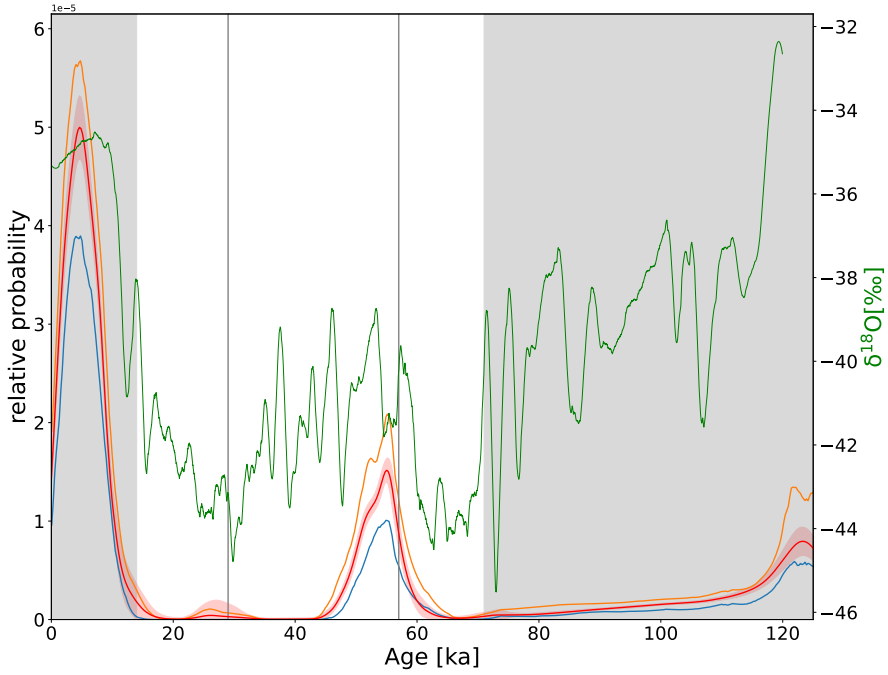

Figure 7.2: KDE description similar to Fig. 7.1. The green curve displays the δ^{18}O record of NGRIP (Bazin et al., 2013).

SISAL, Comas-Bru et al. (2020) and Atsawawaranunt et al. (2019)) or to apply a real random sampling approach to caves covering the whole region (Weij et al., 2020). This does not only allow to resolve climatic changes for different regions, but also to better understand erosion processes within caves by comparing peak heights of speleothem abundance over time (comparing to the description by Scroxton et al. (2016)).

8 Conclusion and outlook

In this thesis, both the generation as well as the evaluation of ^{230}Th/U ages were addressed. While Part 1 focussed on the characterization and optimisation of a fast measurement protocol with Th and U in the same solution, Part 2 examined possibilities of extracting information from age frequency distributions. Here, the results of this thesis will be summarized by answering the research questions put up in the beginning, followed by a short outlook.

Summary

How does an optimized simultaneous Th and U measurement routine look like?

Chapter 3 demonstrated that the setup of measuring Th and U in the same solution, using a 9 slot detector array and 3 magnetic field lines, yields precise and accurate results over multiple years. The proper application of individual raw data corrections is crucial for running such a protocol not only as a test setup, but in yearlong every day routine operation. It was also demonstrated that "non-classical" (referring to only one description in literature, Chiang et al. (2019)) correction factors can have the largest impact on accuracy. Carefully assessed reference materials and data evaluation strategies that allow for easy retroactive data reanalysis, once a new effect is found, also have a great contribution to the long-term performance and value of a measurement routine.

What is the influence of different raw data corrections on the final age accuracy for typical samples?

A completely new assessment of the potential variation in these factors was carried out in this thesis, including the changes in the measurement protocol since Arps (2017). The so-called ghost signals have by far the largest influence on isotopic ratio and age accuracy (can be more than 10 % age deviation for young samples), if they are not tracked correctly. These signals are scattering effects and depend linearly on the ^{238}U concentration of a sample. They are not described by the tailing fit, which in principle should account for all scattered ions influencing other masses. In literature, there is only one description of these signals so far (Chiang et al. (2019) for 229 amu, apart from now Kerber et al. (2023)). There are measurement setups in which the influence of the ghost signals is much smaller, for example when the ^{238}U beam can be collected (Chiang et al., 2019), while

the other isotopes are measured consecutively on SEM. These protocols however need a much larger measurement time to achieve the same precision.
Tailing in turn is the secondmost influential correction (permille level age deviation), followed by process blank (= instrumental background; at maximum on permille level for young, low-intensity samples) and the almost negligible hydride formation correction (far below the measurement uncertainty in every case).

Can the influence of scattering signals on specific masses be properly reduced and accounted for?

Yes, correcting for this scattering (here: the ghost signals on masses 229 and 230 amu) is possible when two aspects are respected:
(i) Additional to the bracketing standard, which is measured before and after each sample to correct for machine drift, a second reference material is measured at the beginning and end of each measurement session. It needs to be measured twice each time: once without addition of spike solution, to determine the k_{229} correction, and another time with added spike to find the current value for k_{230}.
(ii) As the determination of k_{230} works via the age of the reference material, this needs to have a validated age. We employed VRM 06/23 of JRC Karlsruhe (Varga et al., 2015) to find the "true" radiometric age of CRM-112A being (88.3 ± 2.5) years. This "true" age also includes remaining Th at the time of production in the 1950s. CRM-112A is available in many dating labs and can be used as a reference material for correction of k_{230} with this determined age.

How can a reproducible and user-friendly data analysis and age calculation routine be ensured?

Bundling all steps in one program equipped with a graphical user interface helps to accomplish both requirements. This was achieved with the program *U-Th Analysis* (`https://github.com/EnvArchivesHD/UTh_Analysis`). Output .xlsx files contain all constants and settings that were used in the evaluation and thus ensure reproducible data analysis. The GUI is particularly useful for quick re-analysis of data measured in the past, that needs to be updated with new half-life values for ^{230}Th and ^{234}U. It is also available as an open-source programme, so other labs can choose to use it. At the moment, the physical detector setup of the Heidelberg *NeptunePlus* is the only configuration available, but with small changes in the code, different setups can be implemented, too.

Can complex input signals that influence the formation of carbonate archives (i. e. cold-water corals) be reconstructed by building age probability density curves?

Yes, this is possible. Here, the Kernel Density Estimation was used, which has been introduced into geochronology by e. g. Ramsey (2017), Vermeesch (2012) and Weij et al. (2020). In the scope of this thesis, different bandwidth selection algorithms were tested and finally adaptive KDE (with a changing bandwidth, estimated on data density) has been chosen (Shimazaki and Shinomoto, 2010). The ability of this algorithm to reconstruct input signals via random samples was tested for an artificial dataset. At the threshold defined before of 120 samples (Hercman (2000), Weij et al. (2020)), the number of peaks that are identified still depends on the individual subsample. However, as datasets are growing and (for corals) reach more than 120, it is considered a promising way to go.
Applied to CWC, we can resolve the dynamics during growth phases for different regions. Here, the Gulf of Cadiz likely presented a multimodal growth behaviour during the last glacial period. The different peak occurrences of the species *L. pertusa* and *M. oculata* in the Mediterranean Sea are presented quantitatively for the first time. Lastly, a comparison between three regions in the Northern Eastern Atlantic north of 50°N (Porcupine Seabight, Rockall Trough and Norwegian shelf) shows their different individual behaviour during their growth periods in the Holocene.

What are the perspectives for this method?

With regard to ^{230}Th/U dating, speleothems offer a lot of interesting applications for age frequency distribution analysis, as also Weij et al. (2020) pointed out. The adaptive KDE method, that was shown here to work well for ^{230}Th/U age datasets, allows for more reliable peak identification than fixed bandwidth approaches. First results for a dataset of speleothems from Northwestern Europe look promising to give insight into a lot of palaeoclimatic features. Before using full datasets, it is important to develop suited bias control mechanisms. Random sampling from caves in fact would be best (Weij et al., 2020).

Status quo and outlook

The simultaneous ^{230}Th/U dating protocol for the *Neptune Plus* at IUP Heidelberg is able to produce accurate and highly precise ages. Compared to the state described in Arps (2017), relevant improvements regarding the accuracy were achieved - most importantly the development of strategies to minimize the influence of the newly discovered ghost signals, and in this scope, the introduction of a new reference material. Using the current mass-spectrometric setup, samples younger than aprroximately 1.5 ka need to

be measured in separated solutions to minimize the influence of the ghost signals. The Python-based GUI which is in use for about two years has proven to help with the data evaluation and to simplify re-analysis of data. Thus, the ability for further production of reliable ^{230}Th/U ages in Heidelberg is in a good position.
However, a small update in instrumentation in the future will certainly make it possible to use the advantages of a fast non-separated measurement protocol for all, even the youngest, samples. This would further increase the possible sample throughput. For this,

SEM			$10^{11}\Omega$	$10^{13}\Omega$	$(10^{13}\Omega)$	$10^{11}\Omega$	$10^{11}\Omega$	$10^{10}\Omega$	$10^{10}\Omega$
229	230		232	233	234	235	236		238
230		232	233	234	235	236		238	

Table 8.1: Suggested measurement setup in two lines, and the respective detectors. All numbers are masses in amu.

all isotopes would need to be measured in the two magnetic field settings on a spectrometer with 10 slots. Then the ^{238}U beam can be collected in an FC in both lines, which significantly reduces the ghost signal scattering effect to close to zero (Chiang et al., 2019). This observation of Chiang et al. (2019) of course needs to be tested for the setup, as they report a slightly different scattering signal than the one described here. However, the application of the k_{230} and k_{229} factors (obtained for every individual measurement session) corrects for the remaining ghost signal counts anyways. ^{234}U should be measured on a $10^{13}\Omega$ amplifier (as currently, except for very few samples with small U content, where an SEM is used). ^{235}U, which hits the $10^{13}\Omega$ amplified cup in the second line, would go in saturation there. This however poses no problem, because every mass exempt from 229 amu is measured twice in the setup. This also allows to leave some detector slots empty. ^{234}U for example could also be measured in the second line, after ^{233}U, making the other $10^{13}\Omega$ amplifier optional. It is also ensured that 229 amu and 230 amu are measured on the same detector to minimize the influence of SEM calibration.
Such an update only requires an instrument with one more slot and a stable performance of an off-center SEM (the latter was not tested here, but proved to be a bit tricky in Arps (2017)). This would reduce the required measurement time by one third, and possibly even more, when less reference material measurements are neccessary due to the removal of the ghost signal by the collection of the ^{238}U. In addition, the separation of young samples is no requirement anymore, which saves preparation time and labwork. This also massively reduces costs (for argon required for the plasma; for labworkers) and thus makes the production of more ages possible. At the time being, the high costs for ^{230}Th/U dating often limit palaeoclimatic studies.

The second Part of this thesis is a good example of how the availability of more ages pushes our understanding of climatic, environmental and ecological processes, i. e. when combined with appropriate methods for data visualization and description. This work

has been among the very first ones to assess Kernel Density Estimation for ^{230}Th/U ages (first systematic study for speleothems by Weij et al. (2020), none for CWC yet). Given the rising amount of age datasets, this implies that there are a lot of discoveries to make in CWC datasets and beyond.
Random sampling strategies during the physical sample collection are best for this approach, as has been extensively demonstrated. For regions with no or little recent coral growth, such as the Gulf of Cadiz, broad collection of surface samples will provide insights into the reef evolution over time. If all ages can be found at the surface (as is hinted at in the data explored here), reefs would probably start and stop growing at different points of time, also when located next to each other.
For the Norwegian shelf, the question remains if the absence of corals in the mid-Holocene is partly based on sampling bias (due to location of sites) or a real effect, and if the latter, if globally for the full Norwegian shelf. Regional differences would hint at the processes causing this distributions.
Applying adaptive KDE and the associated methods for uncertainty displayment for studies tracing coral mortality events (such as Clark et al. (2014)) has great potential as well for accurate peak reconstruction. This shows that many applications that are highly relevant for today's ecosystems, not only for coral communities of the past, can benefit from the methodical assessment here.

9 List of publications of the author

Inga Kristina Kerber, Jennifer Arps, René Eichstädter, Fabian Kontor, Christoph Dornick, Andrea Schröder-Ritzrau, Athulya Babu, Sophie Warken and Norbert Frank: Simultaneous U and Th isotope measurements for U-series dating using MCICPMS, *Nuclear Instruments and Methods in Physics Research Section B: Beam Interactions with Materials and Atoms*, Volume 539, 2023, Pages 169-178, ISSN 0168-583X, https://doi.org/10.1016/j.nimb.2023.04.003

10 Bibliography

A History of the United States Primary Uranium Reference Material – Origin, Production, Certification of Uranium Metal SRM 960/CRM 112-A. Standard, U.S. Department of Energy - NBL Program Office.

Ian S Abramson. On bandwidth variation in kernel estimates - a square root law. *The annals of Statistics*, pages 1217–1223, 1982.

Anna Maria Addamo, Agostina Vertino, Jaroslaw Stolarski, Ricardo García-Jiménez, Marco Taviani, and Annie Machordom. Merging scleractinian genera: the overwhelming genetic similarity between solitary Desmophyllum and colonial Lophelia. *BMC Evolutionary Biology*, 16(1):1–17, 2016.

Jess F Adkins, Hai Cheng, Edward A Boyle, Ellen RM Druffel, and R Lawrence Edwards. Deep-sea coral evidence for rapid change in ventilation of the deep North Atlantic 15,400 years ago. *Science*, 280(5364):725–728, 1998.

Ahmed Saif Al-Mikhlafi, Lawrence R Edwards, and Hai Cheng. Sea-level history and tectonic uplift during the last-interglacial period (LIG): Inferred from the Bab al-Mandab coral reef terraces, southern Red Sea. *Journal of African Earth Sciences*, 138:133–148, 2018.

Morten Bugge Andersen, Claudine H Stirling, E-K Potter, and Alex N Halliday. Toward epsilon levels of measurement precision on 234U/238U by using MC-ICPMS. *International Journal of Mass Spectrometry*, 237(2-3):107–118, 2004.

Jennifer Arps. *Towards ϵ-precision of U-series age determinations of secondary carbonates*. PhD thesis, Ruprecht-Karls-Universität Heidelberg, 2017.

Yemane Asmerom, Victor J Polyak, and Stephen J Burns. Variable winter moisture in the southwestern United States linked to rapid glacial climate shifts. *Nature Geoscience*, 3 (2):114–117, 2010.

Kamolphat Atsawawaranunt, Sandy Harrison, and Laia Comas-Bru. SISAL (Speleothem Isotopes Synthesis and AnaLysis working group) database version 1b. 2019.

Andy Baker, Peter L Smart, and DC Ford. Northwest European palaeoclimate as indicated by growth frequency variations of secondary calcite deposits. *Palaeogeography, Palaeoclimatology, Palaeoecology*, 100(3):291–301, 1993.

Lucie Bazin, Amaëlle Landais, Bénédicte Lemieux-Dudon, H Toyé Mahamadou Kele, Daniel Veres, Frédéric Parrenin, Patricia Martinerie, Catherine Ritz, Emilie Capron, Vladimir Ya Lipenkov, Marie-France Loutre, Dominique Raynaud, Bo Møllesøe Vinther, Anders M Svensson, Sune Olander Rasmussen, Mirko Severi, Thomas Blunier, Markus Christian Leuenberger, Hubertus Fischer, Valerie Masson-Delmotte, Jérôme A Chappellaz, and Eric William Wolff. The Antarctic ice core chronology (AICC2012), 2013. URL https://doi.org/10.1594/PANGAEA.824894.

J Warren Beck, David A Richards, R Lawrence, Bernard W Silverman, Peter L Smart, Douglas J Donahue, Sofia Hererra-Osterheld, George S Burr, Leal Calsoyas, AJ Timothy, et al. Extremely large variations of atmospheric 14C concentration during the last glacial period. *Science*, 292(5526):2453–2458, 2001.

Arnfried Becker, Karsten Piepjohn, and Andrea Schröder-Ritzrau. The Erdmannshöhle near Hasel, SW Germany: karst environment and cave evolution. *Swiss Journal of Geosciences*, 113(1):1–25, 2020.

Elvira Beisel, Norbert Frank, Laura F Robinson, Marleen Lausecker, Ronny Friedrich, Steffen Therre, Andrea Schröder-Ritzrau, and Martin Butzin. Climate induced thermocline aging and ventilation in the eastern Atlantic over the last 32.000 years. *Paleoceanography and Paleoclimatology*, 2023.

Nicole Biller-Celander, Jeremy D Shakun, David McGee, Corinne I Wong, Alberto V Reyes, Ben Hardt, Irit Tal, Derek C Ford, and Bernard Lauriol. Increasing Pleistocene permafrost persistence and carbon cycle conundrums inferred from Canadian speleothems. *Science Advances*, 7(18):eabe5799, 2021.

Charles D. Bingham. CRM112-A Uranium Metal Assay Standard. Standard, U. S. Department of Energy New Brunswick Laboratory, 1987.

Lucile Bonneau, Christophe Colin, Edwige Pons-Branchu, Furu Mienis, Nadine Tisnérat-Laborde, Dominique Blamart, Mary Elliot, Tim Collart, Norbert Frank, Lorna Foliot, et al. Imprint of Holocene Climate Variability on Cold-Water Coral Reef Growth at the SW Rockall Trough Margin, NE Atlantic. *Geochemistry, Geophysics, Geosystems*, 19(8):2437–2452, 2018.

Charles John Bopp, Craig C Lundstrom, Thomas M Johnson, Robert A Sanford, Philip E Long, and Kenneth H Williams. Uranium 238U/235U isotope ratios as indicators of reduction: results from an in situ biostimulation experiment at Rifle, Colorado, USA. *Environmental science & technology*, 44(15):5927–5933, 2010.

Zdravko I Botev, Joseph F Grotowski, and Dirk P Kroese. Kernel density estimation via diffusion. *The annals of Statistics*, 38(5):2916–2957, 2010.

Bernard Bourdon, Simon Turner, Gideon M Henderson, and Craig C Lundstrom. Introduction to U-series geochemistry. *Reviews in mineralogy and geochemistry*, 52(1):1–21, 2003.

Pascale Braconnot, Sandy P Harrison, Masa Kageyama, Patrick J Bartlein, Valerie Masson-Delmotte, Ayako Abe-Ouchi, Bette Otto-Bliesner, and Yan Zhao. Evaluation of climate models using palaeoclimatic data. *Nature Climate Change*, 2(6):417–424, 2012.

Gregory A Brennecka, Lars E Borg, Ian D Hutcheon, Michael A Sharp, and Ariel D Anbar. Natural variations in uranium isotope ratios of uranium ore concentrates: Understanding the 238U/235U fractionation mechanism. *Earth and Planetary Science Letters*, 291 (1-4):228–233, 2010.

Thomas Breton, Nicholas S Lloyd, Anne Trinquier, Claudia Bouman, and Johannes B Schwieters. Improving precision and signal/noise ratios for MC-ICP-MS. *Procedia Earth and Planetary Science*, 13:240–243, 2015.

Pål Buhl-Mortensen, Lene Buhl-Mortensen, and Autun Purser. *Trophic ecology and habitat provision in cold-water coral ecosystems*, pages 699–732. Springer International Publishing, 2017.

David Burley, Marshall I Weisler, and Jian-xin Zhao. High precision U/Th dating of first Polynesian settlement. *PloS one*, 7(11):e48769, 2012.

Stephen Cairns. World Register of Marine Species (WoRMS) - Desmophyllum pertusum (Linnaeus, 1758) - Notes, 2019. URL https://www.marinespecies.org/aphia.php?p=taxdetails&id=1245747#notes.

Stephen D Cairns. Deep-water corals: an overview with special reference to diversity and distribution of deep-water scleractinian corals. *Bulletin of marine Science*, 81(3): 311–322, 2007.

Tianyu Chen, Laura F Robinson, Matthew P Beasley, Louis M Claxton, Morten B Andersen, Lauren J Gregoire, Jemma Wadham, Daniel J Fornari, and Karen S Harpp. Ocean mixing and ice-sheet control of seawater 234U/238U during the last deglaciation. *Science*, 354(6312):626–629, 2016.

Hai Cheng, Jess Adkins, R Lawrence Edwards, and Edward A Boyle. U-Th dating of deep-sea corals. *Geochimica et Cosmochimica Acta*, 64(14):2401–2416, 2000a.

Hai Cheng, R Lawrence Edwards, J Hoff, Christina D Gallup, DA Richards, and Yemane Asmerom. The half-lives of uranium-234 and thorium-230. *Chemical Geology*, 169(1-2): 17–33, 2000b.

Hai Cheng, R Lawrence Edwards, Chuan-Chou Shen, Victor J Polyak, Yemane Asmerom, Jon Woodhead, John Hellstrom, Yongjin Wang, Xinggong Kong, Christoph Spötl, et al. Improvements in 230Th dating, 230Th and 234U half-life values, and U–Th isotopic measurements by multi-collector inductively coupled plasma mass spectrometry. *Earth and Planetary Science Letters*, 371:82–91, 2013.

Hai Cheng, R Lawrence Edwards, Ashish Sinha, Christoph Spötl, Liang Yi, Shitao Chen, Megan Kelly, Gayatri Kathayat, Xianfeng Wang, Xianglei Li, et al. The Asian monsoon over the past 640,000 years and ice age terminations. *Nature*, 534(7609):640–646, 2016.

Hong-Wei Chiang, Yanbin Lu, Xianfeng Wang, Ke Lin, and Xiaokang Liu. Optimizing MC-ICP-MS with SEM protocols for determination of U and Th isotope ratios and 230Th ages in carbonates. *Quaternary Geochronology*, 50:75–90, 2019.

Markus Christl, Augusto Mangini, Stefan Holzkämper, and Christoph Spötl. Evidence for a link between the flux of galactic cosmic rays and Earth's climate during the past 200,000 years. *Journal of Atmospheric and Solar-Terrestrial Physics*, 66(3-4):313–322, 2004.

Peter M Chutcharavan, Andrea Dutton, and Michael J Ellwood. Seawater 234U/238U recorded by modern and fossil corals. *Geochimica et Cosmochimica Acta*, 224:1–17, 2018.

Malcolm R Clark. *Seamounts, deep-sea corals and fisheries: vulnerability of deep-sea corals to fishing on seamounts beyond areas of national jurisdiction*. Number 183. UNEP/Earthprint, 2006.

Peter U Clark, Arthur S Dyke, Jeremy D Shakun, Anders E Carlson, Jorie Clark, Barbara Wohlfarth, Jerry X Mitrovica, Steven W Hostetler, and A Marshall McCabe. The last glacial maximum. *Science*, 325(5941):710–714, 2009.

Tara R Clark, George Roff, Jian-xin Zhao, Yue-xing Feng, Terence J Done, and John M Pandolfi. Testing the precision and accuracy of the U–Th chronometer for dating coral mortality events in the last 100 years. *Quaternary Geochronology*, 23:35–45, 2014.

Laia Comas-Bru, Kamolphat Atsawawaranunt, Sandy Harrison, et al. SISAL (Speleothem Isotopes Synthesis and AnaLysis Working Group) database version 2.0. 2020.

Guillem Corbera, Claudio Lo Iacono, Christopher D Standish, Eleni Anagnostou, Jürgen Titschack, Orestis Katsamenis, Isabel Cacho, David Van Rooij, Veerle AI Huvenne, and Gavin L Foster. Glacio-eustatic variations and sapropel events as main controls on the Middle Pleistocene-Holocene evolution of the Cabliers Coral Mound Province (W Mediterranean). *Quaternary Science Reviews*, 253:106783, 2021.

Matthias López Correa, Paolo Montagna, N Joseph, Andres Rüggeberg, Jan Fietzke, Sascha Flögel, Boris Dorschel, Steve L. Goldstein, Andy Wheeler, and André Freiwald. Preboreal onset of cold-water coral growth beyond the Arctic Circle revealed by coupled radiocarbon and U-series dating and neodymium isotopes. *Quaternary Science Reviews*, 34:24–43, 2012.

Kristan Cuny-Guirriec, Eric Douville, Stéphanie Reynaud, Denis Allemand, Louise Bordier, Marine Canesi, Claudio Mazzoli, Marco Taviani, Simonepietro Canese, Malcolm McCulloch, et al. Coral Li/Mg thermometry: caveats and constraints. *Chemical Geology*, 523:162–178, 2019.

Andrew J Davies and John M Guinotte. Global habitat suitability for framework-forming cold-water corals. *PloS one*, 6(4):e18483, 2011.

Andrew J Davies, Max Wisshak, James C Orr, and J Murray Roberts. Predicting suitable habitat for the cold-water coral Lophelia pertusa (Scleractinia). *Deep Sea Research Part I: Oceanographic Research Papers*, 55(8):1048–1062, 2008.

Maria Luiza de Carvalho Ferreira, Laura F Robinson, Joseph A Stewart, Tao Li, Tianyu Chen, Andrea Burke, Marcelo V Kitahara, and Nicholas J White. Spatial and temporal distribution of cold-water corals in the Northeast Atlantic Ocean over the last 150 thousand years. *Deep Sea Research Part I: Oceanographic Research Papers*, 190:103892, 2022.

MJ Desforges, PJ Jacob, and JE Cooper. Applications of probability density estimation to the detection of abnormal conditions in engineering. *Proceedings of the institution of mechanical engineers, part c: Journal of mechanical engineering science*, 212(8): 687–703, 1998.

LA Dodds, J Murray Roberts, AC Taylor, and Francesca Marubini. Metabolic tolerance of the cold-water coral Lophelia pertusa (Scleractinia) to temperature and dissolved oxygen change. *Journal of Experimental Marine Biology and Ecology*, 349(2):205–214, 2007.

Boris Dorschel, Dierk Hebbeln, Anneleen Foubert, Martin White, and Andy J Wheeler. Hydrodynamics and cold-water coral facies distribution related to recent sedimentary processes at Galway Mound west of Ireland. *Marine Geology*, 244(1-4):184–195, 2007.

Mélanie Douarin, Mary Elliot, Stephen R Noble, Daniel Sinclair, Lea-Anne Henry, David Long, Steven G Moreton, and J Murray Roberts. Growth of north-east Atlantic cold-water coral reefs and mounds during the Holocene: A high resolution U-series and 14C chronology. *Earth and Planetary Science Letters*, 375:176–187, 2013.

Eric Douville, Eline Sallé, Norbert Frank, Markus Eisele, Edwige Pons-Branchu, and Sophie Ayrault. Rapid and accurate U–Th dating of ancient carbonates using inductively coupled plasma-quadrupole mass spectrometry. *Chemical Geology*, 272(1-4):1–11, 2010.

Quentin Dubois-Dauphin. *Restitution de l'hydrologie de l'Atlantique Nord-Est et de la Méditerranée occidentale depuis la dernière période glaciaire à partir de la composition isotopique du néodyme mesurée dans l'eau de mer et les coraux d'eau froide*. PhD thesis, Université Paris Saclay (COmUE), 2016.

B Duchemin, N Coursol, and M.M Bé. The re-evaluation of decay data for the U-238 chain. *Nuclear Instruments and Methods in Physics Research Section A: Accelerators, Spectrometers, Detectors and Associated Equipment*, 339(1):146–150, 1994.

Gerard CA Duineveld, Marc SS Lavaleye, Magda JN Bergman, Henko De Stigter, and Furu Mienis. Trophic structure of a cold-water coral mound community (Rockall Bank, NE Atlantic) in relation to the near-bottom particle supply and current regime. *Bulletin of Marine Science*, 81(3):449–467, 2007.

Wolf-Christian Dullo, Sascha Flögel, and Andres Rüggeberg. Cold-water coral growth in relation to the hydrography of the Celtic and Nordic European continental margin. *Marine Ecology Progress Series*, 371:165–176, 2008.

Andrea Dutton, Ken Rubin, Noah McLean, James Bowring, Eduoard Bard, RL Edwards, GM Henderson, MR Reid, DA Richards, KWW Sims, et al. Data reporting standards for publication of U-series data for geochronology and timescale assessment in the earth sciences. *Quaternary Geochronology*, 39:142–149, 2017.

Markus Eisele, Dierk Hebbeln, and Claudia Wienberg. Growth history of a cold-water coral covered carbonate mound—Galway Mound, Porcupine Seabight, NE-Atlantic. *Marine Geology*, 253(3-4):160–169, 2008.

Tezer M Esat and Yusuke Yokoyama. Variability in the uranium isotopic composition of the oceans over glacial–interglacial timescales. *Geochimica et Cosmochimica Acta*, 70 (16):4140–4150, 2006.

Tezer M Esat and Yusuke Yokoyama. Coupled uranium isotope and sea-level variations in the oceans. *Geochimica et Cosmochimica Acta*, 74(24):7008–7020, 2010.

Ian J Fairchild and Andy Baker. *Speleothem science: from process to past environments*. John Wiley & Sons, 2012.

Ian J Fairchild and Pauline C Treble. Trace elements in speleothems as recorders of environmental change. *Quaternary Science Reviews*, 28(5-6):449–468, 2009.

Paul G. Falkowski, Zvy Dubinsky, Leonard Muscatine, and James W. Porter. Light and the Bioenergetics of a Symbiotic Coral. *BioScience*, 34(11):705–709, 12 1984.

Kenneth A Farley. (U-Th)/He dating: Techniques, calibrations, and applications. *Reviews in Mineralogy and Geochemistry*, 47(1):819–844, 2002.

Claudia Fensterer, Denis Scholz, Dirk Hoffmann, Augusto Mangini, and Jesus M Pajón. 230Th/U-dating of a late Holocene low uranium speleothem from Cuba. In *IOP Conference Series: Earth and Environmental Science*, volume 9, page 012015. IOP Publishing, 2010.

Robin Fentimen, Eline Feenstra, Andres Rüggeberg, Torsten Vennemann, Irka Hajdas, Thierry Adatte, David Van Rooij, and Anneleen Foubert. Cold-water coral mound archive provides unique insights into intermediate water mass dynamics in the Alboran sea during the last deglaciation. *Frontiers in Marine Science*, 7:354, 2020.

Robin Fentimen, Eline Feenstra, Andres Rüggeberg, Efraim Hall, Valentin Rime, Torsten Vennemann, Irka Hajdas, Antonietta Rosso, David Van Rooij, Thierry Adatte, et al. A 300,000 year record of cold-water coral mound build-up at the East Melilla Coral Province (SE Alboran Sea, western Mediterranean). *Climate of the Past Discussions*, 2022:1–42, 2022.

Hiske G Fink, Claudia Wienberg, Ricardo De Pol-Holz, Paul Wintersteller, and Dierk Hebbeln. Cold-water coral growth in the Alboran Sea related to high productivity during the Late Pleistocene and Holocene. *Marine Geology*, 339:71–82, 2013.

Hiske G Fink, Claudia Wienberg, Ricardo De Pol-Holz, and Dierk Hebbeln. Spatio-temporal distribution patterns of Mediterranean cold-water corals (Lophelia pertusa and Madrepora oculata) during the past 14,000 years. *Deep Sea Research Part I: Oceanographic Research Papers*, 103:37–48, 2015.

Sascha Flögel, W-Chr Dullo, Olaf Pfannkuche, K Kiriakoulakis, and Andres Rüggeberg. Geochemical and physical constraints for the occurrence of living cold-water corals. *Deep Sea Research Part II: Topical Studies in Oceanography*, 99:19–26, 2014.

Jens Fohlmeister, Andrea Schröder-Ritzrau, Denis Scholz, Christoph Spötl, Dana FC Riechelmann, Manfred Mudelsee, Anne Wackerbarth, Axel Gerdes, Silvia Riechelmann, Adrian Immenhauser, et al. Bunker Cave stalagmites: an archive for central European Holocene climate variability. *Climate of the Past*, 8(5):1751–1764, 2012.

Jens Fohlmeister, Nicole Vollweiler, Christoph Spötl, and Augusto Mangini. COMNISPA II: Update of a mid-European isotope climate record, 11 ka to present. *The Holocene*, 23(5):749–754, 2013.

Jens Fohlmeister, Marc Luetscher, Christoph Spötl, Andrea Schröder-Ritzrau, Birgit Schröder, Norbert Frank, René Eichstädter, Martin Trüssel, Vanessa Skiba, and Niklas Boers. The role of Northern Hemisphere summer insolation for millennial-scale climate variability during the penultimate glacial. *Communications Earth & Environment*, 4 (1):245, 2023.

Jan Helge Fosså, PB Mortensen, and Dag M Furevik. The deep-water coral Lophelia pertusa in Norwegian waters: distribution and fishery impacts. *Hydrobiologia*, 471: 1–12, 2002.

Norbert Frank and Freya Hemsing. Dating of Corals and Other Geological Samples via the Radioactive Disequilibrium of Uranium and Thorium Isotopes. *Paleoclimatology*, pages 89–100, 2021.

Norbert Frank, Martine Paterne, Linda Ayliffe, Tjeerd van Weering, Jean-Pierre Henriet, and Dominique Blamart. Eastern North Atlantic deep-sea corals: tracing upper intermediate water Δ14C during the Holocene. *Earth and Planetary Science Letters*, 219 (3-4):297–309, 2004.

Norbert Frank, Estelle Ricard, Audrey Lutringer-Paquet, Cees van Der Land, Christophe Colin, Dominique Blamart, Anneleen Foubert, David Van Rooij, Jean-Pierre Henriet, Henk de Haas, et al. The Holocene occurrence of cold water corals in the NE Atlantic: implications for coral carbonate mound evolution. *Marine Geology*, 266(1-4):129–142, 2009.

Norbert Frank, André Freiwald, Matthias López Correa, Claudia Wienberg, Markus Eisele, Dierk Hebbeln, David Van Rooij, Jean-Pierre Henriet, Christophe Colin, Tjeerd Van Weering, et al. Northeastern Atlantic cold-water coral reefs and climate. *Geology*, 39(8):743–746, 2011.

Rune Frederiksen, Andreas Jensen, and Håkan Westerberg. The distribution of the scleractinian coral Lophelia pertusa around the Faroe Islands and the relation to internal tidal mixing. *Sarsia*, 77(2):157–171, 1992.

André Freiwald. *Cold-water corals and ecosystems*, volume 643. Springer Science & Business Media, 2005.

André Freiwald, A Rogers, J Hall-Spencer, JM Guinotte, AJ Davies, C Yesson, CS Martin, and LV Weatherdon. Global distribution of cold-water corals (version 5.1). Fifth update to the dataset in Freiwald et al. (2004) by UNEP-WCMC, in collaboration with Andre Freiwald and John Guinotte., 2021.

Tim Freudenthal and Gerold Wefer. Drilling cores on the sea floor with the remote-controlled sea floor drilling rig MeBo. *Geoscientific Instrumentation, Methods and Data Systems*, 2(2):329–337, 2013.

Jing Gao, Xun Zhou, Bin Fang, Ting Li, and Liwei Tang. U-series dating of the travertine depositing near the Rongma hot springs in northern Tibet, China, and its paleoclimatic implication. *Quaternary International*, 298:98–106, 2013.

Marcos García-Diez, Dirk L Hoffmann, João Zilhão, Carmen de las Heras, José Antonio Lasheras, Ramón Montes, and Alistair WG Pike. Uranium series dating reveals a long sequence of rock art at Altamira Cave (Santillana del Mar, Cantabria). *Journal of Archaeological Science*, 40(11):4098–4106, 2013.

Melvyn Gascoyne, Henry P Schwarcz, and Derek C Ford. Uranium-series ages of speleothem from northwest England: correlation with Quaternary climate. *Philosophical Transactions of the Royal Society of London. B, Biological Sciences*, 301(1104): 143–164, 1983.

Steven J Goldstein, Michael T Murrell, and Ross W Williams. Half-life of Th 229. *Physical Review C*, 40(6):2793, 1989.

Kunchithapadam Gopalan. *Principles of radiometric dating*. Cambridge University Press, 2017.

Andrea Gori, Covadonga Orejas, Teresa Madurell, Lorenzo Bramanti, María Martins, Elena Quintanilla, Patricia Marti-Puig, Claudio Lo Iacono, Pere Puig, Susana Requena, et al. Bathymetrical distribution and size structure of cold-water coral populations in the Cap de Creus and Lacaze-Duthiers canyons (northwestern Mediterranean). *Biogeosciences*, 10(3):2049–2060, 2013.

Irka Hajdas. Radiocarbon dating and its applications in Quaternary studies. *E&G Quaternary Science Journal*, 57(1/2):2–24, 2008.

D. Hebbeln, C. Wienberg, M. Bender, F. Bergmann, K. Dehning, W.C. Dullo, R. Eichstädter, S. Flöter, A. Freiwald, A. Gori, J. Haberkern, L. Hoffmann, F. João, M. Lavaleye, T. Leymann, K. Matsuyama, B. Meyer-Schack, F. Mienis, I. Moçambique, N. Nowald, C. Orejas, C. Ramos Cordova, D. Saturov, C. Seiter, J. Titschack, V. Vittori, A.M. Wefing, M. Wilsenack, and P. Wintersteller. ANNA Cold-Water Coral Ecosystems off Angola and Namibia - Cruise No. M122 - December 30, 2015 - January 31, 2016 - Walvis Bay (Namibia) -Walvis Bay (Namibia). Technical report, 2017.

Dierk Hebbeln, Maren Bender, Stefanie Gaide, Jürgen Titschack, Thomas Vandorpe, David Van Rooij, Paul Wintersteller, and Claudia Wienberg. Thousands of cold-water coral mounds along the Moroccan Atlantic continental margin: distribution and morphometry. *Marine Geology*, 411:51–61, 2019.

Dierk Hebbeln, Claudia Wienberg, Wolf-Christian Dullo, André Freiwald, Furu Mienis, Covadonga Orejas, and Jürgen Titschack. Cold-water coral reefs thriving under hypoxia. *Coral Reefs*, 39:853–859, 2020.

Nils-Bastian Heidenreich, Anja Schindler, and Stefan Sperlich. Bandwidth selection for kernel density estimation: a review of fully automatic selectors. *AStA Advances in Statistical Analysis*, 97:403–433, 2013.

John Hellstrom. Rapid and accurate U/Th dating using parallel ion-counting multi-collector ICP-MS. *Journal of Analytical Atomic Spectrometry*, 18(11):1346–1351, 2003.

John Hellstrom. U–Th dating of speleothems with high initial 230Th using stratigraphical constraint. *Quaternary Geochronology*, 1(4):289–295, 2006.

John Hellstrom and Robyn Pickering. Recent advances and future prospects of the U–Th and U–Pb chronometers applicable to archaeology. *Journal of Archaeological Science*, 56:32–40, 2015.

Freya Hemsing. *Cold-water corals as archives for ocean dynamics, environmental conditions and glacial reef accumulation*. PhD thesis, Ruprecht-Karls-Universität Heidelberg, 2017.

Gideon M Henderson. New oceanic proxies for paleoclimate. *Earth and Planetary Science Letters*, 203(1):1–13, 2002.

Lea-Anne Henry and J Murray Roberts. Global biodiversity in cold-water coral reef ecosystems. *Marine animal forests: the ecology of benthic biodiversity hotspots*, pages 235–256, 2017.

Helena Hercman. Reconstruction of palaeoclimatic changes in central Europe between 10 and 200 thousand years BP, based on analysis of growth frequency of speleothems. *Studia Quaternaria*, pages 35–70, 2000.

Ernesto Hernández-Mendiola, Juan Pablo Bernal, E Lounejeva, GE Mortimer, and Malcolm Thomas McCulloch. U-series dating of carbonates using inductively coupled plasma-quadrupole mass spectrometry. *Quaternary Geochronology*, 6(6):564–573, 2011.

Dirk L Hoffmann, Julie Prytulak, David A Richards, Tim Elliott, Christopher D Coath, Peter L Smart, and Denis Scholz. Procedures for accurate U and Th isotope measurements by high precision MC-ICPMS. *International Journal of Mass Spectrometry*, 264 (2-3):97–109, 2007.

Steffen Holzkämper, Christoph Spötl, and Augusto Mangini. High-precision constraints on timing of Alpine warm periods during the middle to late Pleistocene using speleothem growth periods. *Earth and Planetary Science Letters*, 236(3-4):751–764, 2005.

Martin Hovland and Pål B Mortensen. *Norske Korallrev Og Prosessor i Havbunnen.(Deep-water Coral-reefs and Processes on the Sea Floor)*. John Grieg Forlag, 1999.

Martin Hovland, Pal Buhl Mortensen, Torleiv Brattegard, Per Strass, and Kare Rokengen. Ahermatypic coral banks off mid-Norway; evidence for a link with seepage of light hydrocarbons. *Palaios*, 13(2):189–200, 1998.

Peter J Huber. *Robust statistics*, volume 523. John Wiley & Sons, 2004.

Miro Ivanovich and Russell S Harmon. Uranium-series disequilibrium: applications to earth, marine, and environmental sciences. 2. 1992.

Tracie R Jackson, Simon D Steidle, Kathleen A Wendt, Yuri Dublyansky, R Lawrence Edwards, and Christoph Spötl. A 350,000-year history of groundwater recharge in the southern Great Basin, USA. *Communications Earth & Environment*, 4(1):98, 2023.

AH Jaffey, KF Flynn, LE Glendenin, WC t Bentley, and AM Essling. Precision measurement of half-lives and specific activities of U 235 and U 238. *Physical review C*, 4(5): 1889, 1971.

Jean Jouzel, Valerie Masson-Delmotte, Olivier Cattani, Gabrielle Dreyfus, Sonia Falourd, Georg Hoffmann, Bénédicte Minster, Julius Nouet, Jean-Marc Barnola, Jérôme Chappellaz, et al. Orbital and millennial Antarctic climate variability over the past 800,000 years. *science*, 317(5839):793–796, 2007.

NB Keller. The deep-sea madreporarian corals of the genus Fungiacyathus from the Kurile-Kamchatka, Aleutian Trenches and other regions of the world oceans (in Russian). *Trudy Instituta Okeanologii*, 99:31–44, 1976.

Douglas J Kennett, Sebastian FM Breitenbach, Valorie V Aquino, Yemane Asmerom, Jaime Awe, James UL Baldini, Patrick Bartlein, Brendan J Culleton, Claire Ebert, Christopher Jazwa, et al. Development and disintegration of Maya political systems in response to climate change. *Science*, 338(6108):788–791, 2012.

Inga Kristina Kerber, Jennifer Arps, René Eichstädter, Fabian Kontor, Christoph Dornick, Andrea Schröder-Ritzrau, Athulya Babu, Sophie Warken, and Norbert Frank. Simultaneous U and Th isotope measurements for U-series dating using MCICPMS. *Nuclear Instruments and Methods in Physics Research Section B: Beam Interactions with Materials and Atoms*, 539:169–178, 2023.

Fabian Kontor. Entwicklung einer graphischen Nutzeroberfläche zur Th/U-Datierung von Speläothemen und Korallen. Bachelor's thesis, Ruprecht-Karls-Universität Heidelberg, 2021.

Thomas Krengel. *550,000 years of marine climate variability in the western Mediterranean Sea revealed by cold-water corals*. PhD thesis, Ruprecht-Karls-Universität Heidelberg, 2020.

Donald Langmuir and Janet S Herman. The mobility of thorium in natural waters at low temperatures. *Geochimica et Cosmochimica Acta*, 44(11):1753–1766, 1980.

Ioan Lascu, Joshua M Feinberg, Jeffrey A Dorale, Hai Cheng, and R Lawrence Edwards. Age of the Laschamp excursion determined by U-Th dating of a speleothem geomagnetic record from North America. *Geology*, 44(2):139–142, 2016.

Marleen Lausecker, Norbert Frank, Claudia Wienberg, Elvira Beisel, Anne-Marie Wefing, Freya Hemsing, Jasmin M. Link, Andrea Schröder-Ritzrau, Steffen Therre, Jens Fohlmeister, Ronny Friedrich, Mathis P. Hain, and Dierk Hebbeln. Rapid eastern South Atlantic thermocline deepening at the end of the Last Glacial Maximum. in prep.

Christophe Leys, Christophe Ley, Olivier Klein, Philippe Bernard, and Laurent Licata. Detecting outliers: Do not use standard deviation around the mean, use absolute deviation around the median. *Journal of experimental social psychology*, 49(4):764–766, 2013.

Willard F Libby, Ernest C Anderson, and James R Arnold. Age determination by radiocarbon content: world-wide assay of natural radiocarbon. *Science*, 109(2827):227–228, 1949.

Björn Lindberg and Jürgen Mienert. Postglacial carbonate production by cold-water corals on the Norwegian Shelf and their role in the global carbonate budget. *Geology*, 33(7):537–540, 2005.

Michael Lomitschka and Augusto Mangini. Precise Th/U-dating of small and heavily coated samples of deep sea corals. *Earth and Planetary Science Letters*, 170(4):391–401, 1999.

KR Ludwig. Mathematical–statistical treatment of data and errors for 230Th/U geochronology. *Reviews in Mineralogy and Geochemistry*, 52(1):631–656, 2003.

Ronzon Mallick and Norbert Frank. A new technique for precise uranium-series dating of travertine micro-samples. *Geochimica et Cosmochimica Acta*, 66(24):4261–4272, 2002.

Augusto Mangini, Michael Lomitschka, René Eichstädter, Norbert Frank, S Vogler, G Bonani, Irka Hajdas, and Jörg Pätzold. Coral provides way to age deep water. *Nature*, 392(6674):347–348, 1998.

Augusto Mangini, Christoph Spötl, and Pablo Verdes. Reconstruction of temperature in the Central Alps during the past 2000 yr from a δ18O stalagmite record. *Earth and Planetary Science Letters*, 235(3-4):741–751, 2005.

Lélia Matos, Furu Mienis, Claudia Wienberg, Norbert Frank, Cornelia Kwiatkowski, Jeroen Groeneveld, François Thil, Fatima Abrantes, Marina R Cunha, and Dierk Hebbeln. Interglacial occurrence of cold-water corals off Cape Lookout (NW Atlantic): First evidence of the Gulf Stream influence. *Deep Sea Research Part I: Oceanographic Research Papers*, 105:158–170, 2015.

Malcolm McCulloch, Marco Taviani, Paolo Montagna, Matthias López Correa, Alessandro Remia, and Graham Mortimer. Proliferation and demise of deep-sea corals in the Mediterranean during the Younger Dryas. *Earth and Planetary Science Letters*, 298 (1-2):143–152, 2010.

Frank McDermott. Palaeo-climate reconstruction from stable isotope variations in speleothems: a review. *Quaternary Science Reviews*, 23(7-8):901–918, 2004.

Furu Mienis, Henko C De Stigter, Martin White, G Duineveld, H De Haas, and TCE Van Weering. Hydrodynamic controls on cold-water coral growth and carbonate-mound development at the SW and SE Rockall Trough Margin, NE Atlantic Ocean. *Deep Sea Research Part I: Oceanographic Research Papers*, 54(9):1655–1674, 2007.

Furu Mienis, Cees Van der Land, Henko C De Stigter, M Van de Vorstenbosch, Henk De Haas, T Richter, and TCE Van Weering. Sediment accumulation on a cold-water carbonate mound at the Southwest Rockall Trough margin. *Marine Geology*, 265(1-2): 40–50, 2009.

Naja Mikkelsen, Helmut Erlenkeuser, John S Killingley, and Wolfgang H Berger. Norwegian corals: radiocarbon and stable isotopes in Lophelia pertusa. *Boreas*, 11(2): 163–171, 1982.

Johannes M Miocic, Stuart MV Gilfillan, Norbert Frank, Andrea Schroeder-Ritzrau, Neil M Burnside, and R Stuart Haszeldine. 420,000 year assessment of fault leakage rates shows geological carbon storage is secure. *Scientific reports*, 9(1):769, 2019.

Christian Mohn, Anna Rengstorf, Martin White, Gerard Duineveld, Furu Mienis, Karline Soetaert, and Anthony Grehan. Linking benthic hydrodynamics and cold-water coral occurrences: A high-resolution model study at three cold-water coral provinces in the NE Atlantic. *Progress in Oceanography*, 122:92–104, 2014.

Paolo Montagna, Malcolm McCulloch, Eric Douville, Matthias López Correa, Julie Trotter, Riccardo Rodolfo-Metalpa, Delphine Dissard, Christine Ferrier-Pagès, Norbert Frank, André Freiwald, Steve Goldstein, Claudio Mazzoli, Stephanie Reynaud, Andres Rüggeberg, Simone Russo, and Marco Taviani. Li/Mg systematics in scleractinian corals: Calibration of the thermometer. *Geochimica et Cosmochimica Acta*, 132:288–310, 2014. ISSN 0016-7037. doi: https://doi.org/10.1016/j.gca.2014.02.005.

PB Mortensen, L Buhl-Mortensen, AV Gebruk, and EM Krylova. Occurrence of deep-water corals on the Mid-Atlantic Ridge based on MAR-ECO data. *Deep Sea Research Part II: Topical Studies in Oceanography*, 55(1-2):142–152, 2008.

Gina E Moseley, Christoph Spötl, Hai Cheng, Ronny Boch, Angela Min, and R Lawrence Edwards. Termination-II interstadial/stadial climate change recorded in two stalagmites from the north European Alps. *Quaternary Science Reviews*, 127:229–239, 2015.

Gina E Moseley, R Lawrence Edwards, Kathleen A Wendt, Hai Cheng, Yuri Dublyansky, Yanbin Lu, Ronny Boch, and Christoph Spötl. Reconciliation of the Devils Hole climate record with orbital forcing. *Science*, 351(6269):165–168, 2016.

Juancho Movilla, Andrea Gori, Eva Calvo, Covadonga Orejas, Àngel López-Sanz, Carlos Domínguez-Carrió, Jordi Grinyó, and Carles Pelejero. Resistance of two Mediterranean cold-water coral species to low-pH conditions. *Water*, 6(1):59–67, 2013.

Malik S Naumann, Covadonga Orejas, and Christine Ferrier-Pagès. Species-specific physiological response by the cold-water corals Lophelia pertusa and Madrepora oculata to variations within their natural temperature range. *Deep Sea Research Part II: Topical Studies in Oceanography*, 99:36–41, 2014.

Stefan Niggemann, Augusto Mangini, Manfred Mudelsee, Detlev K Richter, and Georg Wurth. Sub-Milankovitch climatic cycles in Holocene stalagmites from Sauerland, Germany. *Earth and Planetary Science Letters*, 216(4):539–547, 2003a.

Stefan Niggemann, Augusto Mangini, Detlev K Richter, and Georg Wurth. A paleoclimate record of the last 17,600 years in stalagmites from the B7 cave, Sauerland, Germany. *Quaternary Science Reviews*, 22(5-7):555–567, 2003b.

Tommy Odland. tommyod/KDEpy: Kernel Density Estimation in Python, 2018. URL https://zenodo.org/record/2392268.

Alistair WG Pike, Dirk L Hoffmann, Paul B Pettitt, Marcos García-Diez, and Joao Zilhao. Dating Palaeolithic cave art: Why U–Th is the way to go. *Quaternary International*, 432:41–49, 2017.

Rodrigo da Costa Portilho-Ramos, Jürgen Titschack, Claudia Wienberg, Michael Georg Siccha Rojas, Yusuke Yokoyama, and Dierk Hebbeln. Major environmental drivers determining life and death of cold-water corals through time. *PLoS Biology*, 20(5): e3001628, 2022.

Ali Pourmand, François LH Tissot, Monica Arienzo, and Arash Sharifi. Introducing a comprehensive data reduction and uncertainty propagation algorithm for U-Th geochronometry with extraction chromatography and isotope dilution MC-ICP-MS. *Geostandards and Geoanalytical Research*, 38(2):129–148, 2014.

Zhilong Qin, Wenyuan Li, and Xiaofu Xiong. Estimating wind speed probability distribution using kernel density method. *Electric Power Systems Research*, 81(12):2139–2146, 2011.

Jacek Raddatz and Andres Rüggeberg. Constraining past environmental changes of cold-water coral mounds with geochemical proxies in corals and foraminifera. *The Depositional Record*, 7(2):200–222, 2021.

Jacek Raddatz, Andres Rüggeberg, Volker Liebetrau, Anneleen Foubert, Ed C Hathorne, Jan Fietzke, Anton Eisenhauer, and Wolf-Christian Dullo. Environmental boundary

conditions of cold-water coral mound growth over the last 3 million years in the Porcupine Seabight, Northeast Atlantic. *Deep Sea Research Part II: Topical Studies in Oceanography*, 99:227–236, 2014.

Jacek Raddatz, Volker Liebetrau, Julie Trotter, Andres Rüggeberg, Sascha Flögel, Wolf-Christian Dullo, Anton Eisenhauer, Silke Voigt, and Malcolm McCulloch. Environmental constraints on Holocene cold-water coral reef growth off Norway: Insights from a multiproxy approach. *Paleoceanography*, 31(10):1350–1367, 2016.

Jacek Raddatz, Volker Liebetrau, Andres Rüggeberg, Anneleen Foubert, Sascha Flögel, Dirk Nürnberg, Karen Hissmann, Johannes Musiol, Tyler Jay Goepfert, Anton Eisenhauer, et al. Living on the edge: environmental variability of a shallow late Holocene cold-water coral mound. *Coral Reefs*, 41(4):1255–1271, 2022.

Christopher Bronk Ramsey. Methods for summarizing radiocarbon datasets. *Radiocarbon*, 59(6):1809–1833, 2017.

Paula J Reimer, Edouard Bard, Alex Bayliss, J Warren Beck, Paul G Blackwell, Christopher Bronk Ramsey, Caitlin E Buck, Hai Cheng, R Lawrence Edwards, Michael Friedrich, et al. IntCal13 and Marine13 radiocarbon age calibration curves 0–50,000 years cal BP. *radiocarbon*, 55(4):1869–1887, 2013.

J Murray Roberts, Andrew Wheeler, André Freiwald, and Stephen D Cairns. *Cold-water corals: the biology and geology of deep-sea coral habitats*. Cambridge University Press, 2009.

Laura F Robinson, Nick S Belshaw, and Gideon M Henderson. U and Th concentrations and isotope ratios in modern carbonates and waters from the Bahamas. *Geochimica et Cosmochimica Acta*, 68(8):1777–1789, 2004a.

Laura F Robinson, Gideon M Henderson, Lisa Hall, and Iain Matthews. Climatic control of riverine and seawater uranium-isotope ratios. *Science*, 305(5685):851–854, 2004b.

Laura F Robinson, Jess F Adkins, Norbert Frank, Alexander C Gagnon, Nancy G Prouty, E Brendan Roark, and Tina Van de Flierdt. The geochemistry of deep-sea coral skeletons: a review of vital effects and applications for palaeoceanography. *Deep Sea Research Part II: Topical Studies in Oceanography*, 99:184–198, 2014.

Stephen J Romaniello, Achim D Herrmann, and Ariel D Anbar. Uranium concentrations and 238U/235U isotope ratios in modern carbonates from the Bahamas: Assessing a novel paleoredox proxy. *Chemical Geology*, 362:305–316, 2013.

Peter J Rousseeuw and Christophe Croux. Alternatives to the median absolute deviation. *Journal of the American Statistical association*, 88(424):1273–1283, 1993.

Andres Rüggeberg, Christian Dullo, Boris Dorschel, and Dierk Hebbeln. Environmental changes and growth history of a cold-water carbonate mound (Propeller Mound, Porcupine Seabight). *International Journal of Earth Sciences*, 96:57–72, 2007.

Denis Scholz and Dirk Hoffmann. 230Th/U-dating of fossil corals and speleothems. *E&G Quaternary Science Journal*, 57(1/2):52–76, 2008.

Andrea Schröder-Ritzrau, Augusto Mangini, and Michael Lomitschka. Deep-sea corals evidence periodic reduced ventilation in the North Atlantic during the LGM/Holocene transition. *Earth and Planetary Science Letters*, 216(3):399–410, 2003.

Andrea Schröder-Ritzrau, André Freiwald, and Augusto Mangini. U/Th-dating of deep-water corals from the eastern North Atlantic and the western Mediterranean Sea. *Cold-water corals and ecosystems*, pages 157–172, 2005.

Henry P Schwarcz, Bonnie Blackwell, Paul Goldberg, and Anthony E Marks. Uranium series dating of travertine from archaeological sites, Nahal Zin, Israel. *Nature*, 277 (5697):558–560, 1979.

Nick Scroxton, Michael K Gagan, Gavin B Dunbar, Linda K Ayliffe, Wahyoe S Hantoro, Chuan-Chou Shen, John C Hellstrom, Jian-xin Zhao, Hai Cheng, R Lawrence Edwards, et al. Natural attrition and growth frequency variations of stalagmites in southwest Sulawesi over the past 530,000 years. *Palaeogeography, Palaeoclimatology, Palaeoecology*, 441:823–833, 2016.

Qing-Feng Shao, Chun-Hua Li, Meng-Jie Huang, Ze-Bo Liao, Jennifer Arps, Chun-Yuan Huang, Yu-Chen Chou, and Xing-Gong Kong. Interactive programs of MC-ICPMS data processing for 230Th/U geochronology. *Quaternary Geochronology*, 51:43–52, 2019.

Qingfeng Shao, Yuan Wang, Pierre Voinchet, Min Zhu, Min Lin, William Jack Rink, Changzhu Jin, and Jean-Jacques Bahain. U-series and ESR/U-series dating of the Stegodon–Ailuropoda fauna at Black Cave, Guangxi, southern China with implications for the timing of the extinction of Gigantopithecus blacki. *Quaternary International*, 434:65–74, 2017.

Simon J Sheather and Michael C Jones. A reliable data-based bandwidth selection method for kernel density estimation. *Journal of the Royal Statistical Society: Series B (Methodological)*, 53(3):683–690, 1991.

Chuan-Chou Shen, R Lawrence Edwards, Hai Cheng, Jeffrey A Dorale, Rebecca B Thomas, S Bradley Moran, Sarah E Weinstein, and Henrietta N Edmonds. Uranium and thorium isotopic and concentration measurements by magnetic sector inductively coupled plasma mass spectrometry. *Chemical Geology*, 185(3-4):165–178, 2002.

Chuan-Chou Shen, Kuei-Shu Li, Kerry Sieh, Danny Natawidjaja, Hai Cheng, Xianfeng Wang, R Lawrence Edwards, Doan Dinh Lam, Yu-Te Hsieh, Tung-Yung Fan, et al. Variation of initial 230Th/232Th and limits of high precision U–Th dating of shallow-water corals. *Geochimica et Cosmochimica Acta*, 72(17):4201–4223, 2008.

Chuan-Chou Shen, Chung-Che Wu, Hai Cheng, R Lawrence Edwards, Yu-Te Hsieh, Sylvain Gallet, Ching-Chih Chang, Ting-Yong Li, Doan Dinh Lam, Akihiro Kano, et al. High-precision and high-resolution carbonate 230Th dating by MC-ICP-MS with SEM protocols. *Geochimica et Cosmochimica Acta*, 99:71–86, 2012.

Hideaki Shimazaki and Shigeru Shinomoto. Kernel bandwidth optimization in spike rate estimation. *Journal of computational neuroscience*, 29:171–182, 2010.

Wolfgang Siebel and P Van den Haute. Radiometric dating and tracing. *Radiochemistry and nuclear chemistry*, 1:157–196, 2009.

Bernard W Silverman. Density estimation for statistics and data analysis, 1986 Ed. *Monographs on Statictics and Applied Probability*, 1986.

Peter L Smart and David A Richards. Age estimates for the late Quaternary high sea-stands. *Quaternary Science Reviews*, 11(6):687–696, 1992.

Peter T Spooner, Tianyu Chen, Laura F Robinson, and Christopher D Coath. Rapid uranium-series age screening of carbonates by laser ablation mass spectrometry. *Quaternary Geochronology*, 31:28–39, 2016.

Christoph Spötl and Hai Cheng. Holocene climate change, permafrost and cryogenic carbonate formation: insights from a recently deglaciated, high-elevation cave in the Austrian Alps. *Climate of the Past*, 10(4):1349–1362, 2014.

Christoph Spötl and Augusto Mangini. Stalagmite from the Austrian Alps reveals Dansgaard–Oeschger events during isotope stage 3:: Implications for the absolute chronology of Greenland ice cores. *Earth and Planetary Science Letters*, 203(1):507–518, 2002.

Christoph Spötl, Stephen J Burns, and Augusto Mangini. Stable isotopes in speleothems as proxies of past environmental changes in the Alps. Technical report, 2002a.

Christoph Spötl, Augusto Mangini, Norbert Frank, Rene Eichstädter, and Stephen J Burns. Start of the last interglacial period at 135 ka: Evidence from a high Alpine speleothem. *Geology*, 30(9):815–818, 2002b.

Christoph Spötl, Augusto Mangini, and David A Richards. Chronology and paleoenvironment of Marine Isotope Stage 3 from two high-elevation speleothems, Austrian Alps. *Quaternary Science Reviews*, 25(9-10):1127–1136, 2006.

Christoph Spötl, Denis Scholz, and Augusto Mangini. A terrestrial U/Th-dated stable isotope record of the Penultimate Interglacial. *Earth and Planetary Science Letters*, 276(3-4):283–292, 2008.

Claudio Stalder, Agostina Vertino, Antonietta Rosso, Andres Rüggeberg, Claudius Pirkenseer, Jorge E Spangenberg, Silvia Spezzaferri, Osvaldo Camozzi, Sacha Rappo, and Irka Hajdas. Microfossils, a key to unravel cold-water carbonate mound evolution through time: evidence from the eastern Alboran Sea. *PLoS One*, 10(10):e0140223, 2015.

Simon D Steidle, Sophie F Warken, Nils Schorndorf, Julius Förstel, Andrea Schröder-Ritzrau, Gina E Moseley, Christoph Spötl, Jeronimo Aviles, Wolfgang Stinnesbeck, and Norbert Frank. Reconstruction of Middle to Late Quaternary sea level using submerged speleothems from the northeastern Yucatán Peninsula. *Journal of Quaternary Science*, 36(7):1190–1200, 2021.

Wolfgang Stinnesbeck, Samuel R Rennie, Jerónimo Avilés Olguín, Sarah R Stinnesbeck, Silvia Gonzalez, Norbert Frank, Sophie Warken, Nils Schorndorf, Thomas Krengel, Adriana Velázquez Morlet, et al. New evidence for an early settlement of the Yucatán Peninsula, Mexico: The Chan Hol 3 woman and her meaning for the Peopling of the Americas. *Plos one*, 15(2):e0227984, 2020.

Jan-Berend Stuut, Matthias Zabel, Volker Ratmeyer, Peer Helmke, Enno Schefuß, Gaute Lavik, and Ralph Schneider. Provenance of present-day eolian dust collected off NW Africa. *Journal of Geophysical Research: Atmospheres*, 110(D4), 2005.

Leonardo Tamborrino, Claudia Wienberg, Jürgen Titschack, Paul Wintersteller, Furu Mienis, Andrea Schröder-Ritzrau, André Freiwald, Covadonga Orejas, Wolf-Christian Dullo, Julia Haberkern, et al. Mid-Holocene extinction of cold-water corals on the Namibian shelf steered by the Benguela oxygen minimum zone. *Geology*, 47(12):1185–1188, 2019.

Marco Taviani, P Bouchet, B Metivier, M Fontugne, and G Delibrias. Intermediate steps of southwards faunal shifts testified by last glacial submerged thanatocoenoses in the Atlantic Ocean. *Palaeogeography, Palaeoclimatology, Palaeoecology*, 86(3-4):331–338, 1991.

Thermo Fisher Scientific. *Neptune Plus Hardware Manual*. Thermo Fisher Scientific, b edition, 10 2009.

Steffen Therre, Jens Fohlmeister, Dominik Fleitmann, Albert Matter, Stephen J Burns, Jennifer Arps, Andrea Schröder-Ritzrau, Ronny Friedrich, and Norbert Frank. Climate-induced speleothem radiocarbon variability on Socotra Island from the Last Glacial Maximum to the Younger Dryas. *Climate of the Past*, 16(1):409–421, 2020.

Nivedita Thiagarajan, Dana Gerlach, Mark L Roberts, Andrea Burke, Ann McNichol, William J Jenkins, Adam V Subhas, Ronald E Thresher, and Jess F Adkins. Movement of deep-sea coral populations on climatic timescales. *Paleoceanography*, 28(2):227–236, 2013.

Diane M Thompson. Environmental records from coral skeletons: A decade of novel insights and innovation. *Wiley Interdisciplinary Reviews: Climate Change*, 13(1):e745, 2022.

Jessica E Tierney, Christopher J Poulsen, Isabel P Montañez, Tripti Bhattacharya, Ran Feng, Heather L Ford, Bärbel Hönisch, Gordon N Inglis, Sierra V Petersen, Navjit Sagoo, et al. Past climates inform our future. *Science*, 370(6517):eaay3701, 2020.

Jürgen Titschack, Daniel Baum, Ricardo De Pol-Holz, Matthias Lopez Correa, Nina Forster, Sascha Flögel, Dierk Hebbeln, and André Freiwald. Aggradation and carbonate accumulation of Holocene Norwegian cold-water coral reefs. *Sedimentology*, 62 (7):1873–1898, 2015.

Jürgen Titschack, Mieke Thierens, Boris Dorschel, Christian Schulbert, André Freiwald, Akihiro Kano, Chizuru Takashima, Noriko Kawagoe, Xianghui Li, IODP Expedition, et al. Carbonate budget of a cold-water coral mound (Challenger Mound, IODP Exp. 307). *Marine Geology*, 259(1-4):36–46, 2009.

R Tong, AJ Davies, Autun Purser, X Liu, and F Liu. Global distribution of the cold-water coral Lophelia pertusa. In *IOP Conference Series: Earth and Environmental Science*, volume 1004, page 012010. IOP Publishing, 2022.

John W Tukey et al. *Exploratory data analysis*, volume 2. Reading, MA, 1977.

Cees Van der Land, Furu Mienis, Henk De Haas, Norbert Frank, Rudy Swennen, and Tjeerd CE Van Weering. Diagenetic processes in carbonate mound sediments at the south-west Rockall Trough margin. *Sedimentology*, 57(3):912–931, 2010.

Cees Van der Land, Markus Eisele, Furu Mienis, Henk de Haas, Dierk Hebbeln, John JG Reijmer, and Tjeerd CE van Weering. Carbonate mound development in contrasting settings on the Irish margin. *Deep Sea Research Part II: Topical Studies in Oceanography*, 99:297–306, 2014.

Philippe Van Kerm. Adaptive kernel density estimation. *The Stata Journal*, 3(2):148–156, 2003.

Zsolt Varga, Klaus Mayer, Chloe E Bonamici, A Hubert, Ian Hutcheon, William Kinman, M Kristo, F Pointurier, K Spencer, F Stanley, et al. Validation of reference materials for uranium radiochronometry in the frame of nuclear forensic investigations. *Applied Radiation and Isotopes*, 102:81–86, 2015.

Zsolt Varga, Célia Venchiarutti, Adrian Nicholl, Judit Krajkó, Rožle Jakopič, Klaus Mayer, Stephan Richter, and Yetunde Aregbe. IRMM-1000a and IRMM-1000b uranium reference materials certified for the production date. Part I: methodology, preparation and target characteristics. *Journal of Radioanalytical and Nuclear Chemistry*, 307:1077–1085, 2016.

Celia Venchiarutti, Zsolt Varga, Stephan Richter, Adrian Nicholl, Judit Krajko, R Jakopič, Klaus Mayer, and Yetunde Aregbe. IRMM-1000a and IRMM-1000b: uranium reference materials certified for the production date based on the 230 Th/234 U radiochronometer. Part II: certification. *Journal of Radioanalytical and Nuclear Chemistry*, 308:105–111, 2016.

Pieter Vermeesch. On the visualisation of detrital age distributions. *Chemical Geology*, 312:190–194, 2012.

Pieter Vermeesch and Eduardo Garzanti. Making geological sense of 'Big Data' in sedimentary provenance analysis. *Chemical Geology*, 409:20–27, 2015.

Lissette Victorero, Dominique Blamart, Edwige Pons-Branchu, Mark N Mavrogordato, and Veerle AI Huvenne. Reconstruction of the formation history of the Darwin Mounds, N Rockall Trough: how the dynamics of a sandy contourite affected cold-water coral growth. *Marine Geology*, 378:186–195, 2016.

Nicole Vollweiler, Denis Scholz, Christian Mühlinghaus, Augusto Mangini, and Christoph Spötl. A precisely dated climate record for the last 9 kyr from three high alpine stalagmites, Spannagel Cave, Austria. *Geophysical Research Letters*, 33(20), 2006.

Haozhuang Wang, Claudio Lo Iacono, Claudia Wienberg, Jürgen Titschack, and Dierk Hebbeln. Cold-water coral mounds in the southern Alboran Sea (western Mediterranean Sea): Internal waves as an important driver for mound formation since the last deglaciation. *Marine Geology*, 412:1–18, 2019.

Sophie F Warken, Rolf Vieten, Amos Winter, Christoph Spötl, Thomas E Miller, Klaus P Jochum, Andrea Schröder-Ritzrau, Augusto Mangini, and Denis Scholz. Persistent link between Caribbean precipitation and Atlantic Ocean circulation during the Last Glacial revealed by a speleothem record from Puerto Rico. *Paleoceanography and Paleoclimatology*, 35(11):e2020PA003944, 2020.

Sophie F Warken, Nils Schorndorf, Wolfgang Stinnesbeck, Dominik Hennhoefer, Sarah R Stinnesbeck, Julius Förstel, Simon D Steidle, Jerónimo Avilés Olguin, and Norbert Frank. Solar forcing of early Holocene droughts on the Yucatán peninsula. *Scientific Reports*, 11(1):13885, 2021.

Sophie F Warken, Therese Weißbach, Tobias Kluge, Hubert Vonhof, Denis Scholz, Rolf Vieten, Martina Schmidt, Amos Winter, and Norbert Frank. Last glacial millennial-scale hydro-climate and temperature changes in Puerto Rico constrained by speleothem fluid inclusion δ 18 O and δ 2 H values. *Climate of the Past*, 18(1):167–181, 2022.

K Hans Wedepohl. The composition of the continental crust. *Geochimica et cosmochimica Acta*, 59(7):1217–1232, 1995.

Anne-Marie Wefing, Jennifer Arps, Patrick Blaser, Claudia Wienberg, Dierk Hebbeln, and Norbert Frank. High precision U-series dating of scleractinian cold-water corals using an automated chromatographic U and Th extraction. *Chemical Geology*, 475: 140–148, 2017.

Rieneke Weij, Jon Woodhead, John Hellstrom, and Kale Sniderman. An exploration of the utility of speleothem age distributions for palaeoclimate assessment. *Quaternary Geochronology*, 60:101112, 2020.

JL Westbrook and CW Bloom. Basis for Development of an Exposure Matrix for the Mallinckrodt Chemical Company St. Louis Downtown Site and the St. Louis Airport Site, St. Louis, Missouri. Technical report, ORAUT-TKBS-0005, Rev. 02., 2007.

Andrew J Wheeler, Andreas Beyer, André Freiwald, Henk De Haas, Veerle AI Huvenne, Maxim Kozachenko, Karine Olu-Le Roy, and Jan Opderbecke. Morphology and environment of cold-water coral carbonate mounds on the NW European margin. *International Journal of Earth Sciences*, 96:37–56, 2007.

Martin White, Christian Mohn, Henko de Stigter, and Gareth Mottram. *Deep-water coral development as a function of hydrodynamics and surface productivity around the submarine banks of the Rockall Trough, NE Atlantic*, pages 503–514. Springer, 2005.

Martin White, J Murray Roberts, and Tjeerd van Weering. Do bottom-intensified diurnal tidal currents shape the alignment of carbonate mounds in the NE Atlantic? *Geo-Marine Letters*, 27:391–397, 2007.

Claudia Wienberg. 7 A Deglacial Cold-Water Coral Boom in the Alborán Sea: From Coral Mounds and Species Dominance. *Mediterranean Cold-Water Corals: Past, Present and Future: Understanding the Deep-Sea Realms of Coral*, pages 57–60, 2019.

Claudia Wienberg and Jürgen Titschack. *Framework-Forming Scleractinian Cold-Water Corals Through Space and Time: A Late Quaternary North Atlantic Perspective*, pages 699–732. Springer International Publishing, 2017. ISBN 978-3-319-21012-4.

Claudia Wienberg, Dierk Hebbeln, Hiske G Fink, Furu Mienis, Boris Dorschel, Agostina Vertino, Matthias López Correa, and Andre Freiwald. Scleractinian cold-water corals in the Gulf of Cádiz—first clues about their spatial and temporal distribution. *Deep Sea Research Part I: Oceanographic Research Papers*, 56(10):1873–1893, 2009.

Claudia Wienberg, Norbert Frank, Kenneth N Mertens, Jan-Berend Stuut, Margarita Marchant, Jan Fietzke, Furu Mienis, and Dierk Hebbeln. Glacial cold-water coral growth in the Gulf of Cádiz: Implications of increased palaeo-productivity. *Earth and Planetary Science Letters*, 298(3-4):405–416, 2010.

Claudia Wienberg, Jürgen Titschack, André Freiwald, Norbert Frank, Tomas Lundälv, Marco Taviani, Lydia Beuck, Andrea Schröder-Ritzrau, Thomas Krengel, and Dierk Hebbeln. The giant Mauritanian cold-water coral mound province: Oxygen control on coral mound formation. *Quaternary Science Reviews*, 185:135–152, 2018.

Claudia Wienberg, Jürgen Titschack, Norbert Frank, Ricardo De Pol-Holz, Jan Fietzke, Markus Eisele, Anne Kremer, and Dierk Hebbeln. Deglacial upslope shift of NE Atlantic intermediate waters controlled slope erosion and cold-water coral mound formation (Porcupine Seabight, Irish margin). *Quaternary Science Reviews*, 237:106310, 2020.

Claudia Wienberg, Thomas Krengel, Norbert Frank, Haozhuang Wang, David Van Rooij, and Dierk Hebbeln. Cold-water coral mounds in the western Mediterranean Sea: New insights into their initiation and development since the Mid-Pleistocene in response to changes of African hydroclimate. *Quaternary Science Reviews*, 293:107723, 2022.

Paul S Wilcox, Charlotte Honiat, Martin Trüssel, R Lawrence Edwards, and Christoph Spötl. Exceptional warmth and climate instability occurred in the European Alps during the Last Interglacial period. *Communications Earth & Environment*, 1(1):57, 2020.

JB Wilson. 'Patch'development of the deep-water coral Lophelia pertusa (L.) on Rockall Bank. *Journal of the Marine Biological Association of the United Kingdom*, 59(1): 165–177, 1979.

Ke-Fu Yu, Jian-Xin Zhao, Qi Shi, Te-Gu Chen, Pin-Xian Wang, Kenneth D Collerson, and Tung-Sheng Liu. U-series dating of dead Porites corals in the South China Sea: evidence for episodic coral mortality over the past two centuries. *Quaternary Geochronology*, 1 (2):129–141, 2006.

Ke-Fu Yu, Jian-Xin Zhao, Michael G Lawrence, and Yuexing Feng. Timing and duration of growth hiatuses in mid Holocene massive Porites corals from the northern South China Sea. *Journal of Quaternary Science*, 25(8):1284–1292, 2010.

Adriano Z Zambom and Dias Ronaldo. A review of kernel density estimation with applications to econometrics. *International Econometric Review*, 5(1):20–42, 2013.

Appendix

A Lists

A.1 List of Figures

A.2 List of Tables

B Additional information and data

B.1 Supplement Paper NIMB (Chapter 3)

In the following, remaining details from the supplement of the original manuscript are given for Chapter 3. The age data for BOC2-45mm (IUP-11368) and CPR-55mm (IUP-11369) has already been published with Kerber et al. (2023) and will not be repeated here.

Spike recalibration

UDop was created in 2004 from individual ^{233}U and ^{236}UU spikes calibrated against an inhouse CRM-112A. The ThSpike was created in 2001 from a 229Th solution. Both were calibrated on TIMS (Hoffmann et al., 2007). TriSpike solution was mixed from both individual spikes in 2013 (98.729 g of UDop and 102.785 g of ThSpike filled up with 3 N HNO_3 to 997.888 g in total).
Due to the radioactive decay of ^{229}Th and the improved measurement precision since the last calibration in 2004, we have re-calibrated the concentrations and uncertainties as shown in Table B.1. Here, the decay of ^{229}Th over 17 years was taken into account (half-life 7880 a (Goldstein et al., 1989)). For ^{233}U and ^{236}U this was not necessary due to their half-lives being larger than 100 ka. The new concentrations and uncertainties were calculated from HU-1 reference material ("standard") measurements as HU-1 is in secular equilibrium and its activity ratios are thus known to be 1. 1643 HU-1 standards measured between 2018 and 2021 were employed as presented in Table B.1. In total, 1726 standards were measured. For uncertainty determination, both the ^{238}U concentration as well as ^{238}Th/^{238}U were filtered by excluding measurements outside the 2σ band. All measurements that did not pass either of the filters were discarded.

Isotope	^{233}U	^{236}UU	229Th
Concentration	(0.038556 ± 0.0000009) ng/g	(3.86778 ± 0.00009) ng/g	(0.018055 ± 0.000008) ng/g

Table B.1: Concentrations and 2 standard mean error derived from the 1643 HU-1 standard measurements.

Measurement protocol and performance

FCs	L4	L3	L2	L1	CC	H1	H2	H3	H4
Multiplier					SEM				
Resistor	$10^{11}\Omega$	$10^{11}\Omega$	$10^{11}\Omega$	$10^{11}\Omega$	$10^{13}\Omega$	$10^{11}\Omega$	$10^{11}\Omega$	$10^{10}\Omega$	$10^{11}\Omega$

Table B.2: Detector configuration (CC – centre cup, L – low mass and H – high mass cups compared to the centre).

Amplifier	Signal	Fade-out time
$10^{10}\Omega$	50 V	(1.21 ± 0.13) s
	100 V	(1.07 ± 0.13) s
$10^{11}\Omega$	0.3 V	(1.14 ± 0.13) s
	0.7 V	(1.07 ± 0.13) s
	15 V	(1.41 ± 0.13) s
$10^{13}\Omega$	2.5 mV	(2.95 ± 0.13) s
	4.5 mV	(2.58 ± 0.27) s
	8.9 mV	(4.06 ± 0.13) s

Table B.3: Fade-out times for the three different ohmic resistors. The uncertainties are given as one integration time, thus the "time resolution" of the measurement. Each measurement was repeated twice to see if results agree with one another. This was the case for all measurements except for the 4.5 mV signal on the $10^{13}\Omega$. Hence this measurement was repeated three times and the uncertainty denoted is the population standard deviation of those three values.

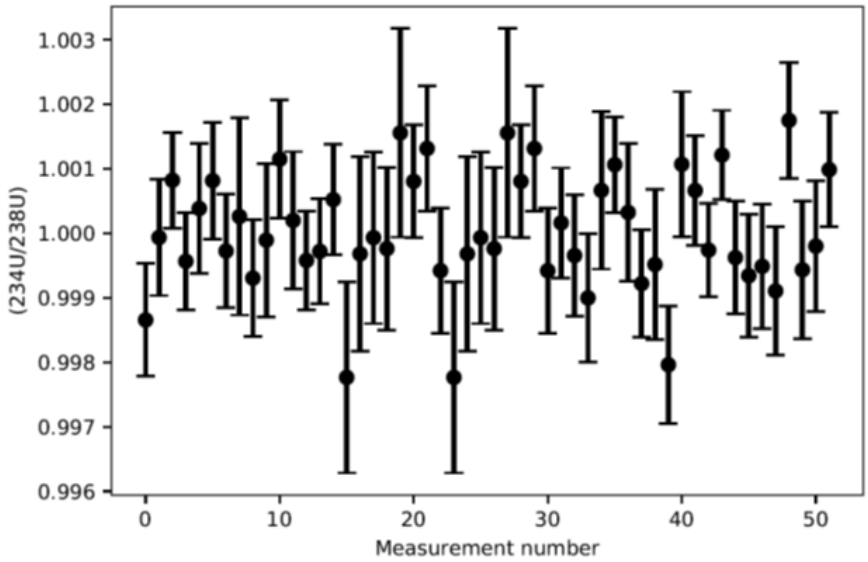

Figure B.1: ($^{234}U/^{238}U$) measurements of HU-1 reference material on 6 measurement days in October 2022

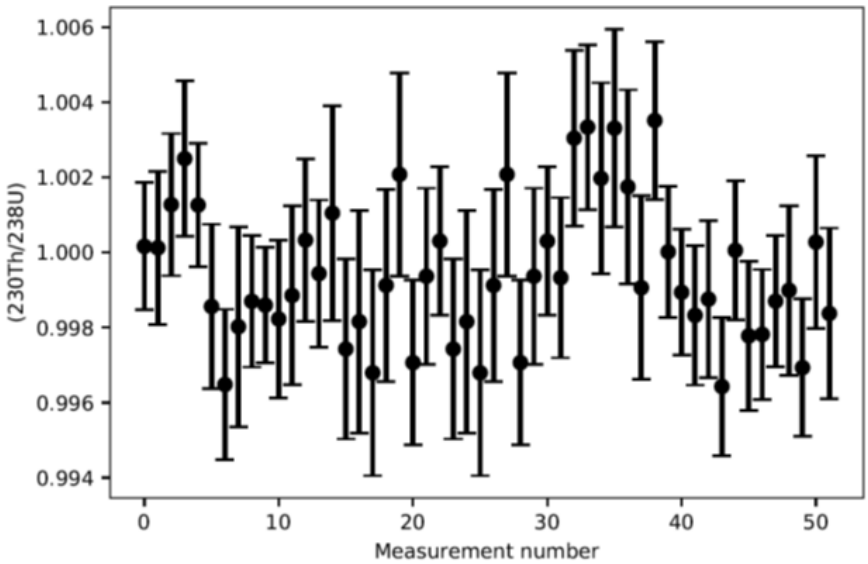

Figure B.2: ($^{230}Th/^{238}U$) measurements of HU-1 reference material on 6 measurement days in October 2022

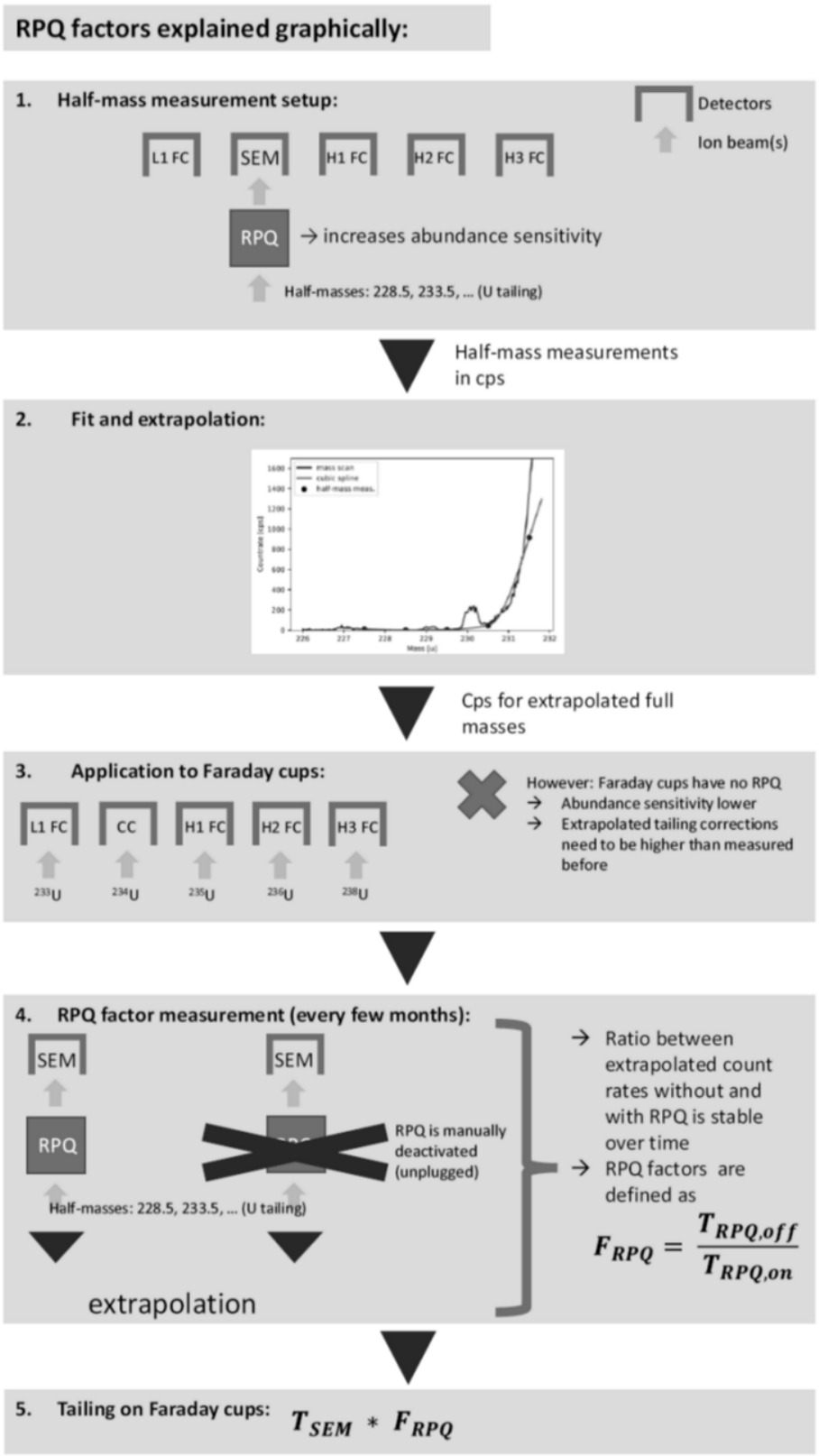

Figure B.3: Graphical explanation of RPQ factors

B.2 Data for Chapters 4 and 5

The data visible in the screenshots (Fig. 5.1 to 5.3) were provided by S. Warken and will be published with the manuscript around Chapter 5.

Lab Code	Sample	^{238}U (μg/g)	^{232}Th (ng/g)	δ^{234}U (‰)	^{230}Th/^{238}U	^{230}Th/^{232}Th	Age (a)	BC age (a)
IUP-11918A	CPR-40mm	2.56613 ± 0.00013	0.191 ± 0.017	145.95 ± 0.74	0.000434 ± 0.000038	17.9 ± 2.3	36.7 ± 4.3	31
IUP-11919	BOC2-35mm	2.49605 ± 0.00023	0.03244 ± 0.00057	145.07 ± 0.48	0.000138 ± 0.000012	32.5 ± 2.9	12.3 ± 1.2	11

Table B.4: Activity ratios and concentrations for the ages of the coral samples presented in Table 4.2, with ^{230}Th/U and band-counting ages. The reported uncertainties are all 2 σ uncertainties. The detrital contamination correction assumes a bulk earth Th/U weight ratio of (4.10 ± 2.05) and the decay chain in secular equilibrium (Wedepohl, 1995). As a detrital thorium correction factor, (2 ± 1) was selected. The ages refer to the time of measurement (March 2023). They were calculated using the half-lives of Cheng et al. (2013) and the final age errors do not include half-life uncertainties.

Lab.No.	Sample ID	^{238}U	$^{238}U_{err}$	^{232}Th	$^{232}Th_{err}$	$^{230}Th/^{238}U$	$^{230}Th/^{238}U_{err}$	$^{230}Th/^{232}Th$	$^{230}Th/^{232}Th_{err}$	$Age_{u.}$	err.	$Age_{c.}$	err
		(μg/g)	(μg/g)	(ng/g)	(ng/g)					ka	ka	ka	ka
11849	Crm112Aspiked	1.271158	0.000128	0.006485	0.000097	0.000817	0.000025	492.7	17.0	0.0924	0.0029	0.0923	0.0029
12108	JRC	0.427078	0.000023	0.003458	0.000021	0.000104	0.000014	39.5	5.1	0.0113	0.0015	0.0111	0.0015
11849	Crm112Aspiked	1.271059	0.000132	0.006355	0.000081	0.000792	0.000019	487.2	13.3	0.0898	0.0022	0.0896	0.0022
12108	JRC	0.426992	0.000030	0.003522	0.000023	0.000118	0.000016	44.1	5.8	0.0129	0.0017	0.0127	0.0017
11849	Crm112Aspiked	1.270769	0.000125	0.006459	0.000066	0.000773	0.000023	468.0	14.6	0.0875	0.0025	0.0873	0.0026
12108	JRC	0.426983	0.000032	0.003495	0.000032	0.000113	0.000017	42.6	6.2	0.0124	0.0018	0.0121	0.0018
11849	Crm112Aspiked	1.271784	0.000129	0.005618	0.000077	0.000745	0.000023	517.8	17.2	0.0843	0.0025	0.0842	0.0026
12108	JRC	0.427340	0.000028	0.003485	0.000035	0.000138	0.000019	52.0	7.2	0.015	0.0021	0.0148	0.0021
11849	Crm112Aspiked	1.270959	0.000144	0.005573	0.000069	0.000774	0.000019	542.3	15.2	0.0877	0.0022	0.0876	0.0022
12108	JRC	0.427267	0.000025	0.003570	0.000034	0.000110	0.000016	40.3	6.0	0.012	0.0018	0.0117	0.0018
11849	Crm112Aspiked	1.270697	0.000097	0.005584	0.000065	0.000785	0.000015	549.0	12.3	0.089	0.0017	0.0889	0.0017
12108	JRC	0.427233	0.000022	0.003514	0.000035	0.000102	0.000013	38.2	4.7	0.0112	0.0014	0.0109	0.0014

Table B.5: Activity ratios and concentrations for the ages of the reference materials presented in Table 4.1. The reported uncertainties are all 2 σ uncertainties. The detrital contamination correction assumes a bulk earth Th/U weight ratio of (4.10 ± 2.05) and the decay chain in secular equilibrium (Wedepohl, 1995). As a detrital thorium correction factor, (0.750 ± 0.375) was selected. However, the effect is minor because the thorium concentration is very low. The ages refer to the time of measurement (May/ June 2023). They were calculated using the half-lives of Cheng et al. (2013) and the final age errors do not include half-life uncertainties. The first block corresponds to the first measurement day (30.05.2023), and the second to 01.06.2023.

B.3 Cold-water coral dataset

The original data compilation has been provided by C. Wienberg and then extended.
All tables in the following present the sample-IDs, their position (core/ surface sample), the dating technique, the labcode, the age in yrs BP with its error and the references.

Two sets of unpublished data are included, for which only the unique lab identifiers and sample-IDs, but no ages are presented. Almost all unpublished measurements have been carried out at the facility at IUP Heidelberg (Norbert Frank).
The set "Beisel (unpublished)" (Table B.6) was provided by E. Beisel and will be published either with the manuscript on Chapter 6 or with her dissertation. The crews, captains and scientific staff of the RV Pelagia cruises 64PE284 (Chief scientist: Dierk Hebbeln), 64PE229 (Chief scientist: Furu Mienis) and the RV Maria S. Merian cruise MSM36 (Chief scientist: Dierk Hebbeln) are thanked for the collection of samples.
The set "unpublished*" (Table B.7) was provided by C. Wienberg and H. Fink and will be published with the manuscript on Chapter 6. The crews, captains and scientific staff of the RV Marion Dufresne cruise MD194 (Chief scientist: David Van Rooij) and the RV Prof. Logachev cruise TTR-17 Leg 1 (Chief scientist: Menchu Comas) are thanked for the collection of samples.

Gulf of Cadiz

No.	Sample-ID	Position	Method	Labcode	Age (yr BP)	error	Reference
1	B09 1404	surface	U/Th	GIF	40600	760	Frank et al. (2011)
2	B09 1405	surface	U/Th	GIF	14340	510	Frank et al. (2011)
3	B09 1405	surface	U/Th	GIF	15200	380	Frank et al. (2011)
4	B09 1405	surface	U/Th	GIF	19640	500	Frank et al. (2011)
5	B09 1406	surface	U/Th	GIF	12030	350	Frank et al. (2011)
6	B09 1406	surface	U/Th	GIF	12430	810	Frank et al. (2011)
7	B09 1408	surface	U/Th	GIF	14140	590	Frank et al. (2011)
8	B09 1408	surface	U/Th	GIF	15100	380	Frank et al. (2011)
9	CP21	surface	14C	GIF	11462	90	Taviani et al. (1991)
10	CP54	surface	14C	GIF	30391	550	Taviani et al. (1991)
11	DR22	surface	14C	GIF	15734	150	Taviani et al. (1991)
12	DR51	surface	14C	GIF	31161	1000	Taviani et al. (1991)
13	GeoB 12102	core	U/Th	GIF-1529	57960	740	Wienberg et al. (2010)
14	GeoB 12103	core	U/Th	GIF-1530	22880	380	Wienberg et al. (2010)
15	GeoB 12103	core	U/Th	GIF	24800	300	Frank et al. (2011)
16	GeoB 12103	core	U/Th	GIF-1392	25720	390	Wienberg et al. (2010)
17	GeoB 12103	core	U/Th	GIF-1531	29980	1260	Wienberg et al. (2010)
18	GeoB 12103	core	U/Th	GIF-1532	30340	960	Wienberg et al. (2010)
19	GeoB 12103	core	U/Th	GIF-1533	49850	800	Wienberg et al. (2010)
20	GeoB 12104	core	U/Th	GIF-1387	23570	180	Wienberg et al. (2010)
21	GeoB 9070	core	14C	KIA-29032	23304	90	Wienberg et al. (2009)
22	GeoB 9070	core	U/Th	GEOMAR	23500	120	Wienberg et al. (2010)
23	GeoB 9070	core	U/Th	GEOMAR	43680	280	Wienberg et al. (2010)
24	GeoB 9070	core	14C	KIA-29031	44967	1110	Wienberg et al. (2009)
25	M2004-02	core	U/Th	GIF-1631	9144	717	Wienberg et al. (2010)
26	M2004-02	core	U/Th	GIF-1632	19308	560	Wienberg et al. (2010)
27	M2004-02	core	U/Th	GIF-1633	19801	540	Wienberg et al. (2010)
28	M2004-02	core	U/Th	GIF-1634	20972	550	Wienberg et al. (2010)
29	M2004-02	core	U/Th	GIF-1635	22563	320	Wienberg et al. (2010)
30	M2004-02	core	U/Th	GIF-1636	23920	260	Wienberg et al. (2010)
31	M2004-02	core	U/Th	GIF-1637	34866	440	Wienberg et al. (2010)
32	M2004-02	core	U/Th	GIF-1638	35991	500	Wienberg et al. (2010)
33	M2005-15	core	14C	KIA-33751	12598	60	Wienberg et al. (2009)
34	M2005-15	core	14C	KIA-33750	22537	130	Wienberg et al. (2009)
35	M2005-31	core	U/Th	GIF	15210	230	Frank et al. (2011)
36	MD08-3212	core	U/Th	GIF	11080	230	Frank et al. (2011)
37	MD08-3212	core	U/Th	GIF	14330	690	Frank et al. (2011)
38	MD08-3212	core	U/Th	GIF	34860	920	Frank et al. (2011)
39	MD08-3212	core	U/Th	GIF	35130	1360	Frank et al. (2011)
40	MD08-3231	core	U/Th	GIF	14782	400	Frank et al. (2011)
41	MD08-3231	core	U/Th	GIF	22052	750	Frank et al. (2011)
42	MD08-3231	core	U/Th	GIF	24727	280	Frank et al. (2011)
43	MD08-3231	core	U/Th	GIF	25491	400	Frank et al. (2011)
44	MD08-3231	core	U/Th	GIF	27792	400	Frank et al. (2011)
45	MD08-3231	core	U/Th	GIF	28839	330	Frank et al. (2011)
46	MD08-3231	core	U/Th	GIF	28900	500	Frank et al. (2011)
47	MD08-3231	core	U/Th	GIF	29551	460	Frank et al. (2011)
48	MD08-3231	core	U/Th	GIF	35169	1260	Frank et al. (2011)
49	MD08-3231	core	U/Th	GIF	35199	570	Frank et al. (2011)
50	MD08-3231	core	U/Th	GIF	37353	700	Frank et al. (2011)
51	GeoB 12712-2	core	U/Th	GIF-1781	34550	870	Frank et al. (2011)
52	GeoB 12740-1	core	U/Th	GIF-1714	14340	320	Frank et al. (2011)
53	GeoB 12740-1	core	U/Th	GIF-1715	25017	440	Frank et al. (2011)
54	GeoB 12740-1	core	U/Th	GIF-1716	32719	720	Frank et al. (2011)
55	GeoB 12740-1	core	U/Th	GIF-1845	41258	380	Frank et al. (2011)

Table B.6: Data table for the Gulf of Cadiz, which continues on the next two pages. For description and details (including on the Beisel (unpublished) dataset) see start of the section.

No.	Sample-ID	Position	Method	Labcode	Age (yr BP)	error	Reference
56	GeoB 9018	core	U/Th	GEOMAR	14650	90	Wienberg et al. (2010)
57	GeoB 9022-1	surface	14C	KIA-24263	27810	275	Wienberg et al. (2009)
58	GeoB 9022-1	surface	U/Th	GIF-1378	31193	230	Frank et al. (2011)
59	GeoB 9022-1	surface	14C	KIA-24262	32487	410	Wienberg et al. (2009)
60	GeoB 9022-1	surface	14C	KIA-24275	32742	415	Wienberg et al. (2009)
61	GeoB 9022-1	surface	14C	KIA-25832	33440	430	Wienberg et al. (2009)
62	GeoB 9022-1	surface	14C	KIA-24267	34179	480	Wienberg et al. (2009)
63	GeoB 9022-1	surface	U/Th	GIF-1379	35373	280	Frank et al. (2011)
64	GeoB 9022-1	surface	14C	KIA-24265	43306	1500	Wienberg et al. (2009)
65	GeoB 9022-1	surface	14C	KIA-24266	43447	1630	Wienberg et al. (2009)
66	GeoB 12722-2	core	U/Th	GIF-1848	32371	390	Frank et al. (2011)
67	GeoB 12743-1	core	U/Th	GIF-1711	27494	580	Frank et al. (2011)
68	GeoB 12743-1	core	U/Th	GIF-1712	30658	400	Frank et al. (2011)
69	GeoB 12743-1	core	U/Th	GIF-1713	53659	1800	Frank et al. (2011)
70	GeoB18141-1_P1_1	core	U/Th	IUP_7545	18033	104	Hemsing (2017)
71	GeoB18141-1_P1_1	core	U/Th	IUP_7547	19728	183	Hemsing (2017)
72	GeoB18141-1_P1_1	core	U/Th	IUP_7550	19809	229	Hemsing (2017)
73	GeoB18141-1_P1_1	core	U/Th	IUP_7546	19853	201	Hemsing (2017)
74	GeoB18141-1_P2_1	core	U/Th	IUP_7555	20055	881	Hemsing (2017)
75	GeoB18141-1_P1_1	core	U/Th	IUP_7549	20237	247	Hemsing (2017)
76	GeoB18141-1_P1_1	core	U/Th	IUP_7548	20784	218	Hemsing (2017)
77	GeoB18141-1_P2_1	core	U/Th	IUP_7554	20977	128	Hemsing (2017)
78	GeoB18141-1_P1_2	core	U/Th	IUP_7552	21062	180	Hemsing (2017)
79	GeoB18141-1_P1_2	core	U/Th	IUP_7551	21066	155	Hemsing (2017)
80	GeoB18141-1_P1_CC	core	U/Th	IUP_7553	21430	159	Hemsing (2017)
81	GeoB18141-1_P2_1	core	U/Th	IUP_7556	21910	140	Hemsing (2017)
82	GeoB18141-1_P3_1	core	U/Th	IUP_7558	22767	240	Hemsing (2017)
83	GeoB18141-1_P3_1	core	U/Th	IUP_7557	22994	134	Hemsing (2017)
84	GeoB18141-1_P3_1	core	U/Th	IUP_7559	23319	136	Hemsing (2017)
85	GeoB18141-1_P3_1	core	U/Th	IUP_7560	24553	157	Hemsing (2017)
86	GeoB18141-1_P3_1	core	U/Th	IUP_7562	24830	189	Hemsing (2017)
87	GeoB18141-1_P3_CC	core	U/Th	IUP_6991	26445	385	Hemsing (2017)
88	GeoB18141-1_P3_CC	core	U/Th	IUP_7563	30691	244	Hemsing (2017)
89	GeoB18141-1_P4_1	core	U/Th	IUP_7564	32829	412	Hemsing (2017)
90	GeoB18141-1_P4_1	core	U/Th	IUP_7565	33808	402	Hemsing (2017)
91	GeoB18141-1_P4_1	core	U/Th	IUP_7566	34206	372	Hemsing (2017)
92	GeoB18141-1_P4_CC	core	U/Th	IUP_7567	39969	390	Hemsing (2017)
93	GeoB18141-1_P5_1	core	U/Th	IUP_7568	44071	494	Hemsing (2017)
94	GeoB18141-1_P5_1	core	U/Th	IUP_7569	47120	550	Hemsing (2017)
95	GeoB18141-1_P5_1	core	U/Th	IUP_7570	51458	2358	Hemsing (2017)
96	GeoB18141-1_P5_1	core	U/Th	IUP_7573	53540	187	Hemsing (2017)
97	GeoB18141-1_P5_1	core	U/Th	IUP_7571	55066	194	Hemsing (2017)
98	GeoB18141-1_P5_1	core	U/Th	IUP_7572	56696	153	Hemsing (2017)
99	GeoB18141-1_P5_CC	core	U/Th	IUP_7574	59651	155	Hemsing (2017)
100	GeoB18141-1_P6_1	core	U/Th	IUP_7105	64218	522	Hemsing (2017)
101	GeoB18141-1_P6_1	core	U/Th	IUP_7111	65167	244	Hemsing (2017)
102	GeoB18141-1_P6_1	core	U/Th	IUP_7577	65887	233	Hemsing (2017)
103	GeoB18141-1_P6_1	core	U/Th	IUP_7575	66145	243	Hemsing (2017)
104	GeoB18141-1_P6_1	core	U/Th	IUP_7576	66904	245	Hemsing (2017)
105	GeoB18141-1_P5_CC	core	U/Th	IUP_6992	67605	675	Hemsing (2017)
106	GeoB 9032	core	U/Th	GEOMAR	17150	150	Wienberg et al. (2010)
107	GeoB 9031	core	U/Th	GEOMAR	20920	120	Wienberg et al. (2010)
108	GeoB 9031	core	U/Th	GEOMAR	37250	230	Wienberg et al. (2010)
109	GeoB 9032	core	U/Th	GEOMAR	41170	250	Wienberg et al. (2010)
110	GeoB 9031	core	U/Th	GEOMAR	45940	330	Wienberg et al. (2010)
111	GeoB12725-1	core	U/Th	IUP11577			Beisel (unpublished)
112	GeoB12725-1	core	U/Th	11579			Beisel (unpublished)
113	GeoB12725-1	core	U/Th	11580			Beisel (unpublished)
114	GeoB12725-1	core	U/Th	11581			Beisel (unpublished)
115	GeoB18139-1	core	U/Th	11573			Beisel (unpublished)
116	GeoB 18139-1	core	U/Th	11877			Beisel (unpublished)

No.	Sample-ID	Position	Method	Labcode	Age (yr BP)	error	Reference
117	GeoB18139-2	core	U/Th	11878			Beisel (unpublished)
118	GeoB 18139-2	core	U/Th	11879			Beisel (unpublished)
119	GeoB18139-3	core	U/Th	11880			Beisel (unpublished)
120	GeoB 18139-3	core	U/Th	11881			Beisel (unpublished)
121	GeoB18139-4	core	U/Th	11882			Beisel (unpublished)
122	GeoB 18139-4	core	U/Th	11884			Beisel (unpublished)
123	GeoB18139-5	core	U/Th	11574			Beisel (unpublished)
124	GeoB 18139-5	core	U/Th	11898			Beisel (unpublished)
125	GeoB18139-6	core	U/Th	11885			Beisel (unpublished)
126	GeoB 18139-6	core	U/Th	11886			Beisel (unpublished)
127	GeoB18139-7	core	U/Th	11887			Beisel (unpublished)
128	GeoB 18139-7	core	U/Th	11888			Beisel (unpublished)
129	GeoB18139-8	core	U/Th	11889			Beisel (unpublished)
130	GeoB 18139-8	core	U/Th	11890			Beisel (unpublished)
131	GeoB18139-9	core	U/Th	11891			Beisel (unpublished)
132	GeoB 18139-9	core	U/Th	11575			Beisel (unpublished)
133	GeoB18139-10	core	U/Th	11576			Beisel (unpublished)
134	GeoB 18139-10	core	U/Th	11578			Beisel (unpublished)
135	GeoB12740-1	core	U/Th	11612			Beisel (unpublished)
136	GeoB12740-1	core	U/Th	11617			Beisel (unpublished)
137	GeoB12740-1	core	U/Th	11613			Beisel (unpublished)
138	GeoB12740-1	core	U/Th	11619			Beisel (unpublished)
139	GeoB12740-1	core	U/Th	11618			Beisel (unpublished)
140	GeoB12740-1	core	U/Th	11614			Beisel (unpublished)
141	GeoB12740-1	core	U/Th	11620			Beisel (unpublished)
142	GeoB12740-1	core	U/Th	11624			Beisel (unpublished)
143	GeoB12740-1	core	U/Th	11622			Beisel (unpublished)
144	GeoB12740-1	core	U/Th	11623			Beisel (unpublished)
145	GeoB12740-1	core	U/Th	11621			Beisel (unpublished)
146	GeoB12740-1	core	U/Th	11625			Beisel (unpublished)
147	GeoB12740-1	core	U/Th	11626			Beisel (unpublished)
148	GeoB12740-1	core	U/Th	11615			Beisel (unpublished)
149	GeoB12740-1	core	U/Th	11627			Beisel (unpublished)
150	GeoB12740-1	core	U/Th	11616			Beisel (unpublished)
151	GeoB12740-1	core	U/Th	11629			Beisel (unpublished)
152	GeoB12740-1	core	U/Th	11628			Beisel (unpublished)
153	GeoB12740-1	core	U/Th	11582			Beisel (unpublished)
154	GeoB12740-1	core	U/Th	11583			Beisel (unpublished)
155	GeoB12740-1	core	U/Th	11584			Beisel (unpublished)
156	M2004-02 PC		U/Th	11662			Beisel (unpublished)
157	M2004-02 PC		U/Th	11663			Beisel (unpublished)
158	M2004-02 PC		U/Th	11664			Beisel (unpublished)
159	M2004-02 PC		U/Th	11665			Beisel (unpublished)
160	M2004-02 PC		U/Th	11666			Beisel (unpublished)
161	M2004-02 PC		U/Th	11667			Beisel (unpublished)
162	M2004-02 PC		U/Th	11668			Beisel (unpublished)

Alboran Sea

No.	Sample-ID	Position	Species	Method	Labcode	Age (yr BP)	error	Reference
1	GeoB 13747-1_A	surface	Mo	14C	UCIAMS-67196	3433	15	Fink et al. (2015)
2	VB7R	?	Lp	U/Th	GIF	4970	440	Frank et al. (2011)
3	VB7R	?	Mo	U/Th	GIF	5600	250	Frank et al. (2011)
4	3048	?	Lp	U/Th	IUPH	8500	115	Schröder-Ritzrau et al. (2005)
5	GeoB 13748-1_A	surface	Lp	14C	UCIAMS-67197	9432	20	Fink et al. (2015)
6	COBAS-33LO	surface	Lp	U/Th	Canberra	10970	100	McCulloch et al. (2010)
7	COBAS-33LY	surface	Lp	U/Th	Canberra	11170	80	McCulloch et al. (2010)
8	VB7R	?	Lp	U/Th	GIF	11230	330	Frank et al. (2011)
9	GeoB 13711-1_A	surface	Mo	14C	UCIAMS-67184	11071	25	Fink et al. (2015)
10	GeoB 13712-1_A	surface	Mo	14C	UCIAMS-67050	11199	30	Fink et al. (2015)
11	GeoB 13712-1_B	surface	Lp	14C	UCIAMS-67051	9469	25	Fink et al. (2015)
12	GeoB 13714-1_A	surface	Mo	14C	UCIAMS-67053	8874	20	Fink et al. (2015)
13	GeoB 13714-1_B	surface	Lp	14C	UCIAMS-67054	11229	25	Fink et al. (2015)
14	GeoB 13717#1_A	surface	Mo	14C	UCIAMS-67055	9553	25	Fink et al. (2015)
15	GeoB 13718-2_A	surface	Mo	14C	UCIAMS-67058	9670	25	Fink et al. (2015)
16	GeoB 13718-3_A	surface	Lp	14C	UCIAMS-67059	9004	25	Fink et al. (2015)
17	GeoB 13751#1_B	surface	Lp	14C	UCIAMS-67061	208	15	Fink et al. (2015)
18	GeoB 13751#2_A	surface	Mo	14C	UCIAMS-67062	409	20	Fink et al. (2015)
19	GeoB 13751#4_A	surface	Mo	14C	UCIAMS-67063	502	15	Fink et al. (2015)
20	GeoB 13753-1_A	surface	Lp	14C	UCIAMS-67064	4883	15	Fink et al. (2015)
21	GeoB 13754-2_A	surface	Lp	14C	UCIAMS-67066	594	20	Fink et al. (2015)
22	GeoB 13755-1_A	surface	Mo	14C	UCIAMS-67067	5135	20	Fink et al. (2015)
23	GeoB 13759-1_A	surface	Lp	14C	UCIAMS-67068	10758	25	Fink et al. (2015)
24	GeoB 13727#1_A	surface	Lp	14C	UCIAMS-67077	339	15	Fink et al. (2013)
25	GeoB 13727#2_A	surface	Mo	14C	UCIAMS-67078	2352	20	Fink et al. (2013)
26	GeoB 13728-1_A	surface	Mo	14C	UCIAMS-67187	2649	15	Fink et al. (2013)
27	GeoB 13728-1_B	surface	Lp	14C	UCIAMS-67188	2700	15	Fink et al. (2013)
28	GeoB 13728-2	core	Lp	14C	UCIAMS-73567	2911	20	Fink et al. (2013)
29	GeoB 13728-2	core	Lp	14C	UCIAMS-96720	11255	20	Fink et al. (2013)
30	GeoB 13728-2	core	Lp	14C	UCIAMS-96721	12769	25	Fink et al. (2013)
31	GeoB 13728-2	core	Lp	14C	UCIAMS-96722	12836	25	Fink et al. (2013)
32	GeoB 13728-2	core	Lp	14C	UCIAMS-73568	12867	30	Fink et al. (2013)
33	GeoB 13728-2	core	Lp	14C	UCIAMS-73569	13194	30	Fink et al. (2013)
34	GeoB 13729-1	core	Lp	14C	UCIAMS-73570	9801	30	Fink et al. (2013)
35	GeoB 13729-1	core	Lp	14C	UCIAMS-73571	10177	25	Fink et al. (2013)
36	GeoB 13729-1	core	Lp	14C	UCIAMS-73572	10606	25	Fink et al. (2013)
37	GeoB 13729-1	core	Lp	14C	UCIAMS-73573	10903	30	Fink et al. (2013)
38	GeoB 13729-1	core	Lp	14C	UCIAMS-73574	11210	30	Fink et al. (2013)
39	GeoB 13730-1	core	Lp	14C	UCIAMS-73575	2567	25	Fink et al. (2013)
40	GeoB 13730-1	core	Lp	14C	UCIAMS-73576	10600	25	Fink et al. (2013)
41	GeoB 13730-1	core	Lp	14C	UCIAMS-73577	10723	25	Fink et al. (2013)
42	GeoB 13730-1	core	Lp	14C	UCIAMS-73578	11213	25	Fink et al. (2013)
43	GeoB 13730-1	core	Lp	14C	UCIAMS-96723	11437	20	Fink et al. (2013)
44	GeoB 13730-1	core	Lp	14C	UCIAMS-96724	12790	20	Fink et al. (2013)
45	GeoB 13730-1	core	Lp	14C	UCIAMS-73579	13298	30	Fink et al. (2013)
46	GP21	core	Lp	U/Th		13900	60	Dubois-Dauphin (2016)
47	GP21	core	Lp	U/Th		28560	90	Dubois-Dauphin (2016)
48	GP21	core	Lp	U/Th		43040	120	Dubois-Dauphin (2016)
49	MD13-3455G	core	Mo	U/Th	IUP-8487	2328	13	Fentimen et al. (2020)
50	MD13-3455G	core	Lp	U/Th	IUP-8488	6759	24	Fentimen et al. (2020)
51	MD13-3455G	core	Lp	U/Th	IUP-8489	13725	49	Fentimen et al. (2020)
52	MD13-3455G	core	Lp	U/Th	IUP-8490	14501	54	Fentimen et al. (2020)
53	MD13-3455G	core	Lp	U/Th	IUP-8491	14519	52	Fentimen et al. (2020)
54	MD13-3455G	core	Lp	U/Th	IUP-8492	14747	52	Fentimen et al. (2020)
55	GeoB 13725-2_A	surface	Mo	14C	UCIAMS-67076	5201	15	Fink et al. (2013)
56	GeoB 13735-1_A	surface	Mo	14C	UCIAMS-67190	3770	15	Fink et al. (2013)
57	GeoB 13737#1_A	surface	Lp	14C	UCIAMS-67192	13460	35	Fink et al. (2013)
58	GeoB 13737#2_A	surface	Lp	14C	UCIAMS-67193	12995	30	Fink et al. (2013)
59	GeoB 13722-3_A	surface	Mo	14C	UCIAMS-67069	3014	15	Fink et al. (2013)
60	GeoB 13722-3_C	surface	Mo	14C	UCIAMS-67071	3465	20	Fink et al. (2013)
61	GeoB 13723-1_A	surface	Mo	14C	UCIAMS-67074	4790	20	Fink et al. (2013)
62	GeoB 13723-1_B	surface	Mo	14C	UCIAMS-67075	5389	20	Fink et al. (2013)
63	TTR-401G	core	Mo	14C	ETH-55621	5426	30	Stalder et al. (2015)
64	TTR-401G	core	Mo	14C	ETH-57100	5829	28	Stalder et al. (2015)
65	TTR-401G	core	Mo	14C	ETH-57102	11612	35	Stalder et al. (2015)
66	TTR-401G	core	Lp	14C	ETH-55623	12242	39	Stalder et al. (2015)
67	TTR-401G	core	Lp	14C	ETH-55625	12717	39	Stalder et al. (2015)
68	TTR-401G	core	Lp	14C	ETH-55627	13023	40	Stalder et al. (2015)
69	TTR-401G	core	Mo	14C	ETH-57101	11326	35	Stalder et al. (2015)
70	GeoB18127-1	core	Mo	U/Th	IUP-7734	5452	115	Wang et al. (2019)

Table B.7: Data table for the Alboran Sea, which continues on the next three pages. For description and details (including on the unpublished* dataset) see start of the section.

No.	Sample-ID	Position	Species	Method	Labcode	Age (yr BP)	error	Reference
71	GeoB18127-1	core	Mo	U/Th	IUP-7735	5829	90	Wang et al. (2019)
72	GeoB18127-1	core	Lp	U/Th	IUP-7736	7632	199	Wang et al. (2019)
73	GeoB18127-1	core	Mo	U/Th	IUP-7737	7878	162	Wang et al. (2019)
74	GeoB18127-1	core	Lp	U/Th	IUP-7738	8301	139	Wang et al. (2019)
75	GeoB18127-1	core	Lp	U/Th	IUP-7739	8370	123	Wang et al. (2019)
76	GeoB18127-1	core	Lp	U/Th	IUP-7741	8577	174	Wang et al. (2019)
77	GeoB18127-1	core	Lp	U/Th	IUP-7740	8619	122	Wang et al. (2019)
78	GeoB18127-1	core	Lp	U/Th	IUP-7742	9345	144	Wang et al. (2019)
79	GeoB18127-1	core	Lp	U/Th	IUP-7743	9770	84	Wang et al. (2019)
80	GeoB18127-1	core	Lp	U/Th	IUP-7744	10415	92	Wang et al. (2019)
81	GeoB18127-1	core	Lp	U/Th	IUP-7745	11211	69	Wang et al. (2019)
82	GeoB18127-1	core	Lp	U/Th	IUP-7746	13365	97	Wang et al. (2019)
83	GeoB18127-1	core	Lp	U/Th	IUP-7747	13467	103	Wang et al. (2019)
84	GeoB18127-1	core	Lp	U/Th	IUP-7748	13521	87	Wang et al. (2019)
85	GeoB18127-1	core	Lp	U/Th	IUP-7749	14140	114	Wang et al. (2019)
86	GeoB18130-1	core	Mo	U/Th	IUP-7751	5067	34	Wang et al. (2019)
87	GeoB18130-1	core	Mo	U/Th	IUP-7750	5351	42	Wang et al. (2019)
88	GeoB18130-1	core	Mo	U/Th	IUP-7752	7941	51	Wang et al. (2019)
89	GeoB18130-1	core	Mo	U/Th	IUP-7753	8471	57	Wang et al. (2019)
90	GeoB18130-1	core	Lp	U/Th	IUP-7754	8894	48	Wang et al. (2019)
91	GeoB18130-1	core	Mo	U/Th	IUP-7755	8944	35	Wang et al. (2019)
92	GeoB18130-1	core	Lp	U/Th	IUP-7756	9134	53	Wang et al. (2019)
93	GeoB18130-1	core	Lp	U/Th	IUP-7759	9440	52	Wang et al. (2019)
94	GeoB18130-1	core	Lp	U/Th	IUP-7758	9448	50	Wang et al. (2019)
95	GeoB18130-1	core	Lp	U/Th	IUP-7757	9462	52	Wang et al. (2019)
96	MD13-3451G	core	Mo	14C	Poz-62332	4510	30	Wang et al. (2019)
97	MD13-3451G	core	Lp	14C	Poz-62333	9540	40	Wang et al. (2019)
98	MD13-3451G	core	Lp	14C	Poz-62334	11470	50	Wang et al. (2019)
99	MD13-3451G	core	Lp	14C	Poz-62335	13790	50	Wang et al. (2019)
100	MD13-3452G	core	Mo	14C	Poz-62336	3470	30	Wang et al. (2019)
101	MD13-3452G	core	Mo	14C	Poz-62337	9280	40	Wang et al. (2019)
102	MD13-3452G	core	Mo	14C	Poz-62338	9850	50	Wang et al. (2019)
103	MD13-3452G	core	Lp	14C	Poz-62339	10850	40	Wang et al. (2019)
104	MD13-3452G	core	Mo	14C	Poz-62340	12910	50	Wang et al. (2019)
105	MD13-3452G	core	Lp	14C	Poz-62341	13300	70	Wang et al. (2019)
106	MD13-3452G	core	Lp	14C	Poz-62342	13620	50	Wang et al. (2019)
107	MD13-3452G	core	Lp	14C	Poz-62343	14020	50	Wang et al. (2019)
108	MD3469G	core	Lp	U/Th		9300	90	Corbera et al. (2021)
109	MD3469G	core	Lp	Laser ablation		9310	680	Corbera et al. (2021)
110	MD3469G	core		Laser ablation		9360	600	Corbera et al. (2021)
111	MD3469G	core		Laser ablation		10070	830	Corbera et al. (2021)
112	MD3469G	core		Laser ablation		11580	870	Corbera et al. (2021)
113	MD3469G	core		Laser ablation		12380	900	Corbera et al. (2021)
114	MD3469G	core		Laser ablation		12070	890	Corbera et al. (2021)
115	MD3469G	core		Laser ablation		13190	920	Corbera et al. (2021)
116	MD3469G	core		Laser ablation		13060	920	Corbera et al. (2021)
117	MD3469G	core		Laser ablation		13140	920	Corbera et al. (2021)
118	MD3469G	core	Lp	Laser ablation		12540	900	Corbera et al. (2021)
119	MD3469G	core		Laser ablation		14160	950	Corbera et al. (2021)
120	MD3469G	core		Laser ablation		11690	880	Corbera et al. (2021)
121	MD3469G	core		Laser ablation		13410	920	Corbera et al. (2021)
122	MD3469G	core	Lp	Laser ablation		13470	930	Corbera et al. (2021)
123	MD3470G	core	Mo	Laser ablation		290	600	Corbera et al. (2021)
124	MD3470G	core		Laser ablation		1070	620	Corbera et al. (2021)
125	MD3470G	core		Laser ablation		1620	630	Corbera et al. (2021)
126	MD3470G	core	Lp	U/Th		2710	60	Corbera et al. (2021)
127	MD3470G	core	Lp	Laser ablation		2760	460	Corbera et al. (2021)
128	MD3470G	core		Laser ablation		2980	660	Corbera et al. (2021)
129	MD3470G	core		Laser ablation		3910	680	Corbera et al. (2021)
130	MD3470G	core		Laser ablation		3890	680	Corbera et al. (2021)
131	MD3470G	core	Lp	Laser ablation		4240	690	Corbera et al. (2021)
132	MD3470G	core		Laser ablation		4850	710	Corbera et al. (2021)
133	MD3470G	core		Laser ablation		5520	720	Corbera et al. (2021)
134	MD3470G	core		Laser ablation		5040	710	Corbera et al. (2021)
135	MD3470G	core		Laser ablation		5510	720	Corbera et al. (2021)
136	MD3470G	core		Laser ablation		6260	740	Corbera et al. (2021)
137	MD3470G	core		Laser ablation		5690	720	Corbera et al. (2021)
138	MD3470G	core	Lp	U/Th		6110	60	Corbera et al. (2021)
139	MD3470G	core		Laser ablation		6550	750	Corbera et al. (2021)
140	MD3470G	core		Laser ablation		6570	750	Corbera et al. (2021)

No.	Sample-ID	Position	Species	Method	Labcode	Age (yr BP)	error	Reference
141	MD3470G	core		Laser ablation		7100	760	Corbera et al. (2021)
142	MD3470G	core		Laser ablation		6630	750	Corbera et al. (2021)
143	MD3470G	core		Laser ablation		8070	790	Corbera et al. (2021)
144	MD3470G	core	Lp	Laser ablation		8250	790	Corbera et al. (2021)
145	MD3470G	core		Laser ablation		8570	800	Corbera et al. (2021)
146	MD3470G	core		Laser ablation		9750	830	Corbera et al. (2021)
147	MD3470G	core		Laser ablation		8640	800	Corbera et al. (2021)
148	MD3470G	core		Laser ablation		9770	830	Corbera et al. (2021)
149	MD3470G	core	Lp	Laser ablation		10630	850	Corbera et al. (2021)
150	MD3470G	core		Laser ablation		10660	850	Corbera et al. (2021)
151	MD3470G	core		Laser ablation		11240	870	Corbera et al. (2021)
152	MD3470G	core		Laser ablation		11540	870	Corbera et al. (2021)
153	MD3470G	core		Laser ablation		11810	880	Corbera et al. (2021)
154	MD3470G	core		Laser ablation		11380	870	Corbera et al. (2021)
155	MD3470G	core	Lp	Laser ablation		11180	860	Corbera et al. (2021)
156	MD3470G	core		Laser ablation		11670	880	Corbera et al. (2021)
157	MD3470G	core		Laser ablation		10720	850	Corbera et al. (2021)
158	MD3470G	core		Laser ablation		11480	870	Corbera et al. (2021)
159	MD3470G	core		Laser ablation		11760	880	Corbera et al. (2021)
160	MD3470G	core		Laser ablation		10670	850	Corbera et al. (2021)
161	MD3470G	core	Lp	U/Th		11810	110	Corbera et al. (2021)
162	MD3470G	core		Laser ablation		11260	870	Corbera et al. (2021)
163	MD3470G	core		Laser ablation		11390	910	Corbera et al. (2021)
164	MD3470G	core		Laser ablation		11050	860	Corbera et al. (2021)
165	MD3470G	core		Laser ablation		11240	1100	Corbera et al. (2021)
166	MD3470G	core		Laser ablation		11640	1430	Corbera et al. (2021)
167	MD3470G	core		Laser ablation		12070	890	Corbera et al. (2021)
168	MD3470G	core		Laser ablation		12900	910	Corbera et al. (2021)
169	MD3470G	core		Laser ablation		11480	880	Corbera et al. (2021)
170	MD3470G	core	Lp	Laser ablation		12770	910	Corbera et al. (2021)
171	MD3470G	core		Laser ablation		13600	930	Corbera et al. (2021)
172	MD3470G	core		Laser ablation		13690	940	Corbera et al. (2021)
173	MD3470G	core		Laser ablation		12960	920	Corbera et al. (2021)
174	MD3470G	core	Mo	U/Th		13690	130	Corbera et al. (2021)
175	MD3470G	core	Mo	Laser ablation		14610	1280	Corbera et al. (2021)
176	GeoB18118-1	core		U/Th	IUPH-8063	8550	41	Krengel (2020), Wienberg et al. (2022)
177	GeoB18118-1	core		U/Th	IUPH-8096	8775	26	Krengel (2020), Wienberg et al. (2022)
178	GeoB18118-1	core		U/Th	IUPH-8102	8913	32	Krengel (2020), Wienberg et al. (2022)
179	GeoB18118-1	core		U/Th	IUPH-8076	9101	25	Krengel (2020), Wienberg et al. (2022)
180	GeoB18118-1	core		U/Th	IUPH-8069	8419	44	Krengel (2020), Wienberg et al. (2022)
181	GeoB18118-1	core		U/Th	IUPH-8367	9148	40	Krengel (2020), Wienberg et al. (2022)
182	GeoB18118-1	core		U/Th	IUPH-8369	9285	37	Krengel (2020), Wienberg et al. (2022)
183	GeoB18118-1	core		U/Th	IUPH-8368	9271	29	Krengel (2020), Wienberg et al. (2022)
184	GeoB18118-1	core		U/Th	IUPH-8067	9406	38	Krengel (2020), Wienberg et al. (2022)
185	GeoB18118-1	core		U/Th	IUPH-8066	9497	34	Krengel (2020), Wienberg et al. (2022)
186	GeoB18118-1	core		U/Th	IUPH-8098	9437	33	Krengel (2020), Wienberg et al. (2022)
187	GeoB18118-1	core		U/Th	IUPH-8370	9482	31	Krengel (2020), Wienberg et al. (2022)
188	GeoB18118-1	core		U/Th	IUPH-8371	9625	36	Krengel (2020), Wienberg et al. (2022)
189	GeoB18118-1	core		U/Th	IUPH-8064	9708	29	Krengel (2020), Wienberg et al. (2022)
190	GeoB18118-1	core		U/Th	IUPH-8077	9747	34	Krengel (2020), Wienberg et al. (2022)
191	GeoB18118-1	core		U/Th	IUPH-8100	9794	40	Krengel (2020), Wienberg et al. (2022)
192	GeoB18118-1	core		U/Th	IUPH-8372	10425	58	Krengel (2020), Wienberg et al. (2022)
193	GeoB18118-1	core		U/Th	IUPH-8373	10370	41	Krengel (2020), Wienberg et al. (2022)
194	GeoB18118-1	core		U/Th	IUPH-8099	11080	35	Krengel (2020), Wienberg et al. (2022)
195	GeoB18118-1	core		U/Th	IUPH-8062	11368	43	Krengel (2020), Wienberg et al. (2022)
196	GeoB18118-1	core		U/Th	IUPH-10157	11542	23	Krengel (2020), Wienberg et al. (2022)
197	GeoB18118-1	core		U/Th	IUPH-10158	11624	29	Krengel (2020), Wienberg et al. (2022)
198	GeoB18118-1	core		U/Th	IUPH-10159	10606	97	Krengel (2020), Wienberg et al. (2022)
199	GeoB18118-1	core		U/Th	IUPH-8071	11514	43	Krengel (2020), Wienberg et al. (2022)
200	GeoB18118-1	core		U/Th	IUPH-8376	12852	45	Krengel (2020), Wienberg et al. (2022)
201	GeoB18118-1	core		U/Th	IUPH-8377	12413	36	Krengel (2020), Wienberg et al. (2022)
202	GeoB18118-1	core		U/Th	IUPH-8378	12798	48	Krengel (2020), Wienberg et al. (2022)
203	GeoB18118-1	core		U/Th	IUPH-8379	12993	42	Krengel (2020), Wienberg et al. (2022)
204	GeoB18118-1	core		U/Th	IUPH-8380	13017	57	Krengel (2020), Wienberg et al. (2022)
205	GeoB18118-1	core		U/Th	IUPH-8381	13004	48	Krengel (2020), Wienberg et al. (2022)
206	GeoB18118-1	core		U/Th	IUPH-8097	13164	56	Krengel (2020), Wienberg et al. (2022)
207	GeoB18118-1	core		U/Th	IUPH-8104	13242	49	Krengel (2020), Wienberg et al. (2022)
208	GeoB18118-1	core		U/Th	IUPH-8095	13328	43	Krengel (2020), Wienberg et al. (2022)
209	GeoB18118-1	core		U/Th	IUPH-8093	13306	53	Krengel (2020), Wienberg et al. (2022)
210	GeoB18118-1	core		U/Th	IUPH-8382	13898	58	Krengel (2020), Wienberg et al. (2022)

No.	Sample-ID	Position	Species	Method	Labcode	Age (yr BP)	error	Reference
211	GeoB18118-1	core		U/Th	IUPH-8070	13621	51	Krengel (2020), Wienberg et al. (2022)
212	GeoB18118-1	core		U/Th	IUPH-8383	13647	52	Krengel (2020), Wienberg et al. (2022)
213	GeoB18118-1	core		U/Th	IUPH-8094	14061	44	Krengel (2020), Wienberg et al. (2022)
214	GeoB18118-1	core		U/Th	IUPH-8384	11526	48	Krengel (2020), Wienberg et al. (2022)
215	GeoB18118-1	core		U/Th	IUPH-8072	13444	50	Krengel (2020), Wienberg et al. (2022)
216	GeoB18118-1	core		U/Th	IUPH-8385	13729	64	Krengel (2020), Wienberg et al. (2022)
217	GeoB18118-1	core		U/Th	IUPH-8386	14216	46	Krengel (2020), Wienberg et al. (2022)
218	GeoB18118-1	core		U/Th	IUPH-8075	14424	45	Krengel (2020), Wienberg et al. (2022)
219	GeoB18118-1	core		U/Th	IUPH-8387	14158	49	Krengel (2020), Wienberg et al. (2022)
220	GeoB18118-1	core		U/Th	IUPH-8103	14086	39	Krengel (2020), Wienberg et al. (2022)
221	GeoB18118-1	core		U/Th	IUPH-8080	14314	46	Krengel (2020), Wienberg et al. (2022)
222	GeoB18118-1	core		U/Th	IUPH-8388	14668	79	Krengel (2020), Wienberg et al. (2022)
223	GeoB18118-1	core		U/Th	IUPH-8101	14403	51	Krengel (2020), Wienberg et al. (2022)
224	GeoB18118-1	core		U/Th	IUPH-8389	14717	61	Krengel (2020), Wienberg et al. (2022)
225	GeoB18118-1	core		U/Th	IUPH-8068	14433	49	Krengel (2020), Wienberg et al. (2022)
226	GeoB18118-1	core		U/Th	IUPH-8390	14466	52	Krengel (2020), Wienberg et al. (2022)
227	GeoB18118-1	core		U/Th	IUPH-8074	14408	45	Krengel (2020), Wienberg et al. (2022)
228	GeoB18118-1	core		U/Th	IUPH-8079	14533	56	Krengel (2020), Wienberg et al. (2022)
229	GeoB18118-1	core		U/Th	IUPH-10160	14726	38	Krengel (2020), Wienberg et al. (2022)
230	GeoB18118-1	core		U/Th	IUPH-8392	15051	58	Krengel (2020), Wienberg et al. (2022)
231	GeoB18118-1	core		U/Th	IUPH-8091	14704	89	Krengel (2020), Wienberg et al. (2022)
232	GeoB18118-2	core		U/Th	IUPH-7621	8250	88	Krengel (2020), Wienberg et al. (2022)
233	GeoB18118-2	core		U/Th	IUPH-7626	10226	24	Krengel (2020), Wienberg et al. (2022)
234	GeoB18118-2	core		U/Th	IUPH-7617	10870	130	Krengel (2020), Wienberg et al. (2022)
235	GeoB18118-2	core		U/Th	IUPH-7614	10850	150	Krengel (2020), Wienberg et al. (2022)
^{236}U	GeoB18118-2	core		U/Th	IUPH-7616	10650	150	Krengel (2020), Wienberg et al. (2022)
237	GeoB18118-2	core		U/Th	IUPH-7615	10970	190	Krengel (2020), Wienberg et al. (2022)
238	GeoB18118-2	core		U/Th	IUPH-10161	11048	43	Krengel (2020), Wienberg et al. (2022)
239	GeoB18118-2	core		U/Th	IUPH-7613	10884	97	Krengel (2020), Wienberg et al. (2022)
240	GeoB18118-2	core		U/Th	IUPH-7619	11812	30	Krengel (2020), Wienberg et al. (2022)
241	GeoB18118-2	core		U/Th	IUPH-7610	12560	150	Krengel (2020), Wienberg et al. (2022)
242	GeoB18118-2	core		U/Th	IUPH-7609	13890	260	Krengel (2020), Wienberg et al. (2022)
243	GeoB18118-2	core		U/Th	IUPH-7089	14170	210	Krengel (2020), Wienberg et al. (2022)
244	GeoB18118-2	core		U/Th	IUPH-8364	14572	49	Krengel (2020), Wienberg et al. (2022)
245	GeoB18118-2	core		U/Th	IUPH-6995	15350	250	Krengel (2020), Wienberg et al. (2022)
246	GeoB18120-1	core		U/Th	IUP-9660	4707	16	Wienberg et al. (2022)
247	GeoB18120-1	core		U/Th	IUP-9661	11659	34	Wienberg et al. (2022)
248	GeoB18120-1	core		U/Th	IUP-9662	12452	28	Wienberg et al. (2022)
249	GeoB18120-1	core		U/Th	IUP-9663	1^{236}U9	33	Wienberg et al. (2022)
250	GeoB18120-1	core		U/Th	IUP-9664	12376	37	Wienberg et al. (2022)
251	GeoB18120-1	core		U/Th	IUP-9665	13334	34	Wienberg et al. (2022)
252	GeoB18120-1	core		U/Th	IUP-9666	13347	34	Wienberg et al. (2022)
253	GeoB18120-1	core		U/Th	IUP-9667	13251	36	Wienberg et al. (2022)
254	GeoB18120-1	core		U/Th	IUP-9668	13832	41	Wienberg et al. (2022)
255	MD13-3462G	core		U/Th	IUP-8500	6270	30	Fentimen et al. (2022)
256	MD13-3462G	core		U/Th	IUP-8501	14250	49	Fentimen et al. (2022)
257	MD13-3460G	core	Lp	U/Th	IUPH-6899			unpublished*
258	MD13-3460G	core	Lp	U/Th	IUPH-6900			unpublished*
259	MD13-3460G	core	Lp	U/Th	IUPH-6902			unpublished*
260	MD13-3460G	core	Lp	U/Th	IUPH-6901			unpublished*
261	MD13-3460G	core	Lp	U/Th	IUPH-6903			unpublished*
262	MD13-3460G	core	Lp	U/Th	IUPH-6904			unpublished*
263	MD13-3460G	core	Lp	U/Th	IUPH-6905			unpublished*
264	MD13-3460G	core	Lp	U/Th	IUPH-6906			unpublished*
265	MD13-3460G	core	Lp	U/Th	IUPH-6907			unpublished*
266	MD13-3460G	core	Lp	U/Th	IUPH-6909			unpublished*
267	MD13-3460G	core	Lp	U/Th	IUPH-6908			unpublished*
268	MD13-3467G	core	Lp	U/Th	IUPH-6910			unpublished*
269	MD13-3467G	core	Lp	U/Th	IUPH-6911			unpublished*
270	MD13-3467G	core	Lp	U/Th	IUPH-6913			unpublished*
271	MD13-3467G	core	Lp	U/Th	IUPH-6912			unpublished*
272	TTR-399G	core	Mo	U/Th	GIF-1692			unpublished*
273	TTR-399G	core	Lp	U/Th	GIF-1691			unpublished*
274	TTR-399G	core	Lp	U/Th	GIF-1695			unpublished*
275	TTR-401G	core	Mo	U/Th	GIF-1694			unpublished*

Porcupine Seabight

No.	Sample-ID	Position	Method	Labcode	Age (yr BP)	error	Reference
1	2419	surface	U/Th	IUPH	460	60	Schröder-Ritzrau et al. (2005)
2	2420	surface	U/Th	IUPH	1050	190	Schröder-Ritzrau et al. (2005)
3	3140	surface	U/Th	IUPH	7720	100	Schröder-Ritzrau et al. (2005)
4	GeoB9213-1	core	14C	KIA31267	8288	45	Eisele et al. (2008)
5	GeoB9213-1	core	U/Th	GEOMAR	9172	148	Eisele et al. (2008)
6	GeoB9214-1	core	14C	KIA31264	7221	40	Eisele et al. (2008)
7	GeoB9214-1	core	U/Th	GEOMAR	8683	160	Eisele et al. (2008)
8	GeoB9214-1	core	14C	KIA31261	8598	45	Eisele et al. (2008)
9	GeoB9214-1	core	U/Th	GIF-1381	10356	87	Van der Land et al. (2014)
10	GeoB9223-1	core	14C	KIA31266	5564	35	Eisele et al. (2008)
11	IODP 1317	core	U/Th	900-09/650-10	1240	30	Raddatz et al. (2014)
12	MD01-2451G	core	U/Th	GIF	3233	106	Frank et al. (2009)
13	MD01-2451G	core	U/Th	GIF	6110	153	Frank et al. (2009)
14	MD01-2451G	core	U/Th	GIF	6520	140	Frank et al. (2009)
15	MD01-2463G	core	U/Th	GIF	261	33	Frank et al. (2009)
16	MD01-2463G	core	14C	GIF	851	99	Frank et al. (2009)
17	MD01-2463G	core	14C	GIF	6811	88	Frank et al. (2009)
18	MD01-2463G	core	U/Th	GIF	9810	220	Frank et al. (2009)
19	MD01-2463G	core	U/Th	GIF	9700	350	Frank et al. (2009)
20	GeoB9212-1	core	14C	KIA31268	3181	40	Wienberg et al. (2020)
21	GeoB9213-1	core	14C	BETA 340729	3043	30	Wienberg et al. (2020)
22	GeoB9213-1	core	U/Th	GIF-3058	5691	55	Wienberg et al. (2020)
23	GeoB9213-1	core	U/Th	GIF-3059	6640	45	Wienberg et al. (2020)
24	GeoB9213-1	core	U/Th	Gif-3060	9258	71	Wienberg et al. (2020)
25	GeoB9214-1	core	14C	BETA 340730	974	30	Wienberg et al. (2020)
26	GeoB14530-1	core	U/Th	GIF-6065	1016	46	Wienberg et al. (2020)
27	GeoB14530-1	core	14C	BETA 340735	6478	30	Wienberg et al. (2020)
28	GeoB14530-1	core	U/Th	GIF-3066	11353	92	Wienberg et al. (2020)
29	GeoB14531-1	core	U/Th	GIF-3054	415	15	Wienberg et al. (2020)
30	GeoB14531-1	core	U/Th	GIF-3055	4290	27	Wienberg et al. (2020)
31	GeoB14531-1	core	14C	BETA 340736	6333	30	Wienberg et al. (2020)
32	GeoB14531-1	core	U/Th	GIF-3057	8922	59	Wienberg et al. (2020)
33	GeoB14531-1	core	U/Th	GIF-3056	9382	44	Wienberg et al. (2020)
34	GeoB14532-2	core	U/Th	GIF-3069	2987	31	Wienberg et al. (2020)
35	GeoB14532-2	core	U/Th	GIF-3067	4901	89	Wienberg et al. (2020)
36	GeoB14532-2	core	U/Th	GIF-3068	5634	43	Wienberg et al. (2020)
37	GeoB14511-1	surface	14C	BETA 344865	246	35	Wienberg et al. (2020)
38	GeoB14511-1	surface	14C	BETA 340732	468	30	Wienberg et al. (2020)
39	GeoB14511-1	surface	14C	BETA 344863	468	30	Wienberg et al. (2020)
40	GeoB14511-1	surface	14C	BETA 344862	499	30	Wienberg et al. (2020)
41	GeoB14511-1	surface	14C	BETA 340731	605	30	Wienberg et al. (2020)
42	GeoB14511-1	surface	14C	BETA 344866	703	30	Wienberg et al. (2020)
43	GeoB14511-1	surface	14C	BETA 344864	1050	30	Wienberg et al. (2020)
44	GeoB14511-1	surface	14C	BETA 340733	1314	30	Wienberg et al. (2020)
45	GeoB14518-1	core	U/Th	GIF-3063	347	29	Wienberg et al. (2020)
46	GeoB14518-1	core	14C	BETA 340734	2371	30	Wienberg et al. (2020)
47	GeoB14518-1	core	U/Th	GIF-3051	4197	36	Wienberg et al. (2020)
48	GeoB14518-1	core	U/Th	GIF-3052	6493	52	Wienberg et al. (2020)
49	GeoB14518-1	core	U/Th	IUPH6142	7810	160	Wienberg et al. (2020)
50	GeoB14518-1	core	U/Th	GIF-3053	8619	61	Wienberg et al. (2020)

Table B.8: Data table for the Porcupine Seabight, which continues on the next page. For description and details, see start of the section.

No.	Sample-ID	Position	Method	Labcode	Age (yr BP)	error	Reference
51	GeoB14539-1	surface	14C	BETA 340740	3^{236}U	30	Wienberg et al. (2020)
52	GeoB14539-1	surface	14C	BETA 344874	3851	30	Wienberg et al. (2020)
53	GeoB14539-1	surface	14C	BETA 340742	7478	30	Wienberg et al. (2020)
54	GeoB14539-1	surface	14C	BETA 344873	7660	40	Wienberg et al. (2020)
55	GeoB14539-1	surface	14C	BETA 344876	7669	30	Wienberg et al. (2020)
56	GeoB14539-1	surface	14C	BETA 340741	7700	30	Wienberg et al. (2020)
57	GeoB14539-1	surface	14C	BETA 344872	7921	40	Wienberg et al. (2020)
58	GeoB14539-1	surface	14C	BETA 344875	8004	40	Wienberg et al. (2020)
59	GeoB14535-2	surface	14C	BETA 344871	1283	30	Wienberg et al. (2020)
60	GeoB14535-2	surface	14C	BETA 344869	1613	30	Wienberg et al. (2020)
61	GeoB14535-2	surface	14C	BETA 344870	1705	30	Wienberg et al. (2020)
62	GeoB14535-2	surface	14C	BETA 340739	1765	30	Wienberg et al. (2020)
63	GeoB14535-2	surface	14C	BETA 340737	4521	30	Wienberg et al. (2020)
64	GeoB14535-2	surface	14C	BETA 344868	8547	40	Wienberg et al. (2020)
65	GeoB14546-1	core	14C	BETA 340743	517	30	Wienberg et al. (2020)
66	GeoB14546-1	core	14C	BETA 340744	7710	30	Wienberg et al. (2020)
67	GeoB14547-1	core	U/Th	GEOMAR	7950	30	Wienberg et al. (2020)
68	GeoB14550-1	core	14C	BETA 340745	7941	35	Wienberg et al. (2020)
69	2491	surface	U/Th	IUPH	1540	160	Schröder-Ritzrau et al. (2005)
70	2350	surface	U/Th	IUPH	8560	390	Schröder-Ritzrau et al. (2005)
71	2307	surface	U/Th	IUPH	8890	160	Schröder-Ritzrau et al. (2005)
72	MD01-2459G	core	U/Th	GIF	4368	95	Frank et al. (2009)
73	MD01-2459G	core	U/Th	GIF	7540	180	Frank et al. (2009)
74	MD01-2459G	core	14C	Saclay, FR	8535	84	Frank et al. (2009)
75	MD01-2459G	core	U/Th	GIF	8765	190	Frank et al. (2009)
76	MD01-2459G	core	14C	Saclay, FR	8604	96	Frank et al. (2009)
77	MD01-2459G	core	U/Th	GIF	8520	100	Frank et al. (2009)
78	MD01-2459G	core	14C	Saclay, FR	8560	110	Frank et al. (2009)
79	MD01-2459G	core	U/Th	GIF	8930	170	Frank et al. (2009)
80	MD01-2459G	core	U/Th	GIF	9290	210	Frank et al. (2009)
81	MD01-2459G	core	U/Th	GIF	9742	74	Frank et al. (2009)

Rockall Trough

No.	Sample-ID	Position	Method	Labcode	Age (yr BP)	error	Reference
1	Coral2012-39PC	core	U/Th	GIF	251	14	Bonneau et al. (2018)
2	Coral2012-39PC	core	U/Th	GIF	276	6	Bonneau et al. (2018)
3	Coral2012-39PC	core	U/Th	GIF	473	79	Bonneau et al. (2018)
4	Coral2012-39PC	core	U/Th	GIF	606	36	Bonneau et al. (2018)
5	Coral2012-39PC	core	U/Th	GIF	663	320	Bonneau et al. (2018)
6	Coral2012-39PC	core	U/Th	GIF	719	9	Bonneau et al. (2018)
7	Coral2012-39PC	core	U/Th	GIF	740	11	Bonneau et al. (2018)
8	Coral2012-39PC	core	U/Th	GIF	854	8	Bonneau et al. (2018)
9	Coral2012-39PC	core	U/Th	GIF	1020	12	Bonneau et al. (2018)
10	Coral2013-18PC	core	U/Th	GIF	1293	33	Bonneau et al. (2018)
11	Coral2012-39PC	core	U/Th	GIF	1427	17	Bonneau et al. (2018)
12	Coral2012-39PC	core	U/Th	GIF	1431	14	Bonneau et al. (2018)
13	Coral2012-39PC	core	U/Th	GIF	1447	14	Bonneau et al. (2018)
14	Coral2012-39PC	core	U/Th	GIF	1475	271	Bonneau et al. (2018)
15	Coral2012-39PC	core	U/Th	GIF	1854	17	Bonneau et al. (2018)
16	Coral2012-39PC	core	U/Th	GIF	2008	15	Bonneau et al. (2018)
17	Coral2012-39PC	core	U/Th	GIF	2214	10	Bonneau et al. (2018)
18	Coral2012-39PC	core	U/Th	GIF	2308	10	Bonneau et al. (2018)
19	Coral2012-39PC	core	U/Th	GIF	2370	29	Bonneau et al. (2018)
20	Coral2012-39PC	core	U/Th	GIF	2530	15	Bonneau et al. (2018)
21	Coral2012-39PC	core	U/Th	GIF	2786	16	Bonneau et al. (2018)
22	Coral2012-39PC	core	U/Th	GIF	3581	15	Bonneau et al. (2018)
23	Coral2012-39PC	core	U/Th	GIF	3673	17	Bonneau et al. (2018)
24	Coral2013-18PC	core	U/Th	GIF	3694	17	Bonneau et al. (2018)
25	Coral2012-39PC	core	U/Th	GIF	3771	69	Bonneau et al. (2018)
26	Coral2012-39PC	core	U/Th	GIF	3797	14	Bonneau et al. (2018)
27	Coral2012-39PC	core	U/Th	GIF	4436	23	Bonneau et al. (2018)
28	Coral2012-39PC	core	U/Th	GIF	4527	21	Bonneau et al. (2018)
29	Coral2012-39PC	core	U/Th	GIF	4884	20	Bonneau et al. (2018)
30	Coral2012-39PC	core	U/Th	GIF	4998	228	Bonneau et al. (2018)
31	Coral2013-18PC	core	U/Th	GIF	5227	23	Bonneau et al. (2018)
32	Coral2012-39PC	core	U/Th	GIF	5258	19	Bonneau et al. (2018)
33	Coral2012-39PC	core	U/Th	GIF	5430	39	Bonneau et al. (2018)
34	Coral2013-18PC	core	U/Th	GIF	5436	56	Bonneau et al. (2018)
35	Coral2012-39PC	core	U/Th	GIF	6023	24	Bonneau et al. (2018)
36	Coral2013-18PC	core	U/Th	GIF	6069	26	Bonneau et al. (2018)
37	Coral2012-39PC	core	U/Th	GIF	6085	17	Bonneau et al. (2018)
38	Coral2012-39PC	core	U/Th	GIF	6110	38	Bonneau et al. (2018)
39	Coral2012-39PC	core	U/Th	GIF	6126	22	Bonneau et al. (2018)
40	Coral2013-18PC	core	U/Th	GIF	6528	78	Bonneau et al. (2018)
41	Coral2012-39PC	core	U/Th	GIF	6670	25	Bonneau et al. (2018)
42	Coral2013-18PC	core	U/Th	GIF	7175	38	Bonneau et al. (2018)
43	Coral2012-39PC	core	U/Th	GIF	7276	33	Bonneau et al. (2018)
44	Coral2012-39PC	core	U/Th	GIF	7562	37	Bonneau et al. (2018)
45	Coral2013-18PC	core	U/Th	GIF	7595	36	Bonneau et al. (2018)
46	Coral2013-18PC	core	U/Th	GIF	8650	89	Bonneau et al. (2018)
47	Coral2012-39PC	core	U/Th	GIF	8680	29	Bonneau et al. (2018)
48	Coral2012-39PC	core	U/Th	GIF	9144	31	Bonneau et al. (2018)
49	Coral2012-39PC	core	U/Th	GIF	9421	57	Bonneau et al. (2018)
50	Coral2012-39PC	core	U/Th	GIF	10024	324	Bonneau et al. (2018)

Table B.9: Data table for the Rockall Trough, which continues on the next two pages. For description and details, see start of the section.

No.	Sample-ID	Position	Method	Labcode	Age (yr BP)	error	Reference
51	Coral2012-39PC	core	U/Th	GIF	10079	53	Bonneau et al. (2018)
52	Coral2012-39PC	core	U/Th	GIF	10105	29	Bonneau et al. (2018)
53	Coral2012-39PC	core	U/Th	GIF	10752	47	Bonneau et al. (2018)
54	ENAM 9915	surface	U/Th	GIF	5	6	Frank et al. (2004)
55	ENAM 9915	surface	U/Th	GIF	31	12	Frank et al. (2004)
56	ENAM 9910	surface	U/Th	GIF	643	22	Frank et al. (2004)
57	ENAM 9915	surface	U/Th	GIF	746	22	Frank et al. (2004)
58	ENAM 9828	surface	U/Th	GIF	10480	140	Frank et al. (2004)
59	MD01-2454G	core	U/Th	GIF	15	15	Frank et al. (2009)
60	MD01-2455G	core	U/Th	GIF	188	32	Frank et al. (2009)
61	MD01-2454G	core	U/Th	GIF	360	140	Frank et al. (2009)
62	MD01-2455G	core	U/Th	GIF	680	250	Frank et al. (2009)
63	MD01-2454G	core	U/Th	GIF	891	89	Frank et al. (2009)
64	MD01-2454G	core	U/Th	GIF	1128	81	Frank et al. (2009)
65	MD01-2454G	core	U/Th	GIF	1456	100	Frank et al. (2009)
66	MD01-2455G	core	U/Th	GIF	2238	68	Frank et al. (2009)
67	MD01-2454G	core	14C	GIF	2371	115	Frank et al. (2009)
68	MD01-2454G	core	14C	GIF	2463	110	Frank et al. (2009)
69	MD01-2454G	core	U/Th	GIF	2560	130	Frank et al. (2009)
70	MD01-2455G	core	U/Th	GIF	2880	220	Frank et al. (2009)
71	MD01-2454G	core	U/Th	GIF	3190	240	Frank et al. (2009)
72	MD01-2454G	core	U/Th	GIF	3345	295	Frank et al. (2009)
73	MD01-2454G	core	U/Th	GIF	3510	91	Frank et al. (2009)
74	MD01-2454G	core	U/Th	GIF	3600	130	Frank et al. (2009)
75	MD01-2454G	core	U/Th	GIF	3831	27	Frank et al. (2009)
76	MD01-2454G	core	U/Th	GIF	4869	42	Frank et al. (2009)
77	MD01-2454G	core	U/Th	GIF	4961	77	Frank et al. (2009)
78	MD01-2454G	core	U/Th	GIF	4976	78	Frank et al. (2009)
79	MD01-2454G	core	U/Th	GIF	5040	61	Frank et al. (2009)
80	MD01-2454G	core	U/Th	GIF	5270	110	Frank et al. (2009)
81	MD01-2455G	core	U/Th	GIF	5420	140	Frank et al. (2009)
82	MD01-2454G	core	U/Th	GIF	5620	240	Frank et al. (2009)
83	MD01-2454G	core	U/Th	GIF	5667	38	Frank et al. (2009)
84	MD01-2454G	core	U/Th	GIF	6080	140	Frank et al. (2009)
85	MD01-2454G	core	U/Th	GIF	6992	214	Frank et al. (2009)
86	MD01-2454G	core	U/Th	GIF	7679	72	Frank et al. (2009)
87	MD01-2454G	core	U/Th	GIF	7730	230	Frank et al. (2009)
88	MD01-2455G	core	U/Th	GIF	7980	280	Frank et al. (2009)
89	MD01-2454G	core	U/Th	GIF	8430	200	Frank et al. (2009)
90	MD01-2455G	core	U/Th	GIF	9370	220	Frank et al. (2009)
91	MD01-2454G	core	U/Th	GIF	9400	160	Frank et al. (2009)
92	MD01-2455G	core	U/Th	GIF	10270	320	Frank et al. (2009)
93	MD01-2455G	core	U/Th	GIF	10660	230	Frank et al. (2009)
94	MD01-2455G	core	U/Th	GIF	10670	460	Frank et al. (2009)
95	MD01-2454G	core	U/Th	GIF	10880	340	Frank et al. (2009)
96	MD01-2455G	core	U/Th	GIF	11270	170	Frank et al. (2009)
97	MD01-2454G	core	U/Th	GIF	83	32	Frank et al. (2011)
98	MD01-2455G	core	U/Th	GIF	200	200	Frank et al. (2011)
99	MD01-2455G	core	U/Th	GIF	240	120	Frank et al. (2011)
100	MD01-2454G	core	U/Th	GIF	680	140	Frank et al. (2011)

No.	Sample-ID	Position	Method	Labcode	Age (yr BP)	error	Reference
101	MD01-2454G	core	U/Th	GIF	750	70	Frank et al. (2011)
102	MD01-2455G	core	U/Th	GIF	2240	68	Frank et al. (2011)
103	MD01-2454G	core	U/Th	GIF	2270	82	Frank et al. (2011)
104	MD01-2454G	core	U/Th	GIF	2460	80	Frank et al. (2011)
105	MD01-2454G	core	U/Th	GIF	2750	125	Frank et al. (2011)
106	M2003-23	core	14C	Utrecht-14972	1369	32	Mienis et al. (2009)
107	M2003-23	core	14C	Utrecht-14973	5450	36	Mienis et al. (2009)
108	M2003-23	core	14C	Utrecht-14974	10489	60	Mienis et al. (2009)
109	M2003-23	core	U/Th	Amsterdam	51	10	Mienis et al. (2009), Van der Land et al. (2010)
110	M2003-23	core	U/Th	Amsterdam	1330	40	Mienis et al. (2009), Van der Land et al. (2010)
111	M2003-23	core	U/Th	Amsterdam	5570	80	Mienis et al. (2009), Van der Land et al. (2010)
112	M2003-23	core	U/Th	Amsterdam	10800	80	Mienis et al. (2009), Van der Land et al. (2010)
113	2706	surface	U/Th	IUPH	560	70	Schröder-Ritzrau et al. (2005)
114	M2001-43	core	U/Th	Amsterdam	110	5	Van der Land et al. (2010)
115	M2001-28	core	U/Th	Amsterdam	830	20	Van der Land et al. (2010)
116	M2001-43	core	U/Th	Amsterdam	5920	480	Van der Land et al. (2010)
117	M2001-43	core	U/Th	Amsterdam	10900	110	Van der Land et al. (2010)
118	M2001-28	core	U/Th	Amsterdam	11000	50	Van der Land et al. (2010)
119	JC060-035-S1-17	core	14C	Beta	3541	30	Victorero et al. (2016)
120	JC060-038-S2-19	core	U/Th	Gif	5950	220	Victorero et al. (2016)
121	JC060-0S38-S2-19	core	U/Th	Gif	6120	50	Victorero et al. (2016)
122	JC060-035-S2-70	core	U/Th	Gif	6200	120	Victorero et al. (2016)
123	JC060-035-S2-70	core	U/Th	Gif	6290	80	Victorero et al. (2016)
124	JC060-038-S2-19	core	U/Th	Gif	6350	70	Victorero et al. (2016)
125	JC060-038-S2-19-outer	core	U/Th	Gif	6680	50	Victorero et al. (2016)
126	JC060-038-S3-60	core	U/Th	Gif	8690	270	Victorero et al. (2016)
127	JC060-038-S2-101	core	U/Th	Gif	8730	90	Victorero et al. (2016)
128	JC060-038-S3-97	core	U/Th	Gif	8780	440	Victorero et al. (2016)
129	JC060-035-S3-26	core	14C	Beta	8862	40	Victorero et al. (2016)
130	JC060-038-S3-80	core	U/Th	Gif	9570	120	Victorero et al. (2016)
131	JC060-035-S3-26	core	U/Th	Gif	9600	110	Victorero et al. (2016)
132	JC060-038-S3-80	core	U/Th	Gif	9630	280	Victorero et al. (2016)
133	JC060-035-S3b-111	core	U/Th	Gif	9950	320	Victorero et al. (2016)
134	JC060-038-S4-75	core	14C	Beta	10000	40	Victorero et al. (2016)
135	JC060-035-S3b-111	core	U/Th	Gif	10130	90	Victorero et al. (2016)
136	JC060-035-S4-08	core	14C	Beta	10138	40	Victorero et al. (2016)
137	JC060-038-S4-75	core	U/Th	Gif	10210	50	Victorero et al. (2016)
138	JC060-038-S4-75	core	U/Th	Gif	10280	110	Victorero et al. (2016)

Norwegian shelf

No.	Sample-ID	Position	Method	Labcode	Age (yr BP)	error	Reference
1	2127	?	U/Th	IUPH	3010	90	Schröder-Ritzrau et al. (2005)
2	JM01-1501	?	U/Th	GIF	554	25	Lindberg and Mienert (2005)
3	JM01-1501	?	U/Th	GIF	1150	210	Lindberg and Mienert (2005)
4	JM01-1501	?	U/Th	GIF	1244	38	Lindberg and Mienert (2005)
5	JM01-1501	?	U/Th	GIF	1321	12	Lindberg and Mienert (2005)
6	KI-1517.011	?	14C		188	65	Mikkelsen et al. (1982)
7	KI-1518.071	on land	14C		8817	95	Mikkelsen et al. (1982)
8	KI-1518.091	on land	14C		9024	90	Mikkelsen et al. (1982)
9	KI-1518.041	on land	14C		9341	105	Mikkelsen et al. (1982)
10	KI-1518.051	?	14C		9186	110	Mikkelsen et al. (1982)
11	KI-1518.131	?	14C		9340	200	Mikkelsen et al. (1982)
12	KI-1518.431	?	14C		9436	70	Mikkelsen et al. (1982)
13	KI-1518.081	on land	14C		9843	145	Mikkelsen et al. (1982)
14	KI-1518.061	on land	14C		9855	130	Mikkelsen et al. (1982)
15	ALK-232-1155	?	U/Th	GIF	8	3	Frank et al. (2011)
16	ALK-232-1147	?	U/Th	GIF	34	2	Frank et al. (2011)
17	ALK-232-1022 1b	?	U/Th	GIF	64	17	Frank et al. (2011)
18	2709	?	U/Th	IUPH	2110	50	Schröder-Ritzrau et al. (2005)
19	ALK-232-1021 2b	?	U/Th	GIF	2694	55	Frank et al. (2011)
20	2711	?	U/Th	IUPH	2980	90	Schröder-Ritzrau et al. (2005)
21	STJ-POS325-470	core	14C	Poz-24318	10927	50	Correa et al. (2012)
22	STJ-POS325-472	core	U/Th	GEOMAR	1615	56	Correa et al. (2012)
23	STJ-POS325-472	core	U/Th	GEOMAR	1828	18	Correa et al. (2012)
24	STJ-POS325-472	core	U/Th	GEOMAR	1918	19	Correa et al. (2012)
25	STJ-POS325-472	core	U/Th	GEOMAR	2284	23	Correa et al. (2012)
26	STJ-POS325-472	core	U/Th	GEOMAR	3035	18	Correa et al. (2012)
27	STJ-POS325-472	core	U/Th	GEOMAR	3206	42	Correa et al. (2012)
28	STJ-POS325-472	core	U/Th	GEOMAR	9413	48	Correa et al. (2012)
29	STJ-POS325-472	core	U/Th	GEOMAR	9528	49	Correa et al. (2012)
30	STJ-POS325-472	core	U/Th	GEOMAR	9561	52	Correa et al. (2012)
31	STJ-POS325-472	core	U/Th	GEOMAR	9606	53	Correa et al. (2012)
32	STJ-POS325-472	core	U/Th	GEOMAR	9609	62	Correa et al. (2012)
33	STJ-POS325-472	core	U/Th	GEOMAR	9851	67	Correa et al. (2012)
34	STJ-POS325-471	core	U/Th	GEOMAR	10034	75	Correa et al. (2012)
35	STJ-POS325-459	core	U/Th	GEOMAR	10142	78	Correa et al. (2012)
36	STJ-POS325-457	core	U/Th	GEOMAR	10174	76	Correa et al. (2012)
37	STJ-POS325-470	core	U/Th	GEOMAR	10666	84	Correa et al. (2012)
38	STJ-POS325-473	core	U/Th	GEOMAR	10813	83	Correa et al. (2012)
39	STJ-POS325-430	core	U/Th	GEOMAR	10822	94	Correa et al. (2012)
40	STJ-POS325-430	core	U/Th	GEOMAR	10896	77	Correa et al. (2012)
41	PS70-35-3GC-1	core	14C	UCIAMS-96731	682	20	Titschack et al. (2015)
42	PS70-35-2GC-1	core	14C	UCIAMS-96725	1524	15	Titschack et al. (2015)
43	PS70-35-3GC-1	core	14C	UCIAMS-96729	1900	15	Titschack et al. (2015)
44	PS70-35-3GC-1	core	14C	UCIAMS-96730	2174	15	Titschack et al. (2015)
45	PS70-35-2GC-1	core	14C	UCIAMS-96726	2283	15	Titschack et al. (2015)
46	PS70-35-3GC-1	core	14C	UCIAMS-96732	2446	15	Titschack et al. (2015)
47	PS70-35-3GC-1	core	14C	UCIAMS-96733	2560	15	Titschack et al. (2015)
48	PS70-35-2GC-1	core	14C	UCIAMS-96728	2623	15	Titschack et al. (2015)
49	TRD-POS325-359	core	U/Th	GEOMAR	2427	19	Correa et al. (2012)
50	TRD-POS325-359	core	U/Th	GEOMAR	3269	32	Correa et al. (2012)

Table B.10: Data table for the Norwegian shelf (and Faroer), which continues on the next page. For description and details, see start of the section. Please note that the ages for samples No. 70-111 are not in yrs BP.

No.	Sample-ID	Position	Method	Labcode	Age (yr BP)	error	Reference
51	TRD-POS325-359	core	U/Th	GEOMAR	3355	26	Correa et al. (2012)
52	TRD-POS325-359	core	U/Th	GEOMAR	3703	23	Correa et al. (2012)
53	TRD-POS325-359	core	U/Th	GEOMAR	3910	42	Correa et al. (2012)
54	2740	?	U/Th	IUPH	100	5	Schröder-Ritzrau et al. (2005)
55	2660	?	U/Th	IUPH	1060	180	Schröder-Ritzrau et al. (2005)
56	3237	?	U/Th	IUPH	1480	100	Schröder-Ritzrau et al. (2005)
57	T-13205	?	14C		1552	80	Hovland and Mortensen (1999)
58	T-13206	?	14C		1564	80	Hovland and Mortensen (1999)
59	T-13207	?	14C		2039	100	Hovland and Mortensen (1999)
60	T-13209	?	14C		2497	85	Hovland and Mortensen (1999)
61	T-13210	?	14C		2707	50	Hovland and Mortensen (1999)
62	T-13208	?	14C		2717	50	Hovland and Mortensen (1999)
63	AAR-4223	?	14C		2819	50	Hovland and Mortensen (1999)
64	T-11349	?	14C		6450	105	Hovland et al. (1998), Hovland and Mortensen (1999)
65	T-11076A	?	14C		6987	90	Hovland et al. (1998)
66	T-11076B	?	14C		7096	95	Hovland et al. (1998), Hovland and Mortensen (1999)
67	T-11348	?	14C		8547	130	Hovland et al. (1998), Hovland and Mortensen (1999)
68	T-13204	?	14C		9125	125	Hovland and Mortensen (1999)
69	AAR-4224	?	14C		9280	70	Hovland and Mortensen (1999)
70	550-1/JAGO/220	surface	U/Th		20	10	Raddatz et al. (2016)
71	551-2/GC/244	core	U/Th		7500	200	Raddatz et al. (2016)
72	551-3/GC/?	core	U/Th		10100	100	Raddatz et al. (2016)
73	557-3/GC/268	core	U/Th		10200	200	Raddatz et al. (2016)
74	557-3/GC/268	core	U/Th		10000	300	Raddatz et al. (2016)
75	559-2/GC/225	core	U/Th		6400	100	Raddatz et al. (2016)
76	559-2/GC/225	core	U/Th		6400	300	Raddatz et al. (2016)
77	559-2/GC/225	core	U/Th		7500	200	Raddatz et al. (2016)
78	559-2/GC/225	core	U/Th		7100	300	Raddatz et al. (2016)
79	559-2/GC/225	core	U/Th		7700	300	Raddatz et al. (2016)
80	559-2/GC/225	core	U/Th		7900	100	Raddatz et al. (2016)
81	559-2/GC/225	core	U/Th		8500	200	Raddatz et al. (2016)
82	559-2/GC/225	core	U/Th		9000	200	Raddatz et al. (2016)
83	559-2/GC/225	core	U/Th		8800	100	Raddatz et al. (2016)
84	559-2/GC/225	core	U/Th		8700	300	Raddatz et al. (2016)
85	559-2/GC/225	core	U/Th		10300	100	Raddatz et al. (2016)
86	559-2/GC/225	core	U/Th		4800	100	Raddatz et al. (2016)
87	559-3/GC/237	core	U/Th		7400	100	Raddatz et al. (2016)
88	559-3/GC/237	core	U/Th		20	10	Raddatz et al. (2016)
89	563-1/v.V.Gr./285	surface	U/Th		20	10	Raddatz et al. (2016)
90	571-1/JAGO/100	surface	U/Th		4600	100	Raddatz et al. (2016)
91	575-2/GC/99	core	U/Th		4700	200	Raddatz et al. (2016)
92	575-2/GC/99	core	U/Th		1580	20	Raddatz et al. (2016)
93	576-1/GC/101	core	U/Th		1630	40	Raddatz et al. (2016)
94	576-1	core	U/Th		1501	19	Raddatz et al. (2022)
95	576-1	core	U/Th		1442	17	Raddatz et al. (2022)
96	576-1	core	U/Th		1940	22	Raddatz et al. (2022)
97	576-1	core	U/Th		2413	22	Raddatz et al. (2022)
98	576-1	core	U/Th		2372	26	Raddatz et al. (2022)
99	576-1	core	U/Th		2407	27	Raddatz et al. (2022)
100	576-1	core	U/Th		2321	21	Raddatz et al. (2022)
101	576-1/GC/101	core	U/Th		2780	80	Raddatz et al. (2016)
102	576-1	core	U/Th		2444	26	Raddatz et al. (2022)
103	576-1	core	U/Th		2679	26	Raddatz et al. (2022)
104	576-1	core	U/Th		2809	24	Raddatz et al. (2022)
105	576-1	core	U/Th		2816	28	Raddatz et al. (2022)
106	576-1	core	U/Th		2833	30	Raddatz et al. (2022)
107	576-1	core	U/Th		2892	25	Raddatz et al. (2022)
108	576-1	core	U/Th		3184	25	Raddatz et al. (2022)
109	576-1	core	U/Th		4132	42	Raddatz et al. (2022)
110	576-1/GC/101	core	U/Th		3400	100	Raddatz et al. (2016)
111	576-1/GC/101	core	U/Th		3510	200	Raddatz et al. (2016)

C Danksagung

Ein so großes Unterfangen wie eine Doktorarbeit wäre nicht möglich ohne Unterstützung von vielen Seiten. Für selbige möchte ich mich an dieser Stelle bedanken (in der Hoffnung darauf, dass die Liste einigermaßen vollständig ist)!

Vielen, vielen Dank zunächst an Norbert Frank - für die Betreuung meiner Arbeit und die Begeisterung für die Umweltphysik und das Paläoklima, die er stets ausstrahlt. Danke auch für das Vertrauen in mich, sodass mir viele Freiheiten in der Ausgestaltung und Themensetzung meiner Projekte gelassen wurden, und ich immer wieder eigene Ideen verfolgen durfte. Gleichzeitig hatte er immer hilfreiche Ratschläge parat, wenn es in einer Richtung sonst nicht weiterging.

An Werner Aeschbach richte ich ein ausdrückliches Danke dafür, das Zweitgutachten zu übernehmen. Außerdem möchte ich mich bei Eva Grebel und bei Matthias Bartelmann dafür bedanken, dass sie in meinem Disputationskomitee sein werden.
Danke an meine Co-Betreuer Denis Scholz und Roland Kröger für die hilfreichen Diskussionen zu meiner Arbeit, und an Roland Kröger für das interessante Forschungsprojekt zur Biomineralisation während meines Erasmus-Aufenthalts in York im Masterstudium. Ohne dieses Projekt wäre ich wahrscheinlich nicht den Weg in die Umweltphysik gegangen.

An Andrea Schröder-Ritzrau danke für die vielen Diskussionen zum Auftreten von Kaltwasserkorallen. Ich konnte ich mich auch immer an sie wenden, wenn ich Rat zu den vielen Metadaten in Bezug auf Kaltwasserkorallen brauchte. Danke für die stetige Hilfsbereitschaft während meiner Arbeit, insb. auch beim Korrekturlesen!
René Eichstädter ein Dankeschön für die ausgiebigen Diskussionen zum Massenspektrometer und zur Datierung, bei denen ich viel gelernt habe.
Danke an Sophie Warken für die immer ausführlichen und hilfreichen Kommentare zu Manuskripten!

Für meinen Aufenthalt am MARUM möchte ich mich bei Jürgen Titschack und Claudia Wienberg bedanken; wie auch für das Interesse und die große Unterstützung bei dem Projekt! Außerdem danke an Dierk Hebbeln, in dessen Gruppe ich zu Gast war, und an Norbert Frank für die Möglichkeit des Aufenthalts dort.

Bei Zsolt Varga vom JRC Karlsruhe bedanke ich mich für die Zusendung des VRM06/23 Referenzmaterials und die Hilfsbereitschaft bei allen Fragen dazu.

An Martin Scharpenberg von der Uni Bremen geht ein herzliches Danke für seine Hinweise und sein Feedback zur KDE Methode.

Fabian Kontor, dessen Bachelorarbeit ich betreut habe, hat mit der Arbeit an der GUI viel zur Th/U Datierung am IUP beigetragen, und seine Entwicklung ist auch Teil meines Projekts und dieser Arbeit geworden. Danke für diese Leistung und die angenehme Zusammenarbeit!

Danke an alle PUAs für die schöne Zeit mit euch! Eva auch vielen Dank für das Teilen ihrer Fähigkeiten im Kartenerstellen und das Korrekturlesen, und Elvira für das Teilen der Alterstabelle. Meinen Büronachbar*innen während der Zeit am IUP (insb. Elvira, Yao, und Steffen) danke für die schöne Atmosphäre. Der Doktorand*innen-Generation vor mir möchte ich für viele hilfreiche Ratschläge danken, v. a. Marleen, Steffen und Jasmin.

Auch bei meinen Freunden, die mich zum Teil vom Anfang des Studiums bis jetzt begleitet haben, vielen herzlichen Dank!

Zum Abschluss nochmal ganz, ganz herzlich Danke:
An meine Eltern, die immer an mich und meine Fähigkeiten glauben und mich jederzeit auf meinem Weg unterstützen.
Und an den wunderbaren Timo, für all die gemeinsamen Erlebnisse, das geteilte Lachen und das Dasein, wenn ich ihn brauche.

Vielen Dank euch allen!